Development of a synthetic trabecular bone graft utilizing a two phase glass-ceramic

Christopher Andrew Serna

Submitted in accordance with the requirements for the degree of Doctor of Philosophy

The University of Leeds

School of Mechanical Engineering

December 2016

The candidate confirms that the work is his/her own and that appropriate credit has been given where reference has been made to the work of others.

Acknowledgements

In Memory of

Leo, Paul and George O’Hagan

Dedicated to

Erin and Finlay Morrow

I will start by thanking my supervisors Dave, Nigel and Xuebin. You listened to all of my ideas and gently steered me towards an achievable conclusion; I will sorely miss our meetings and wish you luck in the future, thank you for giving me this second chance. To Mick; a genius behind the workbench and a gentleman, thank you for all the contraptions. To Claire, thank you for keeping track of my finances so I could replace all of the equipment. Jackie, without you there would be no images in this thesis and therefore no thesis. Adam Steel; a fantastic man with a majestic moustache, whatever happens we'll always have Kazakhstan.

To my estranged friends; I'm sorry I have been noticeably absent over these years but just know I feel privileged to know you all, thank you for being there for me. To the new friends I have made during this time; Scott, Giuseppe, Nikolleta, Adam, to name but a few. Thank you. Sushmita and Liam, who taught me that in the end cells aren't all that scary. Georg, you I must mention in particular, it has been a pleasure. Thank you for guiding me through the void and back.

Dr William Vickers; you taught me everything you could possibly need to know about glass making with ferocious enthusiasm, I hope we remain friends for many years. Maria, you poured every drop of glass and never failed to tell me to "keep going". Asma; thank you for simply listening and smiling over all these years, you never failed to cheer me up.

Paul and Leo O'Hagan; your musical taste has resonated with me through till the present, without which the late hours in the lab would not have been possible. I miss you both dearly. To my parents, this was difficult on us all. I will never be able to thank you enough for all you have done for me. You both truly have the patience of saints. I honestly can't see how you could be better people and role models.

Above all though, I dedicate this thesis to Erin and Finlay. When you are old enough I'll explain how even at this age you helped me reach the end. You, much like this body of work, are the sum of the greatest parts.

Abstract

The aim of this work was to produce and characterise porous glass-ceramic scaffolds that mimicked human trabecular bone through the foam replica technique. Parent glasses were formed via a melt quench route to produce glass frits, these were then processed into powders consisting of <45 µm particles confirmed through particle analysis. DSC analysis confirmed a glass transition region of ~ 750 °C, two crystallisation peaks were noted at 886 °C and 942 °C. Combining multiple glass batches exhibited properties consistent with single batch analysis, allowing for scale up of glass volumes and sample sizes for characterisation. Slurries of varying ratios of glass and binder (polyvinyl alcohol) were then produced and used to coat a polyurethane foam template. Two distinct heat treatments were then designed from initial studies; SEM analysis confirmed a dwell at 800 °C for 5 hours sufficiently sintered the glass particles, XRD analysis confirmed a tertiary dwell at 950 °C for 1 hour formed both apatite and wollastonite phases.

Biaxial flexural testing and micro-CT analysis showed that with decreasing glass content within the initial slurry the resultant mechanical and architectural properties diminished. Excessive use of binder within the initial slurry was also found to diminish the consistency and properties of the scaffolds produced. Coating the porous scaffolds with fluorapatite was shown to be feasible; the crystallinity of the substrate was found to alter the resultant crystal morphologies. Human adipose derived stem cells (hADSC's) were shown to both attach and proliferate on scaffolds, with or without a fluorapatite coating.

Table of Contents

List of Figures

List of Tables

Nomenclature

Abbreviations

α-TCP	α-tricalcium phosphate
αvβ3	Vitronectin receptor
β-TCP	β – tricalcium phosphate
A/W	Apatite Wollastonite
ALP	Alkaline phosphatase
AM	Additive manufacturing
APS	Amorphous phase separation
bBMP	Bovine bone morphogenic protein
BMP	Bone morphogenic protein
BTE	Bone tissue engineering
BV/TV	Bone volume to total volume
BS/BV	Surface density
CAD	Computer aided manufacturing
DMEM	Dulbeco’s modified eagle’s medium
DSC	Differential scanning calorimetry
DTA	Differential thermal analysis
ECM	Extra cellular matrix
EDX	Energy-dispersive X-ray spectroscopy
FA	Fluorapatite
FDA	Food and Drug Administration
FGF	Fibroblast growth factor
FGM	Functional gradient material
FWHM	Full width at half maximum
GC	Glass ceramic
HA	Hydroxyapatite
hADSC	Human adipose derived stem cells
HCA	Hydroxo-carbonate-apatite
IB	Index of bioactivity
ITGA 7	Integrin alpha 7
ITGA 8	Integrin alpha 8
ITGAV	Integrin alpha V
ITGB3	Integrin beta 3
ITGB4	Integrin beta 4
LPS	Liquid phase sintering
MMA	Methyl methacrylate
MSC	Mesenchymal stem cell
PBS	Phosphate buffered saline
PCL	Poly-epsilon-caprolactone
PDLLA	Poly (D,L-lactic acid)
PGA	Poly (glycolic acid)
PGLA	Poly (lactic-co-glycolic acid)

PLLA	Poly (L-lactic acid)
PMMA	Poly (methyl methacrylate)
PPI	Pores per inch
PRP	Platelet-rich plasma
PU	Polyurethane
PVA	Polyvinyl alcohol
PVB	Poly vinyl butyral
rhBMP	Recombinant human bone morphogenic protein
RM	Regenerative medicine
S.D.	Standard deviation
SEM	Scanning electron microscope
SLS	Selective laser sintering
SPP1	Secreted phosphoprotein 1
Tb.N	Trabecular number
Tb.Sp	Trabecular spacing
Tb.Th	Trabecular thickness
TE	Tissue engineering
T_g	Glass transition temperature
TGF-β	Transforming growth factor-β
THBS3	Thrombospondin 3
THR	Total hip replacement
T_m	Melting temperature
Tp1	First crystallisation peak
Tp2	Second crystallisation peak
UHMWPE	Ultra high molecular weight polyethylene
VEGF	Vascular endothelial growth factor

Chemical compounds and elements/ions

$Ca_{10}(PO_4)_6(O,F_2)$	Apatite
$Ca.SiO_3$	Wollastonite

Al_2O_3	Aluminium oxide
Ar	Argon
Au	Gold
B_2O_3	Boron trioxide
Ca^{2+}	Calcium ion
CaF_2	Calcium fluoride
CaO	Calcium oxide
CO_3^{2-}	Carbonate
EDTA-Ca	Calcium-ethylene diamintetraacetic acid
F^-	Fluoride ion
Fe_2O_3	Iron (III) oxide
GeO_2	Germanium oxide
H^+	Hydrogen ion
H_2O	Water
H_3O^+	Hydronium ion
HCl	Hydrochloric acid

He	Helium
K_2O	Potassium oxide
Kr	Krypton
MgO	Magnesium oxide
Na^+	Sodium ion
NaF	Sodium fluoride
Na_2O	Sodium oxide
NaH_2PO_4	Mono sodium phosphate
NaOH	Sodium hydroxide
Ne	Neon
OH^-	Hydroxide
P_2O_5	Phosphorous pentoxide
PO_4^{3-}	Phosphate
Pt	Platinum
SiO_2	Silicon dioxide (Silica)
$Si(OH)_4$	Silic acid
TiO_2	Titanium (IV) oxide

Units

°C	Centigrade (temperature)
µA	Microamps
µg	Micrograms
µl	Microlitre
µm	Micrometer
atm	Atmospheres
cm^3	Centimeters cubed
F	Load
g	Gram
g/cm^3	Density
GPa	Gigapascals
hr	Hour
Hv	Vickers hardness
K	Kelvin (temperature)
kV	Kilovolts
ml	Millilitre
mm	Millimetre
mM	Millimolar
$mgHA/cm^3$	Hydroxyapatite density
MPa	Megapascals
$MPa.m^{0.5}$	Fracture toughness
N	Newton
nm	Nanometer
Pa	Pascal
pH	Scale of acidity (potential of hydrogen)
R_c	Cation radii
R_a	Anion radii
Ra	Roughness average
rad	Radiation absorbed dose

1. Introduction

Throughout human history, materials have been used to alleviate pain, restore functionality and ultimately reduce mortality rates. As technologies advanced through the 20th century, several milestones were reached and medical devices such as hip replacements were becoming "gold standards" in the orthopaedic field (1, 2). In terms of these medical devices, as more information was gathered on their clinical performance it was subsequently discovered that wear debris from the polyethylene component of the hip replacement (UHMWPE) led to osteolysis and prosthesis loosening (2). In addition to this a new phenomenon of "stress-shielding" was reported; due to the disparity between the mechanical properties of the metallic femoral stem, poly(methyl methacrylate) (PMMA) (3) and the surrounding tissue, the natural response of the cells was to remove the "un-necessary" tissue. This led to micro-motion of the metallic stem, pain and ultimately costly revision surgeries.

Towards the end of the 20th century, a new concept was emerging, tissue engineering (TE) and regenerative medicine (RM). By combining engineering principles with cellular biology; materials and constructs could be created to restore functionality in the short term, and allow natural remodelling processes to take over in the long term, ultimately resulting in complete restoration to an affected area with none of the originally implanted material remaining (4).

Several strategies were explored; early successes worth noting are that of Apligraf® and Dermagraft®; skin grafting products composed of synthetic polymers combined with fibroblasts (a common cell found in connective tissue, i.e. skin, muscle, etc.) which were FDA approved in 1998 and 2001 respectively (5). Initially applied to a significantly large wound to provide immediate protection from infection; over time the polymer is broken down through natural processes, ultimately resulting in a fully healed area of skin with none of the original synthetic material remaining. This raised the question of whether this strategy could be employed to all structures of the body, e.g. bone, and whether treatments could reach the stage where previously damaged areas were indistinguishable from healthy areas post-operatively.

Bone has an inherent ability to heal itself in the event of minor fractures, however when a significant wound is created an external material is required to aid in healing. This non-union defect is commonly termed as a “critical bone defect”, consisting of a gap larger than a few millimetres. Currently the gold standard of treatment is an autologous graft; trabecular bone is harvested from a healthy site (e.g. iliac crest) of the patient and transplanted to the affected site. Autologous transplants have the advantages of rapid integration and lack of rejection, this explains their wide use and claim of current “gold standard” in orthopaedic treatment (6). Where this treatment is deemed successful it is primarily limited by donor site availability (and subsequent damage to the surrounding site post extraction) and severe pain suffered from the donor site (7). A synthetic material used as a bone substitute would eliminate the need to perform autologous transplants; it would be more readily available and reliable.

Historically, synthetic implants have been constructed from materials that are classed as biologically “inert”; this results in the implant being encapsulated by fibrous tissue. Whilst encapsulation is an acceptable response to a biocompatible medical implant, this fibrous layer prevents them from bonding directly with the bone. As such, complications can arise after surgery in the form of micro-motion and loosening of the implant, this in turn causes pain, ultimately resulting in revision surgery. An alternative to using an “inert” material is to use a “bioactive” material, such as certain compositions of glasses and ceramics. These materials form a direct bond to bone, achieved from eliciting specific biological responses at the bone-interface site, forming a physiochemical bond. A bioactive material will have a much greater chance of achieving a secure fixation and ultimately a much higher success rate.

Calcium phosphate ceramics present themselves as likely candidates for creating a synthetic bone graft, primarily due to their inherent similarity to the mineral phase of natural bone. They have been shown to be resistant to the corrosive nature of bodily fluids and illicit negligible foreign body reactions (8). Such materials include fluorapatite (FA), hydroxyapatite (HA), β-tricalcium phosphate (β-TCP), and α-tricalcium phosphate (α-TCP). Of these, FA and HA are very stable and will not readily absorb under physiological conditions. β-TCP and α-TCP are less stable and can be combined with HA to control degradation rates and allow for the formation of a bone bonding apatite layer on their surfaces.

Certain compositions of glass-ceramics have also been of great interest in the biomedical field; especially with regards to repair/replacement of natural bone and for dental restoration (9-11). Glass-ceramics are polycrystalline solids prepared by the controlled crystallization of glasses. To produce a glass-ceramic, a base glass is first produced, then a specific heat treatment is applied to that glass, ideally resulting in the volume nucleation and growth of crystal phases within the glass; these act as an impediment for fracture propagation by causing deflection, branching or splitting of propagating cracks. The resultant glass-ceramic displays superior mechanical properties compared to the base glass.

Some glass-ceramics have been commercialised and marketed such as Dicor® (mica glass-ceramic), Ceravital® and Bioverit® (mica-apatite glass-ceramic) (12-15). Among them the glass-ceramics containing apatite [$Ca_{10}(PO_4)_6(O,F_2)$] and wollastonite [$Ca.SiO_3$] crystals (A/W glass-ceramics) as the predominant crystalline phases in the $MgO-CaO-SiO_2$ glass matrix have received great importance as a biomaterial, especially in the replacement of natural bone (16-18). The discovery of A/W glass-ceramics by Kokubo *et al.* in 1982 (16) has drawn great attention principally due to their bioactive nature and ability to bond spontaneously to living bone in a short period. Additionally A/W are noted to have high mechanical properties such as toughness and strength for a long period in a body environment (17, 18).

Currently A/W glass-ceramics have found special applications in the clinic; either in powder form as bone filler, bulk material for fabricating iliac crest prostheses, artificial vertebrae, spinal spacers, and intervertebral spacers (19, 20). Yamamuro (20) reported that A/W glass-ceramic has been successfully used in spine and hip surgery of patients with extensive lesions or bone defects. The development of a porous A/W glass-ceramic is the subject of current research through the use of various strategies, one such strategy is known as the foam replica technique. However, before these strategies are discussed in more detail the following sections aim to introduce the reader to the relative historical context and basic principles that have led to the strategy of tissue engineering and bone replacement materials.

2. Literature Review

2.1. Bone – Form and function

Bone tissue may be considered mechanically as a complex composite material functioning to resist stress, provide articulation sites, and to give rigidity and shape to the body. In an extremely generalized model, bone may be split into two main types: cortical (compact) and cancellous (trabecular) bone. Cortical bone is much denser than cancellous bone, its thickness and shape are dependent upon the support required. Cancellous bone is highly porous (visible to the naked eye), this large porosity provides a large surface area to support complex stresses. Much like the Bauhaus principle of design its form follows its function; as such its remodelling and repair mechanisms are dictated via its structure and environment, as suggested by Wolff (21, 22). However the suggestion that compact bone is merely dense cancellous bone is not accurate when the mechanical properties of these materials are compared (23). The model of bone has changed dramatically over the years; once thought of as merely a static support structure, it is now known that bone is a site of high metabolic activity with constant turnover of extra cellular matrix (ECM) and migration of cells (24-26). However; before the mechanics and functionality of bone are discussed, the structure of bone from micro-to-macro level will be briefly outlined. This section aims to describe defined levels of bone, the constituents at each level and the resulting effect these levels have on the overall functionality of bone.

2.1.1. Bone Anatomy – Microscopic to Macroscopic

Bone is a highly vascularized connective tissue (27); composed of a fibrous protein (collagen) providing flexibility and resistance to extension, stiffened by surrounding calcium phosphate crystals providing hardness rigidity. It is moderately hydrated; in a mature bone ~ 10-20 % of the bone's mass is water. Considering its dry weight, 60-70 % is inorganic mineral salts (i.e. hydroxyapatite) and ~30 % is collagen (28, 29).

Collagen comprises 80-90 % of the protein present in bone, the most common type of collagen found in bone is collagen type I. The collagen is covalently cross-linked which increases mechanical strength and makes the protein more chemically inert (30), the internal gaps between the collagen fibres provide the mineral deposition sites (31). Collagen is synthesised in bone through osteoblast activity; the tropocollagen produced polymerises extracellularly, cross-linking as they mature. Macromolecules are secreted from osteoblasts and young osteocytes, which attach to collagen fibres and crystals. Such macromolecules are osteopontin, osteocalcin and proteoglycans (biglycan and decorin), osteopontin, and transforming growth factor-β (TGF-β) (29).

The mineral portion of bone (in mature bones) has been identified as hydroxyapatite (HA); the minerals exist in bone as small plates roughly 4 nm x 50 nm x 50 nm (32). The plates are closely packed together with their long axes almost parallel to the collagen fibrils; gaps between the crystals contain water and organic macromolecules. As stated previously bone is a site of high metabolic activity and turnover, this activity is regulated via the local cells, these cells shall be briefly described.

2.1.1.1. Mesenchymal Stem Cells

Stem cells are a type of cell that have the potential to divide and mature into multiple cell phenotypes; mesenchymal stem cells (MSC's) give rise to osteoblasts, chondroblasts, adipocytes, tenocytes, etc. MSC's can be harvested from numerous sites in the body, a common site to harvest MSC's is from bone marrow; other sites are noteworthy however, such as adipose tissue, dental pulp, periodontal ligaments, synovial membranes, trabecular bone, skin and muscle (33). Osteogenic differentiation of MSC's are guided by various environmental factors, which shall be described in this section.

2.1.1.1.1. Chemical induction

A common method of inducing osteogenic differentiation *in vitro* is through the use of chemicals such as dexamethasone, ascorbic acid and beta glycerol phosphates (34-36). Aside from these routinely used compounds other hormones and growth factors have been found to have effects on MSC differentiation. Some of these are oestrogen (37), sonic hedgehog (38), fibroblast growth factor (FGF) (39, 40), vascular endothelial growth factor (VEGF) (41), and bone morphogenic protein (BMP) 2, 4, 7 and 9 (42-44). The specifics of these signalling pathways and their controlled effect on MSC's are still debated within the literature; however the use of these growth factors seems necessary, to the point that commercially available versions exist, such as recombinant human BMP-2 (rhBMP-2). Currently these are costly; additionally they have been reported to cause adverse effects in high dosages, such as breathing difficulty, back and leg pain, haematoma and life threatening urogenital events (45).

2.1.1.1.2. Topography

The effect of a substrates topography on cell behaviours was first demonstrated in 1911 (46), this was later developed into the idea of "contact guidance" in 1945 by Paul Weiss (47). Contact guidance refers to cells aligning and orientating themselves to the patterns that they are cultured on; features as small as 5nm have been shown to instigate this effect (48), the key factors to consider are average surface roughness (Ra) and the patterns on the surface (isotropic and anisotropic). In general, osteogenic MSC differentiation is linked with surface roughness's ≈ 1 µm. A study by Yang *et al* (49) cultured human bone marrow stromal cells (hBMSC's) on HA discs (in osteogenic medium) with Ra values ranging from 0.2-1.65 µm; discs with Ra values of 0.7-1.0 µm we found to be optimal in terms of osteogenic differentiation. Faia-Torres *et al* conducted a similar study without the use of osteogenic inducers, i.e. MSC's cultured on poly-epsilon-caprolactone (PCL) discs in basal media (50). Expression of osteogenic markers, alkaline phosphatase (ALP) and mineralization were found to be related to Ra; specifically peak ALP was attributed to an Ra value ≈ 0.93 µm. Anisotropic patterns have been shown to improve osteogenesis with careful design of the pitch of the ridges and grooves (≈ 50 µm) (51). Isotropic patterning is less understood, however it is generally accepted that this enhances osteogenic differentiation (52).

2.1.1.2. Osteoblasts

These cells are derived from osteoprogenitor (stem) cells of mesenchymal origin (bone marrow and other connective tissue). Osteoblasts are basophilic, cuboidal, mononuclear cells roughly 15-30 µm across with features typical of protein secreting cells (53). They are generally found on the forming surfaces of growing or remodelling bones, providing a covering layer (also found within cortical bone where osteons are undergoing remodelling). They are responsible for synthesis, deposition and mineralization of the bone matrix. Once they are embedded within the matrix they differentiate into osteocytes (54). Osteoblasts contain bundles of actin, myosin and other cytoskeletal proteins associated with maintenance of cell shape, motility and attachment. Osteoblasts have extended plasma membranes which can contact neighbouring cells (other osteoblasts and osteocytes) at intercellular gap junctions, providing co-ordination of the activity of groups of cells (54).

2.1.1.3. Osteocytes

These are the major cell type of mature bone; osteocytes saturate the matrix and are interconnected by numerous dendritic processes, forming a complex cellular network. Where osteocytes are derived from osteoblasts, these cells do not secrete any new matrix. Osteocytes are ellipsoidal, with their long axis (~25 µm) parallel to surrounding lamella (53). Osteocytes lie within what is termed lacunae; a cavity filled with fluid with a wall of un-mineralized organic matrix up to 2 µm thick. The dendritic processes contact adjacent cells through their distal tips; these form communicating gap junctions, which maintain the electrical and metabolic equilibrium of the cellular network (29). The channels which these junctions are formed within are termed canaliculi, roughly 0.5 µm in diameter (29), acting to supply a route for information to be transferred between cells and the diffusion of nutrients and waste via neighbouring osteocytes and blood vessels (54).

2.1.1.4. Osteoclasts

As opposed to osteoblasts, osteoclasts are bone-destroying cells. These are large, multinucleated cells derived from precursor cells circulating within the blood (54). These cells may be described as being aggressive; osteoclasts clamp down onto the surface of bone, the ruffled border underneath acts to break down the bone. Organic and inorganic debris are packed into vesicles that pass through the cell body, these in turn are deposited into the space above. Osteoclasts are presumed to die (apoptosis) once the breakdown of the bone is completed (55).

2.2 The Hierarchy of bone

2.2.1. Woven and Lamellar bone

Collagen fibres aggregate to form *fibrils*, these and their mineral counterparts are arranged in two distinct forms to constitute the next defined structures of bone: woven and lamellar bone. Woven bone is laid down quicker than lamellar bone (~ 4 µm/day and ~1 µm/day respectfully (29)) and is present in the foetus and in the callus that is produced during fracture repair. The collagen in woven bone is composed of fibrils 0.1-0.3 µm in diameter with random orientation of the fibrils and minerals (56) compared to lamellar bone which is less mineralized; and whose collagen fibrils (2-3 µm in diameter) and minerals are arranged in sheets (termed lamellae), whose thickness appears to alternate (57). The fibrils in lamellae may be best described as being orientated in small domains roughly 30-100 µm across. Within a domain the fibril orientation is constant; however this changes within one lamella and between each domain.

2.2.2. Harvesian system and Fibrolamellar bone

Osteoclasts form cutting cones ~ 200 µm in diameter and 300 µm long, this cavity is rapidly filled and the walls are smoothed, bone is then deposited on the internal face to create concentric lamellae (58). Through the central cavity lies (in general) a blood vessel and nerves, this system is termed a *Harvesian system* (or *osteon*), the entire process from osteoclastic activity to completion of the structure takes roughly 2-4 months (59). The concentric lamellae are composed of sheets of mineralized matrix and branching collagen fibres (2-3 µm thick).The collagen within these lamellae is orientated longitudinally at sites of tension, and obliquely at sites of compression, functioning to provide the maximum support possible by the material to the applied forces (60).

Fibrolamellar bone is another distinguishable bone structure, woven bone is rapidly laid down to be later filled with lamellar bone. A 2-D vascular network resides between each lamellar layer, which in turn is layered with woven bone (60). At this line the growth of bone is halted before the next stage is initialised, this results in alternating layers of woven and lamellar bone, allowing rapid growth (woven bone) whilst retaining sufficient mechanical properties (lamellar bone).

2.2.3. Cortical and Cancellous bone

These sub-structures all constitute the composite properties of bone at the sub-macroscopic level, however these structures combine to give the two primary macro structures of bone clearly visible with the naked eye: Cortical and cancellous bone. Cortical bone is found primarily around the shafts of long bones and the peripheral lining of flat bones; it is ultimately solid (constituting ~ 80 % of the skeletons weight with a porosity ranging between 5-10 %), composed of the concentric lamellae described previously (54, 60). Spaces exist only for osteocytes, canaliculi and blood vessels. Conversely cancellous bone is highly porous (50-90 % porosity), composed of lamellar bone or fragments of Harvesian bone (29, 60). Cancellous bone is found at the end of long bones under synovial joints, filling of short and flat bones, and beneath protuberances where tendons attached (29). Cancellous bone is formed from struts termed trabeculae, the lamellar that form these struts do not necessarily run parallel with the external surfaces of the struts. The struts may be randomly orientated (usually denoted to struts deep within the bone); or orientated in an organized manner where stress patterns are reasonably constant, this organisation shall be discussed further in section 2.4.2. Anisotropy

2.3. Mechanical properties

The hierarchical structure of bone from the molecular to macroscopic level results in complex mechanical properties. For vertebrates, it is imperative that the skeleton be stiff, stiffness of a material (or its resistance to deformation) can be described simply through calculation of its Young's modulus. Generally, these properties are ascertained via applying a load to a specimen (mechanical testing) or by measuring the velocity of sound waves in bone (ultrasonic testing). Mechanical testing has the advantage of simplicity. Young's modulus of bone can be determined through a variety of directions; additionally cancellous bone may be analysed with the inclusion of its cavities, where ultrasonic methods would struggle to attain properties of a porous medium (61). In general orientation alters the values obtained from either study employed (62), (63) with estimates of stiffness measured along the length of the bone being up to 2.4 times greater than tests applied at right angles to the specimen. The rate at which the specimen is deformed (strain-rate) has a measurable effect on the Young's modulus calculated (64, 65), this is due to the slight viscoelastic property of bone.

Simplistic models have been produced to describe the elastic properties; considering the composite structure of bone incorporating organic (collagen) and inorganic (hydroxyapatite) phases, this idea was built upon further using Voigt and Reuss models (66). These models describe the bone as a sandwich structure, composed of the materials with corresponding stiffness's estimated to that of collagen and hydroxyapatite.

This model proved too simplistic however (67) and was developed further (68) into the following equation:

$$E_b = \frac{E_c V_c (1 - \nu_c \nu_b)}{1 - \nu_c^2} + \Sigma E_{ha} V_{ha} \alpha_n (cos^4 \varphi_n - \nu_b cos^2 \varphi_n sin^2 \varphi_n)$$

where subscript c is collagen, ha is hydroxyapatite, ν is Poisson’s ratio, α_n is fraction of apatite crystals lying at an angle φ_n from the direction of stress.

The first section of the equation relates to the collagen (assumed to have equal modulus in all directions), the second part describes the apatite. This model still proved insufficient to describe the Young’s modulus, with predicted values considerably lower than observed values. Attempts were made to model bone from the lamellar and Harvesian level (69-73); estimations were made of Young’s modulus, crystal spacing and orientation. Where these models showed the effects of fibril and crystal orientation, the scaling up of the values predicted still requires the use of large assumptions, meaning it is difficult to translate the microscopic characteristics to the macroscopic function.

The anisotropy of bone was studied in long bones (62) assuming transversely isotropic properties of the Harvesian bone (i.e. axis of symmetry down the length, behaviours in all right angle directions to this axis are equal). Their study showed that the ultimate tensile strength in the circumferential direction is roughly 40 % of the longitudinal direction. This is expected as the collagen fibrils and subsequent structures are primarily orientated along the long axis. This idea of anisotropy has helped in defining the fracture mechanics of bone; several studies (69, 74) showed that aspects of the hierarchical structure act to dampen the rate at which a crack propagates through bone. In general, it is reported that the microscopic structure of bone reduces stress-concentrating factors. One such example is the cement lines of Harvesian systems, acting to form weak interfaces at which cracks are dissipated, resulting in an increase in the total amount of energy required to fully propagate a crack.

Despite the variations in methods, models and assumptions that must be made estimations of the strength of bone can be drawn. In compression and tension cortical bone is reported to have yield strengths of 131-224 MPa and 78-151 MPa respectfully when tested longitudinally (75). This is diminished to 106-133 MPa and 51-56 MPa when tested in the transverse direction (75); with bending strength ranging from 30-90 MPa. An estimate of the elastic modulus of cortical and cancellous bone has been given as 17 GPa and 6 GPa respectfully (75). Description of the strength of bone is inherently complex, whereas values of whole specimens and cortical bone can be ascertained through loading and bending tests, cancellous bone presents further complications. As this study shall be primarily focusing on replicating trabecular bone, the following section elaborates on the modelling of trabecular bone, specifically outlining the difficulties in determining the mechanical properties of such a complex structure.

2.4. Cancellous bone

In a simplified model, cancellous bone may be thought of as a highly porous cortical bone; however, this model is misleading as cancellous bone is highly specialized and as such has specific mechanical properties. The methods used to estimate stiffness and strength in cortical bone cannot be applied here. As the struts of cancellous bone (trabeculae) form a complex structure the tissue can no longer be described simply as a uniform material. It is important to differentiate between the bone material, which forms the individual trabeculae; and the tissue as a whole, which includes the entire trabecular structure and pores. A wide range of values have been reported through studying trabeculae/or the trabecular structure as a whole. Studying individual trabeculae through buckling studies, standard mechanical testing and nanoindentation has reported values of Young's moduli ranging from 1-14 GPa (76-79). It is generally accepted however that the Young's modulus of trabecular bone (as a whole) lies somewhere around 6 -8 GPa (80), and that cancellous bone has a lower modulus than that of cortical bone.

That begs the question as to why this is so. It has been suggested that the lamellae in trabeculae are less organised than in cortical bone (62), additionally it has been suggested that the mineral content of cancellous bone is less than cortical, about 90-95 % of cortical (81). Errors due to specimen extraction are a significant factor to consider when ascertaining properties of trabecular (or cortical) bone via standard mechanical testing methods (82). End-artefacts created when the specimen is cut result in lower stiffness than when the specimen was in situ; errors due to end-artefacts have been reported to cause under-estimations of stiffness by ~40 % (82, 83). Where these suggestions may account for some discrepancies between values reported for cortical and cancellous bone, the problem is in reality much more complex.

2.4.1. Apparent density

Characterising cancellous bone requires the inclusion of its porous nature; a relationship between the elastic and strength properties with respect to apparent density gives an indication of the structural effect of the cancellous material (23, 64, 80). The apparent density is the dry mass of the bone divided by the volume of the specimen (determined from the dimensions of the sample). The strength and modulus fitted well to a power law (where D is the apparent density):

$$E = kD^3 \,, \qquad Compressive\ strength = \ k'D^2$$

The exponent for stiffness in this relationship has been confirmed as 2 through a comparison of several studies utilising this relationship (23, 80). In the human skeleton, the apparent density of trabecular bone ranges from 0.1-1.0 g/cm^3, in comparison cortical bone has an apparent density ~ 1.8 g/cm^3.

Due to the relatively small sample sizes utilised in standard mechanical tests (trabeculae strut thickness ~100-200 µm, length ~ 1-2 mm) new approaches to this problem have been developed. Using micro-CT scans a model of the tissue can be constructed; the mechanical properties of the model can be estimated from a “grey scale” produced from the scan, depicting the range of densities within the tissue (84). Then results of these calculations can then be compared to laboratory compression tests, through this it is possible to calculate what tissue material properties would provide the best agreement with the experimental results (85).

2.4.2. Anisotropy

Despite the varying values reported in the literature for strength and moduli of cancellous bone, it is agreed that its mechanical properties are a function of its apparent density and the alignment of trabeculae with respect to the applied load (86, 87). Anisotropy is produced in cancellous bone, not through its individual trabeculae, but through the alignment of the trabeculae as an entire structure. This anisotropy has been reported in several studies (77, 88) showing ratios of greatest to least modulus of cancellous bone of almost 5 times when loaded in each of the three orthogonal directions. The architecture of the cancellous bone is therefore a defining characteristic of its mechanical properties, a description of the anisotropy and the direction of this anisotropy can be described through a feature termed fabric.

This characteristic is difficult to pin down, however the general idea is the anisotropy of the material is modelled through an ellipsoid. The ellipsoid is composed of three orthogonal axes is arranged in space to depict the degree of anisotropy; for example, an elongated ellipsoid depicts trabeculae orientated preferentially in one direction, if the ellipsoid tends towards a spherical shape this depicts random orientation of the trabeculae. Cancellous bone acts not only to resist complex stresses, but also to dissipate energy from a whole bony structure.

The ability of cancellous bone to absorb energy has been studied through standard mechanical testing regimes (89) reporting classic stress-strain curves. The report suggests that under compression there is a plateau effect (plastic zone); compared to tension where the peak of the curve is followed by an almost linear drop off. The study also showed the ability of the cancellous network to recover up to 96 % of its original height after compression to 85 % of its original height. This ability of cancellous bone to cope well with compressive forces coincides well with one of its primary locations: beneath the articulating ends of long bones.

In brief: the articulating ends of long bones are coated with articular cartilage; composed of collagen fibrils orientated from parallel to perpendicular from superficial to deep respectfully, saturated with glycosaminoglycans, proteoglycans and water. This material has fantastic frictional properties; however its tensile and compressive strengths leave much to be desired, reported to be roughly 20 MPa and 35 MPa respectfully (90, 91). By underlining the subchondral bone of these articulating surfaces with the cancellous network, the energy is absorbed in a uniform manner, minimising localised stresses that would be produced from an underlying solid material.

2.5. Fracture repair process

In general, bone heals through the following stages: formation of a haematoma, migration of inflammatory and MSC's (inflammation), formation of a callus (repair) and remodelling of the callus (remodelling) (92, 93). There are two mechanisms for bone healing: primary and secondary bone healing. Primary bone healing is rare; occurring when two cortical faces remain in close proximity (92), osteoclasts form a cutting cone through the fracture which is remodelled by osteoblasts. Primary bone healing requires rigid fixation through the use of plates and screws to prevent non-union. Secondary bone healing requires slight mobility in the fixation (micromotion) to allow for proper callus formation (92). Three stages of bone healing are describable, each stage is influenced by local factors such as the degree of trauma and the type of bone affected. Other factors that can affect the bone healing process are the presence or absence of infection and systemic factors such as age, hormones and nutrition

2.5.1. Inflammation stage (within 0 -72 hours of injury)

The site of fracture bleeds extensively (including the surrounding tissues) resulting in the formation of a clot, or fracture haematoma. Platelets in the blood attach to the clot and release vasoactive mediators, growth factors and other cytokines, which attract inflammatory cells to the fracture site. Necrotic bone and tissue debris are removed via mast cells and macrophages followed by the stimulation of cells required to begin repairing the bone (92).

2.5.2. Reparative stage (within 2 days to 2 weeks of injury)

During this stage, osteoblasts (which are derived from the site of fracture and distant sites via the bloodstream) begin to lay down new bone matrix. A collagen rich matrix forms a soft callus into which new blood vessels grow, this is followed by ossification of the matrix that leads to the formation of woven bone (92).

2.5.3. Remodelling stage (from 3 weeks onwards)

The callus stops increasing in size, continuity between the bone fragments is achieved, at this stage maturation and remodelling of the callus begins. Where this stage begins roughly 3 weeks after injury (92) (during the reparative stage) it can continue for 6-9 years (93). Sequential resorption and deposition of woven bone is undertaken, gradually converting the woven bone to lamellar bone. This process of resorption and deposition is balanced via the external stresses placed on the bone; Wolff’s Law dictates the ultimate form of the bone (93).

2.6. Requirements of bone replacement materials

As previously discussed bone has the inherent ability to regenerate, however if a large enough void is formed only a soft tissue scar s formed potentially leading to fracture of the bone. A bone replacement material is needed to aid in the healing process when a void of such a size is present; this replacement material bridges the gap and restores continuity between the tissues. In other scenarios such as treatment of scoliosis or chronic non-healing fractures, this material can be used as a stimulus for new bone formation. Aside from blood, bone is the most commonly transplanted material. Bone replacement materials are biomaterials, all biomaterials must have specific properties dependent upon their application. This section describes the specific properties required of a bone replacement material. Scaffolds designed for the replacement of trabecular bone aim to mimic the properties of native bone; porosity, average pore size, mechanical strengths, biocompatibility, these are the factors that must be considered and characterised when developing a trabecular bone replacement material.

2.6.1. Mechanical Properties

Replicating the mechanical properties of bone is difficult as the interaction of HA crystals and collagen fibres from the nanoscale contribute to its intrinsic properties. The mechanical properties of a trabecular bone replacement material should ideally be similar to natural bone; too low a strength and the graft will fail, too high and stress shielding may occur (94). Load application though normal activities encourages bone formation, a lack of load application causes bone resorption. If the bone replacement material used has a significantly higher modulus than the natural bone, it will lessen the loads applied to the surrounding bone, shielding the natural bone from stresses. This in turn results in bone resorption around the implant leading to loosening of the implant. The mechanical properties of bone varies from site to site and wide range of values are reported in the literature. However, trabecular bone mechanical strengths are reported as: 2 – 12 MPa (compressive strength), 10 – 20 MPa (flexural strength) and 1 – 5 MPa (tensile strengths) (95). These values should be aimed for when characterising the initial scaffold produced, however as stated by Fu *et al* "*Although the requisite mechanical properties of scaffolds for bone repair are still the subject of debate, it is believed that their initial mechanical strength should withstand subsequent changes resulting from degradation and tissue ingrowth in the in vivo bone environment* " (95). Bone in growth and remodelling will alter the mechanical properties *in vivo* over time, however the mechanical properties of the scaffold should initially be within the ranges described above.

2.6.2. Fixation/Osseointegration

Linked to the architectural properties the scaffold must have the ability to allow ingrowth of blood vessels and osteoprogenitor cells (96); if this is accomplished in addition to bonding of the surrounding bone tissue without fibrous encapsulation the scaffold can be described as osteoconductive (97, 98). Fixation of the material into the defect is equally important; with a bioactive material, the formation of a physiochemical bond is possible, increasing the chances of achieving a successful fixation.

2.6.3. Porosity/Osteoconduction

As vital as mechanical properties (perhaps more so in the case of trabecular bone treatments) the internal architecture must mimic that of the native tissue. A highly interconnected structure is required to promote ingrowth of new bone and vascularisation. It is generally accepted that pore sizes ranging from 100-600 μm are required for mechanically strong bone ingrowth (99, 100). A minimum pore size of 100 μm is necessary for cell penetration, tissue ingrowth and vascularisation. A high degree of porosity is noted as being detrimental to scaffold strengths and implant reliability, a careful balance is required.

2.6.4. Biodegradability

Unlike metallic and non-degradable polymers that are currently used, biodegradable materials provide structure and support for timescales necessary to restore functionality and promote initial bone healing processes. As the material degrades, porosity is increased allowing further in-growth of native tissue and vascular networks. This degradation rate must be equal to or less than the natural remodelling rates (101). Another key aspect to consider of a biodegradable material is the removal of degradation products **without** invoking a cytotoxic response (102).

2.6.5. Fabrication

The key advantage of developing a synthetic scaffold is availability compared to conventional grafting options. As such, the fabrication methods must lend themselves to commercialisation; scaling-up is a challenge that must be considered from the earliest stages in the design cycle, reproducible batch production should be the minimum level achieved.

2.7. Fixation techniques

Permanent fixation of the implant into the defect is vital to its success, as previously stated with inert materials fibrous encapsulation can prevent this and result in device failure. Three main types of fixation techniques are definable – morphological, biological, and bioactive.

2.7.1. Morphological fixation

This type of fixation is used for biologically inactive materials (or materials which are non-porous/dense) such as metals or alumina. The main advantage of this type of technique is the application of immediate stability allowing for weight bearing shortly after the procedure. Examples of this technique include press-fitting (103), use of a threaded component (104), or cementing a component in place, i.e. using PMMA during Total Hip Replacement (THR) (105-107). As previously noted if a tight mechanical fit is not achieved movement at the implant:bone tissue interface can result in the formation of a fibrous layer, this layer can thicken over time ultimately leading to implant failure (105). PMMA is a widely used bone cement; the success of using a bone cement is reliant upon the ability of the cement to penetrate into bone trabeculae forming a mechanical interface, PMMA (and other bone cements) do not form a chemical bond with the bone tissue. An advantage of using PMMA is due to its viscoelastic property allowing it to dissipate loads between the bone and implant; this minimizes localized regions of stress (108). PMMA is a self-polymerising material formed from mixing a solid PMMA powder with a liquid methyl methacrylate (MMA) monomer; a concern with the use of PMMA is the polymerising reaction, which is exothermic, this reaction can reach over 70 °C and when in contact with bodily tissue can lead to localised bone necrosis (109, 110).

2.7.2. Biological Fixation

This fixation technique allows implants to withstand more complex stresses than implants fixed morphologically, this is achieved using a porous or textured surface, which allows tissue in growth. As previously stated, pores should be 100-150 μm in diameter to allow for vascularisation; additionally to prevent resorption the in grown tissue should be subjected to mechanical stresses. Drawbacks to this technique are the porous nature, which decreases the implants mechanical strength. Additionally (unlike morphological fixation) the strength of fixation is reliant upon tissue in growth, which can take up to 12 weeks to reach a sufficient level.

2.7.3. Bioactive Fixation

Through the use of a bioactive material a direct physiochemical bond is formed between the implant and the native bone tissue, this provides the strongest bond out of the three types to the extent that the implant or surrounding bone must be broken if revision is required (7, 111). As previously stated numerous bioactive materials are known and have been commersialised including bioactive glasses (Bioglass), bioactive glass-ceramics (e. g. Ceravital®, A/W glass-ceramic) and dense hydroxyapatite (e. g. Durapatite®, Calcitite®) to name a few.

2.8. Currently used materials

2.8.1. Grafts

The idea of using natural tissue to replace damaged tissue has existed for some time; societal restrictions on anatomical research were lifted over time and increased success and understanding of this technique was obtained. The three main types of grafts are xenografts, allografts and autografts, each of which will be briefly discussed.

2.8.1.1. Xenografts

From the Greek “xenos” meaning foreign, xenografts are tissues derived from a different species. Jean-Baptiste Denis performed one of the first blood xenotransfusions in the 17th century; this was followed by skin, corneal and even testicular transplantations through the 18th and 19th centuries (112). The main failings of these early attempts was that of immune rejection, as stated previously with the advent of immunosuppressant drugs whole organ transplants and bone grafts were repeatedly attempted through the 20th century with mixed success. The argument for xenograft/transplantation is that of an almost unlimited supply; however until the immunological and pathological issues associated with xenotransplantation have been addressed the following quote from Norman Shumway (a pioneer in heart transplantation) may hold true indefinitely “*xenotransplantation is the future of transplantation, and always will be*” (112). Possible strategies to counter the current issues associated with xenografts/transplantation are that of genetically modified animals (113-115).

2.8.1.2. Allografts

From the Greek "allo" meaning other, allografts are tissues derived from the same species. As with autografts the most common site for harvesting the bone is from the iliac crest, as with xenografts screening and processing must be undertaken to reduce the risk of infection and rejection. Issues with donor availability, cryogenic storage and risk of fracture post implantation limit the practicality of allografts (116, 117) Although these materials exhibit good biocompatibility (118) they tend to become brittle and when sterilised, experience a significant loss of strength. Other studies conducted have implied that sterilized allografts are of acceptable mechanical strength, however their non-union rates were noted as being poor. Additionally the biomechanical properties of sterilized allografts have been noted to be dependent upon the radiation applied "*moderate to high doses of gamma radiation (≥ 2.5 Mrad) will have a major impact on the allograft tissue biomechanical properties*" (118, 119).

2.8.1.3. Autografts

Derived from auto meaning self, autografts are tissues harvested from the one area of the body to treat an area of the same body. Despite being considered the current gold standard autografts are commonly limited by the amount of tissue that can be harvested at any given time, meaning large defects are difficult to treat. Understandably, this technique has the advantage of alleviating the need for immunosuppressant drugs; however, donor site morbidity and pain are common side effects from such a procedure (120-122). For example; harvesting bone from the iliac crest can result in altered biomechanics of the patient which can lead to further complications, such as increased stress applied to cartilage which may lead to joint failure and ultimately joint replacement surgery (121, 123).

2.8.2. Polymers

Polymers have limited applications in the orthopaedic field due to their low mechanical strength, however are successful in replacing articulating surfaces in hip and knee replacement surgeries. The most widely used polymer is ultra high molecular weight polyethylene; UHMWPE, this form of polyethylene has a high density and is not only able to withstand sterilisation processes (unlike its low density form) and exhibits excellent wear characteristics. Whilst it is able to absorb the cyclic impact stresses subjected to it problems persist in the long term, creep and fatigue of the material are commonly noted. In addition to this the opposing articulating surface is usually replaced with a metal or ceramic, as the polymer has a lower surface hardness it will eventually become scratched and produce wear debris. Wear debris of UHMWPE cannot be broken down by local macrophages through regular phagocytosis processes, this ultimately results in osteolysis (bone cell death) and loosening of the implant (124). Aside from UHMWPE and PMMA polymers are also widely used as surgical sutures; polymers such as poly(L-lactic acid) (PLLA), poly(glycolic acid) (PGA), and poly(lactic-co-glycolic acid) (PLGA) have been successfully used and shown to be degradable and biocompatible. However due to their low mechanical strengths and flexibility their use as a bone replacement material is very limited and unlikely.

2.8.3. Metals

Metals have a long history of use within the orthopaedic field; they have sufficient mechanical strengths and can be manufactured on mass with relative ease. Specifically the three main metallic alloys used are titanium alloys, cobalt chromium and stainless steels. In general, metallic alloys cannot form a direct bond with bone and as previously stated can illicit fibrous encapsulation resulting in implant loosening and failure. A bioactive coating of hydroxyapatite can be applied to the surface to improve their integration with the natural bone (125), however the thickness of this coating must be specifically controlled. The coating must be thick enough to not only provide sufficient material for bone in growth; but also to account for the dissolution of this surface *in vivo* during the union stage, this surface may dissolve by up to 10-15 μm over a few months whilst this is taking place. However if a coating of 100-150 μm is applied the mechanical properties of the implant will be significantly deteriorated, this in turn can lead to fatigue failure under tensile loading. Furthermore the HA coating can have a poor adhesive strength and suffer from delamination (126, 127). Titanium alloys are an exception; they do not form a fibrous capsule and can become fully integrated with natural bone via the formation of an oxide layer (128), additionally their low modulus reduces the effects of stress shielding when compared with most other metallic implants. Friedman *et al* (129) however reported that titanium implants pose a risk due to wear debris. Metallic wear debris is of a significant concern; bodily fluids are corrosive and can not only reduce the mechanical stability of the metallic implant but also release metallic particles into the body, this can result in allergic reactions and neoplastic effects, which are un-desirable. Whilst it was stated that titanium alloys have a low modulus, metallic implants inherently have a higher modulus than that of the surrounding natural bone, leading to stress-shielding. Metallic implants are arguably the most successful type of implant currently in clinical use; however, they present several undesirable drawbacks eliciting the development of alternative materials.

2.8.4. Ceramics and glasses

Ceramics are a relatively new material in the field of orthopaedics, they were first used in 1963 (97) and have been shown to be highly successful. The attraction and potential of using ceramics comes from there inherent similarity to the material they attempt to replace, i.e. their composition is similar to the mineral component of bone. In addition to this they exhibit high compressive strengths, are well accepted by the body and exhibit negligible foreign body reactions (130); however (unlike metallic implants), ceramics are inherently brittle and difficult to machine.

When ceramics are used in a biological application they are usually termed “bioceramics”; they can be inert (i.e. alumina), resorbable (i.e. tricalcium phosphate), or bioactive (e.g. hydroxyapatite, bioactive glasses, and glass-ceramics). Five distinct bioceramics are describable depending upon the heat treatments applied:

1. Glass

2. Cast or plasma-sprayed polycrystalline ceramic

3. Liquid-phase sintered (vitrified) ceramic

4. Solid-state sintered ceramic

5. Polycrystalline glass-ceramic

2.9. Glass-Ceramics

The focus of this project is the production of porous glass-ceramic (GC) scaffolds; this section aims to present in detail to the reader the relevant theory behind glass-ceramics, their structure and formation, and the analysis techniques that can be used to verify their properties.

2.9.1. Forming a glass

As a material is heated or cooled it will undergo conformational changes in its structure as, constituent atoms, ion or molecules re-arrange into states of equilibrium. As a liquid is cooled through these temperatures its viscosity (ν) increases dramatically as the materials constituents attempt to re-arrange into the equilibrium crystalline state; however, rapid cooling of certain materials may result in the formation of an X-ray amorphous glass, exhibiting only a short ranged ordered network (131). To study conformational changes that occur during crystal and glass formation differential thermal analysis (DTA) or differential scanning calorimetry (DSC) must be employed. Upon cooling a liquid to T_m crystallisation occurs, shown by a large exothermic peak in the DTA/DSC plot, as the material settles into its low energy configuration this peak is followed by a drop in specific volume. However if the liquid is super-cooled there is no latent heat evolution (no specific volume change) as it passes through T_m, this indicates that the elements are still in their liquid arrangement. Eventually a small peak is observed in the DTA/DSC plot at T_g, suggesting a glass has formed with a non-equilibrium liquid-like structure. Glasses differ structurally from crystalline materials in that whilst they lack long-range, repeating regular structures, they are comprised of similar interatomic forces, distances and co-ordinations (132). Vitreous silica is a good example of this; both its crystalline and amorphous states are comprised of a silicon ion surrounded by four oxygen ions, each oxygen ion is in turn surrounded by two silicon ions, ultimately forming a tetrahedron (133). A tetrahedron in a crystalline state repeats in a regular manner, supplying long-range order within the structure; whereas in an amorphous state the tetrahedra are only exhibited with short range order. Theories of glass structure have been developed throughout the years; a relationship between the glass forming capacity of an oxide and the relative size of their cation with respect to the anion (oxygen) was established (132):

$$\frac{R_c}{R_a} \cong 0.3$$

Where R_c and R_a are the radii of the cation and anion respectfully. This relationship shows that only specific structures allow for cations to be sufficiently spaced with respect to each other, so their repulsive charges do not interact too greatly with one another. Therefore, any oxide conforming to the equation above should theoretically be termed a glass former. Zachariasen (134) outlined four basic rules to describe a potential glass former:

1. Each oxygen atom must be linked to no more than two cations.
2. Low number of oxygen atoms surrounding a cation, i.e. triangular or tetrahedral co-ordination.
3. Oxygen polyhedra only bonded at their vertices.
4. At least three of the polyhedron vertices must be bonded to other polyhedra.

This in turn allowed the prediction of several glass forming oxides such as SiO_2, GeO_2, B_2O_3, and P_2O_5.

The mechanical properties of the produced glass can be controlled via the crystallisation process (135), partially transforming a glass to a crystal creates a glass-ceramic, a material which comprises properties of both the base glass and the crystal phases formed. Crystallisation changes the atomic arrangement of small localized volumes forming interfaces between the glass and crystal. The crystallisation process can be described through two stages of nucleation and growth. Nucleation includes the initial formation of a small, stable crystal phase within the glass; this may occur randomly throughout the glass or at preferred sites (termed homogeneous and heterogeneous nucleation respectfully).

2.9.2. Nucleating agents

In producing A/W a nucleating agent is included (P_2O_5) inducing amorphous phase separation (APS). If multiple phases are more stable than one, an interface will form between the two causing skewed concentration distributions. Phase separation occurring **above** the liquidus forms two stable phases which remain after cooling; if these phases exist **below** the liquidus metastable phase occur, forming a single phase upon rapid cooling which can be recovered through an appropriate heat treatment.

2.9.3. Heat Treatments

Crystal formation and growth are dependent upon temperatures specific to the system, controlling the fine grain structure of a glass ceramic can be achieved through a controlled heat treatment. The temperatures that define nucleation and growth may overlap to a significant degree, in such a system a single heat treatment may be applied to maximise these factors. However in a system where nucleation and growth temperatures differ significantly a different heat treatment is required; there must be an initial dwell stage for nucleation to occur, followed by a second higher temperature dwell to initiate rapid crystal growth. Nucleation processes must also be considered when defining a heat treatment; i.e. bulk and surface nucleation routes, differential thermal analysis (DTA) may be employed to predict which process governs the system.

Bulk nucleation is depicted as a sharp peak on a DTA/DSC trace, whereas surface nucleation is depicted through a broader peak (136). Another consideration is the average particle size being used; surface nucleation is favoured by smaller particles, in the case of A/W larger particles shifts the crystallisation of the surface nucleating phase of wollastonite to a higher temperature. In the case of crystallisation of more than one phase, APS and surface or bulk nucleation preferences can be studied to define an optimum nucleation temperature. Through the use of DTA traces the variations between crystallisation temperature (constant heating) against crystallisation temperature (following a holding period at an assumed nucleation temperature) are plotted, the largest temperature shift observed depicts the optimum nucleation temperature (137).

2.9.4. Sintering

The sintering process a powder undergoes will determine the bond strengths between sintered particles (and ultimately the strength of the bulk material) and the materials porosity. Sintering temperature is << T_m and is determined by the material composition. During this process interfaces and contact angles within the material are reduced, the smaller the particle size used the faster the sintering rate as diffusion distances are smaller (138). The two main types of sintering shall be discussed: solid state sintering and liquid phase sintering.

2.9.4.1. Solid State Sintering

A simple three stage model describes this process (139), it is assumed that initial contact of particles occurs at a single point and that the particles are spherical (Figure 2.1**Error! Reference source not found.**). At the stages pores between particles are interconnected, progression of necking causes a reduction pore diameter, ultimately resulting in final closure of the pores. During this process any gasses that may have been produced can become trapped, this preserves some pores to a degree and impedes densification.

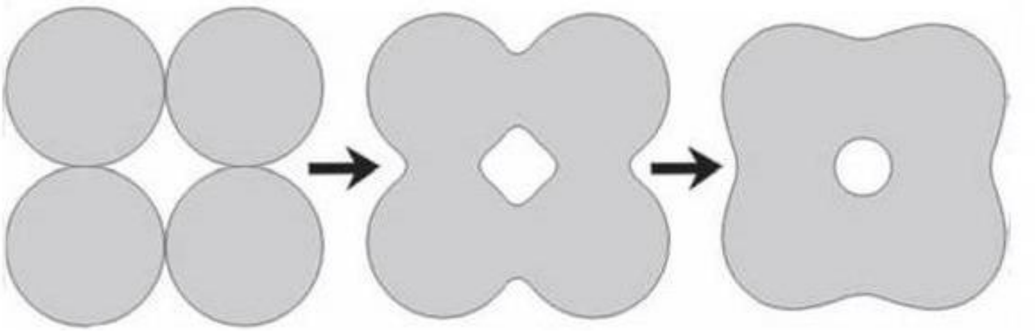

Figure 2.1 - Diagram of necking process which occurs during sintering

The necking process can be described via the transport mechanisms of the pores; assuming they are accumulations of vacancies, the vacancy and mass transport occur via surface and bulk transport. Surface transport occurs at lower temperatures, resulting in necking with minimal densification as mass transport occurs on particle surface, involving surface diffusion and evaporation-condensation resulting in mass transport to necking site. Bulk transport occurs at higher temperatures, involving volume diffusion, grain boundary diffusion, plastic flow and viscous flow. The favoured mechanism in glasses is viscous flow, in crystalline materials grain boundary diffusion, volume diffusion and stress-induced plastic flow is favoured (139).

2.9.4.2. Liquid phase sintering (LPS)

Utilising the formation of a liquid phase during sintering, this process is associated with faster diffusion rates than solid state sintering, it involves three main stages: re-arrangement, solution-precipitation, and densification. In brief, capillary action pulls melted liquid into pores and causes grains to re-arrange into favourable packing structures. High capillary pressures (caused by particles in close proximity) cause atoms to precipitate through the solution to areas of lower chemical potential (areas where particles are close or in contact); termed contact flattening, this process of densification is similar to grain boundary diffusion. During this process the solid phase is (usually) soluble within the liquid phase formed; allowing for high levels of wetting and good contact between components (138). LPS can be utilised in free-form fabrication methods, e.g. selective laser sintering, porous A/W scaffolds have been produced via this method (137).

2.9.5. DSC

This technique of analysis involves exposing a **reference** material and a **sample** to an identical heating regime. The reference material chosen is stable within the temperatures of the heating regime; whereas the sample undergoes an exothermic or endothermic event, this results in a temperature differential which is used to identify the sample material. An exothermic event produces a peak (indicative of glass) and an endothermic event produces a trough, the position of the peaks is dependant the sample's crystal structure and chemical composition. The glass transition temperature can also be investigated through DSC; T_g is not shown as a peak or trough however, it is depicted through a shift of the base line (140).

Tangents drawn from the start and end points of this transformation may be used to estimate T_g, it may also be thought of as the point of inflection during the transformation.

The DSC trace produced is highly susceptible to experimental factors and (potentially) errors; shape and mass of the sample, testing atmosphere, formation of gasses during the test, thermocouple type and position, these factors must be taken into consideration when estimating the thermodynamic properties of the tested material. Theoretically the transformation energy could be estimated from the area under the DSC trace; however in practice this is difficult to achieve as thermodynamic transformation (which occurs during the test) alters heat transfer mechanics, resulting in the start and end points of the peak to lie out of plane with respect to each other (140).

Through the use of multiple DSC studies (performed at different heating rates) the activation energy for crystallisation can be calculated using the Kissinger equation (141):

$$ln\left(\frac{\emptyset}{T_P^2}\right) = -\frac{E}{RT_P} + C$$

Where $\emptyset$ is the heating rate (K/min), R is the gas constant (J/Kmol), T_P the crystallisation peak temperature (K), E the activation energy (KJ/mol) and C is a constant. E can then be determined by plotting $ln\left(\frac{\emptyset}{T_P^2}\right)$ vs $1000/T_P$ and calculating the gradient of this plot.

With the activation energy known the Avrami parameter of an exotherm, n, can then be determined (this utilises full width at half maximum (FWHM) of a peak) which indicates crystal growth occurring at an exotherm (141):

$$n = \frac{2.5RT_P^2}{(FWHM)E}$$

If n = 1, 1-D surface crystallisation; n = 2, planar surface nucleation; n = 3, 3-D bulk nucleation.

2.10. Bioactive materials

As previously stated a bioactive material provides the greatest chance of providing a secure fixation of an implant. Hench *et al* defined a bioactive material as "*a material that elicits a specific biological response at the interface of the -material, which results in the formation of a bond between the tissue and that material*" (142). There are two distinct classes of bioactive materials, class A and class B and are defined as either osteoproductive or osteoconductive respectively (14). Osteoproductive implies that both an intracellular and extracellular response has occurred at the implant interface. Osteoconductive implies that only an extracellular response has occurred and the bone:implant interface promotes cell migration. Ranking of a bioactive material is done via the Index of Bioactivity (IB), this is calculated by dividing 100 by the time taken for 50 % of the bone:implant interface to chemically bond together (14, 143, 144). For reference:

Bioactive materials which bond to hard tissue	$0 < IB < 8$
Bioactive materials which bond to hard and soft tissue	$IB > 8$

For example:

45S5	Class A material
Synthetic HA	Class B material

2.11. Bioactive glasses

Silicon has long been associated with bone formation (145, 146); in vivo studies showed abnormal bone development in silicon deficient chicks, in vitro studies reported collagen type I expression increased significantly in human osteoblasts with the supplementation of orthosilicate acid (147, 148). "Bioglass" was originally discovered in 60's by Larry Hench; composed of a low silica content (<60 %) and a calcium/phosphorous ratio similar to that of HA, this material was developed further into the composition 4S5S and commercially termed Bioglass® (149). This material was shown to support osteoblast attachment and proliferation (150); incorporating the material into healing callus (151), ultimately resulting in extensive scaffold integration with the host bone (142).

Hench *et al* (142) discovered the first compositional ranges of bioactive glasses; these glasses contained SiO_2, Na_2O, CaO, and P_2O_5. Specifically these glasses contained less than 60 % SiO_2, a high CaO/ P_2O_5 ratio and a high Na_2O and high CaO content (142). The composition termed 45S5 (which has been subsequently branded Bioglass®) is noteworthy, this glass has 45 wt % SiO_2 (S acts as the network former), and has a molar ratio of 5:1 of Ca to P, lower ratios of Ca to P are not able to bond to bone (152). Where Bioglass® has been used clinically (153) its mechanical properties are too low to be used for load bearing applications; this is due to its amorphous three-dimensional glass network.

Certain forms of bioactive glasses form a physiochemical bond to bone via the formation of a hydroxy-carbano-apatite (HCA) layer when in contact with body fluid. The formation of this layer was described by Jones and Hench (144) as follows:

Stage 1. Rapid exchange of Na^+ and Ca^{2+} with H^+ or H_3O^+ from the solution

$$Si\text{-}O\text{-}Na^+ + H^+ + OH^- \longrightarrow Si\text{-}OH^+ + Na^+(aq) + OH^-$$

Stage 2. Cation exchange increases the hydroxyl concentration of the solution, soluble silica is lost in the form of $Si(OH)_4$ to the solution, resulting from the breaking of Si-O-Si bonds and the continued formation of silanols at the glass solution interface.

$$Si\text{-}O\text{-}Si + H_2O \longrightarrow Si\text{-}OH + OH\text{-}Si$$

Stage 3. Condensation and repolymerisation of the SiO_2-rich surface layer

$$\text{-}Si\text{-}OH + HO\text{-}Si\text{-} \longrightarrow \text{-}Si\text{-}O\text{-}Si\text{-} + H_2O$$

Stage 4. Migration of $Ca2^+$ and PO_4^{3-} groups to the surface forming a $CaO\text{-}P_2O_5$ rich film on top of the SiO_2 rich layer.

Stage 5. Crystallisation of the amorphous $CaO\text{-}P_2O_5$ film (by incorporation of OH^-, CO_3^{2-}, or F^- anions) forming a HCA layer.

These first five stages comprise the complete bonding of a bioactive glass to bone, these stages occur on the material side independent of the presence of tissues.

2.12. Bioactive glass ceramics – Apatite-Wollastonite

To provide higher mechanical strengths bioactive glass-ceramic have been developed, a specific type contains an apatite crystal phase, which (combined with the uncrystallised residual glass) allows for direct tissue bonding (143). Briefly, comparisons can be made between the bioactivity (i.e. bone-bonding ability) of bioactive glasses and bioactive glass-ceramics, the formation of a surface apatite layer. However, a key difference has been noted for glass-ceramics, an amorphous silica layer is not created (154). Silanol groups are instead suggested, by Kokubo *et al,* to provide favourable nucleation sites which in turn form a HCA layer (18, 155). This mechanism (studied *in vitro* and *in vivo*) is governed via the production of a Ca, P rich layer through the dissolution of components of the glassy phase, this in turn produces a thin layer of apatite which forms a strong chemical bond with bone (154). Where the bioactivity index of A/W is less than that of Bioglass© 45S5 (roughly one fourth) this bond is so strong that reportedly the tensile fracture occurs in the bone itself rather than the A/W-bone interface (154). To reinforce the mechanical strength another crystal phase is present. Accordingly, A/W glass-ceramic developed by Kokubo and co-workers contains both crystalline apatite ($Ca(PO_4)_6(O, F_2)$) and ß-wollastonite ($Ca\text{-}SiO_3$), the increase in strength is attributed to the presence of the additional wollastonite phase. The key mechanical properties of A/W are presented in Table 2.1, however the main aspects of A/W are that the apatite induces direct bone bonding whilst the wollastonite phase prevents crack propagation (18, 156).

An *in vivo* study conducted by Yamamuro *et al* (157) revealed that A/W binds to bone more tightly than hydroxyapatite. The ability of A/W to bond with bone was further described by Nakamura *et al* (158), this study compared the loads required to pull out a bioceramic after 8 weeks of implantation (in the tibial condyle of rabbits). As shown in Table 2.2 the A/W implant exhibited the highest “failure load”, even higher than that of dense hydroxyapatite.

Table 2.1: Physical and mechanical properties of A-W glass-ceramic (159)

Property	Value
Density (g/cm^3)	3.07
Bending Strength (MPa)	215
Compressive Strength (MPa)	1080
Young’s Modulus (GPa)	118
Vickers Hardness (Hv)	680
Fracture Toughness (MPa.m$^{0.5}$)	2.0

Table 2.2 - Failure loads of ceramic materials at 8 weeks after implantation (158)

Bioceramic	Failure Load ± S.D. (kg)
Alumina	0.13 ± 0.002
Bioglass®	2.75 ± 1.80
Dense hydroxyapatite	6.28 ± 1.58^{a,b}
A/W glass-ceramic	7.43 ± 1.19^{a,b}

$^{a}p < 0.001$, significantly different from alumina-ceramics. $^{b}p < 0.05$, significantly different from 45S5 Bioglass.

Further characterisation of A/W in vivo was conducted by Oonishi *et al* (160); quantitative comparison of bone in growth rate was conducted, specifically with granules of Bioglass®, A/W glass-ceramic and HA (synthetic). These three types of bioactive particles were implanted into 6 mm holes drilled into the femoral condyles of rabbits. After 1 week of implantation it was noted that the new bone around Bioglass® and A/W was greater than that of the HA particles. This trend was apparent at 2, 3 and 6 weeks after implantation; new bone formation was greatest around the Bioglass® particles, HA showed the least amount of new bone formation. At twelve weeks, the Bioglass® particles showed significant reduction in size (~ half to two thirds their original size); A/W showed no change in size but it was suggested that at the periphery of the particles chemical changes were occurring, HA bone formation at this time point was noted to be the same as the 6 week time point.

Overall it was concluded that bone in growth rates were Bioglass® > A/W > HA. The suggested cause of this is through the formation of an apatite layer (possible with Bioglass® and A/W) which provides a stimulatory role in osteogenic differentiation (161). Furthermore, it was proposed that the presence of silicon in a class A material accounts for the rapid bone in growth when compared to silicon-deficient class B materials.

The composition of the base glass and the heat treatment applied influences the resultant properties of A/W. Increased amounts of MgO and SiO_2 increase the apatite crystallisation temperature, MgO content has more of an influence than SiO_2. Conversely, the apatite crystallisation temperature decreases when the amount of P_2O_5 and CaO are increased, P_2O_5 content has more of an effect in reducing apatite crystallisation temperature than CaO (162). Minor additives such as Na_2O, Fe_2O_3, CaF_2, TiO_2 and B_2O_3 can be included to enhance the properties of A/W; for example Na_2O and P_2O_5 were shown to increase apatite formation *in vitro*, however B_2O_3, Fe_2O_3 and MgO were shown to decrease bioactivity (163, 164). Furthermore, the addition of Al_2O_3 was shown inhibit the formation of a Ca, P-rich layer, diminishing the bone bonding ability of A/W, rendering it a nonbioactive material (165). For reference, compositions of several bioactive glasses and glass-ceramics that have been developed is given in Table 2.3.

Table 2.3: Compositions of bioactive glasses and glass-ceramics

Material	Composition (wt %)							
	SiO_2	MgO	CaO	K_2O	P_2O_5	B_2O_3	Na_2O	CaF_2
13-93	53	5	20	12	4	0	6	0
13-93B1	34.4	4.9	19.5	11.7	3.8	19.9	5.8	0
13-93B3	0	4.6	18.5	11.1	3.7	56.6	5.5	0
45S5	45	0	24.5	0	6	0	24.5	0
58S	58.2	0	32.6	0	9.2	0	0	0
6P53B	52.7	10.2	18	2.8	6	0	10.3	0
70S30C	71.4	0	28.6	0	0	0	0	0
A/W	**34**	**4.6**	**44.7**	**0**	**16.2**	**0**	**0**	**0.5**
CEL	40.9	4.3	22.1	5.7	12.9	0	14.1	0
CEL2	40.9	4.3	22.1	5.7	12.9	0	14.1	0
ICEL	1.1	1.8	9.1	2.4	79.8	0	5.8	0

2.13. Bioactive coatings - Fluorapatite

Bioactive coatings have been used in orthopaedics and dentistry since the 1980's (166) and have shown good clinical success through 10-15 years follow up clinical studies (167-169). Several methods have been investigated such as enamelling (170-172), electrophoretic deposition (173, 174), thermal spraying (175-177) and "thin film technologies" (178-180). Coatings of hydroxyapatite have been shown to possess relative risk of de-bonding from the implant and limited stability within the body (181, 182); the application of a fluorapatite (FA) coating has been shown to have lower solubility, improved osseointegration and overall increased stability than that of HA coatings (182-184). Coating an A/W scaffold with FA in addition to possibly achieving faster osseointegration, has a second potential advantage; a common cause of implant failure is bacterial infection and the possibility of inducing an anti-bacterial surface modification through FA is worth investigating. Taking a biomimetic approach, cells present in the human body encounter features on both micrometre scale and nanometre scales. The use of a nanoscale (as opposed to a micro-scale) coating is also worth investigating as, in general, nanoscale surfaces have a high surface energy leading to increased initial protein adsorption which is very important in regulating the cellular interactions on the scaffold surface (185). Surface properties also have an impact on adhesion, together with charge distribution and the chemistry of the material. Indeed. the use of an FA nano-crystalline coating in bone grafts was recently patented under the claim that "*wherein fluorapatite crystallites from the fluorapatite nano-crystalline coating immediately and continuously release fluorapatite to the cellular environment over the course of treating the cells. The compositions and methods promote cell differentiation, migration, and proliferation. Through the use of compositions and* *methods provided herein, inhibition of the migration of connective tissue and epithelial cells to bone defect sites is realized for better bone restoration by osteoblast cells. Moreover, inhibition of inflammatory cells and bacteria at the surgical site are realized, further enhancing bone restoration*" (186).

A method of applying an ordered fluorapatite (FA) layer onto a substrate has been extensively studied via Liu *et al* (187). This method of coating is achieved via a hydrothermal processes (187-189); through control of the autoclaving time and pressures applied, ordered and disordered FA crystals can be produced. In brief; the ordered crystal structure is favoured over the disordered precipitate (Figure 2.1), in vitro studies have shown increased cellular densities and responses (188). Furthermore, Al-Hilou *et al* looked at both disorded and ordered FA coatings with respect to their anti-bacterial behaviour and found that an ordered FA coating layer reduced not only bacterial viability but adhesion too (190).

A/W alone has been shown to be bioactive and illicit a strong physiochemical bond at the bone:implant interface; however, the potential success of a porous glass-ceramic scaffolds is reliant upon cellular attachment and proliferation throughout the entire scaffold. The work conducted utilising an FA coated substrate showed that vital cell adhesion molecules were up-regulated, such as:

Secreted phosphoprotein 1 (SPP1) Thrombospondin 3 (THBS3) Integrin alpha 7 and 8 (ITGA 7 and 8) Integrin beta 3 and 4 (ITGB3 and 4) Vitronectin receptor (αvβ3) and integrin alpha V (ITGAV). Where a purely porous AW scaffold may form a physiochemical bond at the interface site, including an FA coating throughout a porous scaffold could enhance cellular adhesion and promote rapid mineralisation. An FA coating has not been applied to a glass-ceramic, additionally the hydrothermal process described has never been applied to a 3-D construct, the potential advantages of including an FA coating are therefore worth investigating. Another potential benefit is that such a coating may also enhance mechanical properties through occluding residual porosity in the struts caused by the burn out process during scaffold manufacture.

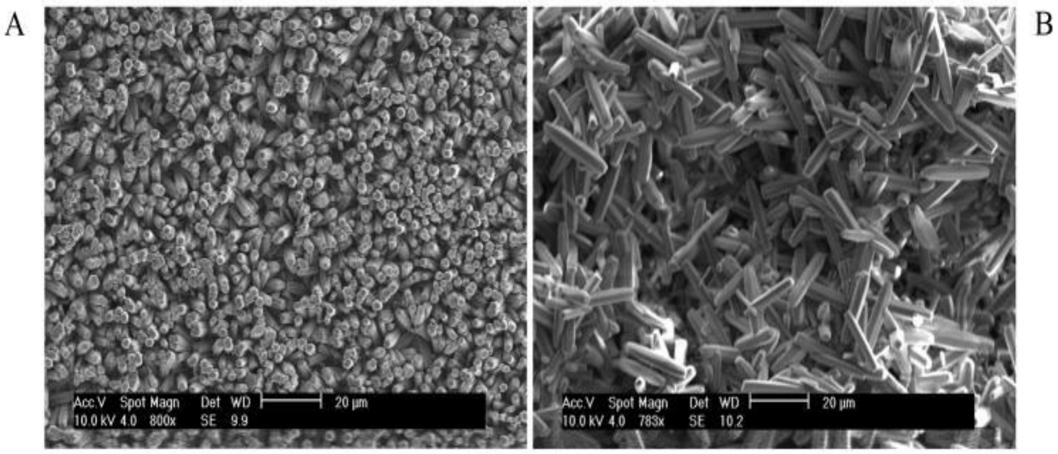

Figure 2.1 – A) Ordered FA coating; B) Disordered precipitate. Reprinted with permission from Liu *et al*, 2011 (187)

2.14. Current Strategies

Construction of 3-D glass-ceramic scaffolds that satisfy these criteria can be achieved through a variety of methods, which have been extensively reviewed within the literature (191-195). In general, broad similarities can be drawn between these methods: the desired interconnected architecture is imposed upon the glass, which is subsequently heat-treated. The glass is commonly a component of a slurry/paste, which usually includes the use of a binder to adhere the glass particles to a mould. From this the desired architecture is formed through several creative methods such as through the use of foaming agents or even freezing the material, this section shall discuss these methods in more detail.

2.14.1. Organic filler (Porogen burn-out)

A relatively simple method of introducing porosity to a scaffold is through the use of organic fillers, this method is arguably the most commercially viable in terms of the materials required and the limited number of steps required. The process involves mixing a chosen precursor powder (which like other methods discussed will undergo a final heat treatment) with an organic filler material; unlike other methods an aqueous solution is not always produced, simplifying the process further. Once the powder and organic filler has been mixed it generally undergoes uniaxial compression to form a crack free "green part", the pressure applied is usually >100 MPa for 10 s, however some methods negate this step through the use of PVA as a binder. Once the green part has been formed it undergoes a heat treatment, the organic filler is burnt out leaving a porous scaffold. Where this method has the advantage of simplicity it equally suffers from this. There is little control over the interconnected structure; excessively large pore sizes (>500 µm) can form due to agglomeration of the organic filler particles and relatively low overall porosities are reported in the literature (196, 197) (see Table 2.4)

Table 2.4: Porogen burn-out scaffold properties

Glass powder	Binder	Other	Pore Sizes (µm)	Porosity (%)	Strength (MPa)	Year	Author	Ref
CDA	N/A	Naphtalen	/	/	/	2006	Tancret *et al*	(196)
SNCM	N/A	Starch (Corn, Potato and Rice)	20-100	40	6_c	2005	Vitale-Brovarone *et al*	(197)

Mechanical strengths: subscript c – compressive

2.14.2. Sol Gel

A relatively complex method of creating a porous foam structure is through the sol-gel technique (198-200). Briefly, the initial "sol" is prepared through a careful mixing of sol-gel precursors in distilled water with nitric acid, which acts as a hydrolysis catalyst. Once hydrolysis is completed the gelling agent is added with a surfactant followed by vigorous agitation; as the viscosity of the sol increases to an appropriate level the foamed sols are transferred to moulds, sealed, allowed to age and finally the residual solvent is allowed to evaporate. Once this preparation is completed the final thermal stabilization is undertaken. When compared to melt-derived bioactive glasses, sol-gel derived glasses are reported to exhibit enhanced resorb-ability and bioactivity in vitro, additionally when implanted in vivo they exhibit improved bone bonding. These improved properties over melt-derived scaffolds have been attributed to excellent mesoporous textures (pores ranging from 2-50 nm), high interconnectivity (interconnected channels of 100 µm) and a high specific surface area (see Table 2.5). Obtaining this structure however requires a lengthy and complex process when compared to melt-derived scaffolds, furthermore when attempts were made to scale up the technique issues were immediately encountered (198). Where this technique presents a novel method of producing a highly porous (and well interconnected) glass-ceramic scaffold it is questionable whether its inherent complexity is suitable for large scale commercialisation.

Table 2.5: Sol gel scaffold properties

Glass powder	Other	Pore Sizes (µm)	Porosity (%)	Mechanical Strength (MPa)	Year	Author	Ref
100S, 70S30C, 58S	TEOS, TEP, calcium nitrate, HNO_3, polyethyleneglycol trimethylnonyl ether, Tergitol TMN10, Teepol	10 - 200	/	/	2001	Sepulveda *et al*	(199)
100S, 70S30C, 58S	TEOS, TEP, calcium nitrate, HNO_3, polyethyleneglycol trimethylnonyl ether, Tergitol TMN10, Teepol	10 - 225	/	/	2003	Jones and Hench	(201)
Snowtex-S	Hcl, sodium lauric sulfate ester	/	73 and 84 (Calcined), 66 and 68 (sintered)	2.4_f	2004	Tomita and Kawasaki	(200)
58S	TEOS, TEP, calcium nitrate, HNO_3, polyethyleneglycol trimethylnonyl ether, Tergitol TMN10, Teepol	10 - 200	/	/	2004	Jones and Hench	(202)
70S30C	2N Nitric acid, TEOS, Teepol, HF, water	87 -122	82 - 88	$0.36 – 2.26_c$	2006	Jones *et al*	(203)
70S30C	2N Nitric acid, TEOS, Teepol, HF, water	561 - 743 (modal pore diameter)	84.5 - 92.0	/	2007	Jones *et al*	(204)
70S30C	PEO, acetic acid, TMOS, Calcium nitrate tetrahydrate, De-ionized water, HF, NH_4OH	5 - 300	80 - 90	/	2009	Marques and Almeida	(205)
45S5	De-ionized water, 2N Nitric acid, TEOS, TEP, Sodium nitrate, Calcium nitrate, Teepol, HF	200-1000	>90	$\sim 0.5 – 2_c$	2011	Chen and Thouas	(206)
70S30C and 58S	PEO, acetic acid, TMOS, Calcium nitrate tetrahydrate, De-ionized water, HF, NH_4OH	620 - 790	74 - 82	/	2011	Almeida *et al*	(207)

Mechanical strengths: subscript c – compressive, subscript f - flexural

2.14.3. Freeze Casting

Freeze casting is similar in some respects to the foam replica technique; a slurry is produced that subsequently undergoes a heat treatment to produce a porous scaffold. However rather than using a polyurethane foam as a template, directional freezing is employed to introduce porosity (notably unidirectional which is specifically attractive for trabecular mimicry) which then undergoes a final heat treatment. The general process involves ball milling a slurry consisting of the precursor material, which remains as the final structure (glass or ceramic powder) after the application of a heat treatment, combined with an aqueous sublimable constituent, and a dispersant, which aids in producing a homogeneous mixture. Once the slurry has been prepared it is poured into moulds (usually polyethylene or rubber) which are in contact with a copper plate and kept sealed to prevent sublimation at this stage (208). The temperature of the copper plate is carefully controlled (liquid nitrogen is commonly used) to induce unidirectional freezing; samples then undergo an annealing step, a sublimation step and finally a heat treatment to produce a porous sintered scaffold.

Table 2.6 details the various constituents and processes that have been investigated, the use of camphene has been extensively investigated as it freezes at room temperature making it an attractive prospect as a sublimation vehicle. This step can simply be done at room temperature by removing the cap on the moulds, unlike other methods which employ (for example) deionized water and require freeze drying under a vacuum pressure (commonly 2.1 Pa) (209). Where the freeze casting technique shows an obvious advantage of producing anisotropic scaffolds similar to trabecular bone, the use of camphene has been noted as being unsuitable for scale up due to its inherent cost. Recent efforts have been made to employ de-ionized water as the aqueous component to improve commercial viability; however as previously stated this requires further complications to the processing method (i.e. freeze drying under vacuum conditions), it is questionable as to whether this technique will lend itself to large scale production.

Table 2.6: Freeze casting scaffold properties

Glass powder	Binder	Other	Pore Sizes (µm)	Porosity (%)	Mechanical Strength (MPa) (compressive)	Year	Author	Ref
Al_2O_3	/	Camphene, Perfad 9100	/	41	/	2005	Araki *et al*	(209)
45S5	/	Camphene, Hypermer KD-4	/	~ 53	/	2006	Song *et al*	(210)
Alumina (AKP 30)	/	Camphene, Hypermer KD-4	102 - 210	59 - 82	11 to 95	2008	Yoon *et al*	(211)
CaP	/	Camphene, Hypermer KD-4	121 (± 33) – 163 (± 47) [1-3 days freezing]	62 - 65	Normally – 4.6 (± 1); Parallel – 9.3 (± 1.6)	2009	Soon *et al*	(208)
HA	Polystyrene	Camphene, Hypermer KD-4	277 (± 47) to 141 (±11)	71 - 73	1.1 (± 0.2) to 2.3 (± 0.5);	2009	Yook *et al*	(212)
13-93	/	Camphene, Isotearic acid	6 - 115	19 (± 4) to 59 (± 3)	16 (± 2) - 180 (± 70) [Parallel] 2 – 13 [Perpendicular]	2011	Liu *et al*	(213)
Baghdadite powder (Ca:Si:Zr 3:2:1)	PVA	De-ionized water, Dolapix PE62	/	58.22 – 64.27	1.3 - 2.1	2014	Sadeghpour *et al*	(214)

2.14.4. Additive Manufacturing

The concept of additive manufacturing (AM) is a process involving the use of computer aided design (CAD) files which are converted into multiple 2-D cross sectional layers, this in turn allows complex 3-D shapes to be precisely reproduced without the need of tools, moulds or dies. Several variations to this process have been developed; however two key strategies can be distinguished, powder deposition (3-D printing) and extrusion deposition (robocasting), the resultant scaffold properties of using these methods is described in Table 2.7.

In general, a 3-D structure is formed through sequentially spraying a binder in the required 2-D shape and then applying the powder onto the binder. This process is undertaken on a mechanical platform that is lowered between the applications of each layer; these steps are repeated until the full 3-D structure is produced and is ready for a final heat treatment, this process is usually termed 3-D printing. Limitations to the precision with which the pre-heat treated scaffold can be produced are dictated by the minimum size of the nozzle used to form the 2-D binder shape and the step size the mechanical platform can be lowered by. Prior to the application of the heat treatment the scaffold is supported by the surrounding loose powder (which is not in contact with the binder layers); this material must be removed prior to heat treatment by a process termed “de-powdering”, usually involving the use of compressed air and/or ultrasonication. This has been noted as being another limitation to this method as the application of the de-powdering step damages the pre-sintered scaffold architecture.

Two methods of 3-D printing are described in the literature, direct and indirect. Direct SLS involves sintering solely a layer of powder directly via a laser to form a 2-D structure, during this step adjacent particles are heated sufficiently to fuse together. Once this 2-D layer has been sintered the platform is lowered, an additional powder layer is rolled over and the process is repeated until the 3D structure has been formed. As with 3-D printing the surrounding material is removed post-processing, however as sintering has already been undertaken the risk of damage to the scaffold architecture is absent. Indirect SLS differs by using a binder, the laser power is reduced which only bonds the powders; this creates a “green part”. This method allows for the production of composite materials before the final heat treatment is applied, an example of this is a study conducted by Xiao *et al* which introduced phosphate prior to the final heat treatment, allowing for specific material phases to be controlled during the final heat-treatment (137). Robocasting is a similar method that may be employed using similar technology, where 3-D printing involves sintering 2-D layers of powder sequentially; robocasting (direct-ink-write assembly, extrusion fabrication, etc) uses a CAD modelling system to sequentially layer a paste into a 3-D structure, which then undergoes a final heat treatment. This method has been shown to produce scaffolds with high mechanical properties and repeatable interconnected structures (215, 216).

Table 2.7: Additive manufacturing scaffold properties

Glass powder	Binder	Other	Pore Sizes (μm)	Porosity (%)	Mechanical Strength (MPa)	Year	Author	Ref
A/M and HA	N/A	N/A	/	/	/	2005	Lorrison *et al*	(217)
A/M and 45S5 (control)	Acrylic binder	N/A	/	~40	/	2007	Goodridge *et al*	(218)
A/W	Acrylic binder	N/A	/	~40	~ 102_c	2008	Xiao *et al*	(137)
13-93	Steric acid	Distilled water	300 - 800	50	20.4_c	2011	Kolan	(219)
6P53B	/	Pluronic F-127	500	~60	55_c (perpendicular) 136_c (parallel)	2011	Fu *et al*	(220)
6P53B	PEI	Distilled water, Pluronic F-127	~100	60	136_c	2011	Fu *et al*	(221)
13-93	Aquazol 5	De-ionized water, EasySperse, Surfunol, Glycerol, PEG 400	~300	50	140_c (± 70)	2011	Huang *et al*	(216)
13-93	/	Pluronic F-127, Distilled water	300	47	86 $(\pm 9)_c$ 11 $(\pm 3)_f$	2013	Liu *et al*	(215)

Mechanical strengths: subscript c – compressive, subscript f - flexural

2.14.5. Porous A/W glass ceramic scaffolds

To date there have been limited studies conducted using porous A/W scaffolds; Ijiri *et al* conducted an in vivo study by subcutaneously implanting A/W glass rods in rats to determine potential ectopic bone induction (222). The rods were combined with either bovine bone morphogenic protein (bBMP), collagen or both to determine whether A/W would be suitable as a carrier for BMP. It was determined that porous A/W rods exhibited good osteoconductivity and; combined with their inherent high mechanical strength and ease of handling, showed potential for clinical use in terms of treating large cancellous bone defects or cranio-maxillofacial lesions. Two in vivo studies conducted by Fujita *et al* (223) and Teramoto *et al* (224) used porous A/W rods provided by Nippon Electric Glass Co Ltd; the former investigated its potential use as an intermedullary plug in THR, the latter compared the resorption rates of A/W with that of β-TCP.

The study by Fujita *et al* was conducted over the time scale of two years; the study replicated a standard THR procedure, after which all animals subjected the porous A/W-GC to load bearing expected of clinical use, i.e. within three weeks all animals were completely bearing their own body weight. radiological evaluation showed a gradual decrease in radiopacity until 24 months at which time the plug became radiolucent. Histological evaluation reported new bone formation around the plug at one month, at 6 months bone formation was apparent even at the centre of the plug. At 24 months resorption of the plug was almost complete and replaced by newly formed bone, this was confirmed additionally through SEM analysis which showed a Ca-P rich layer 10 micrometers thick. The results of the study by Fujita *et al* confirmed that porous A/W-GC is effective as an intramedullary plug and has good resorption rates over two years.

The study by Teramoto *et al* used the same scaffolds for a comparative study investigating the resorption rates of A/W-GC and β-TCP (produced by OLYMPUS Co Ltd); each were implanted into femurs of rabbits and examined up to 36 weeks, the porosities of the A/W-GC scaffold ranged from 70-90 % and the β-TCP scaffolds were set at 75 %. The main observation noted was the more gradual resorption rate of A/W-GC over the entire 36 weeks; compared to that of β-TCP which showed greater resorption rates and overall less abundant new bone formation. The main conclusions from this study showed that an A/W-GC scaffold of 70 % porosity provides not only the closest mechanical strength to that of human cancellous bone (compressive strength 20.1 ± 6.3 MPa), it presents good resorption rates, osteochonductive activity and new bone formation.

2.14.6. Foam Replica Technique

This technique can produce porous scaffolds composed of a microstructure comparable to that of dry human trabecular bone. The foam replica technique involves selecting appropriate polyurethane (PU) foam to be used as a sacrificial green body; a slurry is then prepared containing the bioactive glass, a solvent and commonly a binder of some sort. The foam is then immersed in the slurry leading to a homogenous coating of the glass on the polymer substrate surface. Once dried a heat treatment (specific to the thermodynamic properties of the glass) is applied; the heat treatment is designed as such to ensure "burn-out" of the organic constituents, leaving only sintered glass in the required microarchitecture. This process has several fabrication advantages, the foam can be tailored to suit the required porosity and shape, porosities and pore sizes are capable of reaching high values (> 90 % porosity, > 500 µm). Choosing and characterising the polyurethane foam is relatively simplistic; commercially available foams can be utilised for the green body, whose porous nature may be verified through SEM analysis. It is worth noting that where pore sizes are characterised in terms of micrometres, manufacturers generally use pores per inch (PPI), this term is also widely used throughout the literature when describing the foam used in a study.

The challenges associated with this technique are the methods of infiltrating the slurry homogeneously, ensuring retention of the inter-connected structure post burn-out, and application of a heat treatment used to ensure maximum densification of the ceramic. Two of the key disadvantages of the foam replica technique are removal of excess slurry from the foam template and residual hollow struts, which may remain post-heat treatment. Table 2.8 outlines the varying solutions to these problems investigated through the foam replica technique, comparing the variations of bio-glass and glass-ceramics utilised.

Chen *et al* (225) first attempted to apply the foam replica technique using a bioactive glass in 2006 using 45S5 Bioglass. The focus of the work was to:

- Determine a suitable heat treatment to achieve sufficient densification (by ranging the dwell temperatures and times)
- Perform initial characterisation through mechanical testing, and to,
- Assess potential bioactivity through the application of the standard in vitro procedure described by Kokubo *et al* (226).

High porosities were obtained (~90 %) and large pore sizes were noted (510-720 μm) for all sintering conditions. An important observation was reported; in terms of achieving densification via viscous flow, increasing the dwell time was not a defining factor in achieving sufficient densification, for 45S5 Bioglass a dwell temperature at 1000 °C for 1h (deemed the optimal condition) produced the most extensive densification when compared to sintering at 900 °C for 5 h. Mechanical strengths were noted to be comparable to that of natural cancellous bone (0.2 – 0.4 MPa) and HA scaffolds previously produced by Ramay and Zhang (227) with similar porosities, however difficulties were noted in obtaining the data due to samples shearing during uniaxial compression.

A noteworthy study is that of Jun *et al* (228) who produced a composite scaffold of HA-A/W via the foam replica technique. The main argument for this approach is the difficulty in applying a sufficient heat treatment whilst retaining the desired architecture. It is stated that excessive viscous flow when sintering A/W above its glass transition temperature "*often causes its three-dimensional (3-D) porous* *structure to collapse*". However, its high strength, fracture toughness, excellent biocompatibility and bonding ability to real bones makes it an attractive addition to a scaffold produced using HA (45S5). Standard foam replica techniques were employed; slurries of HA and A/W were produced, HA slips were coated onto PU foams and heat-treated, A/W slips were then subsequently applied to the HA scaffold. As expected it was noted that scaffolds produced using HA alone were too fragile to handle to perform mechanical testing. When coated with A/W the mechanical strengths were increased significantly with only a slight drop in porosity (97 % to 93 %); increasing the compressive strength to ~ 1 MPa, attributed additionally to the elimination of sintering defects present from the underlying HA scaffold. This study showed conclusively the applicability of A/W for the use/enhancement of porous glass-ceramic bone tissue engineering (BTE) scaffolds; this study however still relied on HA as a base for scaffold production.

The vast majority of foam replication studies utilise a single type of PU template (or compare multiple template types with one another), however two studies worth discussing are those of Hsu *et al* (229) and Bretcanu *et al* (230). Hsu *et al* suggested combining two PU foam templates of differing pore sizes (20, 30 and 45 PPI) via two techniques, scaffolds prepared in such a manner were termed functional gradient materials (FGM's). The first technique involved stitching together two differing PU foam templates; the second involved cutting out a section of foam and press fitting it into a pre-cut space into the other differing foam, these templates then underwent a standard dip coat process. To compare these FGM's to "standard" foam replica scaffolds homogeneous HA/TCP scaffolds were produced using 20, 30 or 45 PPI foams and were prepared into standard four point bend test specimens. Through visible inspection, it is clear that combining two, differing PU foams (through either method reported) creates differing zones of porosity and pore size morphology; however no porosity or pore size data is given for either method. The authors reported flexural strengths of 18.32–19.65 MPa for the homogeneous samples and 15.61 (± 2.72) MPa for the FGM samples. Though the bend strengths reported are high it is apparent (through visual inspection alone) that the porosities of the mechanical samples are low, visually differing significantly from the successfully created bi-modal structure shown. Given that no architectural analysis is given, it is difficult to ascertain whether the mechanical properties reported are representative of the highly porous FGM's.

Bretcanu *et al* reported an alternative approach to introducing anisotropy in 2008 (230). This study could be considered a continuation of the work conducted by Chen *et al* in 2006; 45S5 glass was utilised in this study as before, however poly(D,L-lactic acid) (PDLLA) was used as a binder and the heat treatment was slightly altered to 1100 °C for 1h to sufficiently sinter and crystallise the scaffold. The key difference in this study was the pre-forming of the PU foam template; an aluminium mould was used to apply a porosity gradient prior to the coating and heat treatment steps, when heated for 30 mins at 200 °C it was found that the foam would retain its moulded shape. In a similar manner as Hsu *et al* (2007), two PU foams of differing PPI (45 and 60 PPI) were combined within an aluminium mould and pre-formed in the same manner. Post-sintering analysis via SEM showed that a gradient porosity can be introduced to a scaffold produced via the foam replica technique; it is not known whether the most compacted end would allow for cell migration, however again this is an interesting approach.

Vitale-Brovarone *et al* (2007) investigated applying the foam replica technique utilising a glass termed CEL2 (231); this glass is similar in composition to A/W, belonging to the system SiO_2-P_2O_5-CaO-MgO-Na_2O-K_2O and produced through the melt quench route. As with the work by Chen *et al* (225) the initial studies focused on slurry constituents and optimising thermal treatments. By ranging the binder content (PVA) from 2-8 wt % and glass content from 40-50 % an optimal slurry was determined, namely 6 wt % PVA and 40 wt % glass. Where Jun *et al*'s group produced a porous HA-A/W scaffold to counter act strut collapse due to viscous flow, Vitale-Brovarone's initial study showed that it is possible, by careful design of the thermal treatment, to achieve sufficient densification whilst retaining the desired architecture. The compressive strengths reported in this initial study were 1 (± 0.4) MPa; this reportedly low value was attributed to insufficient coating of the inner sections of the PU foam, further optimisation of the coating regime was expected to improve upon this value. Overall however this was a promising result; pore sizes ranged from 100-500 µm, porosities achieved were 70-75 % (agreeable with previous scaffolds implanted in vivo (223)), good biological behaviour via osteoblast proliferation was noted and the scaffold had sufficient mechanical strength to be handled.

Further work by Vitale-Brovarone *et al* (2008 and 2009) investigated alternative materials to that of CEL2 (232, 233). The study in 2008 produced glass-ceramic containing fluorapatite crystals; this study was conducted primarily to compare the antibacterial effects of doping with an Ag aqueous solution, however the scaffold was also assessed architecturally and mechanically. The key points from this study (in terms of scaffold production) again confirmed that slurry constituents must be carefully balanced; insufficient binder and powder wt % leads to poor resultant architecture, coupled with this a final step to remove excess slurry can result in improved architectures. Overall, the production of a Fa-GC scaffold was successful; they exhibited compressive strengths of 2MPa, open pores >100 µm and overall porosities of 75 % which lie within recommended values.

The study conducted in 2009 focused on comparing a "specular" glass (based on P_2O_5) to that of CEL2 (based on silica), the key differences in these glasses are the relative amounts of SiO_2 and P_2O_5. The silica based glass (CEL2) was composed of 45 mol. % SiO_2 and 3 mol. % P_2O_5, the specular glass (termed ICEL2) was inverted and composed of 45 mol. % P_2O_5 and 3 mol. % SiO_2. Thermal characterisation showed that ICEL2 (when compared to CEL2) exhibited a lower glass transition temperature; a single crystallisation peak (as opposed to two) and two crystal melting points, which again were both lower than that of CEL2. Both glasses exhibited a good degree of sintering, however a higher degree of sintering was noted for CEL2. Additionally the scaffolds produced using ICEL2 exhibited a "*greyish*" colour, indicating that residual carbon remained due to the lower sintering temperature used, due to the lower glass transition temperature. Mechanical characterisation showed inferior compressive strengths when using ICEL2, a 10-fold decrease was reported, 5.2 MPa for CEL2 compared to 0.4 MPa for ICEL2. Furthermore, *in vitro* testing showed the ICEL2 scaffolds underwent a high degree of dissolution, weight losses after 1 month of soaking in SBF were up to 17 (± 3) %. This suggests that a phosphate based GC could exhibit un-desirable absorption rates *in vivo*, much like the β-TCP scaffold comparison conducted by Teramoto *et al* (224). In summary, a silica-based GC scaffold presents itself as a more likely successful candidate.

Another silcate based glass derived from the well established 45S5 is designated 13-93, Fu *et al* (234) conducted a study utilising this glass and applied the foam replica technique. The optimal slurry constituents were defined as 35 wt % glass, 1 wt % PVA and 0.5 wt % EasySperse (used as a dispersant), subsequently excess slurry was removed via squeezing. Reported pore sizes ranged from 100-500 µm, overall porosity was 85 (± 2) % and the scaffolds had a compressive strength of 11 (± 1) MPa. As with other studies that used uniaxial compression to characterise the mechanical properties, multiple failure regions were noted due to the complex failure characteristics. Again, this implies that porous GC's fail in a manner unlike isotropic materials and could be an un-applicable testing method. However, this study provided further proof that a silicate based glass ceramic produced via the foam replica technique shows promise in producing a viable trabecular bone graft.

Vitale-Brovarone *et al* continued developing a porous glass-ceramic scaffold utilising the previously described CEL2; the study conducted in 2009 is worth noting due to its emphasis on scaffold preparation, a detailed description of production methods and resultant mechanical properties was reported (235). The main emphasis is on slurry infiltration, applied heat treatment and use of a drying agent (ethylene glycol). The slurry impregnation methods were altered by repeating a 60 % compression of the saturated foam (3 times – Method A), applying an additional saturation step followed by 33 % compression (method B), or an additional saturation step followed by no compression (Method C). In addition to these methods alterations in drying times, the use of a drying agent and the applied thermal treatment were compared to assess their effect on the resultant scaffold properties. The heat treatments investigated were 950 °C for 3 h and 1000 °C for 3h.

All impregnation methods exhibited acceptable porosities (>50 %) showing good interconnectivity, where Method C showed the best coating of the PU foam, all methods exhibited clotted pores due to excess residual slurry. The porosities varied from 53.5 (± 3.7) to 72.3 (± 3.3) %; the compressive strengths ranged from 1.3 ± 0.4 to 5.4 (± 1.5) MPa, the main attribute to these ranges was increased coating of the struts and refinement of the heat treatment to increase strut densification. Applying additional drying steps to the pre-heat treated scaffold was reported to have minimal effect. For example with method A vs A-1 (A-1 included an additional drying step with extended heat treatment at 600 °C) the resulting porosities were 68.5 ± 4.6 and 72.3 ± 3.3 % , the compressive strengths were 1.6 ± 0.5 MPa and 1.3 ± 0.4.

Mantsos *et al* conducted a study in 2009 in a similar manner as Vitale-Brovarone *et al* (2009), a major focus of this study was varying sintering temperatures and times to assess the resultant effect on scaffold properties (236). A bioactive glass powder termed "0106" was used, this glass powder is silicate based belonging to the system SiO_2–CaO–Na_2O–P_2O_5–K_2O–MgO–B_2O_3. The reasoning behind using this specific composition was that "*it is anticipated that the glass will retain its amorphous structure after heat treatment*", this was expected to improve its potential bioactivity. In addition to using a boron containing glass scaffold a PDLLA coating was applied which has been reported to enhance mechanical properties (237). A key finding in terms of optimising the heat treatment was not only sintering at a high enough temperature but to apply a sufficient dwell at this temperature. Applying a heat treatment of 650 °C for 10 h resulted in poor densification; sintering at 680 °C for 3 h produced dense struts through excessive viscous flow, however the pore sizes were significantly reduced. An optimised heat treatment was determined (through trial and error) as 670 °C for 5 h, this produced pores in the range of 105-515 µm with an average porosity of 68 %. However the compressive strengths of the produced scaffolds were low, with or without a

PDDLA coating they were reported as 0.40 MPa (±0.05) and 0.60 MPa (±0.08). Furthermore the stress-strain curves produced are extremely erratic, completely absent of a linear slope (requiring a best fit line to "*guide the eye*"), implying multiple failure regions at all applied loads. From this study alone the use of a boron containing glass would appear to be a poor choice for producing a porous glass-ceramic scaffold, however further studies by Fu *et al* showed that this is not the case.

Fu *et al* developed upon replacing the silica content of the previously described 13-93 glass with B_2O_3; specifically comparing 13-93 with that of 13-93B1 (one third of the molar SiO_2 with B_2O_3) and 13-93B3 (completely replacing the SiO_2 with B_2O_3), porous scaffolds were produced through the foam replica technique (234) and their resultant properties assessed. The main issues with using a borate-based bioactive glass are their rapid dissolution rates and potential toxicity, the first study (part I) concentrated on boron content in the pre-cursor glass and its *in vitro* characteristics. Scaffolds were produced in the same manner as described by Fu *et al* (234); compressive strengths increased with increased boron content, from 13-93, 13-93B1 and 13-93B3 strengths were reported as 11 (± 1.0), 7 (± 0.5) and 5 (± 0.5) MPa respectively (238).

In terms of porosity and pore size distributions all scaffolds produced were reportedly the same, porosities ranged from 78-82 % and pore sizes ranged from 100-500 µm. When *in vitro* conditions were applied it was shown that with increasing boron content (from 13-93 to 13-93B3) total weight loss of the scaffold decreased as did overall strength. A further *in vitro* study and *in vivo* implantation showed similar results, increased B_2O_3 content increased degradation and exhibited an increased toxic response (239). The *in vivo* results differed however; all scaffold types were reported to support tissue in growth, this was attributed to the "*dynamic*" conditions as opposed to the "*static*" *in vitro* conditions.

A further study conducted by Gu *et al* (240) continued this work by implanting 13-93B1 scaffolds in rabbits to assess the *in vivo* response, scaffolds were implanted in a femoral head defect model and a critical size defect radii model. A key comparison in this study is the use of a platelet-rich plasma (PRP). PRP is known to stimulate bone formation through the introduction of growth factors; this study argues that the 13-93B1 scaffold could be used as such a carrier to promote bone growth, it is also arguable that any porous scaffold could be a carrier of PRP. Both scaffolds reportedly showed biocompatibility, when compared to un-filled defect control the PRP treated defect performed the best. It is noted in this paper that "*scaffolds composed of borosilicate and, in particular, borate bioactive glasses is the toxicity of boron released during degradation*". Low concentrations of borate have been shown to be beneficial to new bone formation; high concentrations have been shown to be toxic. In terms of scale-up this implies that a higher degree of manufacturing tolerance would be required when compared to conventional silicate-based scaffolds, especially when the *in vivo* success of previously used scaffolds.

Table 2.8: Foam replica scaffold properties

Glass powder	Binder	Other	Pore Sizes (µm)	Porosity (%)	Mechanical Strength (MPa)	Year	Author	Ref
45S5	PVA	De-ionized water	510 - 720	89-92	$0.27 - 0.42_c$ $0.4 - 0.5_f$	2006	Chen *et al*	(225)
CEL2	PVA	Distilled water	100 - 600	~ 70	1_c (± 0.4)	2007	Vitale *et al*	(231)
HA and A/W	PVB	Ethanol	300-800	~ 93	~1_c	2007	Jun *et al*	(228)
Fa-GC	PVA	Distilled water	0-50: 53 %, 50-600: 47 %	74.6 (± 3.4)	2_c (± 0.6)	2008	Vitale *et al*	(232)
13-93	PVA	Easysperse, Ethanol	~ 100 - 500	85 (+/- 2)	11_c (±1)	2008	Fu *et al*	(234)
45S5	PVA	De-ionized water	510-720 (assumed to be same as Chen 2006)	90 - 95	$0.27- 0.42_c$ (assumed to be same as Chen 2006)	2009	Ochoa *et al*	(241)
CEL2	PVA	Distilled water	0-100: 84 %, 100-1000: 16 %	53.5 ± 3.7 to 72.3 ± 3.3	1.3_c ± 0.4 - 5.4_c ± 1.5	2009	Vitale *et al*	(235)
CEL and ICEL2	PVA	Distilled water	100 - 500	54.8 ± 4.5 (CEL2) and 82.0 ± 6.7 (ICEL2)	5.2_c (± 2.0) and 0.4_c (± 0.2)	2009	Vitale *et al*	(233)
CEL2	PVA	Distilled water	100 - 500	54.0 ± 0.9	Not Stated (assumed to be same as Vitale *et al*, 2009)	2009	Renghini *et al*	(242)
0160	PVA	De-ionized water	105 – 515 (optimised scaffold)	68 (optimised scaffold)	0.40_c (±0.05) - 0.60_c (±0.08) [with PDLLA]	2009	Mantsos *et al*	(236)
13-93, 1393B1, 13-93B3	PVA	Easysperse, Ethanol	100 - 500	78 (± 2) - 82 (± 3.0)	5_c (± 0.5) - 11_c (± 1)	2010	Fu *et al*	(238)
13-93B1	Ethylcellulose	Ethanol	400 - 650	78 (± 8)	5.1_c (+/-1.7)	2014	Gu *et al*	(240)

Mechanical strengths: subscript c – compressive, subscript f - flexural

3. Aims

The overall aims were to produce a porous A/W scaffold with characteristics comparable to that of trabecular bone, and to assess the biocompatibility of the optimised scaffold through the use of live/dead assays. To achieve the first aim; a range of slurry constituents, foam templates and heat treatments were used. The subsequent architectural and mechanical properties of the produced scaffolds were then characterised to assess their reproducibility and physiological relevance. To achieve the second aim; *in vitro* studies were conducted with hADSC's on scaffolds which presented themselves as the most consistent and physiologically relevant post characterisation. Potential optimisation of *in vivo* integration was investigated through the use of a hydrothermal process, with the aim of applying a fluorapatite coating to the porous A/W scaffold.

3.1. Objectives

- Confirm glass production consistency through particle analysis and DSC.
- Select key variables of scaffold production to carry forward to characterisation.
- Characterise the architectural and mechanical properties of scaffolds produced through selected key variables.
- Apply a hydrothermal process to glass-ceramic scaffolds, assess the ability of the scaffold to support an FA coating.
- Conduct *in vitro* studies, with and without FA coatings, to assess the short term biocompatibility of the scaffold.

4. Methods

4.1. Glass Production and Analysis

The A/W parent glass used in this study is that used by Xiao (137); glasses were produced in single 200 g batches and double 400 g batches to the final compositions listed in Table 4.1. The process and timing of producing multiple double batches is described in appendix 8.1.

Table 4.1: List of reagents used for single and double batches of glass

Reagent	**MgO**	**CaO**	**SiO_2**	**P_2O_5**	**CaF_2**
Supplier	VWR International	Fisher Scientific	Tilcon Sands	Sigma-Aldrich	VWR International
mol. %	7.1	49.9	35.4	7.1	0.4
wt %	4.6	44.7	34.0	16.2	0.5
Mass (g) (single batch)	9.2	159.6	68.0	32.5	1.0
Mass (g) (double batch)	18.4	319.2	136.0	65	2.0

Reagents were weighed to the nearest 0.1 g (using a Satorius Roughing Balance, PT3100) and placed into a mixing container, a stainless steel agitation bar was added to the reagents which were mixed for 1h. The powder mix was transferred to a slip cast alumina crucible, which in turn was placed within a larger mullite crucible containing a separating coating of calcined alumina powder, and covered with a lid. The crucible was then pre-heated in an Elite BCF 13/12-2416 furnace at 500 °C and held at this temperature for 45 minutes. Following this the crucible was transferred to a Pyrotherm 1600 °C furnace (pre-heated to 1400 °C), the temperature was increased to 1450 °C where the powders are left to melt for 2 h. Following melting, the liquid glass was shock quenched into a cold water bath, and collected in a 36 µm filter using a Clarke CPE 110p pump. The glass frits were then placed in a drying cabinet for 24 h to dry. The glass frits were ground for 4 minutes (8 cycles of 30 seconds) using a Gy-Ro Mill puck mill, the resulting powders were then sieved using a sieve stack (Otagon Digital) at amplitude 6 on a pulse setting for 90 minutes.

All sieves used were BS1410/1986 certified, particles were sieved into the following fractions: <45 µm, 45-90 µm, 90-125 µm, 125 µm-1 mm, 1-2 mm and >2 mm. Sub 45 µm particle sizes were assessed through DSC (at a constant heating rate of 5K/min) within the temperature range 400-1100 °C in a nitrogen atmosphere to determine the glass transition temperature (T_g) and apatite (Tp1) and wollastonite (Tp2) crystallisation peaks.

4.1.1. Particle Analysis

Particle size and distribution of the ground glass was analysed using a Malvern Mastersizer 2000; before each run the system was flushed with distilled water three times, after which a background reading was taken. A slurry was then prepared containing ~ 1 wt % glass particles, a dispersing agent and distilled water. The slurry was passed through the light scattering laser and optics using a Hydro S (Malvern) small volume sample dispersion unit, a constant stirring rate of 1800 rpm was used throughout all readings. A glass bead refractive index of 1.520 was assigned to the glass particles, the water was assigned a refractive index of 1.330. 3 readings were taken from each sample and an average was subsequently calculated.

4.2. Scaffold Production

4.2.1. Foam Templates

Reticulated PU foam templates ranging from 45 PPI - 90 PPI were supplied by Foam Engineers Ltd (see Figure 4.1) ; following the initial template optimisation study only the 90 PPI foam (pore sizes ranging from 40-450 µm) were used (see section 5.2.). 1000 cylinders 20 mm Ø x 10 mm and 1000 cylinders 20 mm Ø x 20 mm of the 90 PPI foam were ordered, the dimensions of these templates were verified by sampling 10 % of each size using a travelling microscope.

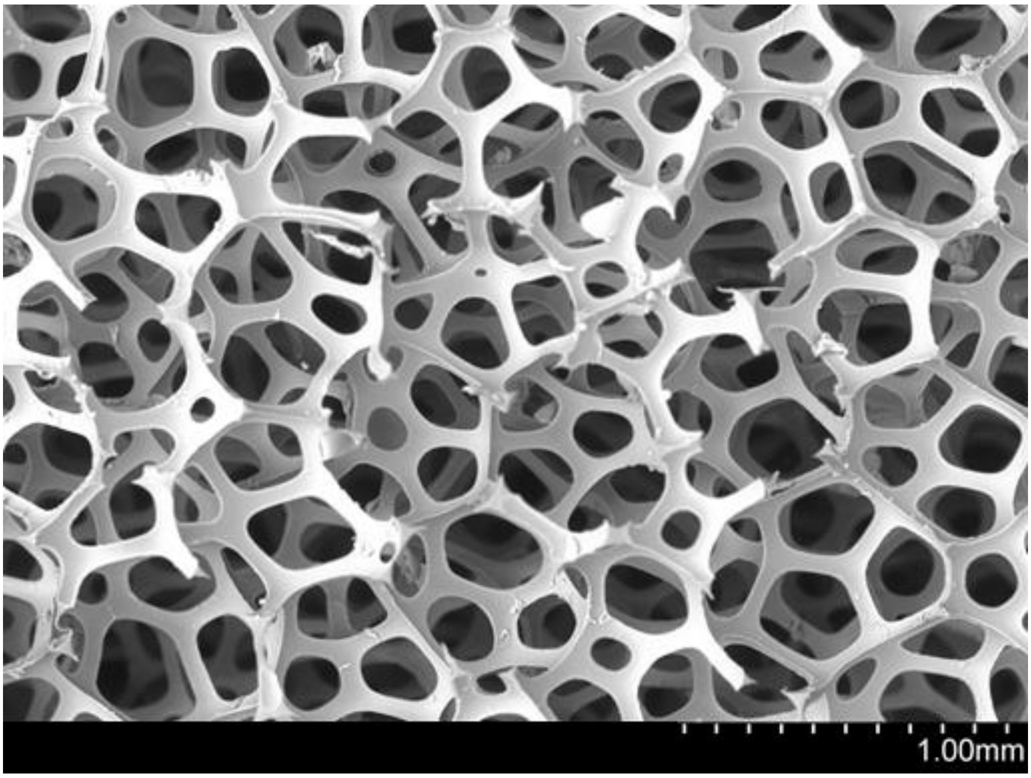

Figure 4.1 – Reticulated polyurethane foam template, 90 PPI. Original magnification x100

4.2.2. Slurry Preparation and Coating Regime

All slurries were prepared using distilled water, high molecular weight polyvinyl alcohol (Mowil 98, Mw ~ 196 000) and sub 45 µm A/W glass. To determine the optimal slurry constituents 2 variables were considered for each group investigated. Polyvinyl alcohol (PVA) was used as a binder for all slurries produced; PVA is used as an adhesive to bind the glass particles to the PU foam. Two types of PVA were initially investigated: low (average Mw 11 000 – 31 000) and high molecular weight (average Mw 196 000). As is discussed in section 5.2.1. the high molecular weight PVA was used for all subsequent testing.

The slurry variables investigated thoughout this study are:

1) The amount of binder used within the slurry, and
2) The amount of glass used in the slurry.

The first variable was denoted “binder solution”; this is simply the wt % of PVA dissolved in the distilled water, which was varied from 4-6 %. The second variable considered was denoted “Binder solution: Glass”, this was varied from a 2:1 ratio to a 1:1 ratio. Table 4.2 lists all slurry constituents that were investigated, depending on the slurry a specific code was given to that group which shall be used herein.

To produce each slurry a 500 ml stock solution of PVA/distilled water mix was prepared to the required wt % prior to addition of the glass for each test. The distilled water was heated in a borosilicate beaker on a magnetic heating plate to 91 °C and covered with tin foil to retain the required volume of water. PVA was weighed on a balance and gradually added over 1 h until it was completely dissolved. Once the PVA/distilled water stock was prepared the required volume was pipetted into a separate beaker (which was kept stirring throughout this process). The sub 45 µm A/W glass was weighed in the same manner as the PVA and gradually added to this beaker, which was allowed to cool to room temperature; this final complete slurry was stirred for 2 h to ensure it was homogenous.

Once the homogenous slurry was made the PU foam templates were coated; the templates were compressed between plastic tweezers, immersed in the slurry and allowed to relax, saturating the template. Following this the template was compressed for 5 seconds and allowed to relax for a further 15 seconds, this process was repeated 3 times to ensure the template was fully saturated with the slurry. The template was then removed from the slurry, briefly placed onto a glass microscope slide (to remove the excess which immediately pools at the base of the template) and allowed to dry for 24 h at room temperature.

For clarification a brief example of an investigated slurry and its resultant code is given below:

Example: A slurry containing **4 wt %** PVA and a **1:1 ratio** of binder solution to glass.

1. 20 g of HMw PVA dissolved in 480 ml distilled water (binder solution stock)
2. 100 ml of binder solution stock pipetted into beaker (binder solution)
3. 100 g of sub 45 µm A/W glass homogeneously mixed into binder solution
4. Slurry denoted **411**

Table 4.2: Slurry constituents investigated

PVA wt % in binder solution	Binder solution:Glass	Code
4	1:1	411
	4:3	443
	10:7	4107
	20:13	42013
	2:1	421
5	1:1	511
	4:3	543
	2:1	521
6	1:1	611
	4:3	643
	2:1	621

4.2.3. Alternative coating regimes

4.2.3.1. Applying compression

Based upon the original foam template height a compression step was applied once the scaffold was coated; this was achieved by using a modified height gauge with a custom-built attachment, which housed a brass sieve pan (1 mm aperture). The sieve pan was lowered until it contacted the coated scaffold, zeroed, and then lowered to 10-50 % of the foam template height. A vacuum nozzle was then carefully used to remove the excess slurry which pooled around the base of the scaffold; the height gauge was then raised, the scaffold was turned over and the process was repeated. Once the process had been repeated the scaffold was left to dry for 24 h.

4.2.3.2. Vacuum Oven

Once a batch of scaffolds had been coated they were placed on a sieve pan which was covered with a sheet of perforated parafilm; this was then placed within a vacuum oven, the pressure was set to 1-2 atm for 15 minutes to 1 h, followed by 24h of drying at room temperature.

4.2.3.3. Suspended

Once scaffolds were coated they were suspended on a rack using high tensile nylon wire (0.1 mm φ) and left to dry for 24 h.

4.2.4. Preparation of flat plates

Slurries were prepared in the manner as described in section 4.2; using a 10 ml syringe the slurry was squeezed onto the lids of 12 well and 48 well cell culture plates (care was taken to contain the slurry within the raised lip of each well) and allowed to dry for 24 h. The plates were used as reference materials to estimate that the heat treatments applied were uniform across the furnace chamber by measuring the cross sectional shrinkage (see Figure 4.2). In addition to their use as reference samples, the plates were used to investigate higher crystallisation temperatures employed in heat treatment B (see section 4.3). Flat plates were also used as substrates for initial FA coating as they closer mimicked the stainless steel discs used in previous work.

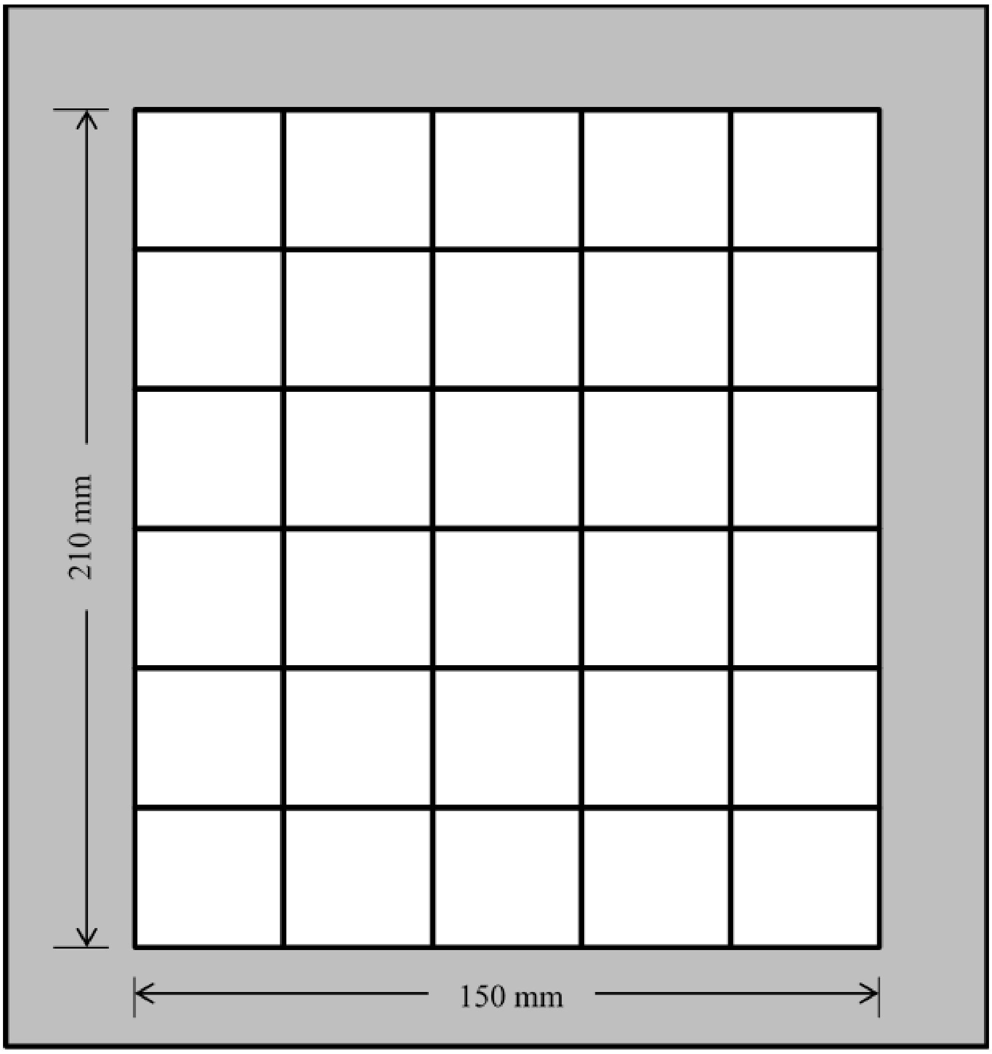

Figure 4.2 –Furnace map. Grey area depicts region of furnace chamber assumed to be a "dead zone" unsuitable for sample placement.

4.2.5. Application of a "cortical shell"

To simulate the cortical shell an additional step was investigated; scaffolds were produced through the method described in 4.2.2 and sintered through heat treatment A (see section 4.3.). Following this a beaker of paraffin wax was heated until melted; the sintered scaffold was then submerged by ~1 mm on either side to seal the faces off. Once the wax had dried the scaffold was fully submerged into a second slurry 543 slurry, allowed to dry and fired through heat treatment B.

4.3. Sintering and Crystallisation

Once dried the scaffolds and plates were placed on plates of carbon free investment material and heat treated; the following diagrams depict the heat treatments that were investigated during this study and will be referred to as heat treatments A and B:

Heat Treatment A:

0 - (4k) -> 400 (1h) – (5K) -> α (x)

Heat Treatment B:

0 - (4k) -> 400 (1h) – (5K) -> 800(5h) – (5K) -> $\beta_{1\text{-}3}$ (1h)

For each heat treatment an initial **burn out stage** was undertaken, the temperature was ramped at 4 K/min to 400 °C and held at this temperature for 1h to ensure the PU foam and PVA was removed. To investigate the minimum dwell temperature and time necessary to sinter the glass particles heat treatment A was employed, the temperature was ramped at 5 K/min to α and held for (x) hours. The dwell temperature (α) ranged from 750 °C to 850 °C and dwell time (x) ranged from 1 to 5 h. Once heat treatment A was optimised to provide sufficient sintering of the glass particles it was used to design heat treatments B and C. These required the addition of a third step in the heat treatment, the temperature was ramped at 5 K/min (from the previously defined α) to β and held for 1 h. The dwell temperatures (β) investigated were 950 °C (β_1), 1025 °C (β_2) and 1100 °C (β_3) all with a dwell time of 1 h. Heat treatment B was used to investigate the dwell temperature and time required to crystallise the scaffold **whilst retaining the desired architecture.** Heat treatment C was used for comparative purposes, utilising a tertiary dwell temperature sufficiently high enough to be detrimental to the resultant scaffold properties. Generalized heat treatment profiles are illustrated in Figure 4.3 and Figure 4.4.

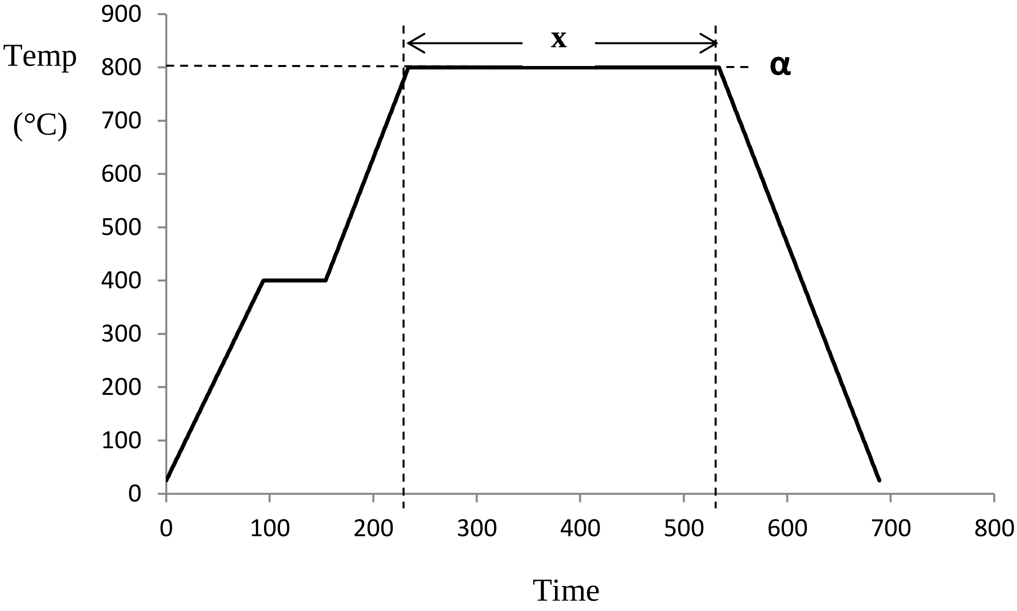

Figure 4.3 – Generalized profile for heat treatment A

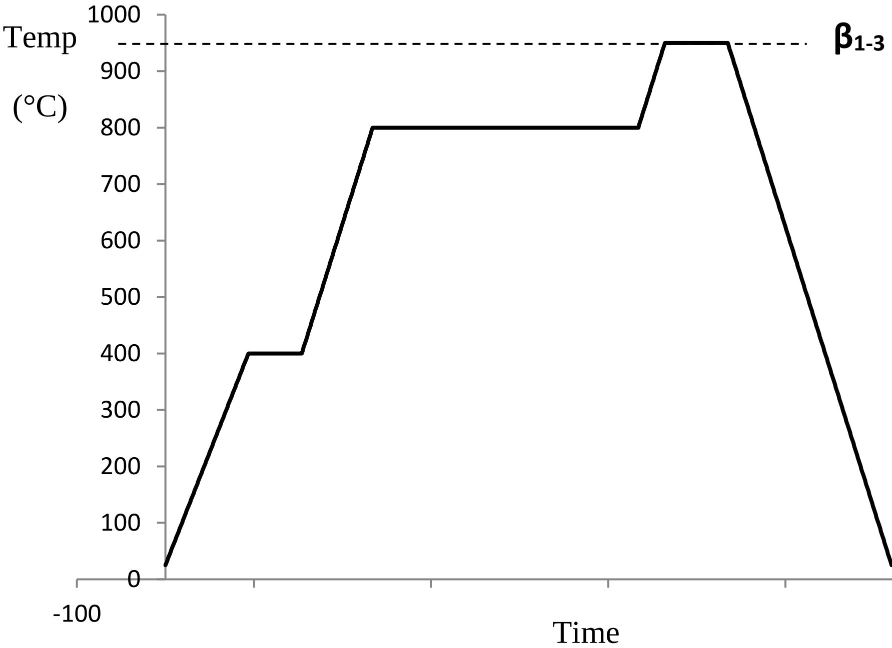

Figure 4.4 – Generalized profile for heat treatment B

4.4. Fluorapatite (FA) coating

The hydrothermal process previously described (187) was scaled up to a larger volume. A two part solution was prepared for the synthesis of FA crystals (all materials supplied via Sigma-Aldrich); the first part of the solution was prepared using 140.4 g of EDTA-Ca and 31.05 g of NaH_2PO_4 added to 1350 ml of distilled water, the pH was adjusted to 6.0 using NaOH and was continually stirred until fully dissolved. The second part of the solution was prepared using 3.15 g of NaF which was added to 150 ml of distilled water; the pH was adjusted to 7.0 using HCl and combined with the first part of the solution. Scaffolds, sectioned discs and plates were placed onto a custom made sample holder (Figure 4.5) in the EDTA-Ca-Na^2/ NaH_2PO4 / NaF mixture and autoclaved at 121 °C at 2.4 $x10^5$ Pa for 10 h.

Following this, the sample holder was removed from the remaining solution and the coated substrates were washed to remove the undesired disordered precipitate that forms within the solution. Coated substrates with placed in beakers of distilled water and sonicated for up to 1 h (one to four 15 min cycles), with the distilled water being replaced throughout this process. Once sonicated the substrates were placed in a drying cabinet at 60 °C for 24 h to ensure they were dried.

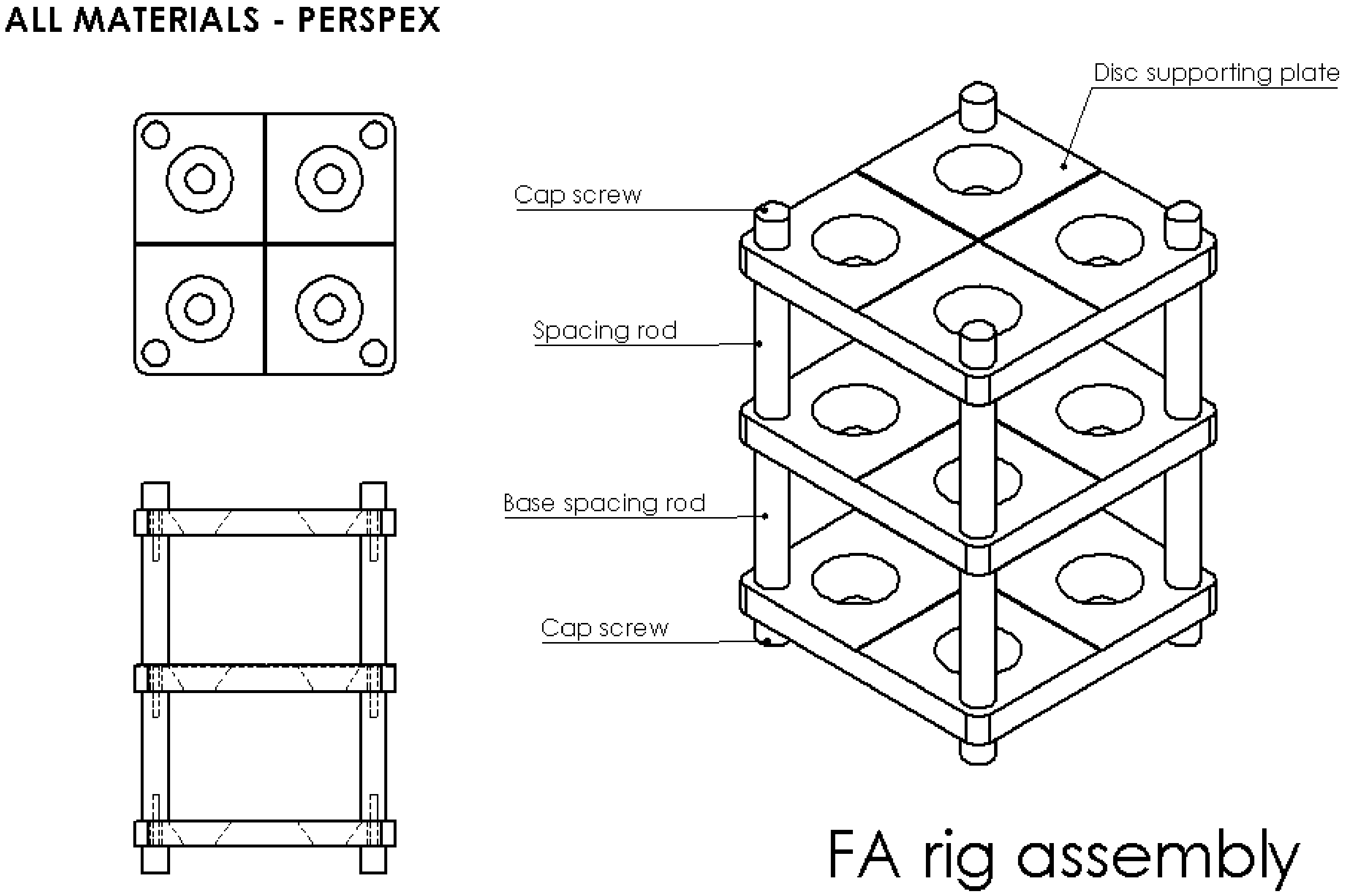

Figure 4.5 - Diagram of FA coating rig, each tier consists of 4 countersunk holes of 17 mm Φ and a through hole of 10 mm Φ

4.5. Architectural Analysis

4.5.1. Scanning electron microscopy (SEM) and energy-dispersive x-ray spectroscopy (EDX)

SEM and EDX analysis was conducted on a Hitachi S-3400N variable pressure SEM (University of Leeds) and a Phillips XL30FEG SEM (University of Michigan), FA coated scaffolds were coated with Au (University of Leeds) or Pt (University of Michigan) using an Agar auto sputter coater to prevent charging.

4.5.2. Micro Computed Tomography (micro-CT)

Each scaffold was sectioned to ensure the maximum diameter was < 17 mm and the height was ≥ 7 mm, scaffolds were stacked into the sample holders and spaced using 90 PPI PU foam. The computed tomography scanning was conducted in a micro-CT scanner (μCT-100, Scanco Medical AG, Switzerland) consisting of a cone-beam x-ray source. The scanner settings were; voltage 90 kV, current 44 μA, integration time 300 ms, in combination with a beam hardening correction algorithm based on a HA- phantom (1200 mgHA/cm^3) provided by the CT manufacture. Initial scans were conducted to optimise scanning protocol. Voxel sizes of 5, 10 and 15 µm were investigated for a range of slurry constituents and heating regime**s**. From these initial results voxel sizes of 10 µm were used for the subsequent studies.

The morphological analysis of scans was conducted on volumes of interest. In all cases a Gaussian filter (sigma = 0.8, support = 1.0) was applied to minimize high frequency noise. Greyscale thresholding was conducted and the best fit was obtained considering the entire stack rather than a single slice. The following morphological parameters were obtained from each of the thresholded image stacks using the manufacturer provided algorithms:

Bone volume to total volume	BV/TV
Surface density	BS/BV (mm^{-1})
Trabecular number	Tb.N (mm^{-1})
Trabecular separation	Tb.Sp (mm)
Trabecular thickness	Tb.Th (mm)

Additionally the pore size distribution of each image stack was obtained, this was given as a percentage distribution determined by the voxel size chosen. For clarity; using a 10 µm voxel size reported the percentage of pores within 0-10 µm, 10-20 µm, 20-30 µm, etc, up to the maximum pore size within the sample. The porosity of each sample was calculated by subtracting BV/TV from 1 and converted to a percentage,

i.e: Porosity = (1 – BV/TV) x 100

As previously noted in the literature review pore sizes ranging from 100-500 µm are desirable properties, as are porosities ranging from 50-90 %. After analysis through mechanical testing the scaffolds chosen for micro-CT characterisation were: 521A, 443A, 443B, 543B and 643B. A sample size of 12 was used for each of the scaffold types characterised through micro-CT.

4.6. X-ray Diffraction (XRD)

Phase compositions of heat treated A/W glass were analysed using a Philips X'Pert diffractometer with a spinning disc attachment and recorded using X'Pert Data Collector Software. A 10 x 10 fixed incident beam mask was used with a CuKα x-ray source. The step size used was 0.033423 °, the dwell was 3.18 seconds and the rotation speed was 4 seconds. Scans were conducted from 10-70 °2θ and 20-60 °2θ.

4.7. Mechanical Properties

Common methods used to characterise the mechanical properties of scaffolds are uniaxial compression and flexural tests (195, 225). Uniaxial compression is the most commonly used due to its simplicity however ceramics generally have a higher compressive strength than tensile strength, they are most likely to fail in tension and as such is the most important mechanical property to determine (243). Uniaxial compression testing of porous, brittle materials suffers from trabecular buckling; resulting in multiple failure regions. Biaxial flexural testing allows for characterisation based on depth of a sample and averaging of a single specimen, this test method is also un-affected by sample edge defects. Furthermore, biaxial flexural testing requires disc shaped samples. This allowed for sample preparation to be kept consistent with respect to micro-CT preparation, FA coating and *in vitro* testing. Moreover, it was possible to carry out micro-CT and flexural strength measurements on the same samples.

The BS EN ISO 6872:2008 standard describes the derivation of biaxial flexural strength with a piston on three ball bearing experimental setup. Where ISO 6872 specifies a specimen thickness of 1.2 mm the ASTM standard F 394-78 (of which ISO 6872 is based upon) does not specify a thickness.

A study by Huang *et al* (243) investigated the BS EN ISO 6872:2008 standard; this was originally derived for piston-on-ring tests (not piston on three ball bearing tests), also this study investigated the use of this ISO standard with multilayered discs up to ~2 mm comprised of varying material properties. Huang *et al* concluded that the formula described in BS EN ISO 6872:2008 was still applicable for piston on three ball bearing testing. The work by Ban *et al* (244) investigated biaxial flexural strength of samples of varying thickness and concluded that “the biaxial strengths of the specimens with different dimensions were not significantly different”. Additionally this study concluded that the effect of geometry on biaxial strength is negligible. Though the BS EN ISO 6872:2008 standard specifies specific sample geometries, it has been shown to be widely applicable and flexible to user’s needs.

Furthermore Fan *et al* (245) successfully conducted biaxial flexural testing of porous HA discs using a ring-on-ring experimental setup. The porosities investigated in their study ranged from 59 – 62 %. For the purposes of this study, it was decided that applying the BS EN ISO 6872:2008 standard would still be applicable, sample thicknesses were set at 1.5 mm ± 0.1 mm.

4.7.1. Biaxial flexural testing

All scaffolds were sectioned using a Struers Accutom-5; an initial facing-off at the base of the scaffold was performed to zero the blade before subsequent cuts were performed (Figure 4.6). Each scaffold was sectioned into 4 discs of 1.5 ± 0.1 mm and air dried for 24 h in an Elite Lenton furnace at 65 °C prior to testing. The dry mass of each disc was measured using a Satorius 0.1 g balance, the cross-sectional area of each disc was obtained from the mean of 3 measurements of the diameter using a 150 mm electronic digital calliper (RS Components Ltd, certificate no: 1348296).

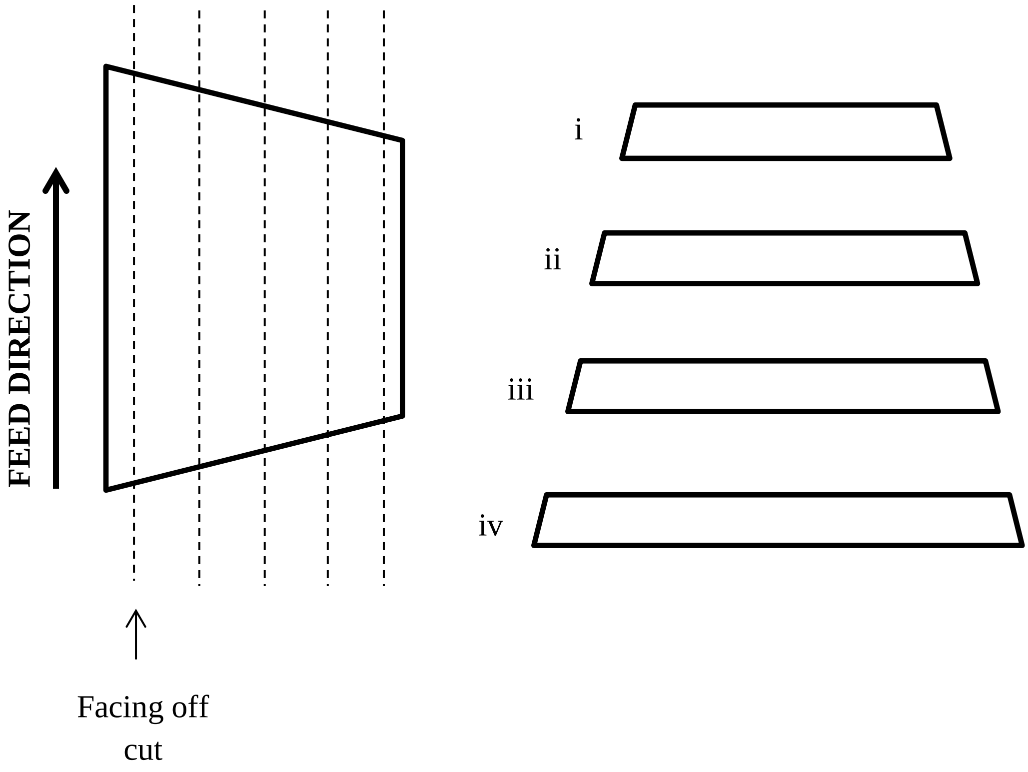

Figure 4.6 – Machining process applied to all scaffolds.

Once the dimensions were obtained, the discs/plates were placed loaded into the biaxial testing rig. The rig consists of a silver steel rod (10 mm Ø) with a flat 1.5 mm tip, 3 mm stainless steel ball bearings arranged in an angle of 120 ° to each other formed a support circle of 10 mm. The discs were placed centrally and loaded at 1mm/min until failure using a 500 N load cell (LC500N/012845, certificate: E182100413090017). Prior to each testing session (or after the rig was cleaned with ethanol to remove the residual from previous tests) a run not containing a sample was performed, the rig was extended at 1 mm/min over 5 mm to ensure the average error of the machine was ≤ 0.5 N.

Biaxial flexural strengths of each disc were calculated using the following equation:

$$\sigma = \frac{-0.2387F(X-Y)}{d^2}$$

Where σ is the maximum centre tensile stress (MPa), F is the load at fracture (N), d is the specimens thickness at the fracture origin (mm),

$$X = (1+\nu)\ln(r_2/r_3)^2 + [(1-\nu)/2](r_2/r_3)^2$$

and

$$Y = (1+\nu)\ln(r_1/r_3)^2 + [(1-\nu)/2](r_2/r_3)^2.$$

In which, ν is the Poisson's ratio (assumed to be 0.25 for all specimens), $r_1$the radius of the support circle (mm), $r_2$the radius of the the loaded area (mm) and $r_3$the radius of the specimen (mm).

4.7.2. Uniaxial compression testing

The uniaxial compressive strength of specific scaffolds was determined using an Instron 3365 testing machine. Cylindrical scaffolds (20 mm in diameter and 10 mm in height) were compressed at a rate of 0.5 mm min^{-1}, the contact surfaces were machined flat to provide parallel surfaces for the tests. Six samples were used for each test, the peak load was recorded from each test and the mean strength and standard deviation was calculated, the compressive strength for each scaffold type was calculated using the equation given below.

$$\sigma_c = \frac{F_p}{A_o}$$

Where σ_c is the compressive strength, F_p is the peak load recorded and A_o is the original cross-sectional area of the sample.

4.7.3. Statistical Analysis and sample sizes

Data for biaxial flexural strength and apparent density were checked for normality using a Kolmogorov–Smirnov test and Shapiro-Wilk test. Both tests suggested that the data was not normally distributed. Data was subsequently analysed by Kruskal-Wallis Test, with Post Hoc Bonferroni, with a significance of ($p < 0.05$) using SPSS version 19. A sample size of 12 was used for each group tested through micro-CT analysis and biaxial flexural testing.

4.8. In vitro hADSC culture

4.8.1. Scaffold and cellular preparation

Scaffolds were sectioned through the method previously described in section 4.7.1 to thicknesses of 0.8 ± 0.1 mm, this thickness was sufficient for fluorescent and confocal microscopy. Once sectioned, scaffolds were sterilized via high temperature and pressure autoclave process. STEMPRO® human adipose derived stem cells (Invitrogen - Catalog no. R7788-110) were revived from an initial population ($1x10^6$/ml in freezing medium) in a T-75 flask using MesenPRO RS™ basal medium (supplemented with MesenPRO RS™ growth supplement, penicillin streptomycin and L-glutamine) ; at ~ 80 % confluency the cells were washed 3 times with PBS , trypsinized and re-seeded into 3 T-175 flasks. Once this second passage had reached ~80 % confluency the cells were detached in the same manner and stored in liquid nitrogen (~$1x10^6$ cells/vial).

4.8.2. Concentrated cell seeding and seeding density validation

Seeding onto porous scaffolds required cells to be resuspended to a high concentration of ~ $5x10^3$ cells/µl; the concentrated droplet was pipetted directly onto the scaffold surface, 50-100 µl of culture medium was added to the edge of each well to aid in retaining moisture during this process. After 2 hours of incubation the required amount of culture medium was finally added to each well. Seeding densities of $5x10^4$, $1x10^5$, $5x10^5$ and $1x10^6$ were investigated for 24 h and 8 days, each time point and density consisted of 3 scaffolds, all cells used were expanded up to their third passage.

4.8.3. Confocal microscopy

At the end of each required time point seeded discs were fluorescently marked with cell tracker green CMFDA (Mw: 464.86, 50 µg powdered, Ref: C7025) and ethidium homodimer-1 (Mw: 856.77, 2 mM in 1:4 DMSO/H_2O, Ref: L3224) this was then diluted into Dulbeco’s modified eagle’s medium (DMEM) at 2 µl/ml and 4 µl/ml respectively. After 2 h of incubation in the marking medium the discs were washed 3 times with PBS and imaged on a Leica TCS SP2 confocal laser scanning microscope with AOBS, 488 nm Ar/Kr laser line and HeNe 543 nm laser were used to excite the live/dead markers.

4.8.4. Fixing and SEM observation

Seeded discs were fixed with 2.5 % gluteraldehyde (25 % stock solution diluted to 10:1 in PBS) for 3 h followed by serial dehydration in ethanol; 10 min in 50, 70 and 90 % ethanol solutions diluted with distilled water, followed by 30 min in absolute ethanol. Once this process was completed, the discs were placed in a vacuum sealed desiccator for 24 h to ensure the samples were dried.

5. Results and Discussion

5.1. Glass Production

This section describes how the initial glass was analysed post-processing; DSC, SEM and particle analysis was conducted to verify that the precursor glass produced was acceptable for further use in subsequent studies.

5.1.1. DSC

Sub 45 µm A/W glass particles were analysed through a constant heating rate of 5 K min^{-1}; Figure 5.1 shows an example comparison of DSC traces, from each scan Tg was obtained from inflection of the trace, Tp1 and Tp2 were obtained from their respective peaks. Table 5.1 depicts the range of Tg, Tp1 and Tp2 from glasses produced at various dates; the production of a double batch or combining different batches of glass (bold in Table 5.1) showed no significant changes to the crystallisation peaks as shown in Figure 5.1. It was observed however that resultant Tg of the mixed glass was an approximate average of the two initial glasses, whereas Tp1 and Tp2 showed little change due to the mixing of different batches of glass powder. From this study it was assumed that combining several differing batches of glass was acceptable, allowing for an increase in slurry volume and ultimately sample size for characterisation.

Table 5.1 – Example of DSC analysis conducted at varying dates; samples in bold indicate double batches.

Sample	Tg	Tp1	Tp2
1	752.5	878.7	928.3
2	758.4	891.5	947.6
3	**773.4**	**887.4**	**948.2**
4	**755**	**889.8**	**947**
Average	759.8	886.9	942.8
S.D.	9.37	5.7	9.7
3+4	**763.8**	**889.6**	**947.2**

The use of an alumina crucible has been suggested to potentially introduce aluminium contamination when used at high temperatures. A study conducted by Vickers (246), in parallel to this study, investigated this by conducting EDX analysis on A/W glass particles produced in exactly the same manner presented in this study. It was found that only very low levels (~ 0.3 mol. %) of aluminium were detected in the glasses produced.

Furthermore, glass transition temperatures in this study are comparable to those in the literature; Kokubo (17) reported a Tg of 750 °C for particles of 44 µm average diameter when a heating rate of 5 K min^{-1} was used. If aluminium had indeed been incorporated into the glass structure as an intermediate oxide, it would be expected to push up Tg.

Vickers (246) went on to investigate the effects of immersion of the scaffolds in SBF and saw significant apatite crystal formation within 24 hours comparable to previous studies and furthermore carried out an *in vitro* assay on the viability of A/W glass-ceramic scaffolds cultured with hMSC’s with no adverse effects reported. This supported the conclusions of an earlier *in vitro* study from our group

(247) in which hMSC’s were seeded in porous A/W glass ceramic scaffolds produced via SLS. MSC’s adhered, retained viability and proliferated on the scaffolds. Indeed, the expression of osteogenic markers by MSC’s was equivalent to or significantly greater on A/W scaffolds than on tissue culture plastic. In a subsequent *in vivo* study by Lee *et al* (248), MSC seeded and un-seeded A/W scaffolds were implanted subcutaneously in MF1 nude mice where osteoid formation and tissue in-growth were observed following histological assessment confirming the osteo-productive capacity of A/W scaffolds made at Leeds.

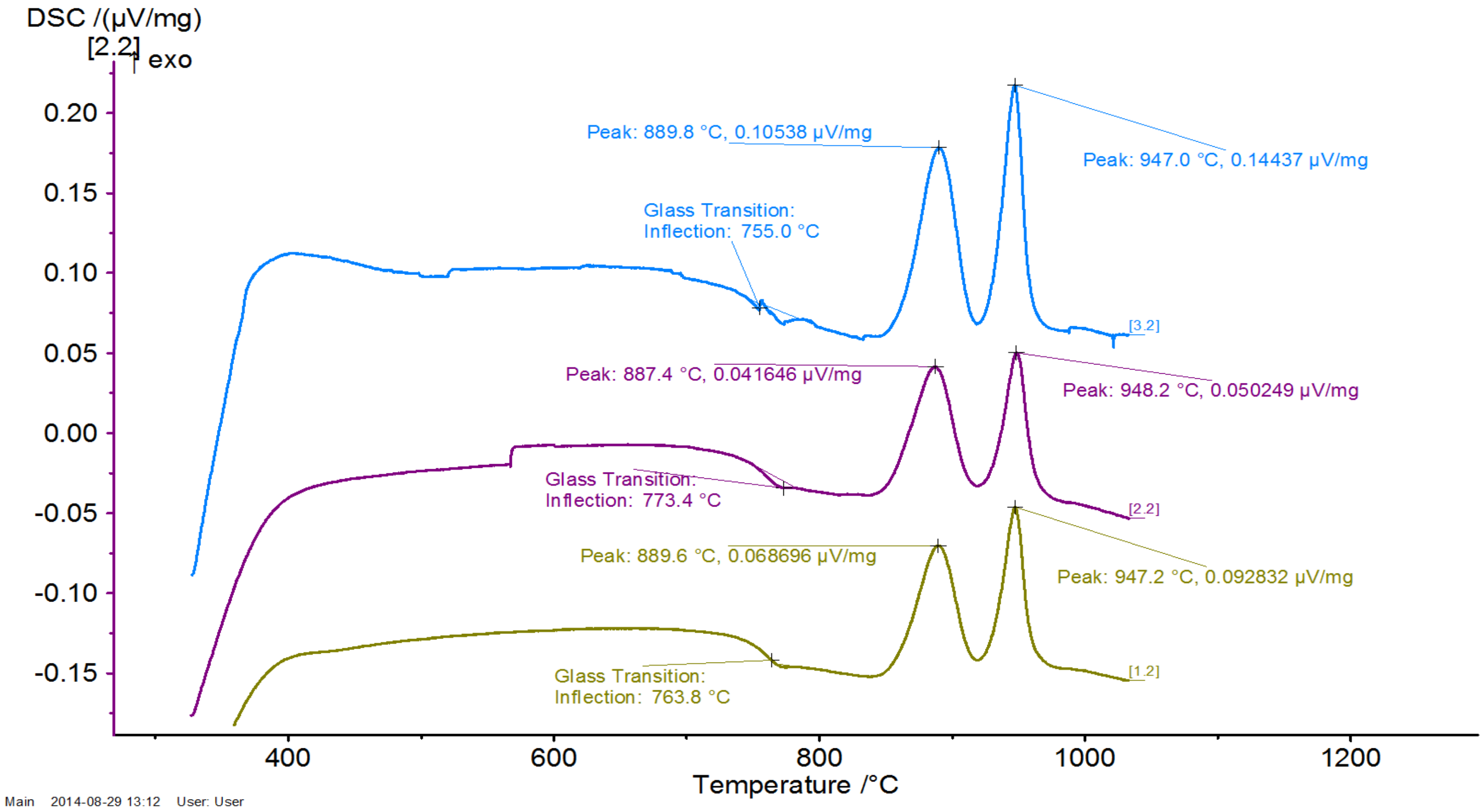

Figure 5.1 - Example of DSC traces from analysing glasses produced in double batches. Blue line – 4; Purple line – 3; Green line – 4+3 combined (equal weights).

5.1.2. Particle Analysis

Glasses were analysed periodically to ensure production was kept sufficiently constant; Figure 5.2 depicts the averaged particle size distribution of each glass sampled as a volume percentage, the codes correspond to the date at which the glass was produced. Overall it was observed that the distributions were skewed towards the desired particle size, i.e. 45 µm, and is comparable to previous studies (249, 250). Glass frit from multiple pours was mixed, ground and analysed; the particle size distribution was also within acceptable limits, this allowed for excess frit from previous grinds to be combined to a workable weight. The same was repeated for glass powders that had previously been ground and sieved, the process described in section 4.1 was repeated and the subsequent glass powder was analysed.

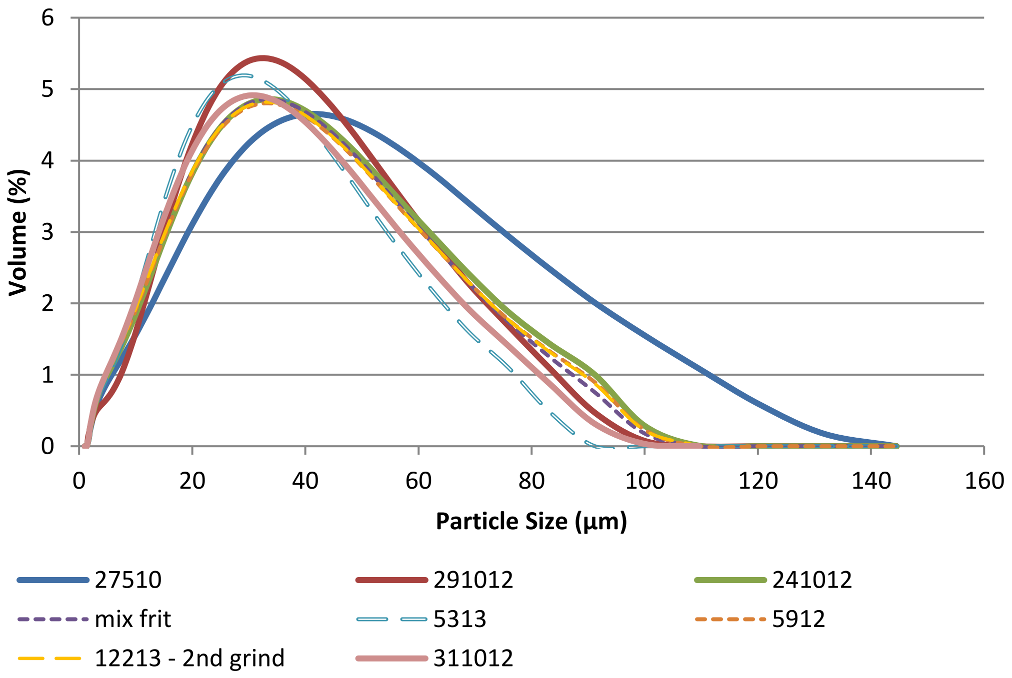

Figure 5.2 – Particle analysis of various samples

The results showed that re-grinding would also produce glass powder within the desired size range. Figure 5.3 and Figure 5.4 depict glass particles post-processing through both routes. Considering the sieving process, it is reasonable to assume that a particle whose width is less than 45 µm but length is greater than this would not be separated out and would pass through the mesh. During the particle analysis, the beam is scattered and its diameter is reported assuming it is spherical; depending on the particles orientation as it passes the beam would result in larger particle sizes to be reported. It was therefore assumed that the sieving process produced sub-45 µm particles to a sufficiently accurate degree.

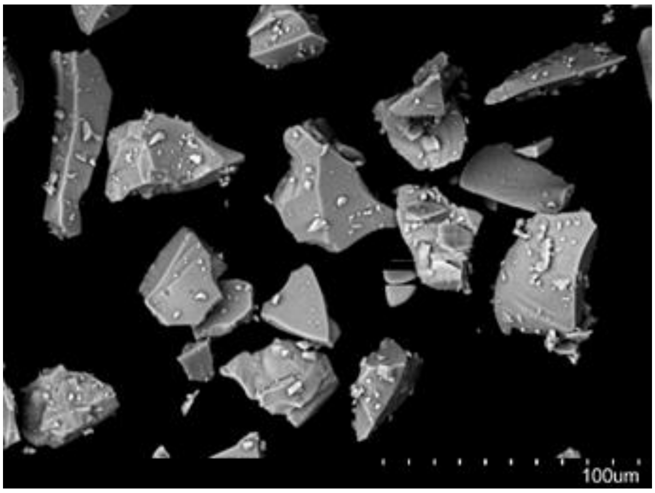

Figure 5.3 – SEM of glass particles produced after milling and sieving

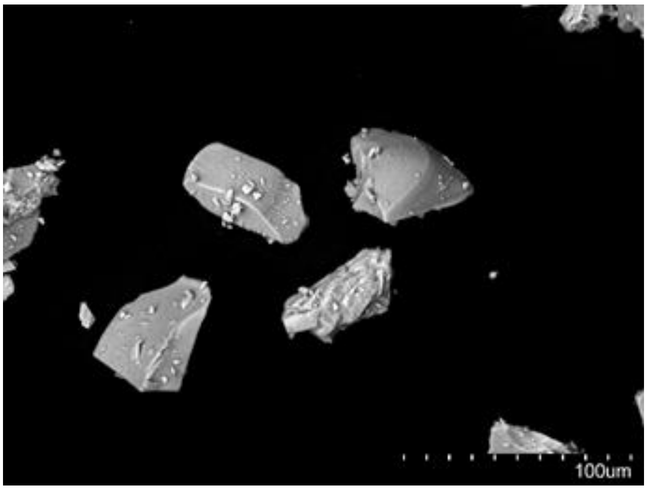

Figure 5.4 – SEM of particles produced after re-grinding, milling and sieving

5.2. Initial scaffold production

The aim of this section was to specify:

- The PPI of the PU foam templates that would be used
- The type of PVA to use (and if it is necessary)
- The range of PVA wt % to investigate
- The range of binder solution: glass ratios to investigate
- The heat treatments that would be investigated
- To confirm that the heat treatments to carry forward for characterisation produced distinctly different crystal phases

5.2.1. Initial selection of a foam template and binder

Initial studies were conducted to select an appropriate foam template and binder (if any) to use for the subsequent investigations conducted throughout this project. From the initial DSC results heat treatment A was employed with a dwell temperature of 800 °C, the dwell times used for the initial studies ranged from 1-5 h. It was immediately observed that a binder was required, Figure 5.5 to Figure 5.7 depict the resulting scaffolds produced in absence of a binder for foams of 90, 60 and 45 PPI.

Considering that each scaffold produced in this initial study was prepared using 1:1 slurries (i.e. one part glass for one part water) the resulting architectures post-heat treatment were surprisingly poor with almost negligible mechanical strengths. This study was repeated with low (average Mw 11 000 – 31 000) and high molecular weight (average Mw 196 000) PVA at 4 wt % (411 slurries). Improved results were only observed for scaffolds produced using the 90PPI foam template and HMw PVA. Reducing the wt % of PVA below 4 % produced similar results to not using

PVA at all; raising the PVA content over 6 wt % was impractical. Mixing the PVA into the distilled water homogenously was barely achievable even before adding the glass, which immediately increased the viscosity of the slurry further. From these initial tests it was evident that varying the wt % of PVA from 4-6 wt % and use of the 90 PPI foam would allow for a more controlled investigation. Prior to optimising the slurry constituents the 90 PPI PU foam was characterised to allow for the volumetric shrinkage of each scaffold to be calculated based upon the initial preparation techniques applied. The foam templates supplied were found to be acceptably uniform; sampling 10 % of each template type (20 mm Ø x 10 mm and 20 mm Ø x 20 mm) showed the dimensions to be 19.778 mm Ø ± 0.408 x 10.151 mm ± 0.051 and 19.885 mm Ø ±0.413 x 20.104 mm ± 0.06.

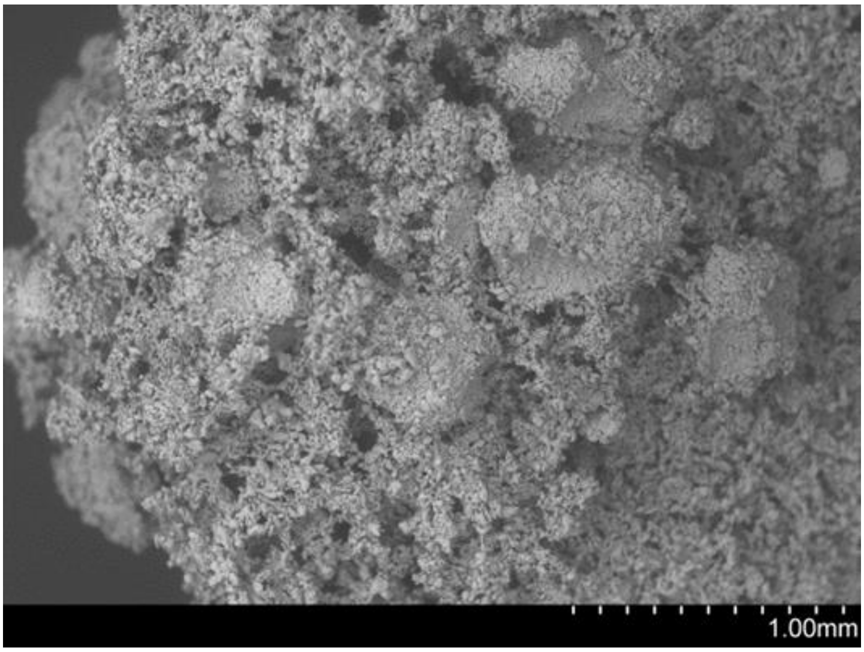

Figure 5.5 - Initial scaffold produced using a 90PPI foam template, 1:1 slurry containing no PVA

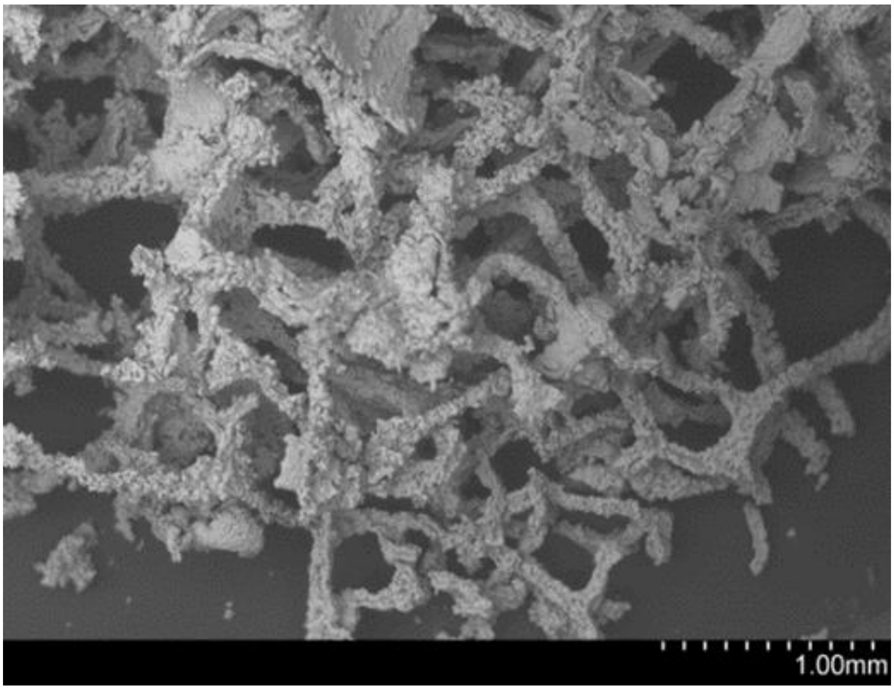

Figure 5.6 - Initial scaffold produced using 45 PPI foam template, 1:1 slurry and no PVA

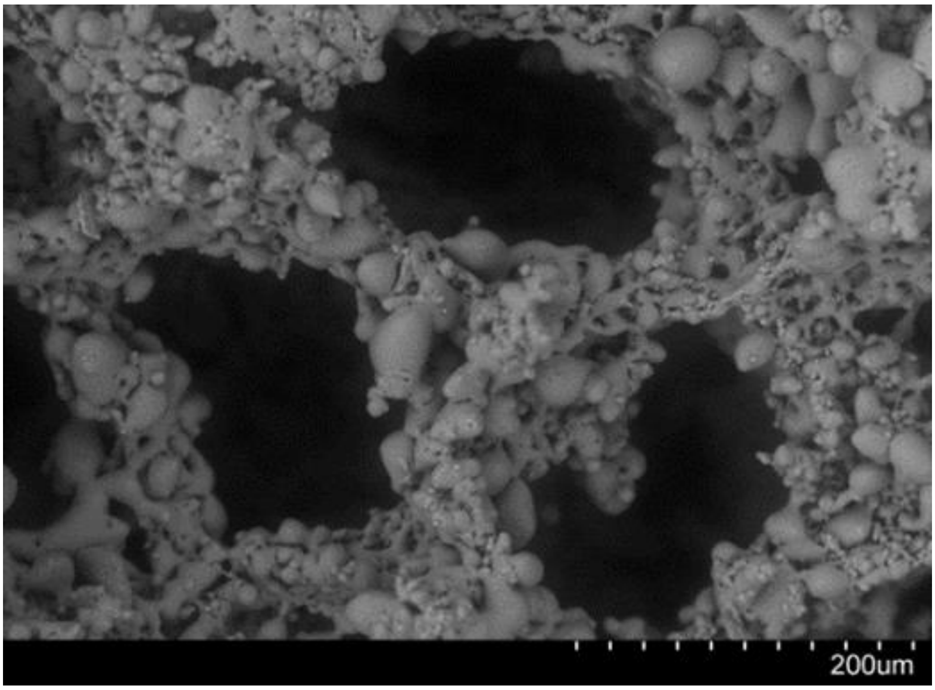

Figure 5.7 - Initial scaffold produced using 60 PPI foam template, 1:1 slurry and no PVA

5.2.2. Designing heat treatment A

To confirm the minimum dwell time and temperatures required to produce a sufficiently sintered scaffold heat treatment A was further investigated. All scaffolds were produced using 411 glass slurries, at this stage only qualitative assessment was used via the SEM to confirm necking of the particles and retention of the desired architecture.

As previously described the dwell times ranged from 1-5 h and dwell temperatures from 750 °C-850 °C (i.e. from ~Tg to ~Tg +100 °C); Figure 5.8 to Figure 5.10 depict the scaffolds formed from a dwell time of 1 h only; it was clearly evident that to merely sinter the scaffold a longer dwell time was required. It was originally predicted that at the very least minimal necking of the particles would be observed based upon Tg predicted via the DSC. The lack of sintering at these temperatures may be due variations in heat transfer; the DSC is conducted using a minute, evenly distributed volume of powder within a platinum crucible, it may be considered an ideal scenario to heat treat the material being tested. Whereas in practice; the scaffold is composed of a much larger powder volume, un-evenly distributed across a foam template. Whether the sintering activation energy had been reached may still be insufficient to initiate the required viscous flow mechanisms.

This may explain why a dwell time of 5 h was required at 800 °C; Figure 5.11 to Figure 5.16 depict scaffolds sintered for 5 h from 760 to 800 °C. As the dwell temperature and time was increased the desired necking and densification was achieved. Increasing the dwell temperature up to 850 °C with longer dwell times showed similar results. However, the aim of developing heat treatment A was to merely sinter the scaffold with minimal crystallisation at this stage, it was therefore concluded that a dwell temperature of 800 °C and dwell time of 5 h was to be used as the basis for all subsequent tests. This result is directly comparable to a study conducted by Jun *et al* (251) who reported sintering at temperatures lower than Tg resulted in poor densification of the glass-ceramic particles.

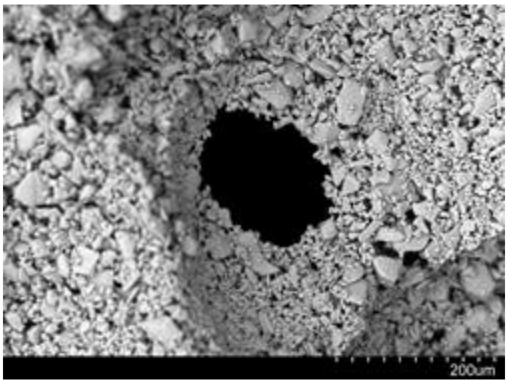

Figure 5.8 – 1 h dwell at 750 °C, 411 slurry

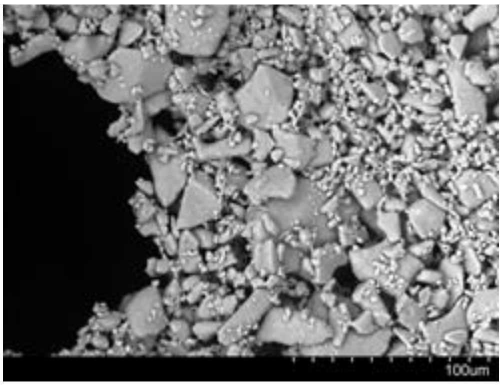

Figure 5.9 – 1 h dwell at 750 °C, glass particles still exhibit angular morphology

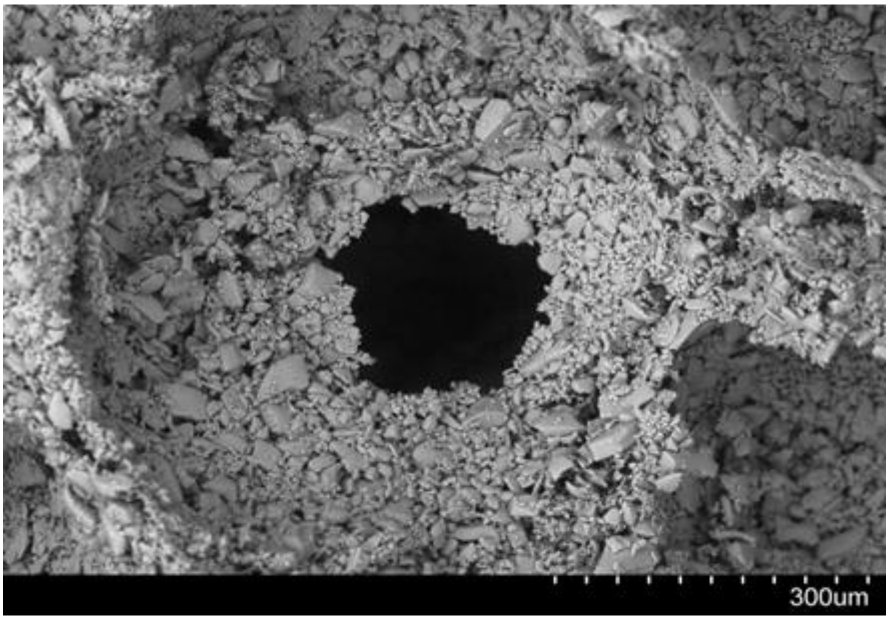

Figure 5.10 – 1 h dwell at 850 °C, 411 slurry. No evidence of sintering.

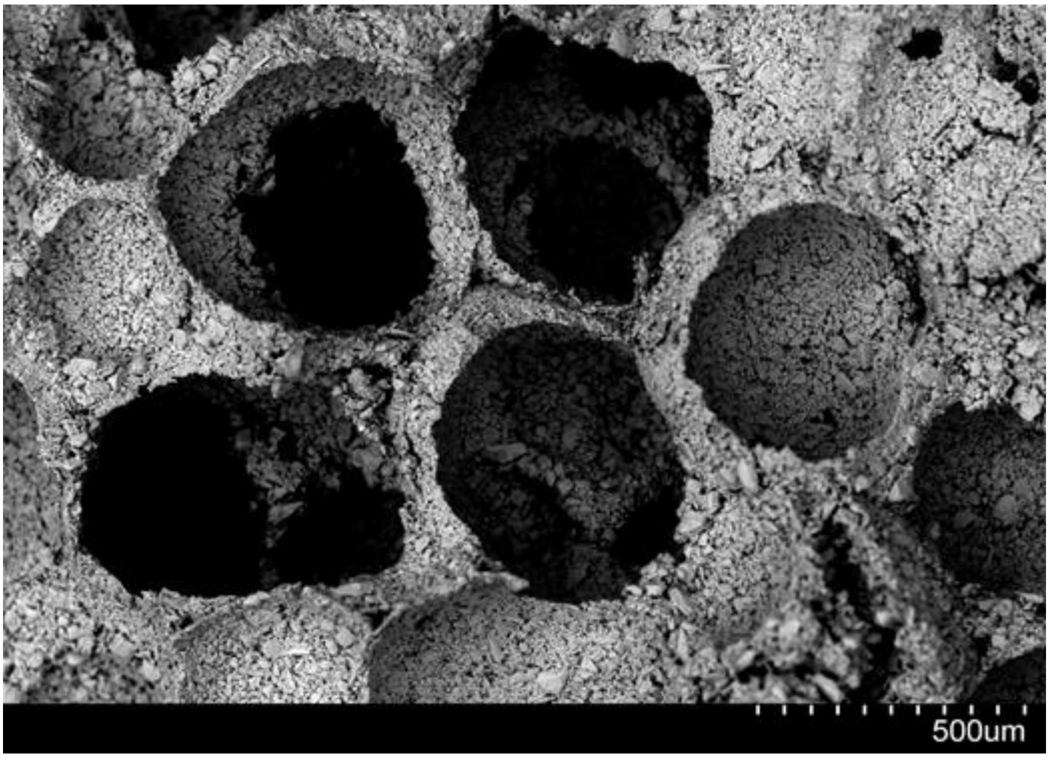

Figure 5.11 – 5 h dwell at 760 °C, 411 slurry

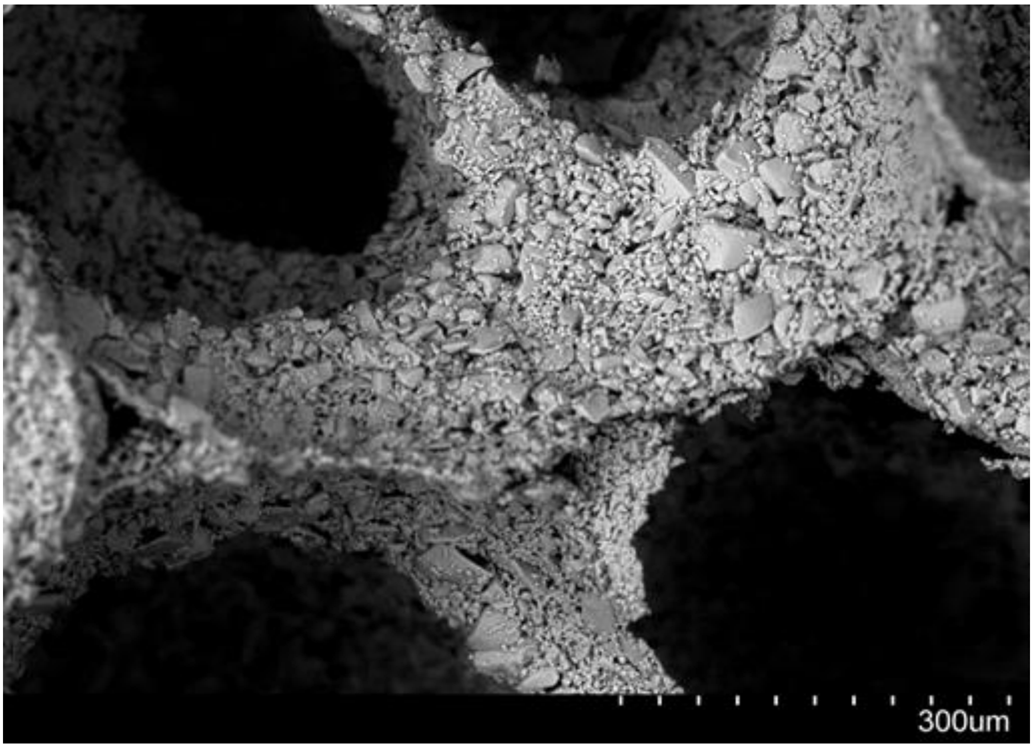

Figure 5.12 - Increased magnification image of scaffold depicted in Figure 5.11, angular particle morphology still apparent.

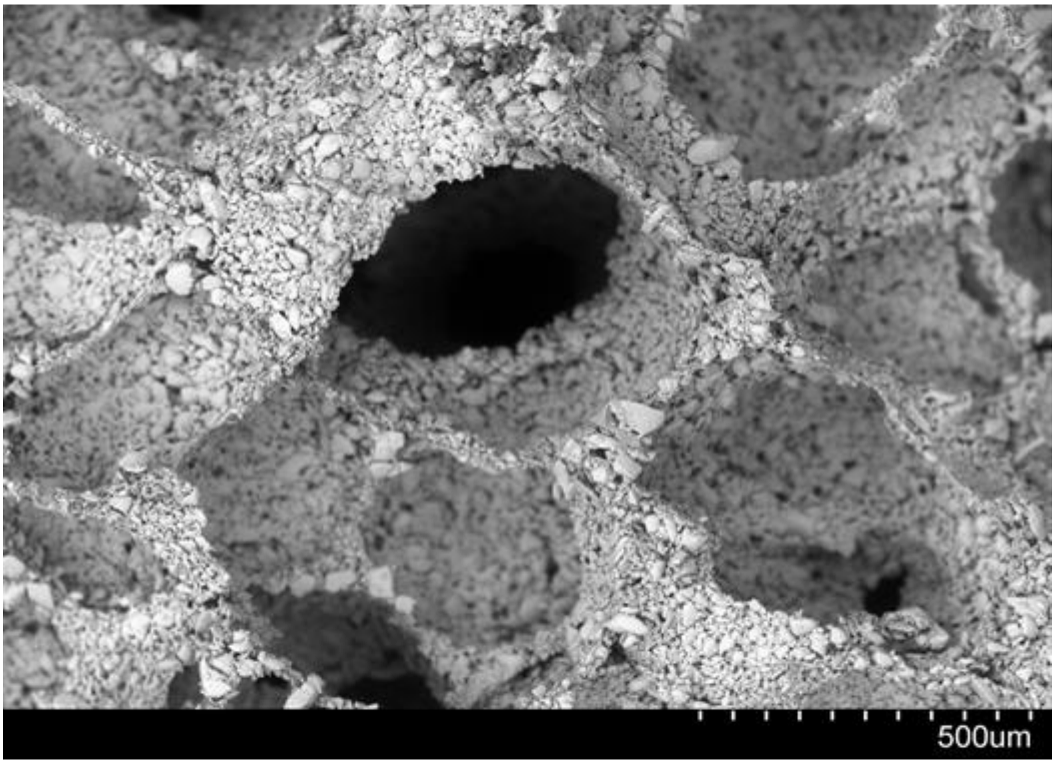

Figure 5.13 – 5 h dwell at 785 °C, 411 slurry

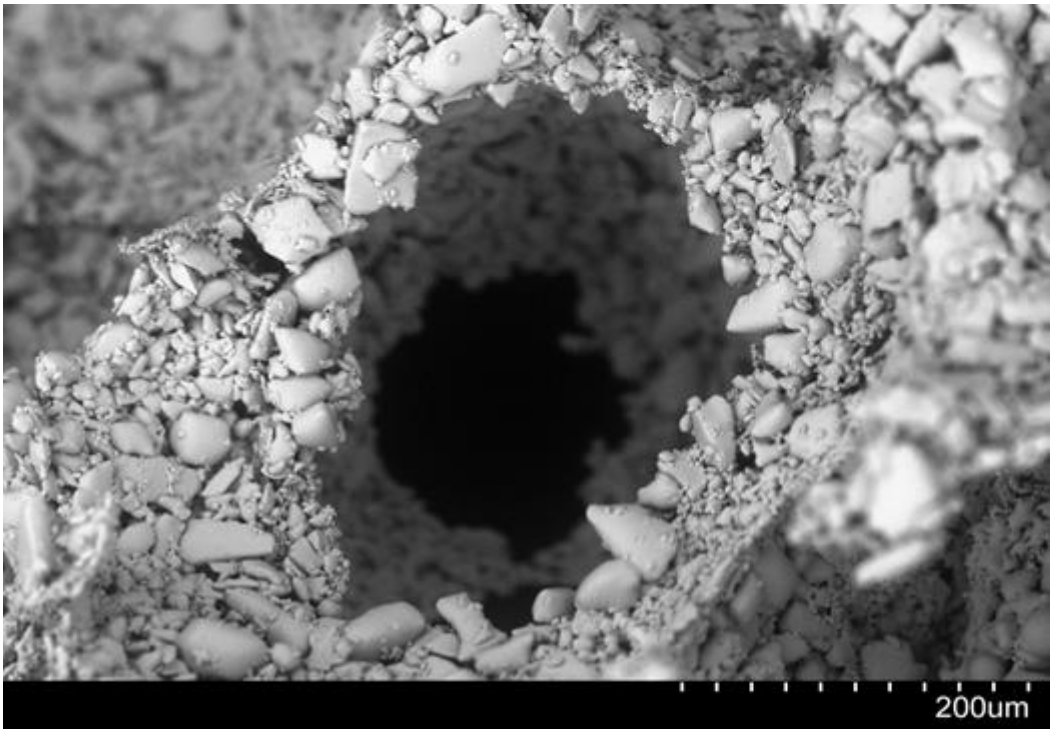

Figure 5.14 - Magnified image of scaffold depicted in Figure 5.13 Error! Reference source not found.**. Some evidence of particle rounding can be seen however, necking is still not evident.**

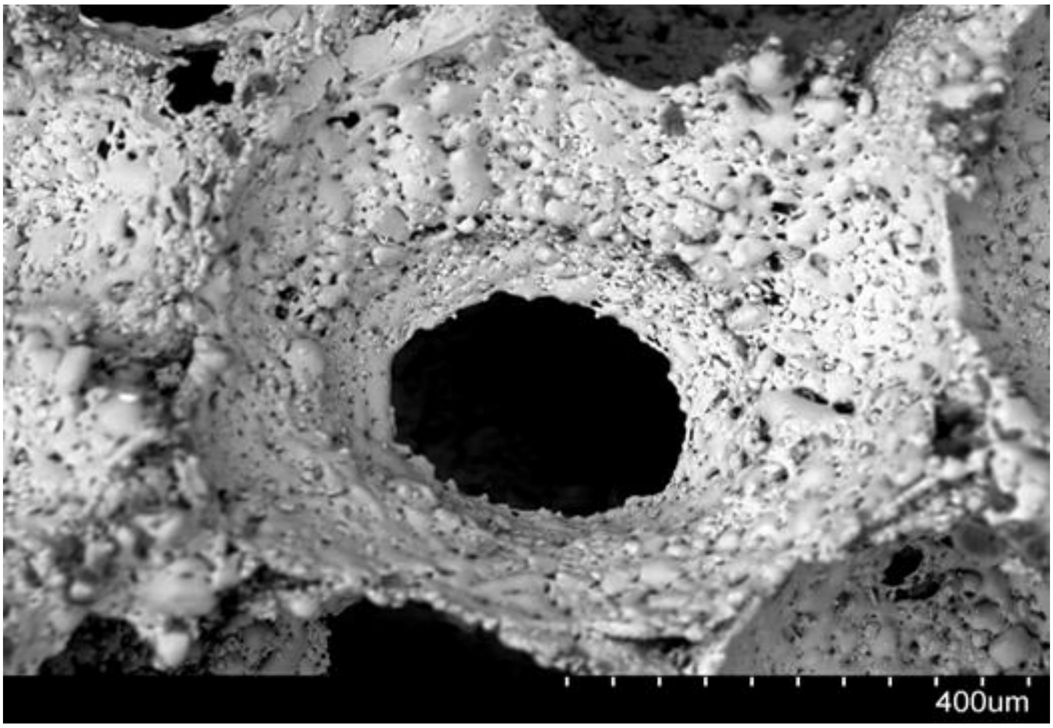

Figure 5.15 – 5 h dwell at 795 °C, 411 slurry. Particle necking is visible, however densification is insufficient

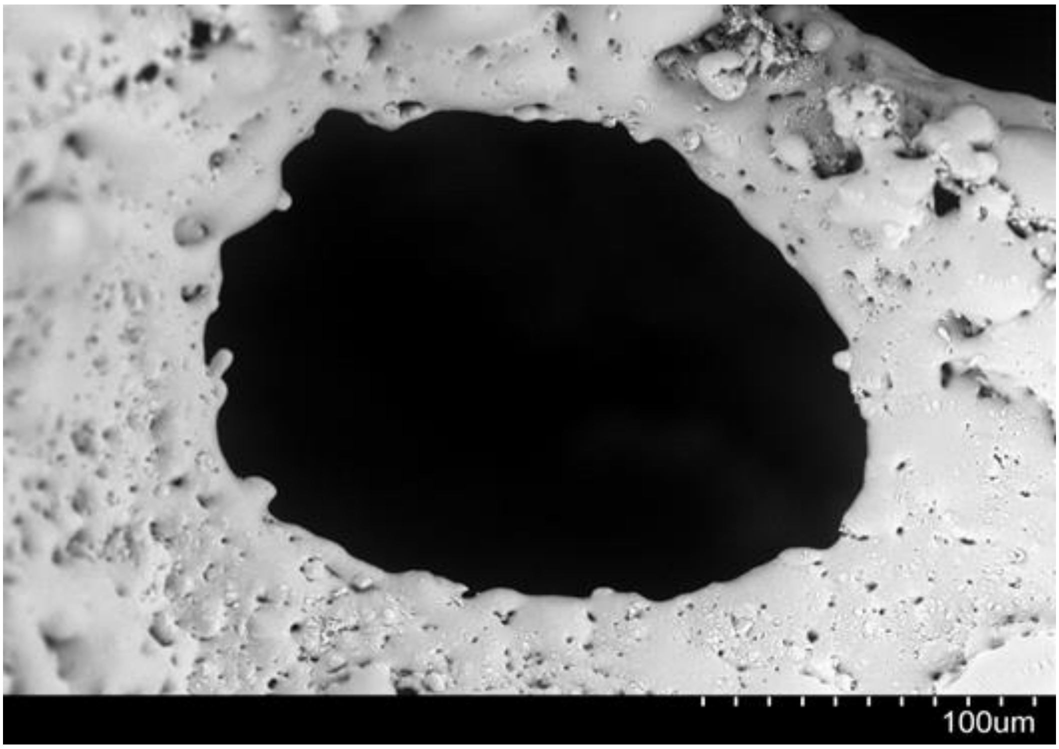

Figure 5.16 – 5 h dwell at 800 °C, 411 slurry. Increased level of densification and necking.

5.2.3. Reducing the glass required

It was evident from an early stage that producing slurries of 1:1 binder solution: glass was impractical; the sheer volume of glass required immediately limited the sample size that could be produced. Coupled with this, from the SEM analysis it was clear that slurries of 1:1 ratio formed a scaffold with minimal unblocked pores as shown in Figure 5.17.

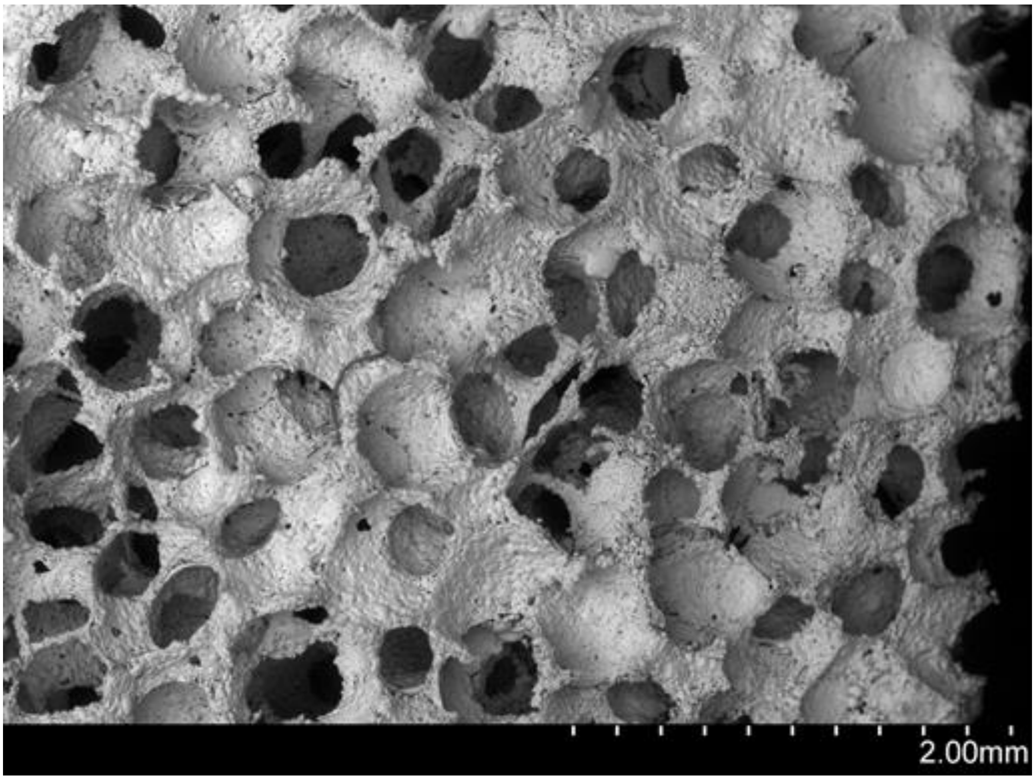

Figure 5.17 - Scaffold depicting majority of blocked pores; heat treatment A, 411 slurry.

Initial tests were performed using the method described in section 4.2.3; however, regardless of the compression cycle performed the resulting scaffolds exhibited poor sintering, if at all, similar to that of scaffolds produced through insufficient dwell temperatures and times. Interestingly though the architecture of such scaffolds was retained in some areas to a surprising degree as shown in Figure 5.18 this was not reproducible however and as such the compression method was discarded. It is worth noting however that such a method is employed by Vitale-Brovarone *et al* (235)**,** perhaps through characterisation of the slurry viscosity prior to each coating and further optimisation of the PVA used such a method could be employed with this material. Regardless, reducing the glass content of the slurry is also desirable with respect to possible future scale up, the subsequent tests therefore concentrated on varying the slurry constituents without the compression method. Initial small scale tests were conducted with 443 slurries (produced using heat treatment A); immediately it was observed that the architecture was improved as was the degree of necking visible through SEM analysis. It was concluded from these initial tests that reducing the glass content would allow for a controlled investigation into optimising the scaffold production.

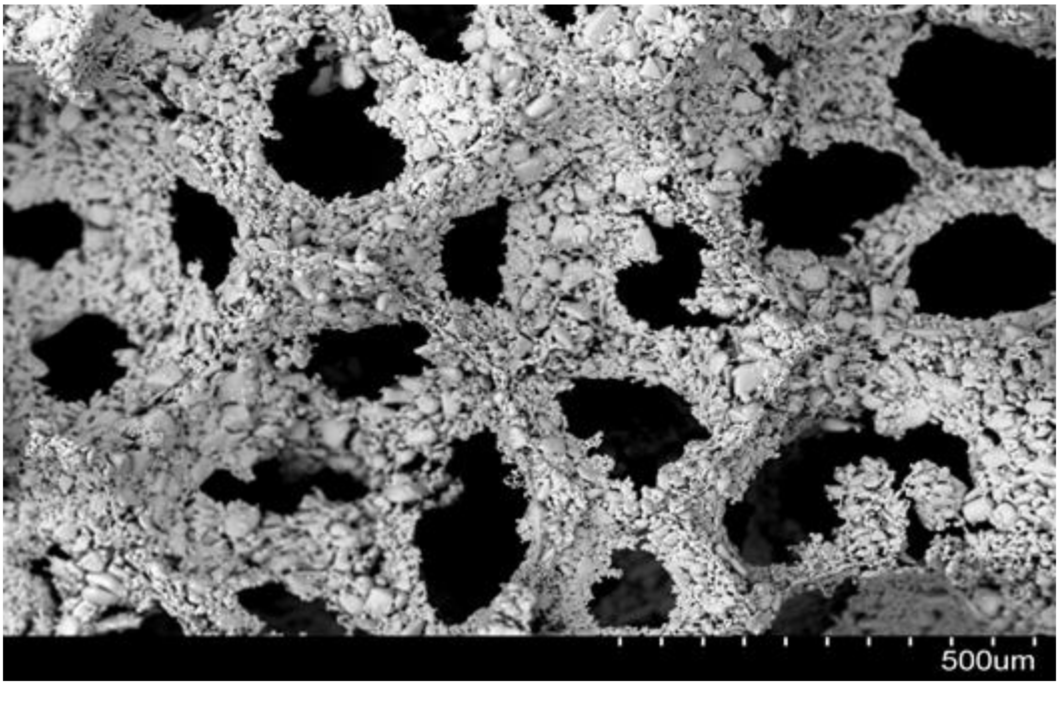

Figure 5.18 - Example of a scaffold produced through 33 % compression of original foam template height post coating. Removal of slurry resulted in an extremely fragile scaffold post heat treatment.

5.2.4. Designing heat treatments B and C

Determining an appropriate third step in the heat treatment was necessary to allow comparisons to be drawn between an **amorphous** scaffold and a **crystallised** scaffold. The results from the DSC showed the wollastonite crystallisation peak at ~943 °C; dwell temperatures were tested from 950 °C – 1100 °C (previously termed $\beta_{1,}$ β_2 and β_3 in section 4.3), as with the design of heat treatment A qualitative assessment of architecture retention was then performed. Figure 5.19 and Figure 5.20 illustrate that a dwell temperature above 950 °C produced an overall weakened structure, which is again comparable to the study conducted by Jun *et al* (251). It was postulated that at higher temperatures the viscosity could decrease to a level such that the glass particles flow away from one another, resulting in poorly defined trabecular struts and large areas that had collapsed.

From these initial tests, a dwell temperature of 950 °C and dwell time of 1 h was carried forward for characterisation and comparison. This was denoted heat treatment B, Figure 5.21 to Figure 5.22 show scaffolds produced using a 443 slurry and heat treatment B (443B scaffolds). To quantify the potentially detrimental effect upon the resultant scaffolds properties a third heat treatment was defined, a tertiary dwell temperature of 1025 °C for 1h was used, this was denoted heat treatment C.

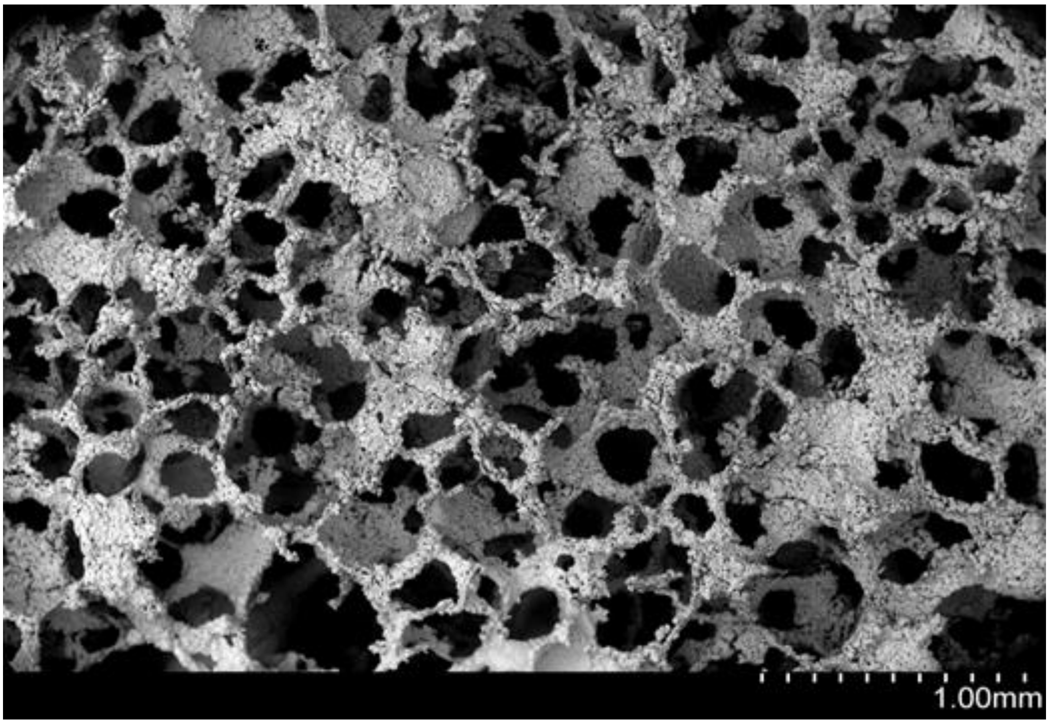

Figure 5.19 - Example of a scaffold produced through heat treatment C with a tertiary dwell temperature of 1025 °C

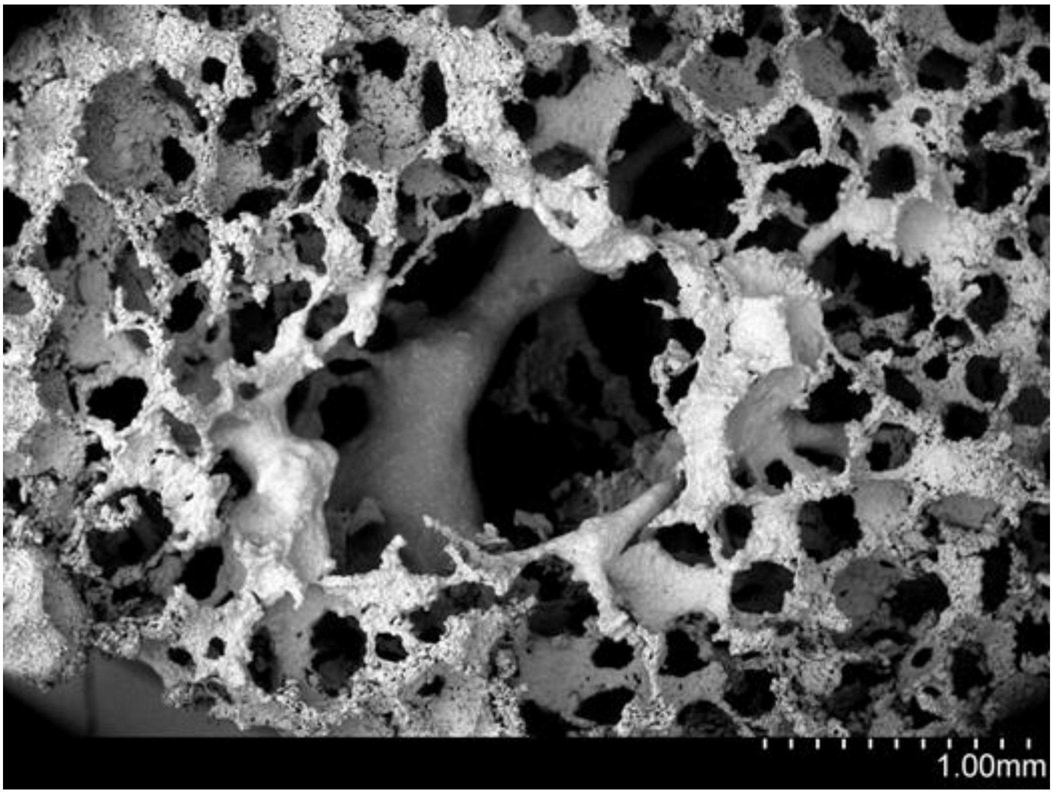

Figure 5.20 - Large areas of strut collapse evident.

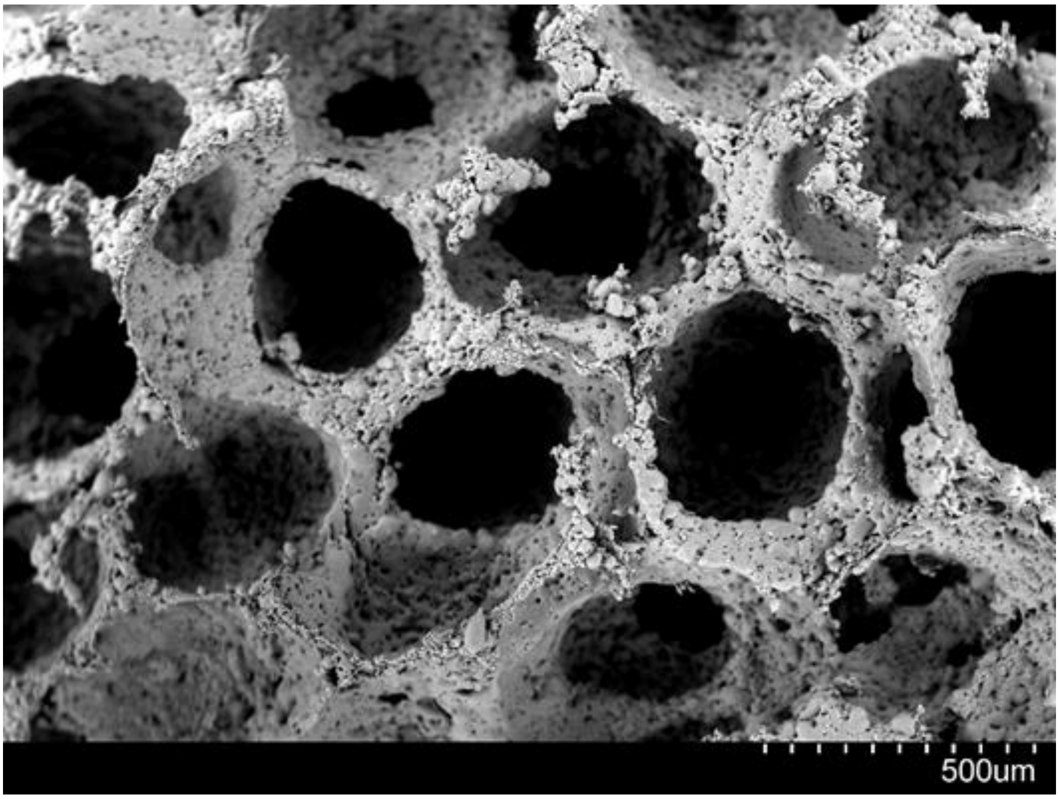

Figure 5.21 – SEM of a 443 scaffold produced using heat treatment B

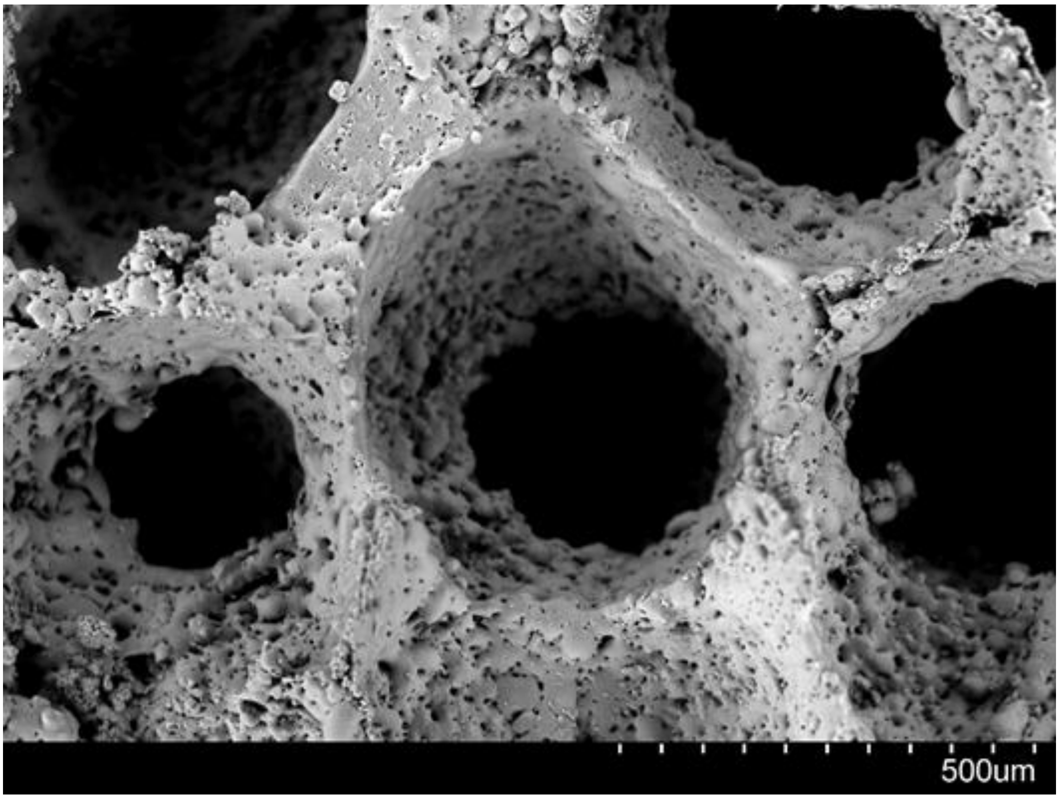

Figure 5.22 - SEM of a 443 scaffold produced using heat treatment B

5.2.5. XRD

Scaffolds were prepared through heat treatments A and B, sectioned into discs (as described in section 4.7.1.) and analysed through XRD. Figure 5.23 Figure 5.24 depict the differences in crystal phases present due to the applications of heat treatment A and B respectively. As expected heat treatment A does not fully crystallise the scaffold resulting in the “amorphous halo”, compared to that of heat treatment B which exhibits both apatite and wollastonite phases and a “flattening” of the XRD trace. These initial XRD scans confirmed that heat treatments A and B would produce scaffolds of contrastable characteristics, allowing subsequent studies to be undertaken.

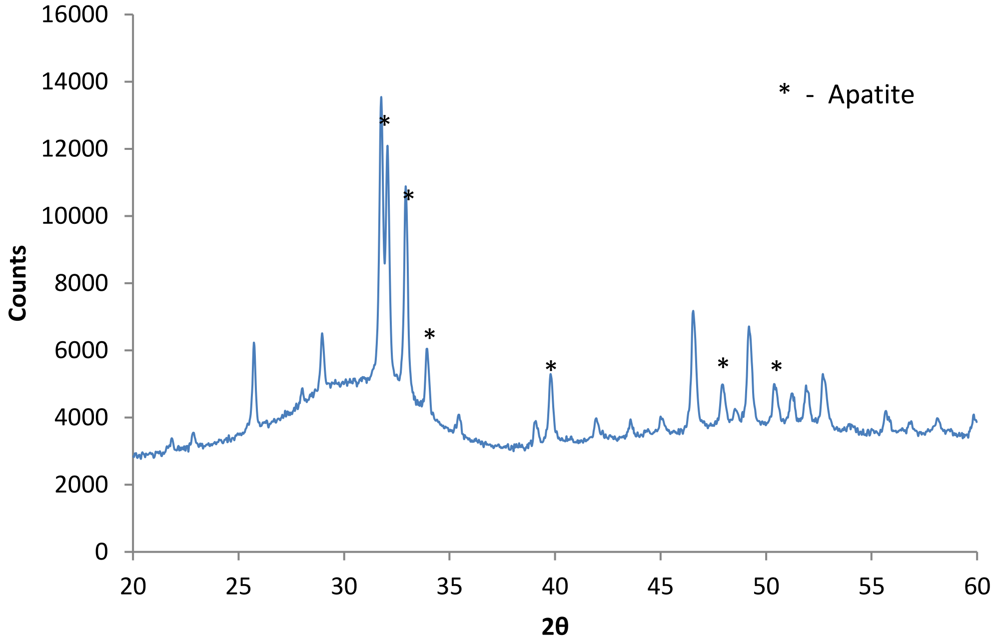

Figure 5.23 – XRD trace of a scaffold after heat treatment A was applied (443 slurry).

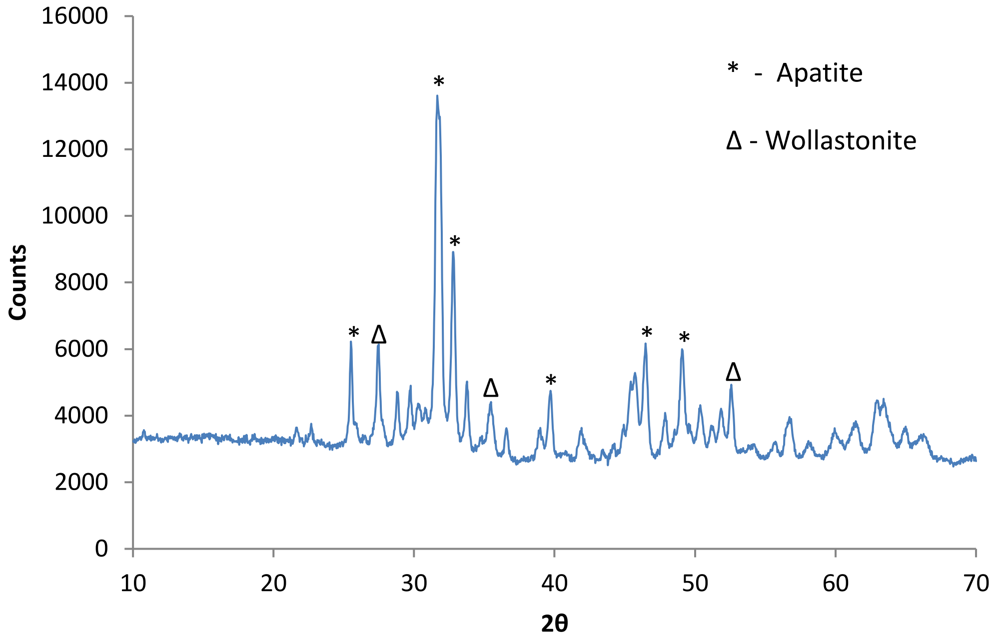

Figure 5.24 – XRD trace of a scaffold after heat treatment B was applied (443 slurry).

5.2.6. Summary

Producing a porous A/W scaffold using the foam replica technique requires careful consideration of the foam template, slurry constituents and heat treatment. The initial studies aimed to design a practical approach to quantitatively characterise the key variables in scaffold production, narrowing down the broad possible inputs to a select few. Several variables were immediately discounted following initial testing (e.g. varying the PPI of the foam template, use of differing molecular weights of PVA, varying the heating rates, etc.). It is to be noted however that these variables were not considered insignificant. Future studies would investigate the significance of these variables with respect to the broad characterisation conducted in this project, allowing for further refinement of the scaffolds produced. From these initial studies heat treatments A, B and C were defined and carried forward for quantitative assessment.

5.3. Characterisation

5.3.1. Production consistency

The aim of this section was to:

- Confirm that the area used within the furnace applied the heat treatments uniformly
- Characterise and compare the resultant scaffold geometries

5.3.1.1. Furnace Map

Flat plates were prepared as described in section 4.2.4 using the slurry constituents listed in Table 5.2; heat treatment B was applied and the shrinkage in size was measured. It was noted that with decreasing glass wt % the shrinkage in size diminished slightly, however the standard deviation was low for both groups. From this, it was concluded that the furnace area used would provide a uniform application of the heat treatment for each subsequent batch of scaffold produced.

Table 5.2: Shrinkage in size of flat plates

Slurry	Shrinkage of cross sectional area (%)	S.D.
443	8.24	0.4
4107	7.28	0.55

5.3.1.2. Scaffold shrinkage

As described in section 4.7.1 the diameter of each sectioned disc was measured; this also allowed for the reduction in size post-heat treatment to be analysed down the length of the scaffold. Table 5.3 depicts the change in diameter from the original green part for each scaffold level (levels i-iv); overall the scaffolds showed a maximum change of ~ 24 %, this is at level i with the application of heat treatment B. The reduction in size diminishes towards the base of the scaffold resulting in a (consistently) truncated shape.

Table 5.3: Scaffold shrinkage

PVA (wt %)	Binder Solution: Glass	Heat Treatment	Disc Level							
			i		ii		iii		iv	
			Average (%)	S.D.	Average (%)	S.D.	Average (%)	S.D.	Average (%)	S.D.
5	2:1	B	23.9	0.8	23.0	0.5	21.4	0.9	18.9	1.1
4	10:7	A	19.6	0.5	19.0	0.6	17.3	0.6	15.4	0.4
4	10:7	B	20.7	1.4	20.0	1.1	17.9	0.7	15.1	1.0
4	4:3	A	22.3	0.5	21.4	0.5	20.2	0.7	17.8	0.8
4	4:3	B	24.5	0.7	23.2	0.7	21.3	0.5	18.9	0.4
5	4:3	B	23.9	0.8	21.9	0.8	20.1	1.0	17.2	0.8

5.3.2. Architecture

- Characterise and compare the architecture of the scaffolds
  - Porosity
  - Pore size distributions
- Compare resultant architectural properties to natural trabecular bone at clinically relevant sites

5.3.2.1. Porosity

Considering primarily the porosity of scaffolds produced through varying glass ratio the general trend observed was an inverse relationship, i.e. increasing the glass ratio resulted in a decrease in scaffold porosity. The porosities ranged from 43.1 ± 0.7 to 56.3 ± 0.6 % respectively. Table 5.4 details the porosities of all scaffold types that were assessed through micro-CT. The range of porosities achieved in this study are comparable to that of previous studies (250, 252-254); however the vast majority of porous glass-ceramic scaffolds reported throughout the literature are much higher than 40 %, ranging commonly between 70-95 % (255-257).

Table 5.4: Comparison of resultant scaffold porosities

PVA wt %	Binder Solution:Glass	Heat Treatment	Porosity (%)	S.D.
5	2:1	A	56.3	0.6
		B	56.0	0.4
4	4:3	A	44.0	0.1
4		B	41.4	0.6
5			43.1	0.7
6			40.4	0.7

The effect of varying the wt % of PVA exhibited a more complex relationship; from 4 to 5 wt % a decrease in porosity was observed, however from 5 to 6% the porosity increased to levels similar to that of using 4 wt % PVA. This may suggest that the upper limit of the PVA wt % has been reached; rather than beneficially contributing binding of glass to the foam template, an excess of PVA may cause the glass to agglomerate within the pores rather than aiding the binding of particles to the foam template. Figure 5.25 to Figure 5.27 show 3D reconstructions of 543B scaffolds. Analysing solely the porosity is insufficient to reach such a conclusion; however, this trend was observed repeatedly when characterising other scaffold properties and is discussed in later sections.

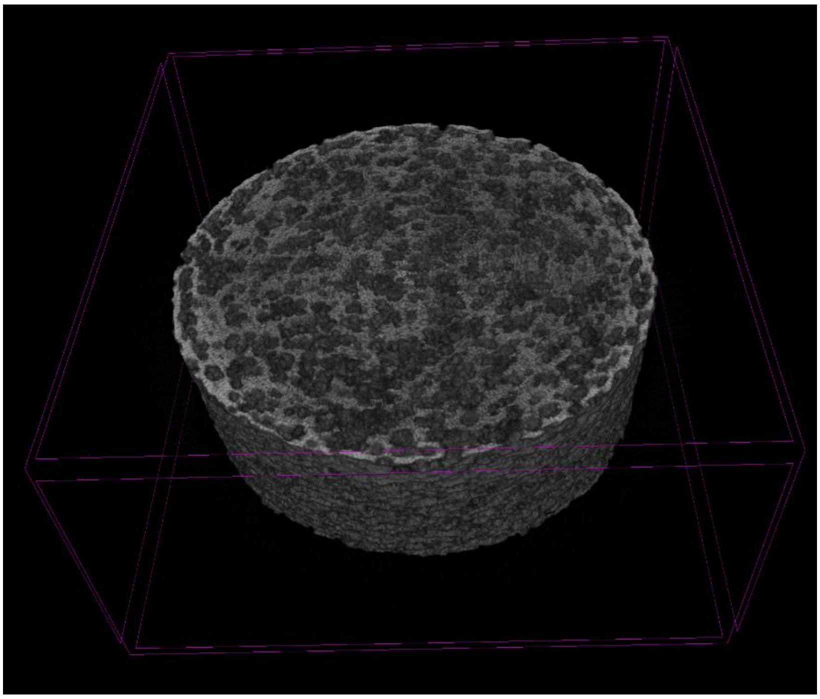

Figure 5.25 – 3D reconstruction of micro-CT scan, 543B scaffold

Considering the heat treatment applied and the resultant porosity a similar trend was observed, in general scaffolds produced through heat treatment B exhibited a lower porosity than those produced through heat treatment A. This trend was less apparent than that of varying the slurry constituents as can be seen when considering scaffolds produced using 521 slurries. These results suggest therefore that crystallising the scaffold has a minimal effect upon the overall porosity, this does not hold true however when considering the pore size distribution.

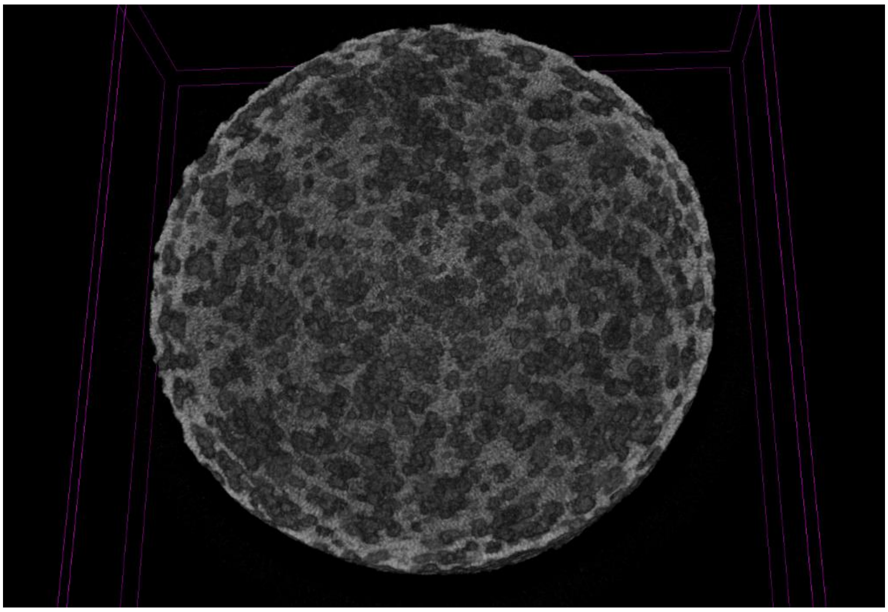

Figure 5.26 – Cross-section of micro-CT scan of 543B scaffold (plan view)

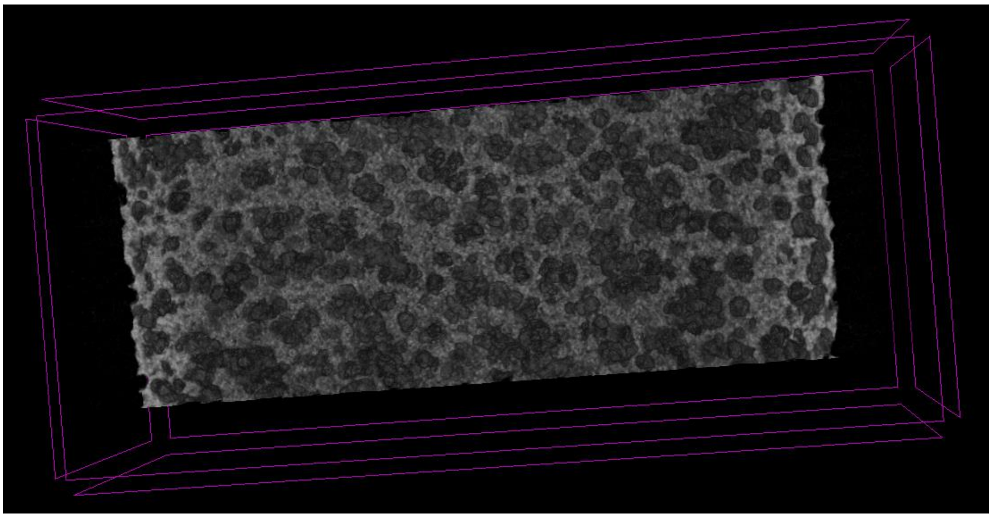

Figure 5.27 - Cross-section of micro-CT scan of 543B scaffold (profile view)

5.3.2.2. Pore Size Distribution

When analysing the pore size distributions, three size groups are considered: pores ≤ 40 µm, pores > 40 µm and ≤ 450 µm, pores > 450 µm. Pores > 40 µm and ≤ 450 µm are not only within the recommended range reported in literature (203, 258, 259) but are within the original bounds of the foam template. Pores larger than 450 µm suggest insufficient coating of the foam template and/or collapse of struts. Table 5.5 and Figure 5.28 depict the pore size distributions of scaffolds produced through varying the slurry constituents and heat treatment. Overall, the pore size distributions are comparable to numerous strategies reported within the literature (260-262)

Considering scaffolds produced using 521 slurries the pore size distribution is significantly dependent upon the heat treatment applied. Applying heat treatment A resulted in scaffolds with ~25 % of the pores larger than 450 µm, compared to applying heat treatment B which resulted in ~0.1 % of pores within this range. This trend diminishes with an increased glass ratio; considering 543 scaffolds, ~8 % of the pores were larger than 450 µm with the application of heat treatment A. When heat treatment C was used (i.e. a dwell temperature approaching the crystal melting point) the resultant pore size distribution is comparable to that of scaffold produced through heat treatment A.

Table 5.5: Comparison of pore size distributions (%) within desired ranges

PVA wt %	Binder Solution: Glass	Heat Treatment	$\Phi \leq 40$	$40 < \Phi \leq 450$	$450 < \Phi$
5	2:1	A	1.07	74.12	24.93
		B	1.95	98.04	0.08
4	4:3	B	2.60	97.41	N/A
5		A	1.46	90.35	8.14
		B	2.67	97.35	N/A
		C	1.38	92.59	6.07
6		B	1.33	87.88	10.78

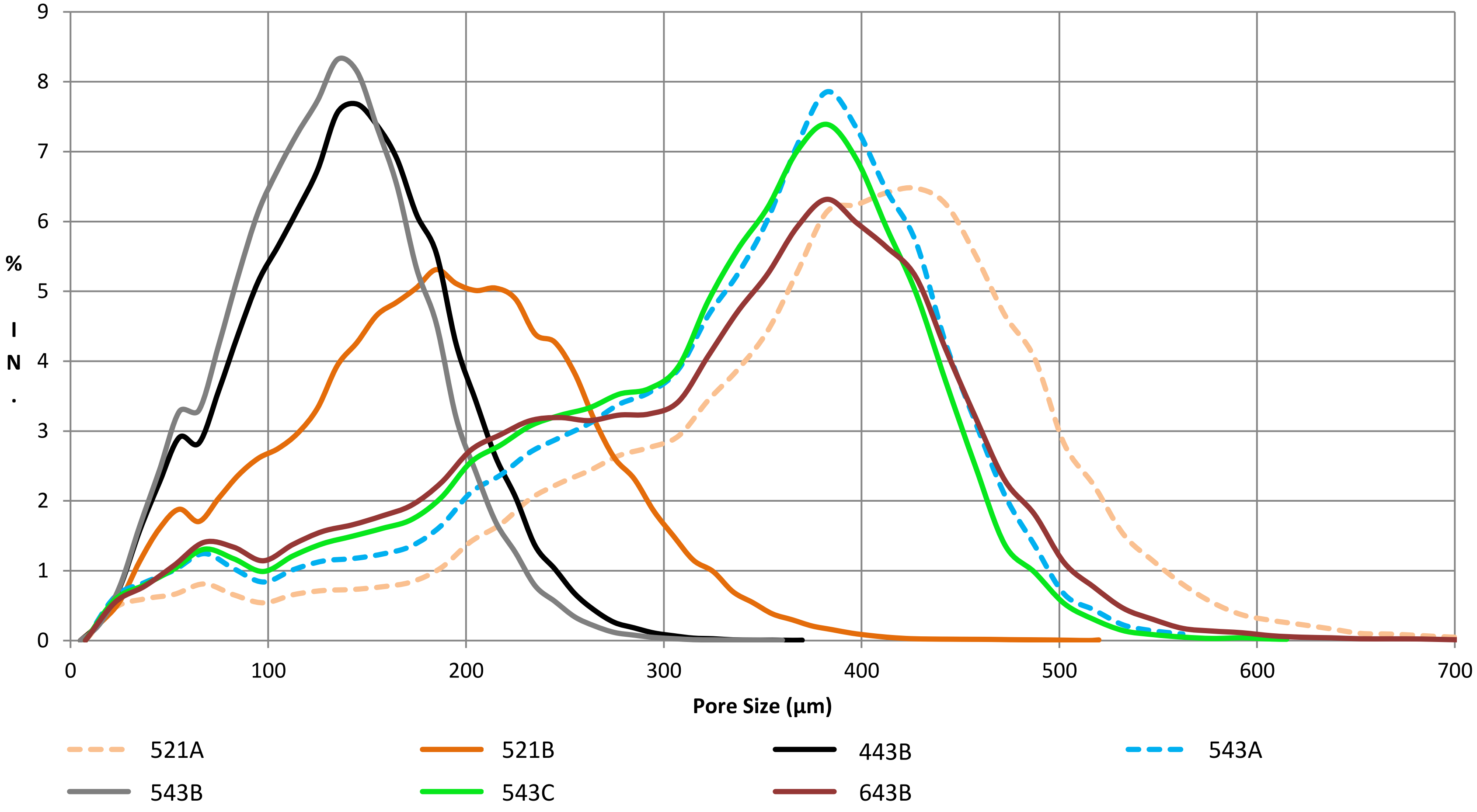

Figure 5.28 – Pore size distributions of scaffolds measured via µCT (10 µm resolution)

As mentioned previously the PVA wt % affects the overall porosity; initially decreasing the porosity with increasing PVA content until an excessive amount is used and the trend reverses, this trend is also seen when analysing the pore size distribution. With the use of 643 slurries and heat treatment B the pore size distribution is similar to that of scaffolds produced through heat treatment A and C, with ~10 % of the pores larger than 450 µm. Comparing this to the use of 4 and 5 wt % PVA the differences in pore size distributions are insignificant. This provides further evidence that excess use of a binder within the slurry negatively affects the resultant properties.

5.3.2.3. Comparison to physiological values

As the micro-CT scans were calibrated for bone (i.e. mgHA/ccm) the architectural characteristics of the scaffolds produced can be compared to that of natural tissue. Table 5.6 compares the common properties of natural trabecular bone to that of the scaffolds produced; values displayed in bold are of A/W scaffolds produced, specifically 521B and 443B scaffolds. The data presented in Table 5.6 is from a study conducted by Hildebrand *et al* (1999); this study was a detailed micro CT analysis of trabecular bone, 260 trabecular bone biopsies were scanned and analysed in the same manner as the scaffolds presented in this thesis. The key architectural properties obtained from these scans are as follows: Bone volume (BV/TV), surface density (BS/BV), trabecular thickness (Tb.Th), trabecular separation (Tb.Sp) and trabecular number (Tb.N). Bone samples were obtained from the following anatomical zones: iliac crest (ICF), femoral head (FRA), second and fourth lumbar spine (LS2B and LS4A) and calcaneal core (CAB). The properties of these trabecular bone samples are highly applicable to the potential use of a synthetic bone graft, these areas are commonly treated with metallic fixation devices and as such are potential areas in which a porous A/W graft would be used. Furthermore, the iliac crest is commonly excised and used as an autograft material in orthopaedic surgery.

It is immediately evident that BV/TV of natural tissues are much lower than that of the scaffolds, even when considering the scaffolds produced using the lowest content of glass (2:1 ratio of Binder solution:Glass). For clarification, the calculation of porosity (as a percentage) is as follows:

Porosity = (1 – BV/TV) x 100

As stated in Table 5.4 porosities of 521B and 443B scaffolds were 56 % and 41.1 %; compared with natural trabecular bone whose porosities range from 73.9 % (FRA) to as high as 91.7 % (LS2B), it is evident that natural trabecular bone is of a much higher porosity. However throughout the literature (through the use of the foam replica technique) lower porosities ranging from 50-80 % have been reported as desirable (7).

Comparison of Tb.Th* shows that the struts that are present are similar to that of native bone; this suggests that where the foam template was successfully coated the resultant struts formed are physiologically relevant.

The current issue in terms of architecture are the blocked regions of the scaffold; comparing Tb.Sp* and Tb.N* shows that the scaffolds are not only too dense but are occupied by too many struts. Interestingly the BS/BV ratios are similar to the lower levels reported for the human femoral head, iliac crest and the 2nd and 4th lumbar vertebra. This might suggest that the microenvironment that the cells would initially be exposed to *in vivo* would be similar to that of the native tissue;

specifically if the bone surface is similar it could ensure that cellular densities and therefore remodelling rates are comparable to that of natural processes (263).

The difference in anisotropy of the scaffolds could be considered insignificant, additionally the scaffolds could almost be considered isotropic as their DA values are ~1. As the glass content within the slurry is decreased the structure of the scaffold trends towards rod-like as can be seen with the increasing SMI value. This would suggest that for future optimisation for the scaffold specific application could be targeted by careful slurry selection. For example, decreasing the glass content further could result in a scaffold mimicking that of the lumbar vertebra. However, as will be outlined in section 5.3.3. Mechanical properties, solely decreasing the glass content to further increase the porosity could prove detrimental to the mechanical stability of the scaffold.

5.3.2.4. Accuracy of measurements

All scans were conducted using the same sized volume of interest (VOI); this ensured that the porosities and pore sizes reported were calculated from equal amounts of scaffold material. The voxel size chosen was 10 µm; this was decided upon due to scanning and reconstruction times required, smaller voxel sizes would have significantly increased the processing time of scans. Decreasing the voxel size (to 5 or 1 µm, for example) would increase the resolution and give more details to pores of smaller geometries. Pores of a smaller size will still be present due to insufficient densification of A/W particles post-sintering, however this was not then focus of the micro-CT analysis. The focus was to assess the pore size distributions that were present within the recommended ranges for clinical use (100-500 µm), scans at 10 µm were sufficient to achieve this. Porosities reported would also differ if smaller voxel sizes were used. Micro porosities due to insufficient sintering of A/W particles would not be represented in current scans, which could affect the results reported. The effect of decreasing voxel size on resultant architectural properties reported could be repeated, if a single scaffold type was chosen (same slurry constituents and heat treatment). However, for the purposes of investigating a range of starting conditions, the scanning conditions chosen are adequate to draw comparisons upon the differences in resultant architectural properties.

5.3.2.5. Summary

In general it was shown that with increasing glass wt % the porosity and pore size distribution of the scaffold decreased, however this decrease was countered with an increase in architectural consistency. Overall porosities of scaffolds were dependant primarily on glass wt %, pore size distribution was dependent upon the application of a tertiary dwell stage. Comparison to physiological values showed that overall the porosities of the scaffolds produced were lower; however, the areas of the scaffold that are not blocked exhibit similar characteristics to that of natural trabecular bone.

Table 5.6 - Comparison of scaffold architectural properties to human trabecular bone from various anatomical sites (264).

Property	Site/Specimen	Mean	SD	Min	Max
BV/TV	ICF	0.156	0.054	0.048	0.279
	LS2B	0.083	0.024	0.04	0.158
	LS4A	0.087	0.033	0.04	0.226
	FRA	0.261	0.078	0.118	0.481
	CAB	0.12	0.035	0.054	0.19
	521B	**0.47**	**0.95**	**0.455**	**0.485**
	443B	**0.586**	**0.006**	**0.577**	**0.596**
BS/BV (mm^{-1})	ICF	17.65	3.45	10.84	32.13
	LS2B	23.73	3.41	17.16	34.29
	LS4A	21.17	3.59	11.37	32.94
	FRA	13.12	2.92	7.17	21.19
	CAB	21.64	3.23	14.5	28.34
	521B	**13.872**	**0.31**	**13.193**	**14.342**
	443B	**11.728**	**0.155**	**11.426**	**11.917**
Tb.Th (mm)	ICF	0.151	0.027	0.087	0.225
	LS2B	0.122	0.019	0.082	0.165
	LS4A	0.139	0.028	0.092	0.224
	FRA	0.194	0.033	0.127	0.284
	CAB	0.129	0.018	0.102	0.169
	521B	**0.144**	**0.003**	**0.139**	**0.152**
	443B	**0.171**	**0.002**	**0.168**	**0.175**
Tb.Sp (mm)	ICF	0.747	0.15	0.523	1.307
	LS2B	0.792	0.135	0.572	1.268
	LS4A	0.854	0.143	0.602	1.164
	FRA	0.638	0.114	0.454	0.94
	CAB	0.679	0.107	0.456	0.982
	521B	**0.162**	**0.011**	**0.15**	**0.189**
	443B	**0.118**	**0.002**	**0.115**	**0.122**
Tb.N (mm^{-1})	ICF	1.402	0.265	0.788	2.051
	LS2B	1.278	0.201	0.77	1.774
	LS4A	1.161	0.181	0.843	1.609
	FRA	1.595	0.292	1.092	2.387
	CAB	1.462	0.202	0.998	2.09
	521B	**3.287**	**0.109**	**3.078**	**3.419**
	443B	**3.463**	**0.026**	**3.418**	**3.513**

5.3.3. Mechanical properties

- For all scaffold types tested:
    - Characterise biaxial flexural strength
    - Determine effect of slurry constituents
    - Determine effect of heat treatment applied
    - Characterise the Weibull modulus
- Determine whether an additional layer could be applied and if this had a significant effect on the mechanical strength

5.3.3.1. Biaxial Flexural Strength

The biaxial flexural strength was calculated for the scaffold types by calculating the average flexural strength of each specimen from the four levels (i-iv), the mean flexural strength of each scaffold type was then derived from the averaged values. The resultant values for all scaffolds types tested are depicted in Table 5.7 and Figure 5.43. The following sections will present and discuss in detail the trends observed by varying the slurry constituents and heat treatments.

Table 5.7: Average biaxial flexural strength of scaffolds

PVA wt %	Binder solution:Glass	Heat Treatment	Biaxial Flexural Strength (MPa)	S.D.
5	2:1	A	2.06	0.54
		B	3.6	1.08
		C	1.96	0.67
4	20:13	B	6.04	0.55
4	10:7	A	4.08	0.20
		B	5.66	0.90
4	4:3	A	7.06	1.12
		B	8.85	1.23
5		B	9.82	1.47
		C	4.7	1.06
6		B	5.46	0.83

5.3.3.2. Effect of slurry constituents

In general, it was observed that the biaxial flexural strength of the scaffold increased as the glass content was increased. Considering scaffolds produced using heat treatment B only (see Figure 5.29) the strengths ranged from 3.60 ± 1.08 MPa to 9.82 ± 1.47 MPa. Varying the PVA wt % does not exhibit the same trend, increasing the PVA wt % eventually exhibits a detrimental effect on the mechanical properties. Figure 5.30 highlights the biaxial flexural strengths of scaffolds produced using 4:3 ratio of binder solution to glass and heat treatment B.

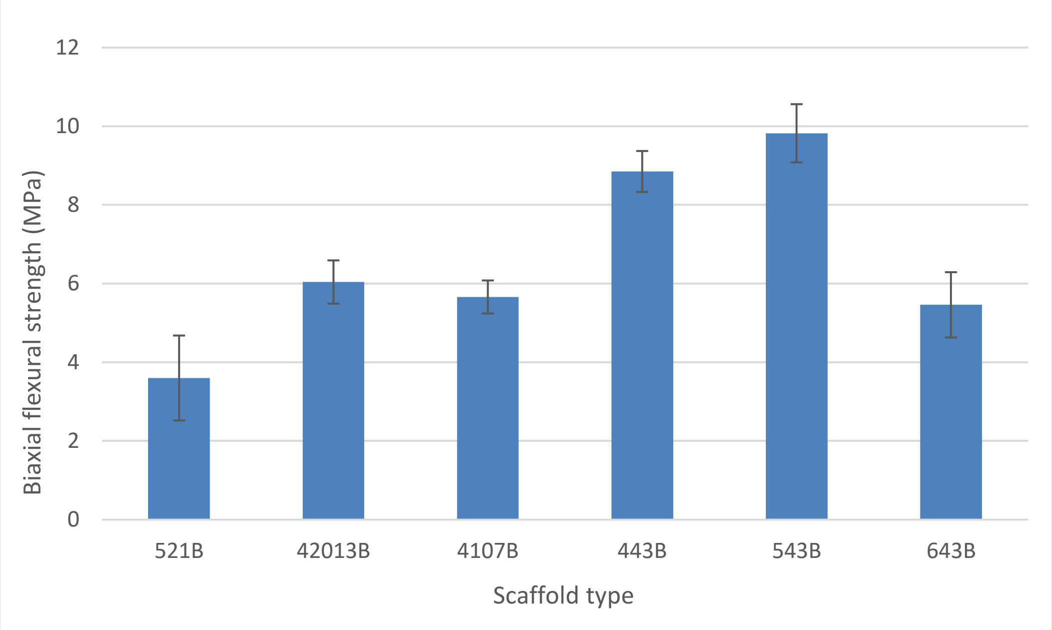

Figure 5.29 - Comparison of change in biaxial flexural strength with increasing glass content

As can be seen the strength increases from 4 to 5 wt %. PVA, increasing the PVA content to 6 % results in a dramatic drop in the strength by ~ 56 %. Additionally, statistical analysis showed that the strengths of the 643 scaffolds were not significantly different from scaffolds prepared from a 4103 slurry. This result reinforces the previous remark that there is a limit to the amount of binder that can be used within the slurry.

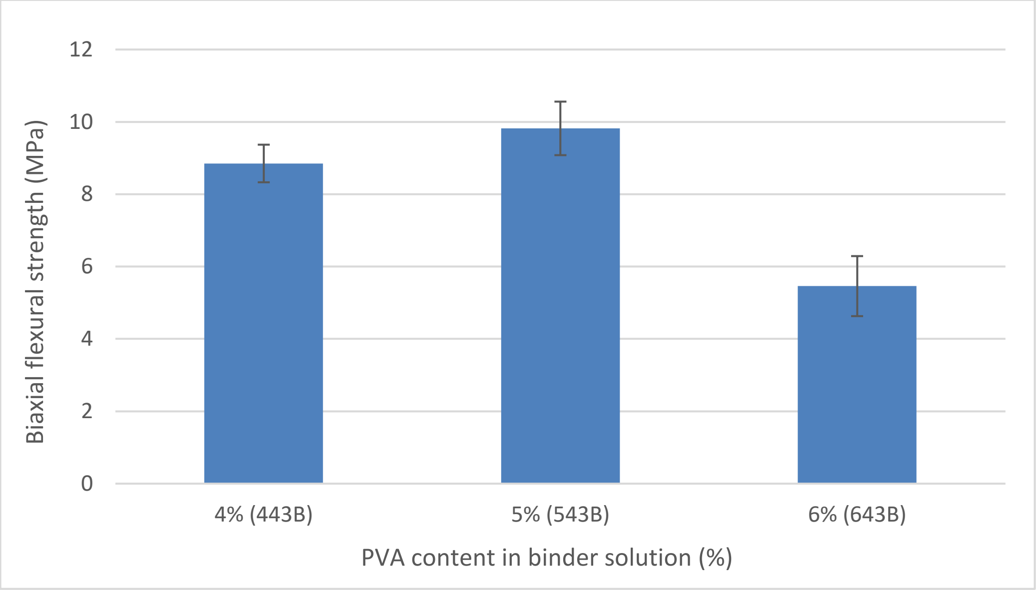

Figure 5.30 – Comparison of average biaxial flexural strength with varying PVA wt %.

5.3.3.3. Effect of heat treatment

A similar trend to increasing the glass content was observed when comparing heat treatments A and B as shown in Figure 5.43. However; increasing the tertiary dwell temperature further (approaching the crystal melting point) showed a similar trend to that of varying the PVA wt %. Statistical analysis revealed that the application of heat treatment C resulted in scaffolds with strengths equivalent to those produced through heat treatment A, lower glass content and higher PVA wt %. This result implies that (as with varying the PVA wt %) there is an optimal tertiary temperature that can be employed.

5.3.3.4. Apparent Density

The apparent density of scaffolds was obtained whilst dimensioning the discs for biaxial flexural testing; a comparison of scaffold types is depicted in Table 5.8**,** only scaffolds produced from 2:1 slurries fell below values obtained from natural trabecular bone (0.1-1.0 g/cm^3 (23, 80)).

Table 5.8: Comparison of apparent densities

PVA wt %	Binder solution: Glass	Heat Treatment	Apparent Density (g/cm^{-3})
5	2:1	B	0.089
4	10:7	A	0.105
		B	0.104
4	4:3	A	0.121
		B	0.116
5		B	0.121
		C	0.106

As shown in Figure 5.31 an increase in apparent density correlates well with an increase in biaxial flexural strength. Such a relationship could be useful in estimating the potential strengths of scaffolds made in the future (see section 5.6.1.)

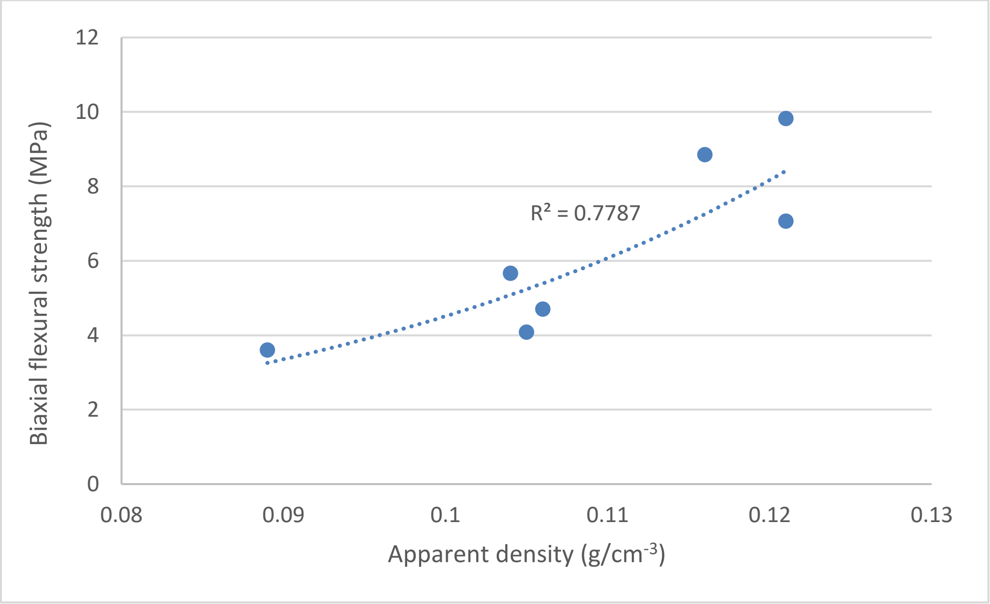

Figure 5.31 – Biaxial flexural strength vs apparent density

5.3.3.5. Potential stability

As previously described increasing the glass content resulted in an increase in mechanical strength; however, 42013B and 4107B scaffolds showed no significant difference in strength. Closer inspection of the load vs extension traces helps to explain this deviation from the trend. Figure 5.32 to Figure 5.35 illustrate varying scaffold types that were loaded until failure. As can be seen scaffolds produced from slurries containing 10:7 binder solution to glass ratio (Figure 5.35) or higher exhibit a consistent loading profile; whereas scaffolds produced using lower binder solution to glass ratios (see Figure 5.32 to Figure 5.34) exhibit multiple failure regions.

This implies that these scaffolds are in fact failing at much lower loads in small regions; perhaps due to insufficient coating in certain regions resulting in poorly defined struts. Considering the potential application, the peak stresses that can be supported are not the only mechanical characteristic to value. It is worth noting that 421A and 421B scaffolds were prepared for mechanical testing; however, as shown in Figure 5.32 the loading profiles were extremely erratic (if produced at all). This was due to random centralized flaws, which caused the loading tip to punch straight through the disc; it is suggested that if such scaffolds were to be re-tested, uniaxial compression could provide sufficient data to comment on their mechanical strengths.

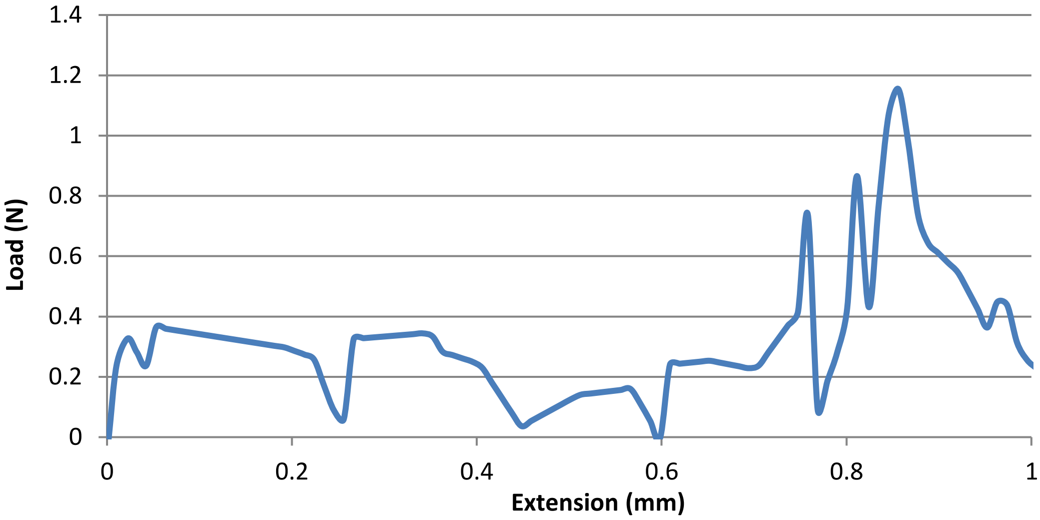

Figure 5.32 – Example of a load vs extension trace - 421B scaffold. Loading tip punched through disc during test.

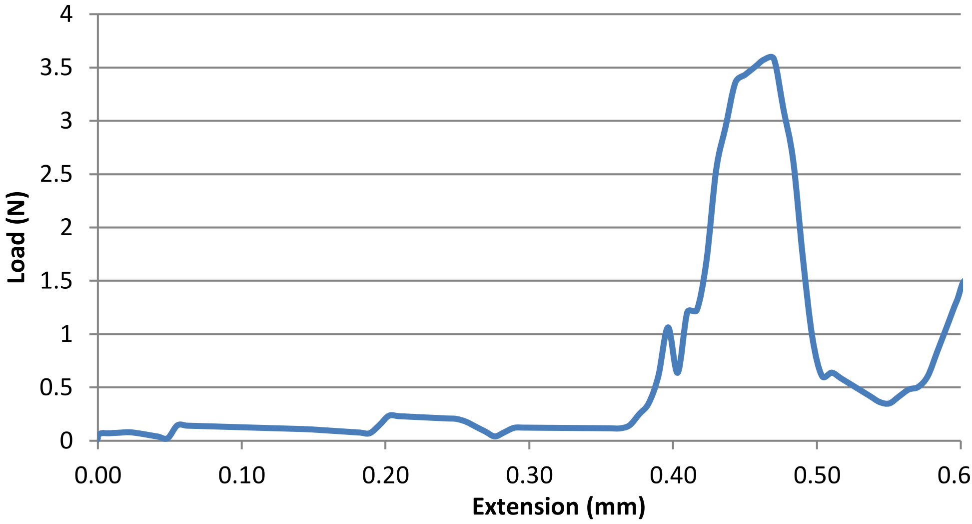

Figure 5.33 – Example of a load vs extension trace – 521B scaffold

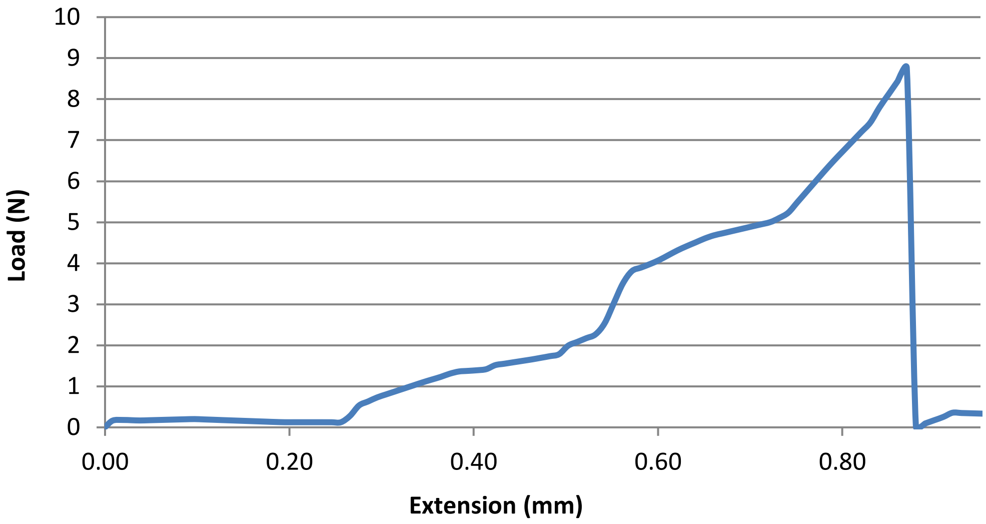

Figure 5.34 - Example of a load vs extension trace – 42013B scaffold

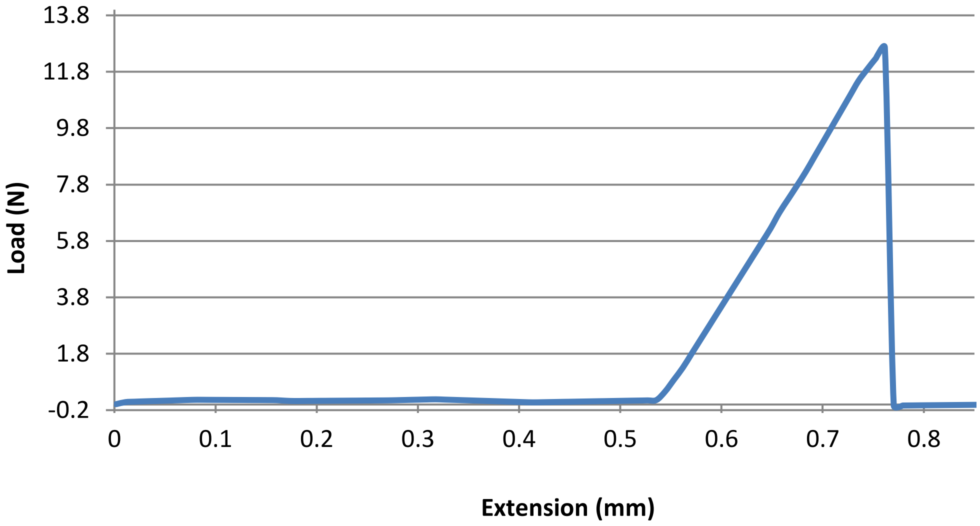

Figure 5.35 - Example of a load vs extension trace – 4107B scaffold

5.3.3.6. Uniaxial compressive strength vs Biaxial flexural strength

Limited testing was conducted using the uniaxial test method; however as it is commonly described in the literature a comparative test was conducted. 443A, 443B, 543B and 643B scaffolds were produced and underwent uniaxial compression through the method previously described (see section 4.7.2.),the results are given in Table 5.9 and illustrated in Figure 5.36. The compressive strengths ranged from 2.32 (± 0.47) to 3.61 (± 0.42) MPa.

Table 5.9: Uniaxial compressive strengths of 443A, 443B, 543B and 643B scaffolds

Scaffold	Average compressive strength (MPa)	S.D. (MPa)
443A	2.32	0.47
443B	3.61	0.42
543B	3.31	0.73
643B	3.40	0.64

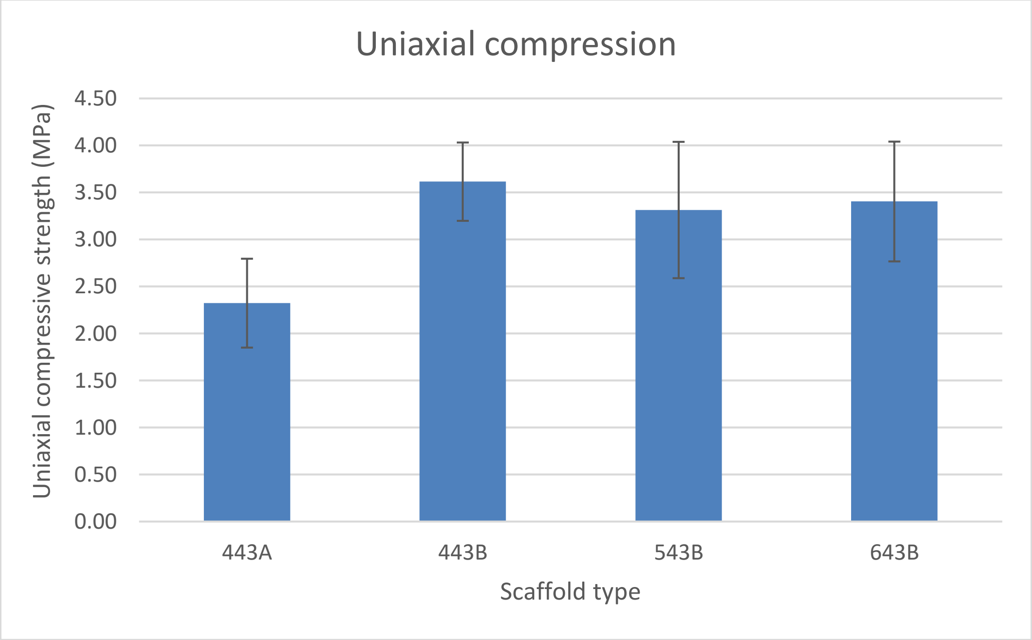

Figure 5.36 – Uniaxial compressive strengths of 443A, 443B, 543B and 643B scaffolds

The values reported for the uniaxial test are lower than that of the biaxial test (illustrated in Figure 5.37), which is unexpected, it is generally agreed that the compressive strengths are higher than tensile strengths. However, the load vs extensions traces for the uniaxial tests show multiple failure regions, most likely due to repeated trabecular buckling (see Figure 5.39). This is unlike the trace shown in Figure 5.38, which depicts a clearly linear elastic region until failure of the material.

Chen *et al* (225) in their work on bioglass derived glass-ceramic scaffolds noted that the scaffolds they had produced using a 60 PPI foam had compressive strengths (0.3-0.4 MPa) at the lower bounds of those of much more porous bone. They were considerably weaker, by a factor of ten, than those samples produced in this study, although direct comparison is difficult due to geometric considerations (rectangular samples were used) and a different starting glass formulation. They indicated that they considered these strengths sufficient to allow the samples to be manipulated and commented that scaffolds may not need to match the mechanical properties of bone. New tissue formation will create a biocomposite and increase the time-dependant strength. Liu *et al* (2013) demonstrated for 13-93 bioactive glass scaffolds, that after 2-4 week subcutaneous implantation in rats, the initial elastic, brittle mechanical response of these caffolds changed to an elasto-plastic response (215).

In terms of the test data, Chen *et al* noted that a typical stress strain curve for uniaxial compression was jagged; with distinct regimes corresponding to the failure in the thin struts, followed ultimately by densification of the collapsing foam (225). It was noted that compressive testing was often accompanied by shear processes such that compressive testing can lead to an underestimation of the modulus and strength. Such features are also seen in this study. Measured values of flexural strength were also reported to be higher than compressive strength, as in this study. This finding may be explained by the above argument.

Magdeski (265) found that when looking at the flexural and compressive properties of sintered alumina with a porosity range of 55-80 % that whilst there was a good correlation between data and theoretical model for flexural strength, there was no such correlation for compressive strength. This was attributed to the sensitivity of the alumina samples in compression to the method of load application, i.e. the load distribution over the entire contact surface, resulting in a failure mode characterised by a damage accumulation process.

Sabree *et al* (266) produced porous wollastonite scaffolds with an internal porosity of ~42 %. They reported a considerable variation in the mechanical response of individual scaffolds during crushing experiments and attributed this, like the previous authors, to the fact that the top and bottom surfaces of the scaffolds were neither flat nor parallel. Unlike many studies they did not see a plateau region nor final increase in stress as the scaffold remnants were further compressed, rather the scaffolds displayed a chaotic region after the initial peak load followed by total collapse of the scaffold; they attribute this difference to geometric differences and the size of the scaffolds tested. Weibull modulus was low at ~3, compared to a value of 4.2 for a 4 point flexural test with compressive strengths reported in the range 12-24 MPa, claimed to be just larger than that of cancellous bone at ~10 MPa, taken from Gibson (267).

It is suggested that future work could repeat this comparison of mechanical test methods to ascertain which method is the most reliable. It is suggested however that the tensile properties of a glass-ceramic are the most important to characterise as this is the most likely method of failure.

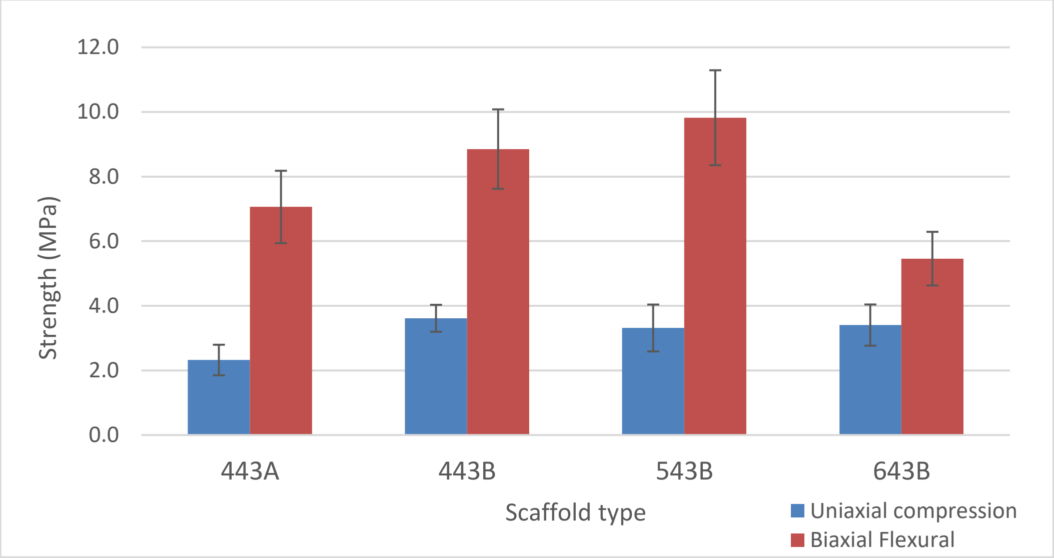

Figure 5.37 – Comparison of uniaxial compressive strengths and biaxial flexural strengths

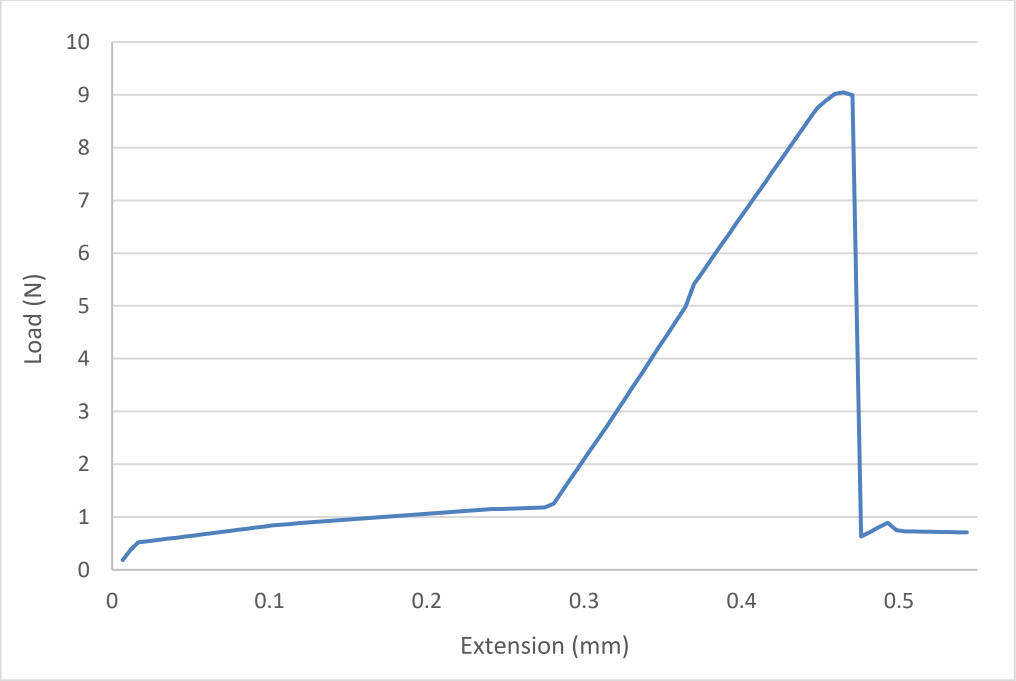

Figure 5.38 – Load vs extension trace for 643B (Biaxial flexural test)

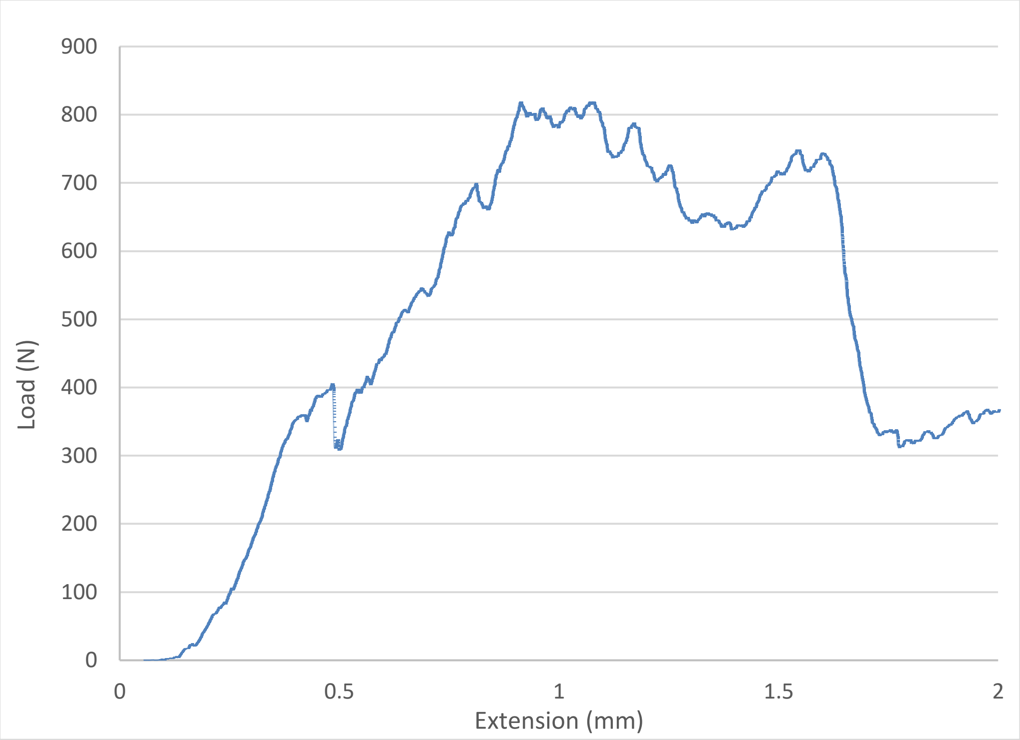

Figure 5.39 – Load vs extension trace for 643B (Uniaxial compression test)

5.3.3.7. Weibull Modulus

The Weibull modulus is a dimensionless parameter that is used to characterise the variability in failure of brittle materials. Due to the lack of ductility in brittle materials, the maximum stress that can be supported is dependent upon the distribution of flaws within the material. Aside from the desired porous structure, flaws within the scaffold are generated via lack of glass particle densification during sintering and the hollow struts formed via the burn out step. An even distribution of flaws will result in a high Weibull modulus value, implying a high level of repeatability in material properties (i.e. failure loads). Table 5.10 and Figure 5.40 depict the Weibull modulus for all scaffold types that underwent mechanical testing.

Table 5.10: Weibull modulus of varying scaffold types

PVA (wt %)	Binder solution: Glass	Heat Treatment	Weibull Modulus
5	2:1	B	3.38
4	20:13	B	5.87
4	10:7	A	5.85
		B	7.66
4	4:3	A	7.41
		B	8.68
5		B	8.04
		C	5.24
6		B	7.82

In general, a similar trend was observed with respect to the biaxial flexural strength, increasing the glass content increases the Weibull modulus, application of heat treatment B results in a higher Weibull modulus. As discussed in section 5.3.3.3. application of a tertiary dwell temperature above 950 °C is detrimental to the resultant scaffold properties; this is further illustrated by the drop in the Weibull modulus from 8.04 to 5.24. Interestingly the use of 6 wt % PVA does not exhibit such a significant reduction; this suggests that the decrease in biaxial flexural strength due to slurry constituents is more consistent than that attributed to the heat treatment applied. In a comprehensive study looking at biaxial flexural strength of porous hydroxyapatite discs, Fan *et al* (268) combined their data with that of six other published studies on BFS of HA. It was determined that, irrespective of manufacturing route or pore size distributions (unimodal or bimodal) for samples with a porosity between 10 and 55 %, the Weibull modulus was always in a relatively narrow band of ~4-11. The values determined in the current study agreed with this study. They further extended their study to incorporate data from other porous ceramic materials and found a similar trend in the relationship between Weibull modulus and porosity.

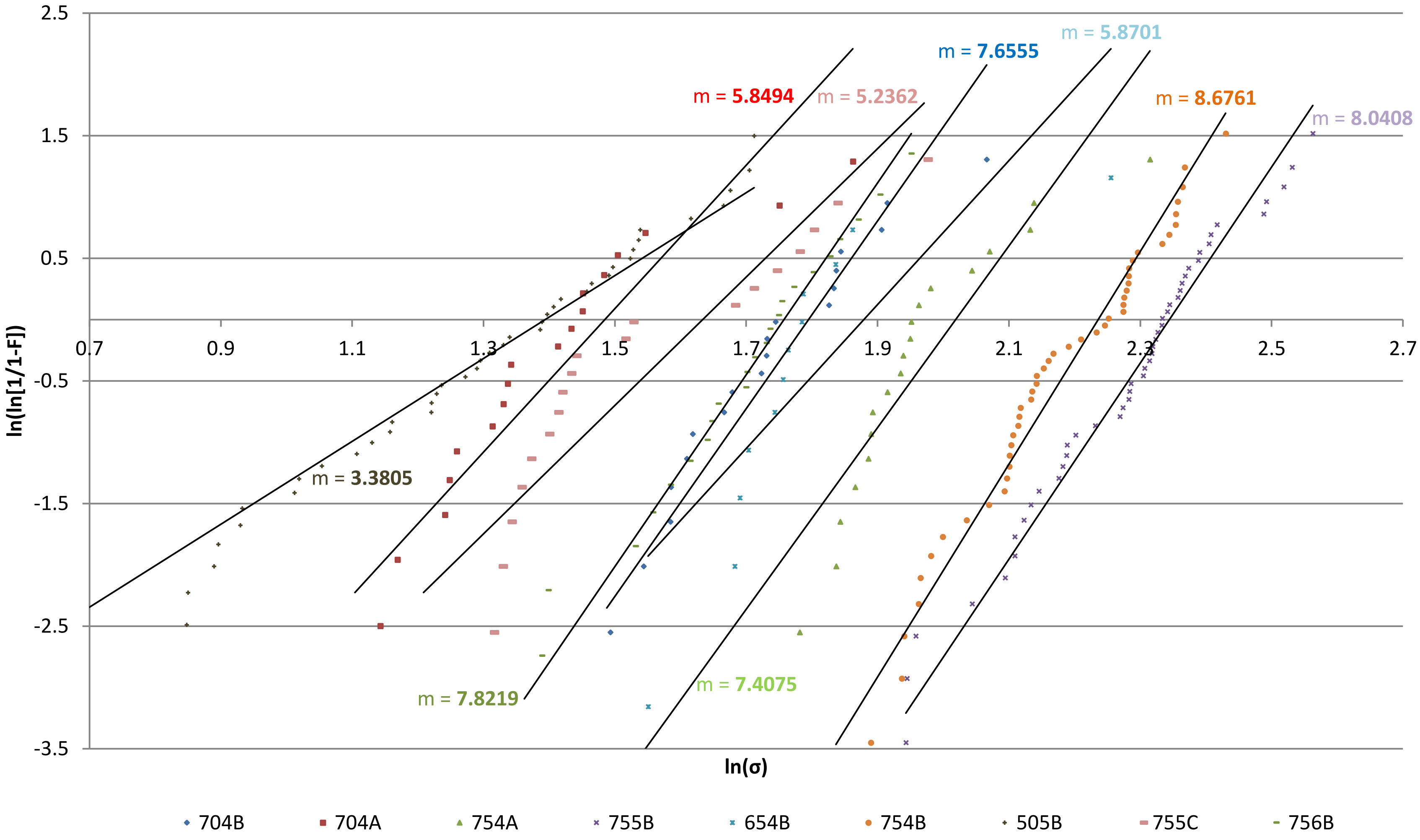

Figure 5.40 - Weibull modulus plots – Modulus derived from the gradients of the linear regressions.

5.3.3.8. Application of a "cortical shell"

543A scaffolds were prepared and subsequently underwent additional processing steps as described in section 4.2.5. It was postulated that the addition of an "outer shell" would produce a scaffold with the highest biaxial flexural strengths; the resulting strengths were 9.56 ± 1.93 MPa. Statistical analysis showed there were no significant differences between these scaffolds and those produced through the "standard method" and fired through heat treatment B (i.e. standard 543B scaffolds). It was observed however that the outer shell had sintered and formed a dense outer coating ~ 60 µm thick whilst retaining the original porous structure (see Figure 5.41 and Figure 5.42); this implies that perhaps if additional coats were applied a thick enough layer could be deposited, increasing the scaffold strength further.

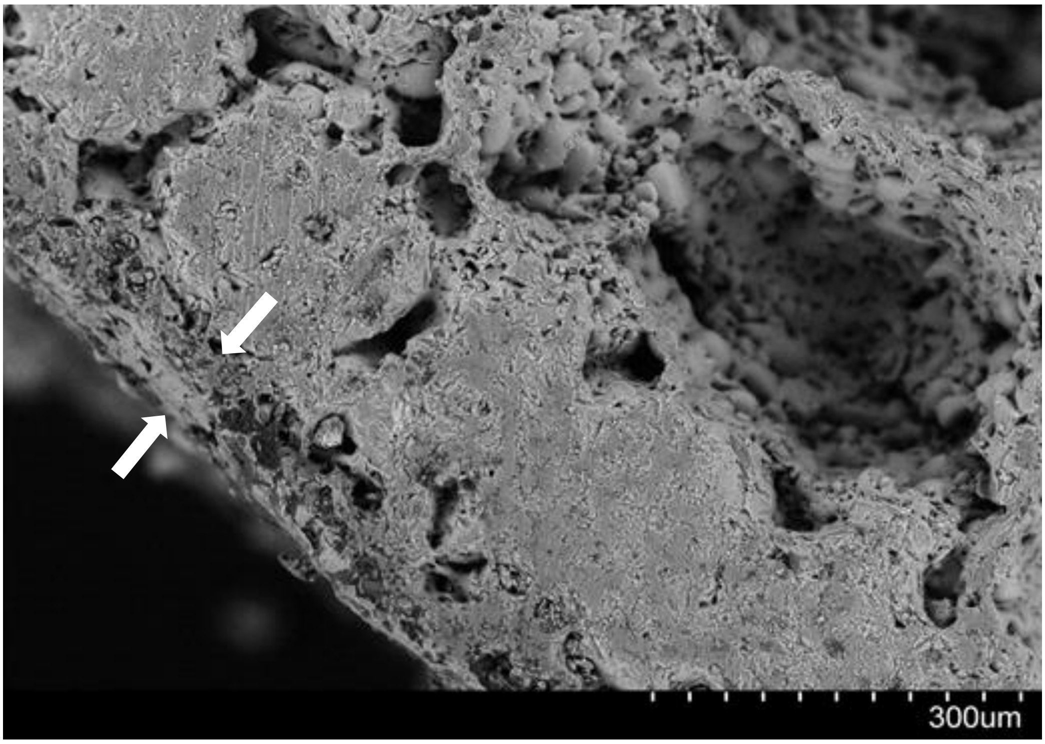

Figure 5.41 – Attempt at applying an additional dense shell to a 543A scaffold. White arrows indicate additional thin deposited layer.

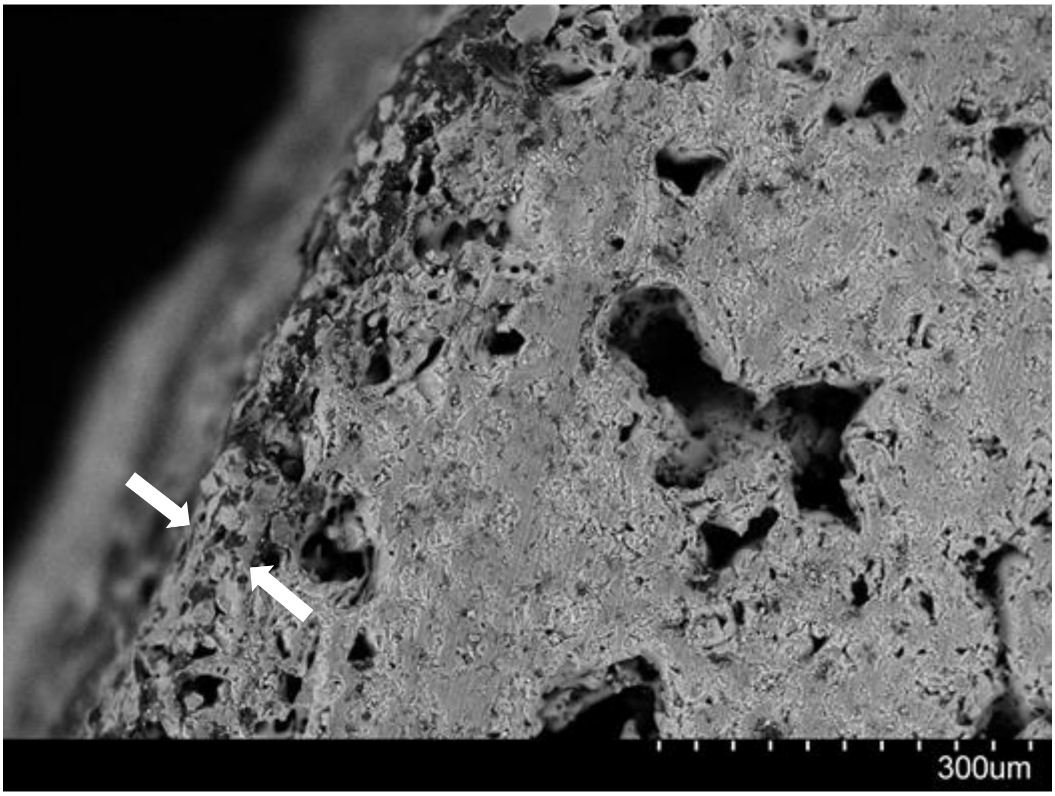

Figure 5.42 - Attempt at applying an additional dense shell to a 543A scaffold. White arrows indicate additional thin deposited layer.

5.3.3.9. Summary

Similar trends were observed to the architectural properties; increasing the glass content resulted in an increase in the biaxial flexural strength, an increase in strength was observed as PVA content in the binder solution was increased up to 5 %. The heat treatment applied had a significant effect upon the flexural strength, heat treatment B resulted in the highest strengths for all scaffold types

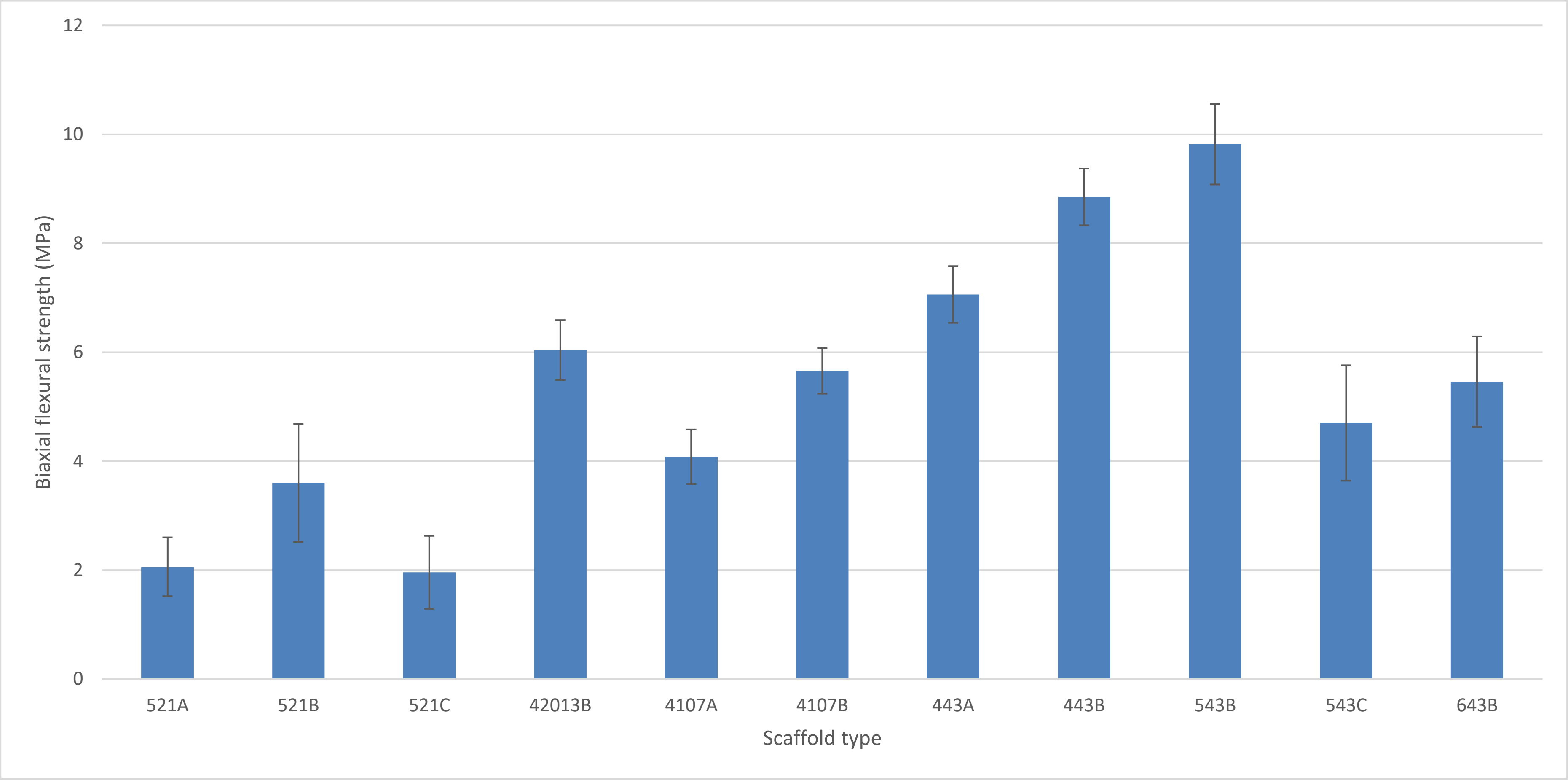

Figure 5.43 – Average biaxial flexural strengths of varying scaffold types

5.4. Fluorapatite coating

The aim of this section was to:

- Determine whether a fluorapatite coating could be applied to A/W
- Determine if the initial slurry constituents had an effect on the resultant FA coating
- Investigate whether the heat treatment applied to the scaffold effects the resultant FA coating
- Investigate the effect of applying the FA coating technique to a 3D A/W structure

Flat plates with varying glass content and PVA wt % were used to determine whether these variables could be discounted for investigating FA coating on scaffolds. Figure 5.44 illustrates an example of a flat plate coated with FA; from SEM observation there appeared to be no dependence between the initial slurry constituents and the resulting FA coating produced. It was noted however that the surface that was in contact with the investment material (i.e. the underside of the plate) was less sintered and as such detrimentally affected the FA coating produced. Subsequent scaffolds therefore were prepared from 543 slurries, the only substrate variables considered were the heat treatments (i.e. A or B). Overall it was shown that an FA layer could be formed regardless of the heat treatment applied; however, the crystallinity of the substrate strongly dictates the resulting FA crystal morphology and density.

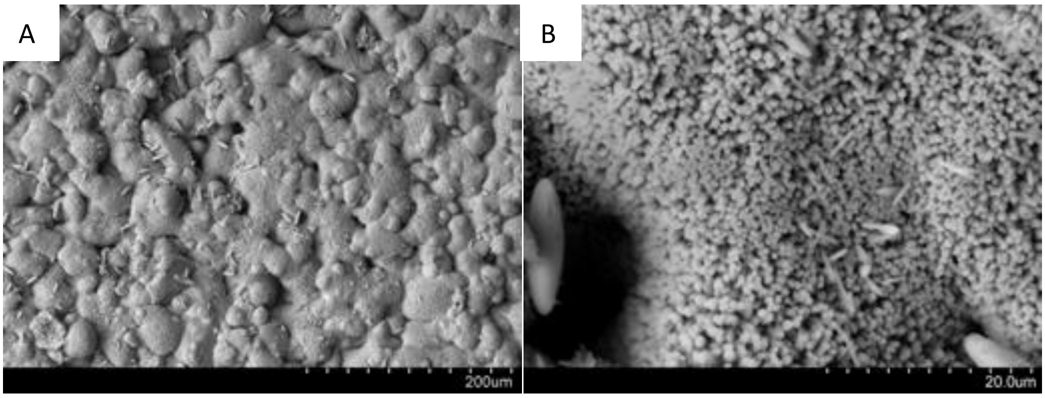

Figure 5.44 – A) FA coating on a flat 543B plate, B) Magnification x10

To confirm that a layer of fluorapatite had been formed EDX analysis was conducted on coated samples. As silicon would only be present in the amorphous glass phase and not in the fluorapatite needles EDX mapping was conducted comparing silicone and calcium. As shown in Figure 5.45 the underlying scaffold shows a high distribution of silicon unlike the surrounding coating; this is either due to presence of the amorphous glass phase or wollastonite ($CaSiO_3$). Figure 5.46 shows EDX mapping of silicon and calcium; the contrast in calcium content is clearly visible, traces of calcium are present in the underlying scaffold but vividly present in the surrounding FA coating.

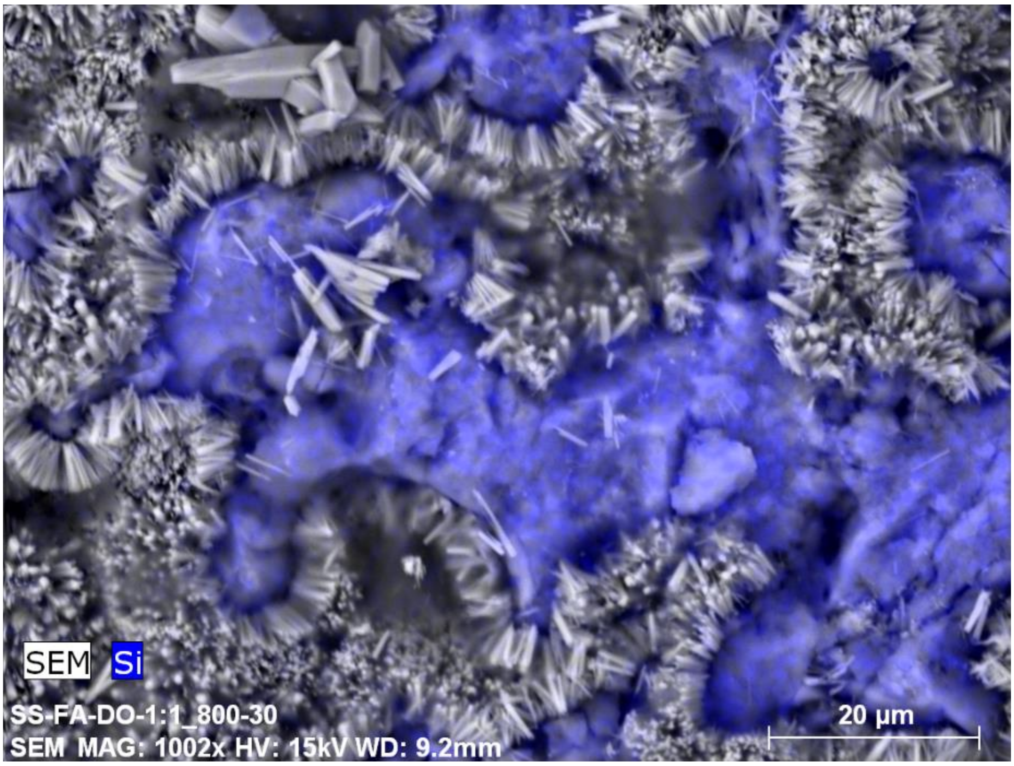

Figure 5.45 – EDX map of a sectioned disc coated with FA, silicone only

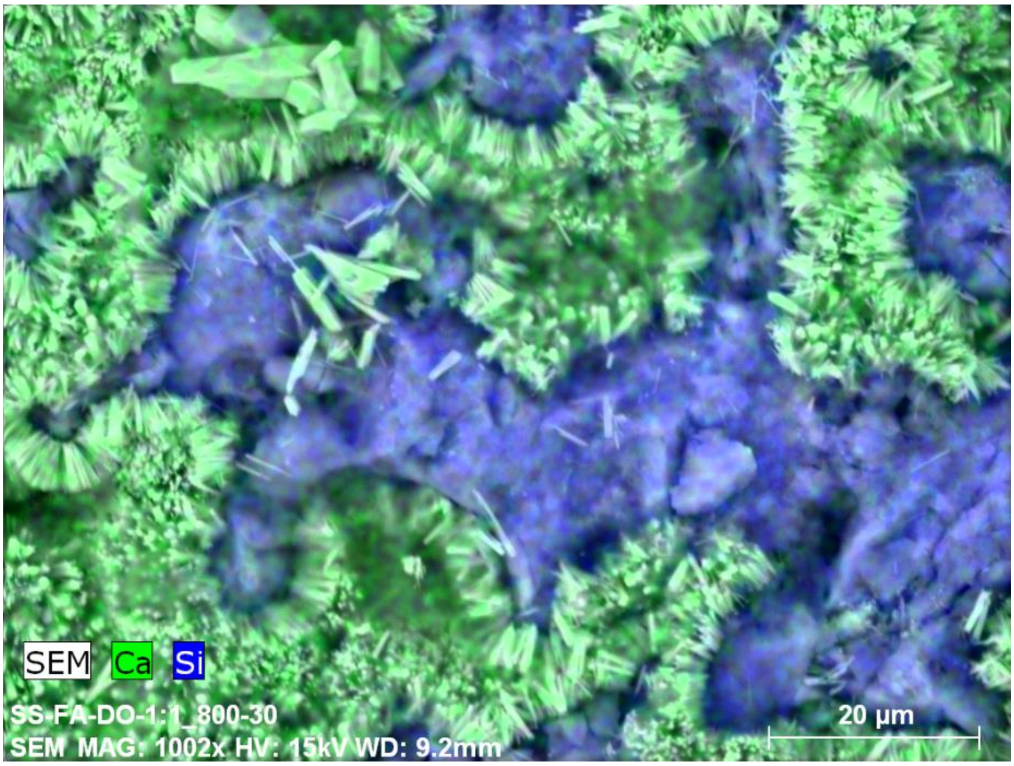

Figure 5.46 – EDX map of a sectioned disc coated with FA, silicone and calcium

5.4.1. FA coating on sectioned discs

The FA coating formed on discs produced through heat treatment A are shown in Figure 5.47 to Figure 5.51, the coating produced exhibits a “semi-ordered” morphology, comparable to previous studies conducted by Liu *et al* (187). From SEM observation alone there was no evidence of the 3-D structure negatively affecting the coating. It was postulated that on the underside of the pores/struts the ordered crystal structure would form and around the upper surfaces the previously described disordered structure would form. However; through SEM analysis it was clear that a consistent layer which followed the curvature of the pores and struts was produced across the entire surface of the scaffold. The crystals exhibit the same hexagonal cross section as previous studies; however they are much larger in size, a rough estimate from the SEM images would suggest the crystals are 500 nm in width and almost 4 µm in length.

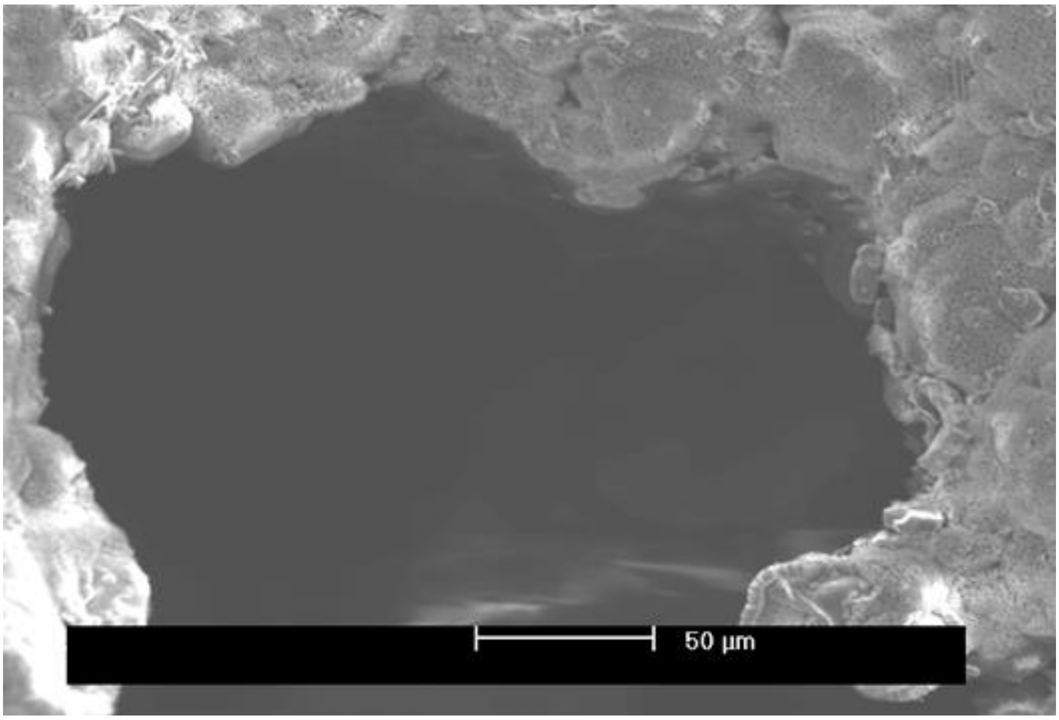

Figure 5.47 – FA coated sectioned disc; 543 slurry, heat treatment A.

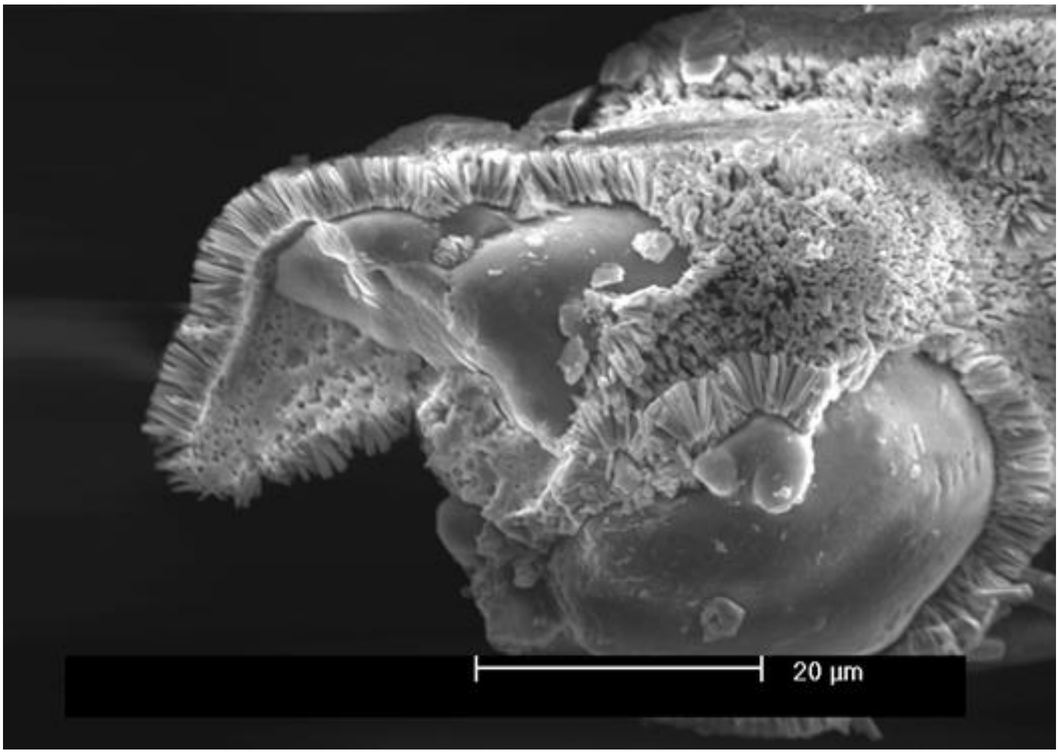

Figure 5.48 – Magnified image of FA coated strut, crystals can be seen to follow the 3-D contours.

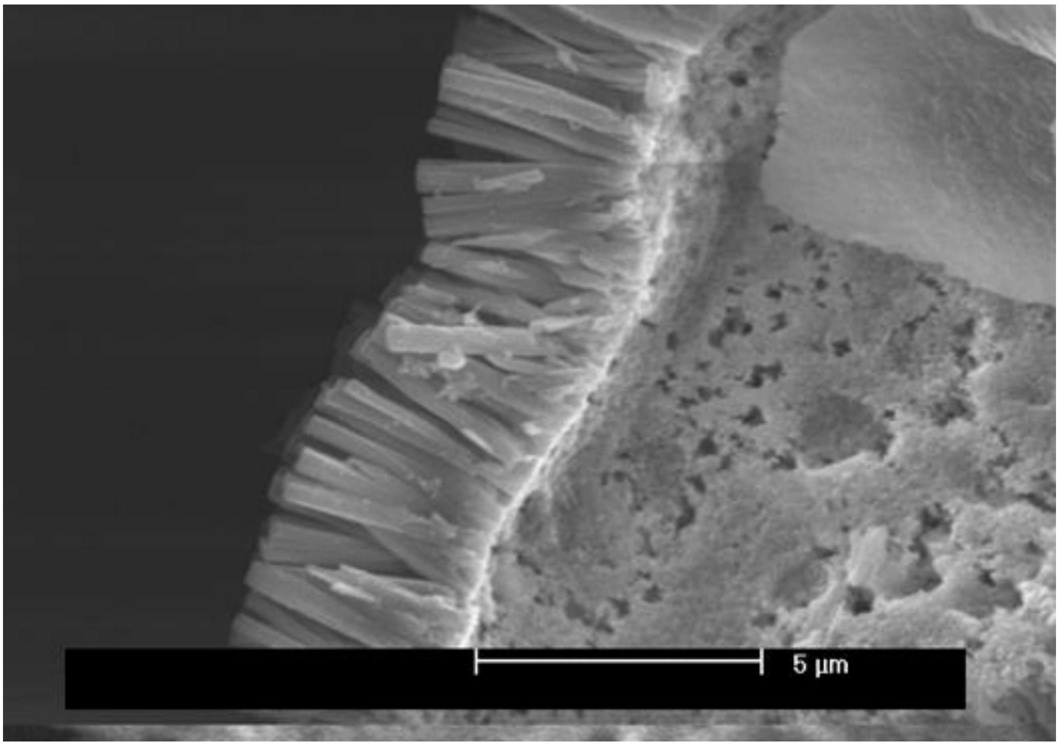

Figure 5.49 – Interface of FA coating and underlying glass-ceramic strut; crystal length and width are estimated to be 4 µm and 500 nm respectfully.

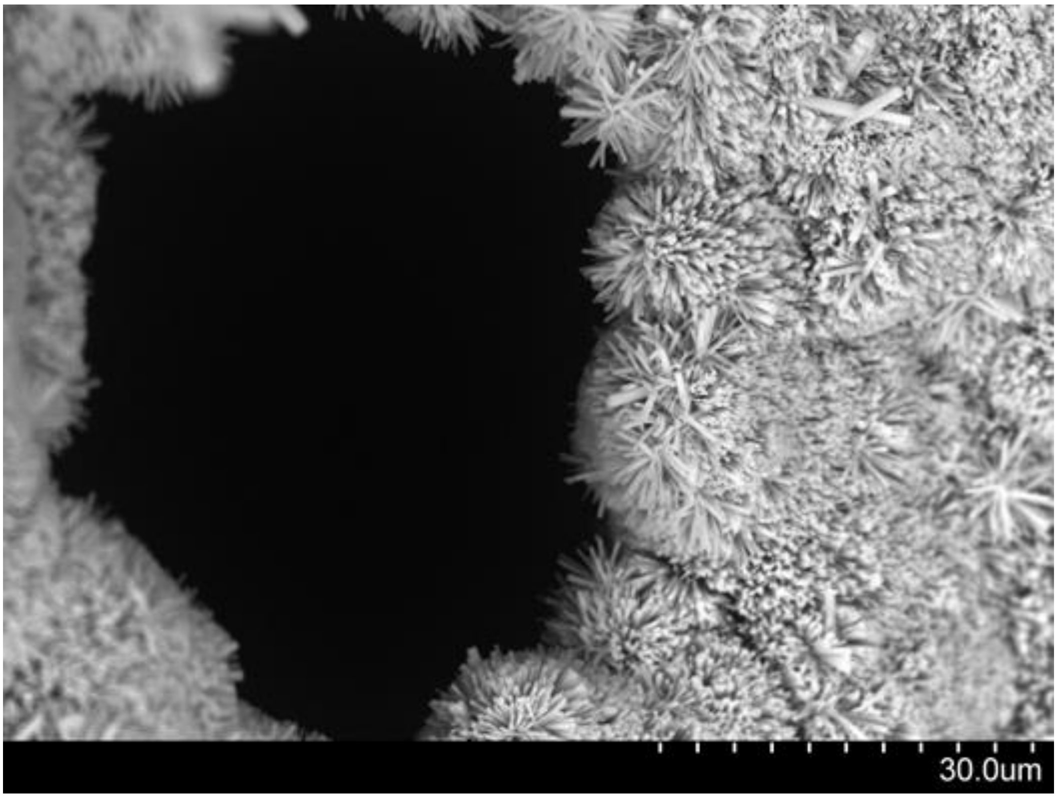

Figure 5.50 - FA coating of a relatively small pore, 543A scaffold.

Figure 5.51 – FA coating of thin strut, size disparity between ordered coating and disordered precipitate clearly visible.

The FA coating formed on the scaffolds produced through heat treatment B are shown in Figure 5.52 to Figure 5.54; the coating is much denser and is more comparable to the ordered structure described in previous work (187). Again, it was noted that the ordered coating layer was uniform over the 3-D surface with the c axis of the crystals orientated normally to the underlying substrate.

Previous studies reported that with an increase in autoclave time the size of the crystals increased due to the disassociation of Ca^{2+} ions from the EDTA-Ca complex (189). The XRD analysis showed that scaffolds produced through heat treatment A were comprised predominantly of an apatite phase and an amorphous glassy phase. This could suggest that these scaffolds are contributing further to the crystal growth providing additional Ca^{2+}, this is when compared to scaffolds produced through heat treatment B. XRD analysis showed that heat treatment B vastly decreased the amorphous phase, forming the more stable wollastonite phases in addition to apatite. This suggests that the FA layer produced on heat treatment B scaffolds is essentially dependent upon the Ca^{2+} within the solution, which is again more comparable to that of the previous studies. Performing mechanical testing on scaffolds post-coating could allude to this; if scaffolds produced through heat treatment A are contributing to the crystal growth it is expected that they would exhibit a reduction in strength.

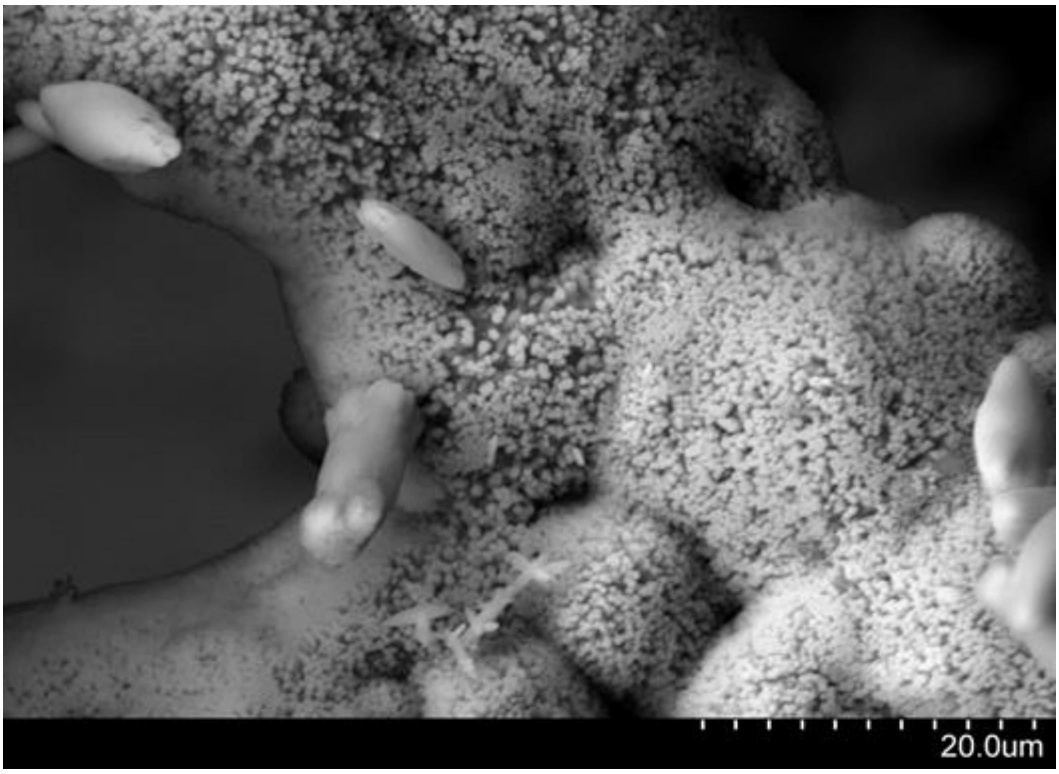

Figure 5.52 – FA coating on a scaffold produced through heat treatment B.

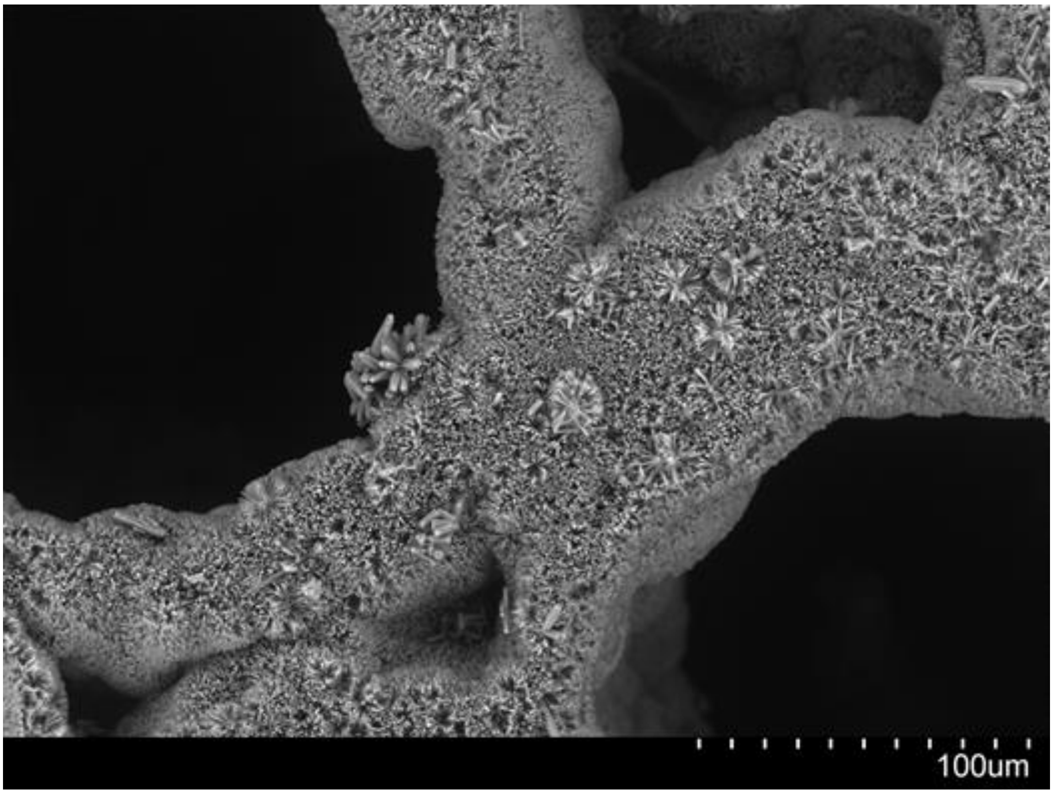

Figure 5.53 - FA coating on a scaffold produced through heat treatment B.

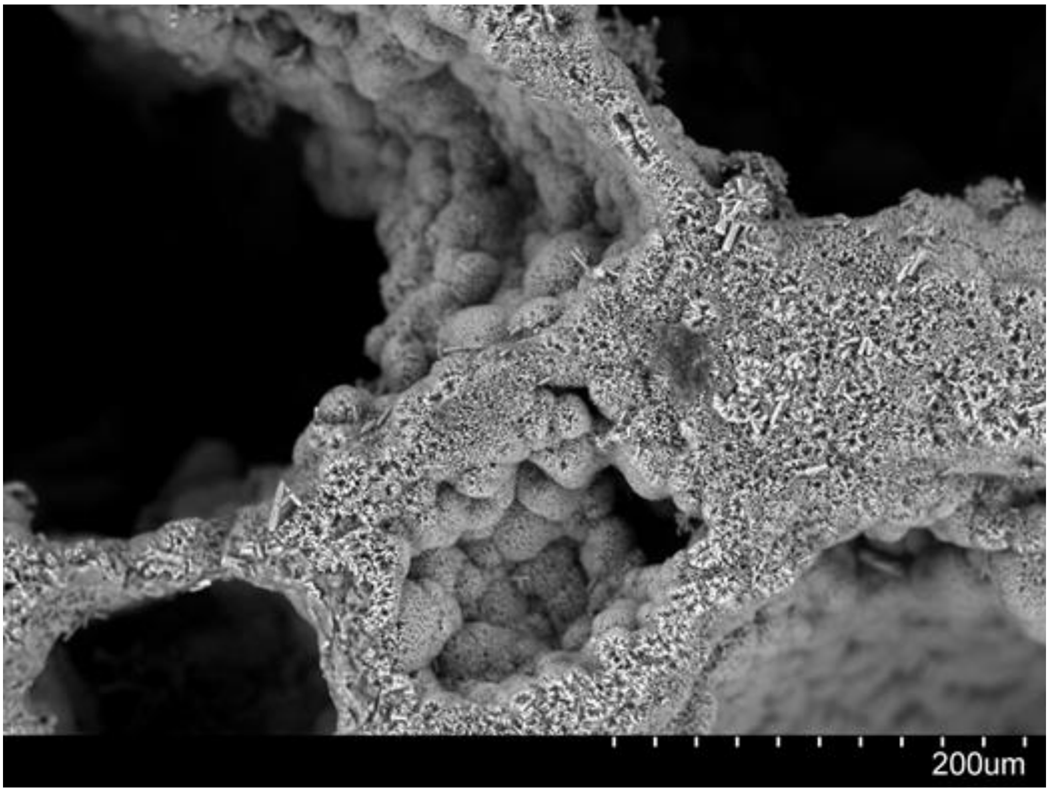

Figure 5.54 - FA coating on a scaffold produced through heat treatment B.

5.4.2. FA coating through the scaffold

The outer surfaces exhibited the same coating morphology as the sectioned discs as shown in Figure 5.55 and Figure 5.56, this implied good consistency not only with the scaffold production but also with the coating methodology. Upon sectioning the scaffold it was evident that the heat treatment alone does not dictate the type of coating produced, Figure 5.57 to Figure 5.59 illustrate this. Through the centre of the scaffold FA crystals are present yet sparse; regions of un-coated scaffold can be seen as can transitional areas showing the initial formation of crystals to their subsequent growth. Compared to the FA crystals formed at the surface their morphology and orientation diminishes with depth; even a rough estimation of their size is barely possible, the c-axis alone appears to be around 200-300 nm. The orientations of these crystals appear to be less ordered; however, in areas where the crystals have grown sufficiently they exhibit similar directionality, growing normally from the underlying substrate.

As previously stated, the outer surfaces exhibited FA coating comparable to that of the sectioned discs; this was expected as they had undergone the same heat treatment, the dramatic reduction in crystal size however was not expected. If it is assumed that the pressure and temperature is uniform throughout the scaffold during the autoclaving process this reduction in crystal size must be due to either the pores decreasing the convection of the solution, a rapid depletion of Ca^{2+} within the pores, or a combination of the two. Compared with coating on the plates and sectioned discs there was virtually no disordered precipitate within the scaffold; in addition to this it is worth noting that the precipitate within the scaffold that could be observed was also significantly smaller.

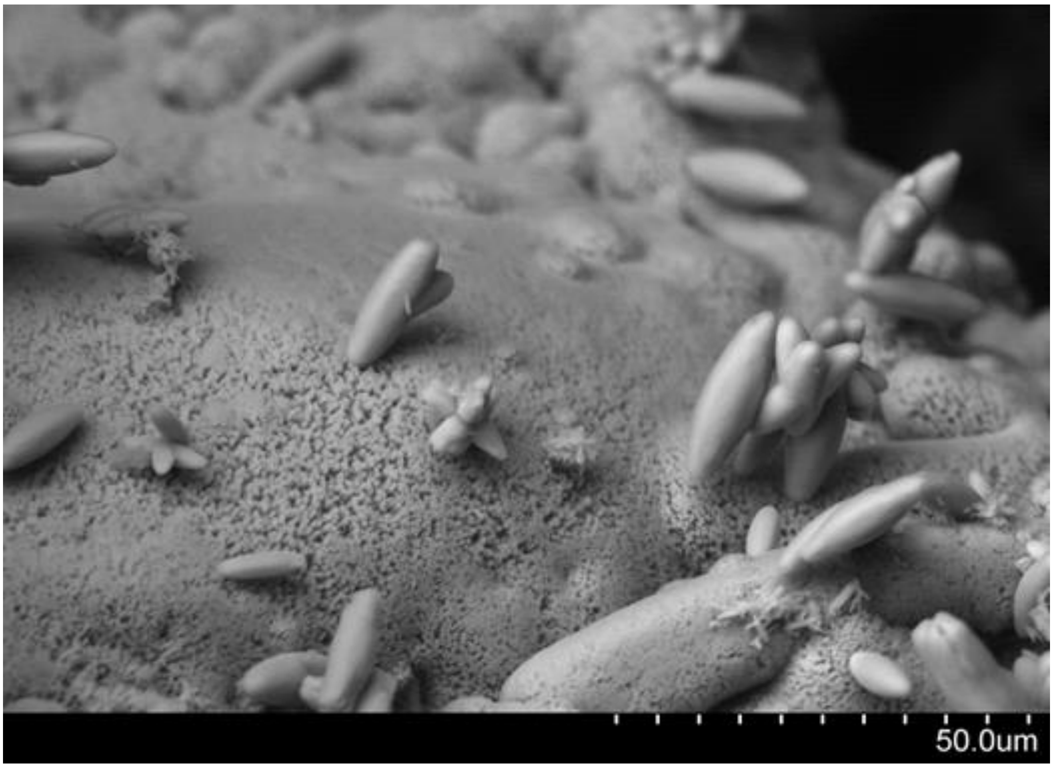

Figure 5.55 – FA coating of the outer surface of an un-sectioned scaffold.

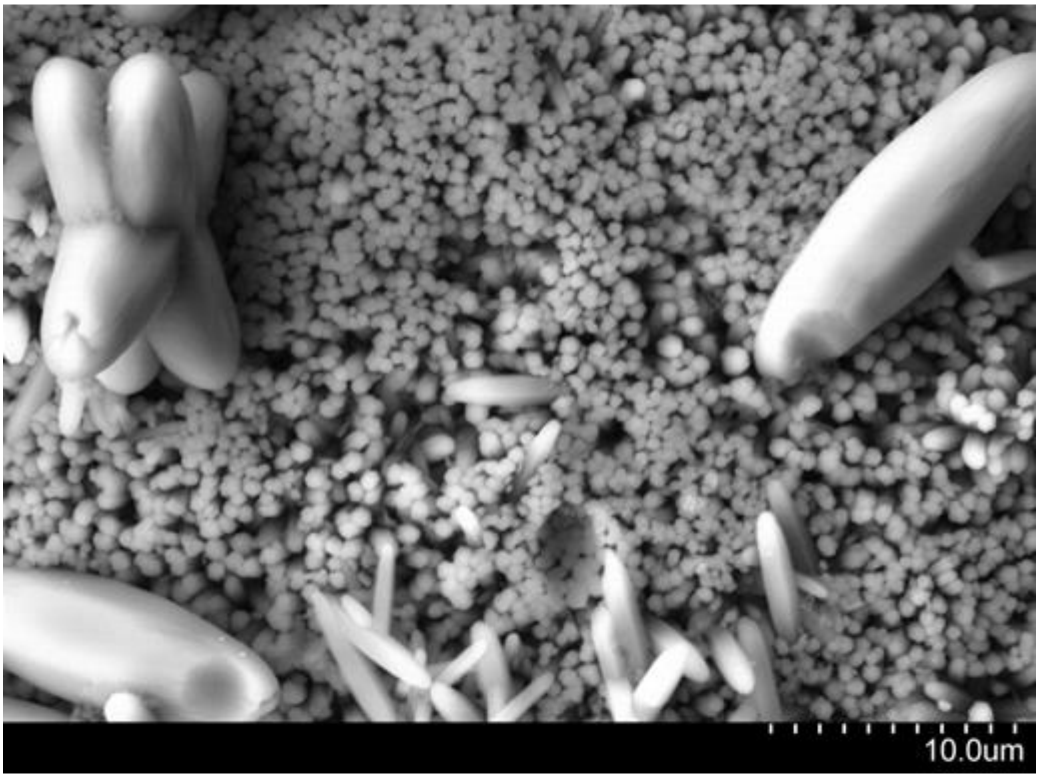

Figure 5.56 - FA coating of the outer surface of an un-sectioned scaffold.

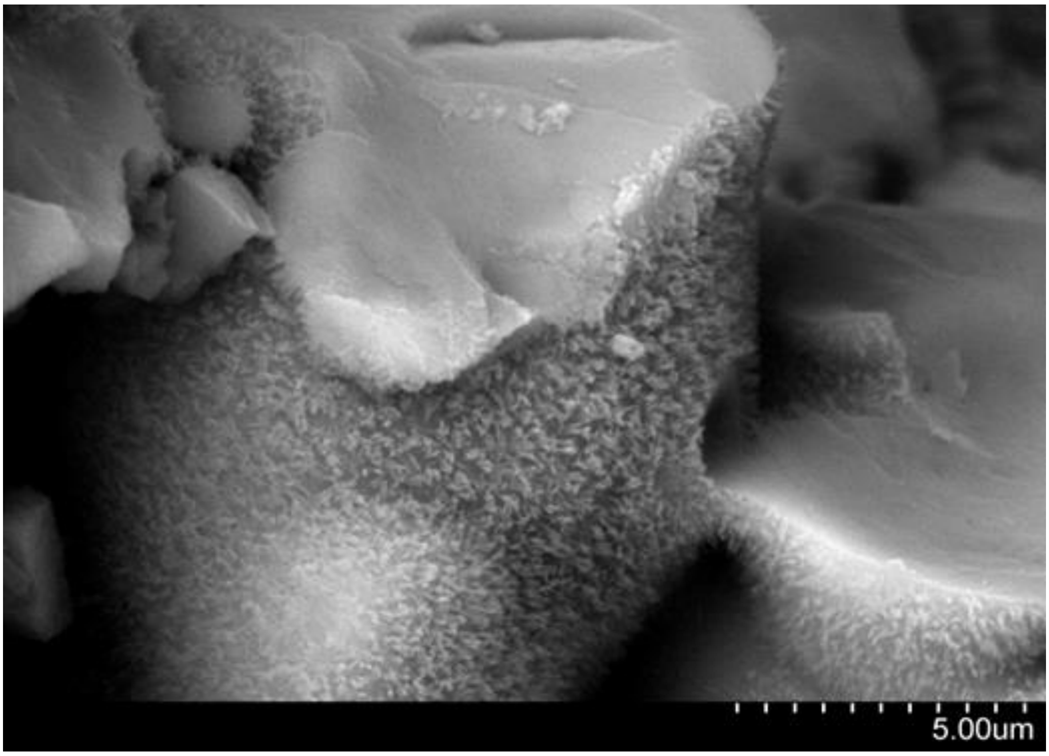

Figure 5.57 – Sectioned scaffold depicting the FA coating produced within the interconnected structure

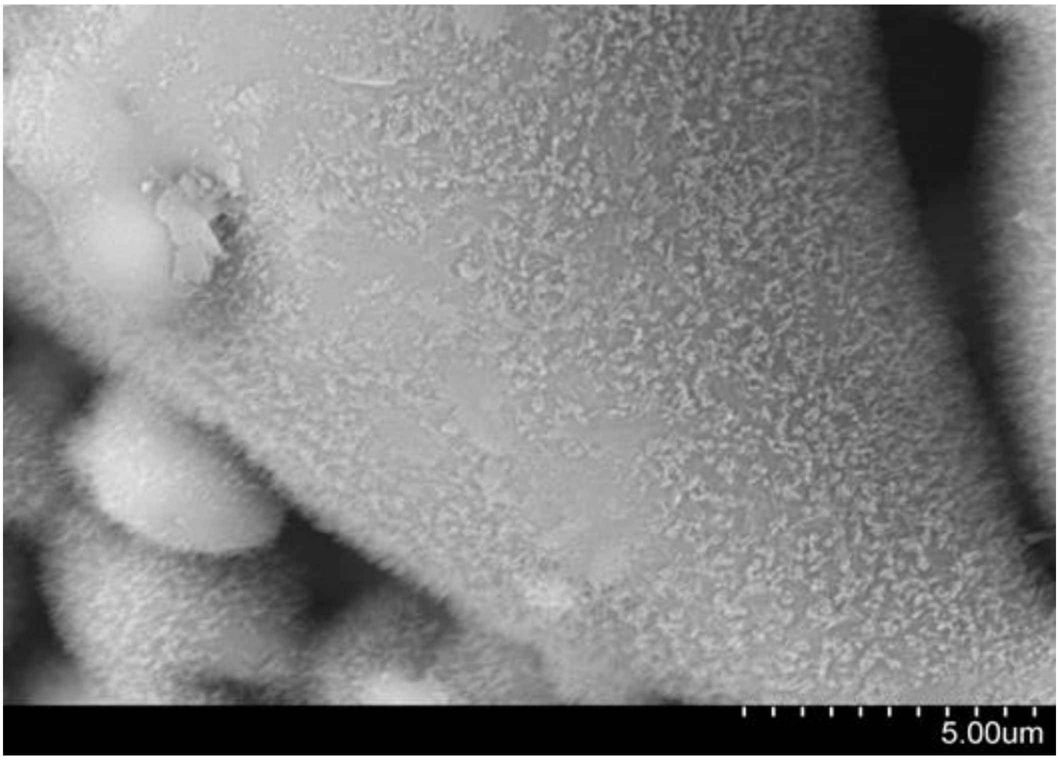

Figure 5.58 - Sectioned scaffold depicting the FA coating produced within the interconnected structure, patches of the un-coated substrate are visible

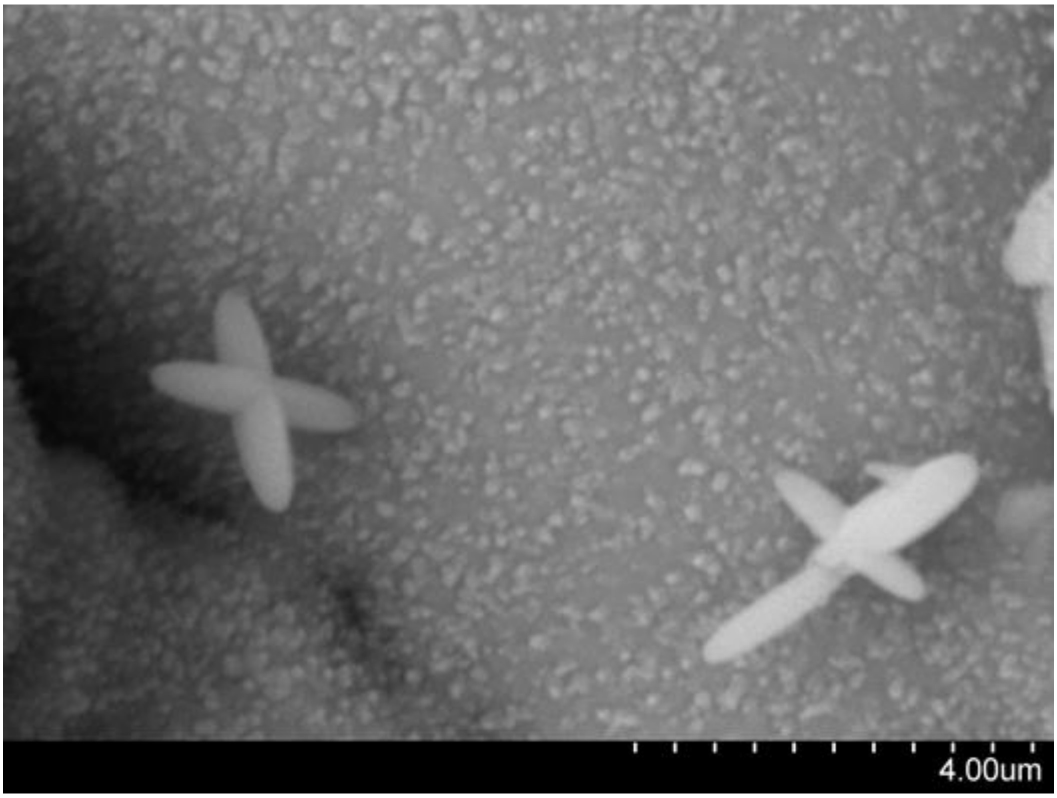

Figure 5.59 – Example of disordered precipitate found within the scaffold.

5.4.3. Summary

A coating of FA can be applied to a 3-D A/W scaffold; the crystallinity of the substrate dictates the morphology of the resultant FA crystals. Nano-scale FA crystals can be formed when the hydrothermal process is applied to a porous, interconnected structure. Scaffolds produced following heat treatments A and B showed significant coalescence and provide a relatively smooth surface. By coating a scaffold, its topography, chemistry and/or mechanical properties can be altered with respect to the original surface. For the first time an ordered, nanostructured bioactive coating has been applied to a 3D scaffold. For a trabecular bone scaffold, a coating process offers the potential for hierarchical topography, from the bulk (the scaffold) to the micro (the individual strut) to the nano (the coating). A nano-structured surface has a large surface energy compared to a smooth surface, which in turn can have a significant effect on surface-protein interactions. The introduction of a nano topography through a coating can influence bone ingrowth by providing attachment sites for proteins important during healing. FA coatings produced hydrothermally have been shown by Liu *et al* to support, even without an osteoinductive supplement, MG-63 and human adipose derived stem cells to differentiate and mineralize (187, 269). Liu *et al* looked at as number of adhesion and matrix-focused pathway genes, and up- or down- regulation of 15 genes such as integrin molecules; integrin alpha M and integrin alpha 7 and 8 was noted, suggesting a modulating effect on these adhesion molecules by the ordered FA surface.

5.5 In vitro studies

The aim of this section was to:

- Define a suitable cell seeding density for confocal microscopy
- Perform live/dead assays to ensure the scaffold can support hMSC's
- Investigate through SEM analysis (14 and 28 day time points) whether cells proliferated and the extent to which they had
    - With and without FA coatings

5.5.1. Seeding density validation

Initial confocal microscopy at the 18 h time point showed that seeding densities of $5x10^5$ and $1x10^6$ per scaffold were sufficient to illustrate cell attachment; densities lower than $5x10^5$ per scaffold were insufficient to allow for fluorescent detection. From these initial tests, it was clear that the scaffold could maintain good cell viability in the short term. At the 8-day time point cell spreading was observed as shown in Figure 5.60 and Figure 5.61; it was noted however that the vast majority of the dead marker was detected towards the surface of the scaffold that the cells were initially seeded onto (see Figure 5.62). Where the pores are clearly visible there were areas of the confocal, which appeared completely blank, this was due to blocked regions of the scaffold. It was concluded however that scaffolds sectioned into 800 µm thin discs would suffice for the subsequent long-term tests.

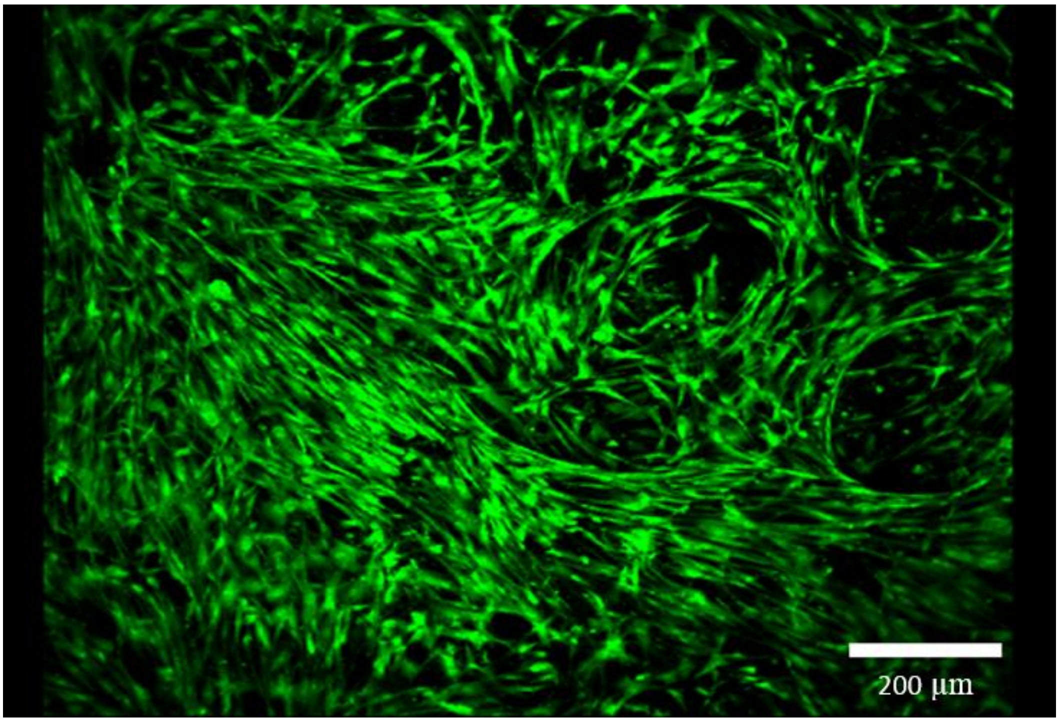

Figure 5.60 – Confocal microscopy image of hADSC's cultured for 8 days on A/W scaffold, seeding density 1 x10^6.

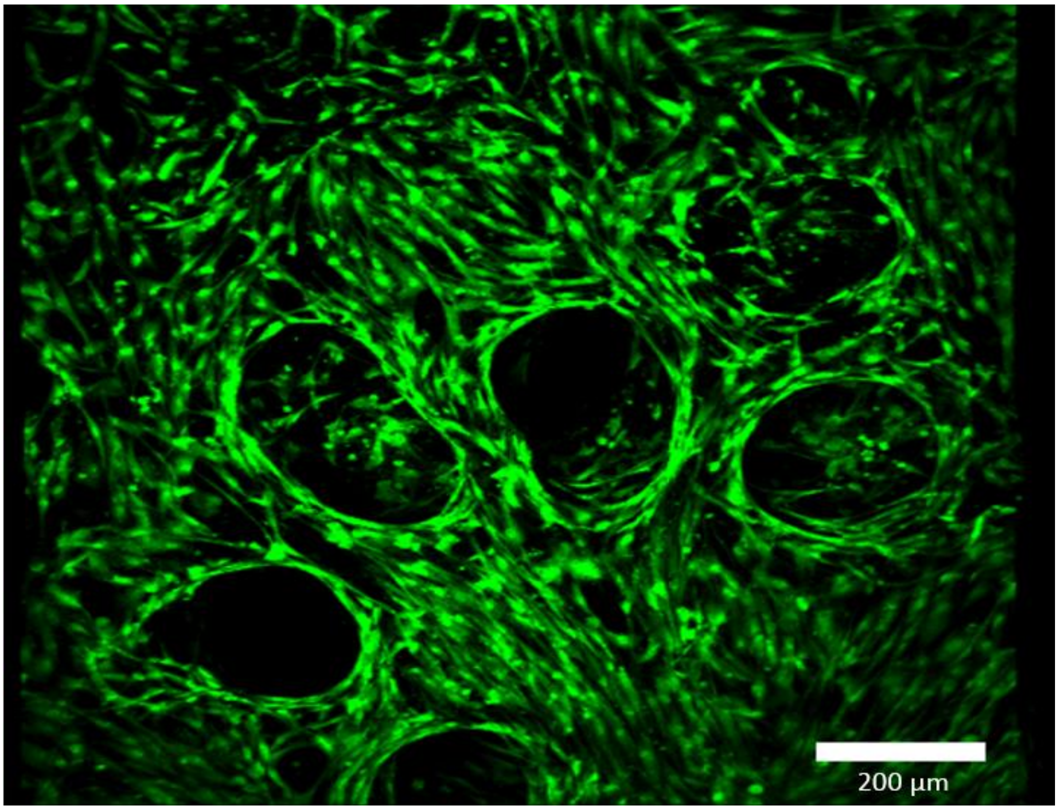

Figure 5.61 - Confocal microscopy image of hADSC's cultured for 8 days on A/W scaffold, seeding density 1x10^6

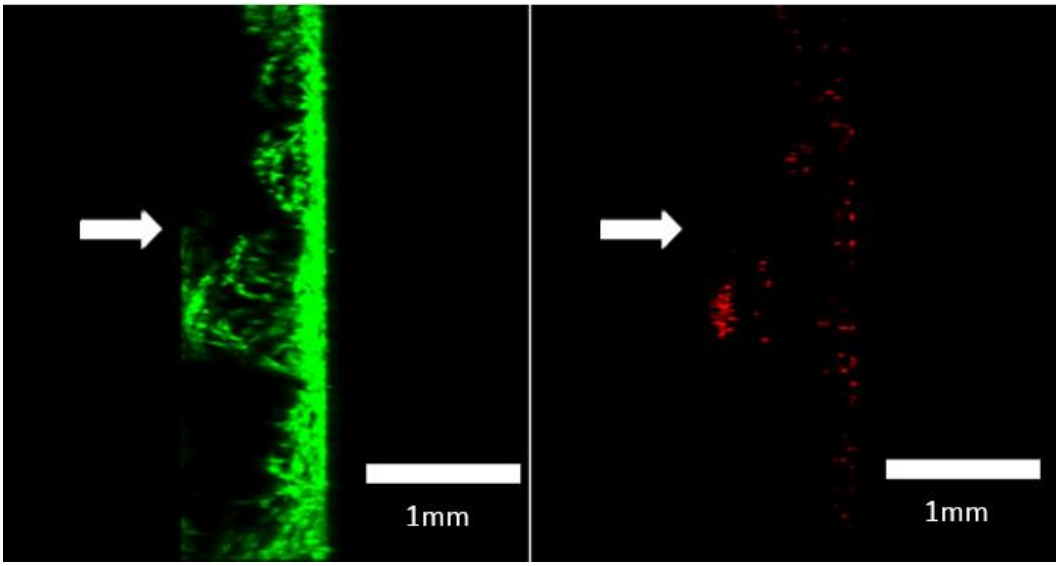

Figure 5.62 – Profile view of scaffolds cultured for 8 days at 1x106 seeding density. White arrows indicate the direction of the initial cell seeding.

5.5.2. 14 and 28 day culture

Seeding densities of $5x10^5$ and $1x10^6$ were carried forward for longer culturing periods; by day 14 the cells were well connected and beginning to form confluent sheets for both seeding densities. At day 28 for both seeding densities the architecture of the underlying scaffold was completely masked by the fluorescence of the confluent sheets that had formed, SEM observation of dehydrated scaffolds allowed for clearer observation. It can be seen in Figure 5.63 to Figure 5.66 that preparing the discs for cell seeding creates artificially large pores that are greater than 500 µm across; despite this the cells were observed to bridge these gaps and form confluent sheets several cell layers thick.

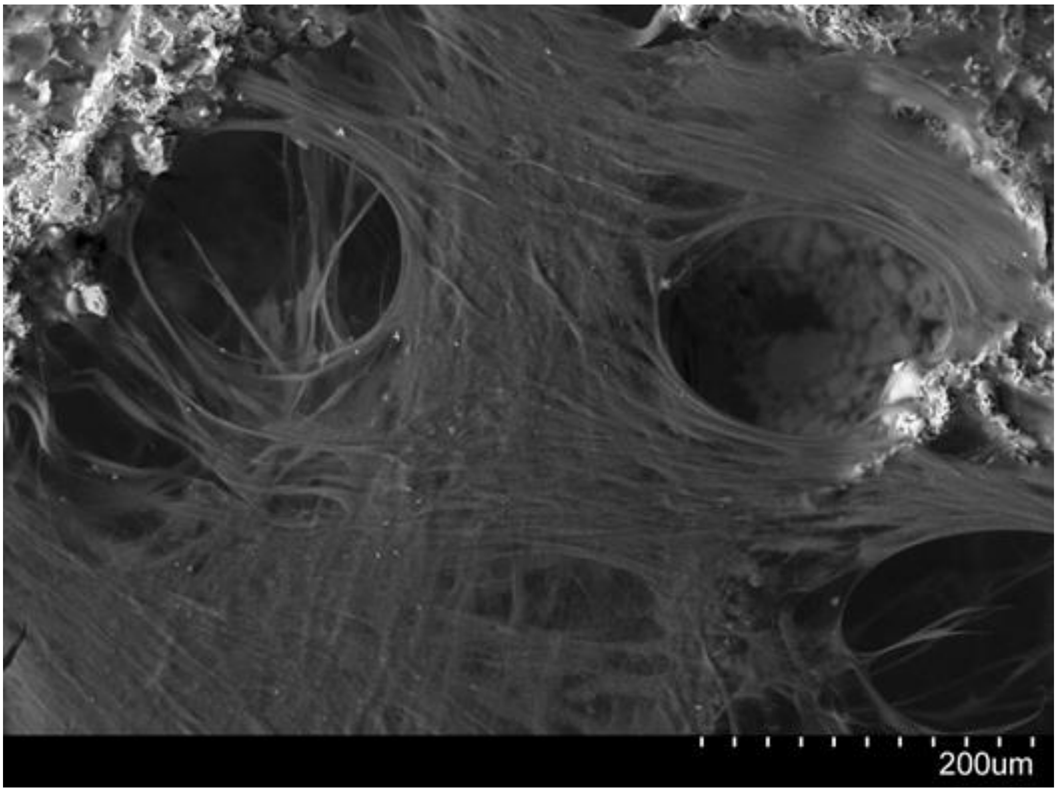

Figure 5.63 - Scaffold cultured for 28 days, seeding density 5x10^5.

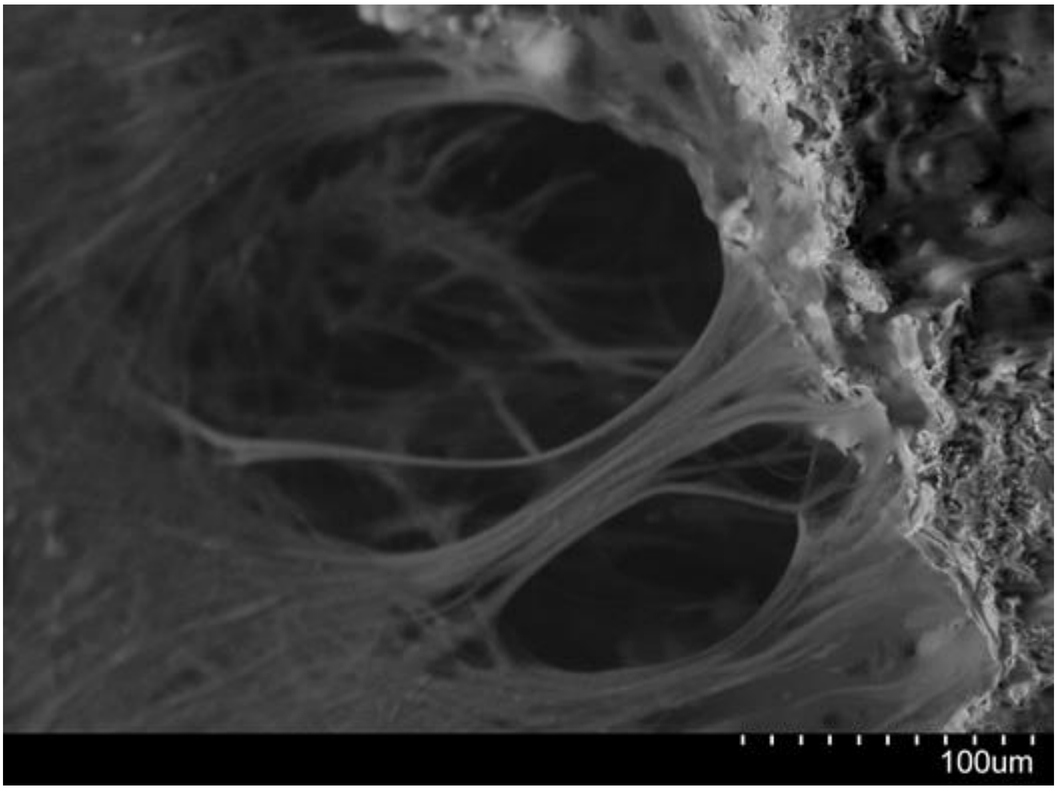

Figure 5.64 - Scaffold cultured for 28 days, seeding density 5x10^5.

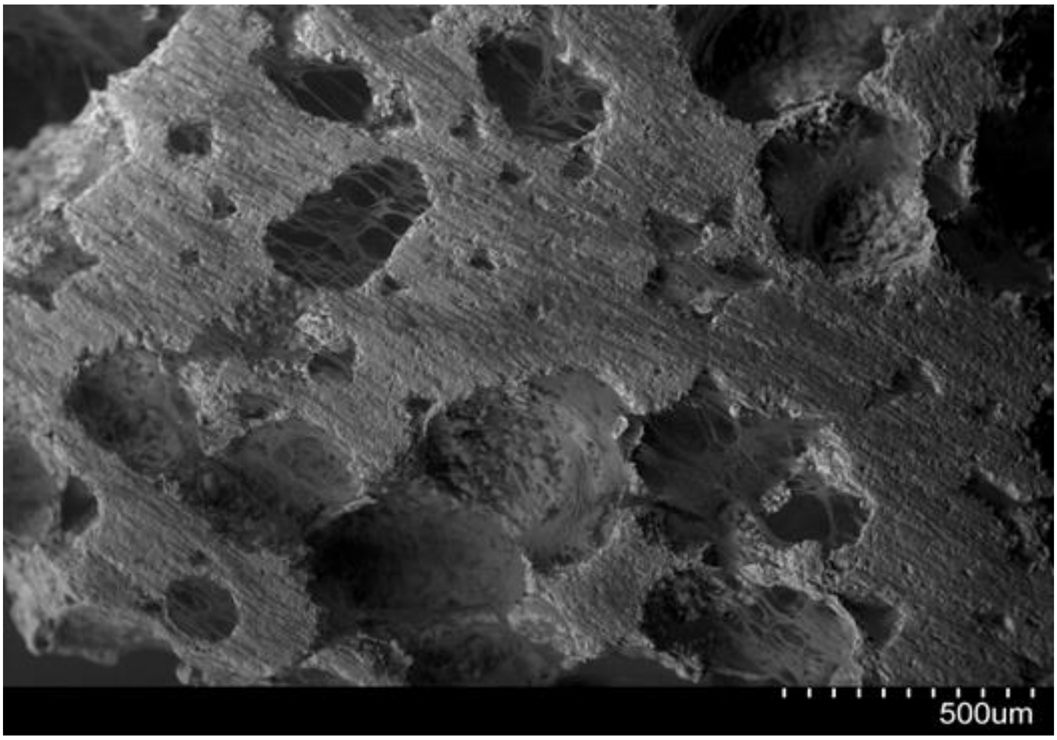

Figure 5.65 - Scaffold cultured for 28 days, seeding density 5x10^5. Cells observed to preferentially attach and proliferate around un-machined surfaces.

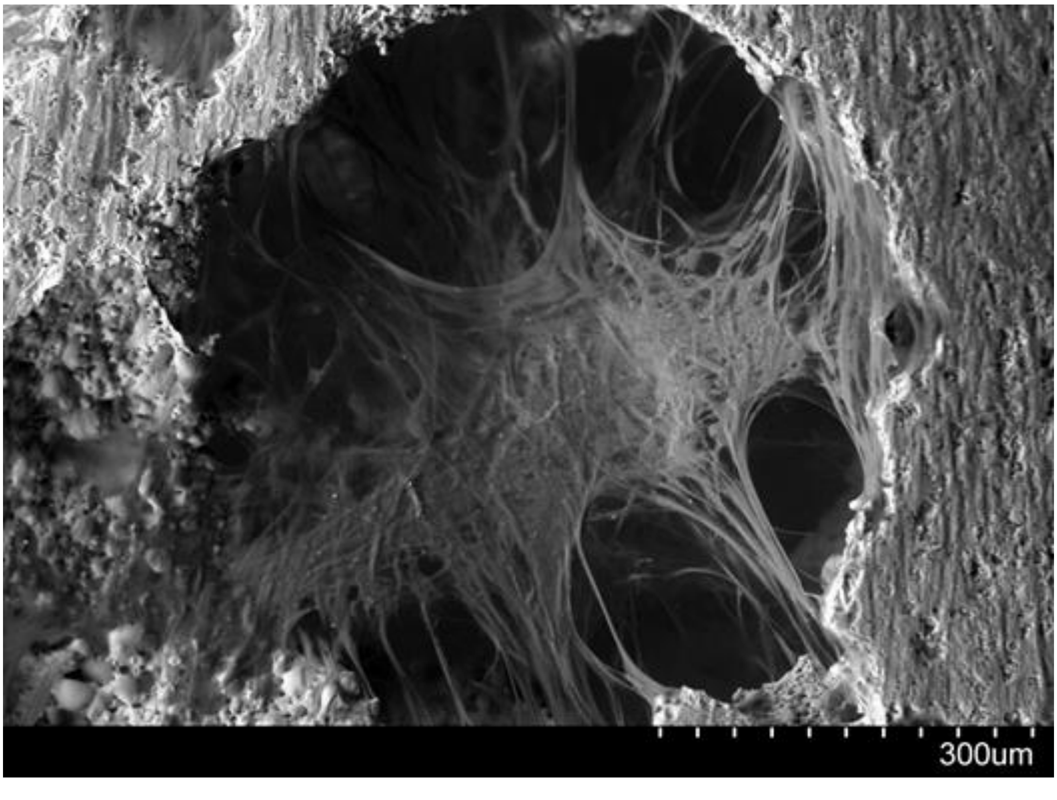

Figure 5.66 - Scaffold cultured for 28 days, seeding density 1x10^6.

The cells appear to preferentially attach and proliferate on the un-sectioned surface; as can be seen in Figure 5.65, this is worth noting with respect to future *in vivo* study. If the scaffold is to be machined prior to implantation the internal architecture would appear to immediately support cell attachment; however if the machined surfaces are impeding cell attachment this could be detrimental to the scaffolds stability and ultimately its potential success.

5.5.3. Short term FA culture

Scaffolds were prepared as described in section 4.4. Fluorapatite (FA) coatingand section 4.8.1. Scaffold and cellular preparation, $1x10^6$ hADSC's were seeded onto each scaffold through the concentrated cell suspension method and cultured for up to 8 days. As no evidence can be presented to prove sporal contamination did not adversely affect the results this section has been omitted from the final report. The SEM analysis for the 36 h time point is supplied in appendix 8.2.

5.5.4. Summary

Qualitative assessment of hADSC's cultured for up to 28 days showed basic biocompatibility of the scaffold; at seeding densities of $5x10^5$ and $1x10^6$ hADSC's attached, proliferated and formed confluent sheets.

5.6. General Discussion

Designing a synthetic replacement material for the application of treating critical bone defects requires control over specific characteristics; with respect to trabecular bone defects the primary needs of the scaffold are architecture and strength. Considering the potential application the process of secondary bone healing must be aided; during this process, the initial mechanical environment must be stable to ensure integration, not encapsulation, is achieved. The architecture must be such to support sufficient fluid flow and internal marrow pressures to illicit the appropriate cell signalling, nutrient transfer and subsequent long term remodelling processes. The aim of this work was to investigate whether these primary scaffold functions could be achieved with the use of A/W and the foam replica technique. Some aspects of these functions have been achieved through this initial study; scaffolds were shown to be composed of pores within the recommended range, struts were of appropriate dimensions, strengths ranged within acceptable limits and cells were shown to attach and proliferate *in vitro* to a promising degree. In addition to this, some aspects of specific optimisation for the treatment of bone defects have been shown. Fluorapatite can be coated on various scaffold types in all three spacial directions; this coating layer has been shown to be osteoinductive in previous work, however (to the authors knowledge) the application of this technique with a 3-D glass-ceramic scaffold has not yet been investigated. Some aspects were not achieved; the major of which is the overall porosity and coating consistency, other aspects of the scaffold production will be discussed within this section. These aspects are either difficult to characterise, basic observations or require a specific study to focus on them.

5.6.1. Architecture vs Strength

It is a common comparison to make that is found prevalently in the literature; architecture vs strength, or more specifically porosity vs mechanical failure. The general trends are in agreement with previous studies (270); with increasing porosity the mechanical strength decreases, less material to support the load results in a lower failure load. Figure 5.67 shows the change in biaxial flexural strength with increasing porosity; however, the resultant strength of the scaffold is also dependent upon the amount of PVA used and the applied heat treatment. Comparing scaffolds produced using a 4:3 ratio of binder solution to glass the mechanical strengths differ drastically, however their porosities differ by only ~4%.

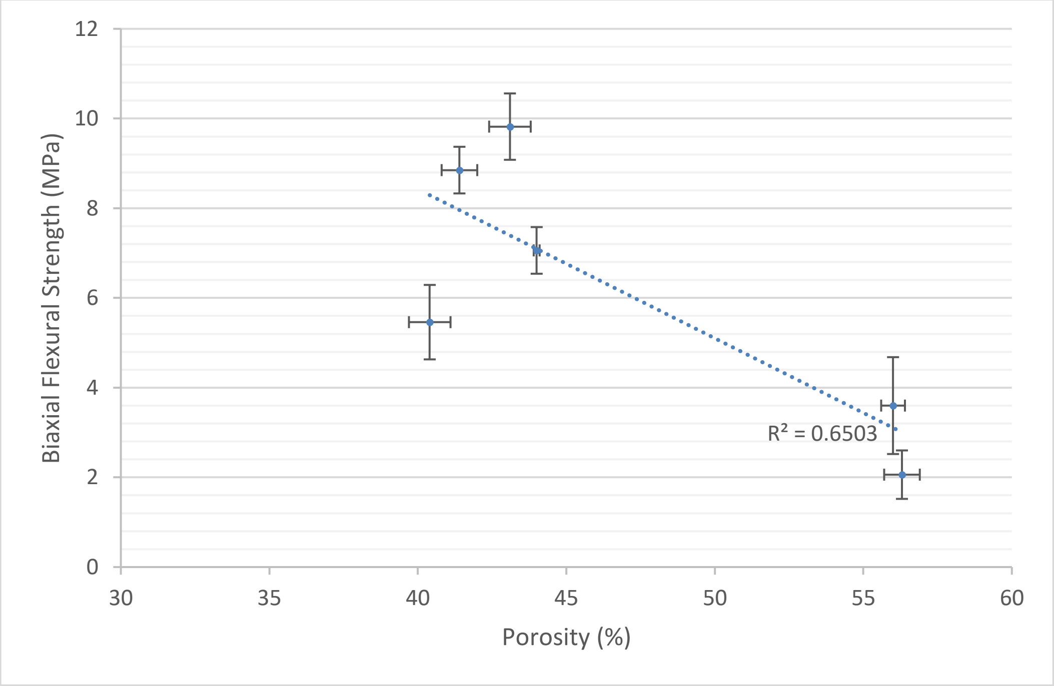

Figure 5.67 – Biaxial flexural strength vs porosity

Applying a heat treatment with a tertiary dwell temperature (950 °C, i.e. heat treatment B) increases the mechanical strength. Considering scaffolds 443A and 443B (the only difference being the applied heat treatment) the biaxial flexural strengths differed by 1.79 MPa and their porosities differed by 2.6 %. This confirmed that heat treatment B improved upon the mechanical strength by producing both apatite and wollastonite crystal phases. When comparing scaffolds 443B, 543B and 643B (the only difference being the amount of PVA used in the slurry) the resultant mechanical strengths differ to a much greater degree with little difference in porosities. The mechanical strengths differed by 4.36 MPa (543B = 9.82 MPa, 643B = 5.46 MPa) and the porosities differed by 2.7 % (543B = 43.1 %, 643B = 40.4%), further comparison are given in Table 5.11.

Table 5.11: Comparison of change in porosity and biaxial flexural strengths

Δ Porosity (%)	Δ Biaxial Flex Strength (MPa)	Scaffolds compared
15.61	1.86	643B and 521B
12.85	6.22	543B and 521B
2.76	4.36	543B and 643B
0.85	2.76	543A and 543B

This may imply that if future work focused on increasing the porosity of the scaffold (and producing a uniform coating of the PU foam) it may not necessarily result in a drastically weaker scaffold.

Both compressive and flexural tests are affected by porosity. In 1953, Ryshkewitch (271) first suggested the following equation to describe the porosity dependence of the strength, σ,

$$\sigma = \sigma_0 \exp^{(-nP)}$$

where σ_0 is the strength for nonporous body, P is the volume fraction porosity and n is a unitless, material-dependent constant. This has been refined over the last sixty years with a recent model being described by Fan *et al* (268) as:

$$\sigma/\sigma_0 = A[1\text{-}P/Pg]^n = A\phi$$

where σ is fracture strength of the porous ceramic, σ_0 is fracture strength of the theoretically dense ceramic, A and n are dimensionless constants. The degree of densification, ϕ, is defined as (1-P/Pg), where Pg is the porosity at green porosity.

Similarly, for young’s modulus the relationship between modulus and porosity can be described as

$$E/E_0 = A[1\text{-}P/Pg]^n = A\phi$$

Where e is the Young’s modulus of the porous ceramic and E_0 is the modulus of the theoretically dense ceramic

Liu (1997) produced porous hydroxyapatite ceramics with porosities varying between 33 % to 78 % using polyvinyl butyral (PVB) as a pore forming agent (272). Uniaxial compressive strength was investigated as a function of pore size and porosity and the results were found to follow existing models linking strength to porosity (273). Without error bars and a small sample size it is difficult to interpret the data but it looks like for ~50 % porosity, the compressive strength was

~20 MPa. Until high levels of porosity, specimens with smaller (but still macro-) pores exhibited higher strengths for a given porosity than specimens with larger macro-pores. Le Huec *et al* similarly varied porosity (20-60 %) and pore size (5 to 400 µm) in hydroxyapatite ceramics and tested compressive strength (274), it was found that not only pore volume but also pore size influenced compressive strength.

Latella *et al* used biaxial flexure (piston and three ball support as in this study) to investigate the flexural strength of porous (43-71 %, pore size 6-22 µm) mullite-alumina ceramics (275). They found that the data followed a typical exponential type relationship consistent with previous work by the group and with other ceramics. Kwan *et al* (276) measured biaxial flexural strength of a range of alumina ceramics with different final porosities (range 10-44 %) using two concentric rings of ball bearings. For comparison, they also produced 4-point bend specimens. Results demonstrated that both a power law model and exponential model could adequately describe the relationship between the porosity and strength (as for other ceramics). Strength values were dependant on test set up with the beams having a higher strength than the discs. The authors attributed the lower values to the bi-directional stresses in the loading system, compared to uniaxial stresses for the bending test.

Peng *et al* (277) found no differences in biaxial (piston on three ball as in this study) and 3-point bending flexural strength of lightly porous fluorapatite glass ceramics with applications as a veneer material in dentistry. They noted as did Kwan (276) that an assumption might be that for highly porous ceramics, strength could become dependent on the cross sectional area of solid material rather than the weakest flaw, i.e. the Griffith flaw model of ceramic strength could break down at high porosity. Lopes *et al* (278) measured ring on ring biaxial flexural strength of glass reinforced

HA and found that flexural strength depended more on porosity and the presence of secondary phases rather than on grain size. The effect of porosity on strength followed the classical exponential model proposed by Ryshkewitch.

5.6.2. Comparison to values within the literature

Three-point/four-point bend tests and biaxial flexural testing data can be compared (279); the study by Jin *et al* (2004) showed that, depending on the test method used, the resultant mechanical properties would differ yet still be reliable. In general, it was found that: "3-point bending strength > biaxial flexural strength > 4-point bending strength". This should be taken into account when comparing the values of other scaffolds reported in the literature. The "optimised" scaffolds developed though this study are that of 443B and 543B, the properties of these scaffolds (see Table 5.12) are compared to other scaffolds reported in the literature.

Table 5.12: Optimised scaffold properties

Scaffold	Porosity (%)	Biaxial flexural strength (MPa)	Uniaxial compressive strength (MPa)
443B	41.4 (± 0.6)	8.85 (± 1.23)	3.61 (± 0.42)
543B	43.1 (± 0.7)	9.82 (± 1.47)	3.31 (± 0.73)

The study conducted by Tomita and Kawasaki (200) reported flexural strengths of 2.4 MPa with porosities ranging from 66 to 68 % (see table 2.5). Where the flexural strengths of these scaffolds are lower than that of the optimised scaffolds presented in this study this could be account for by the higher porosities. The scaffolds in this study were however produced via the sol-gel technique, rather than the foam replica technique. The study by Chen *et al* (as previously discussed) produced scaffolds via the foam replica technique and achieved much higher porosities than reported for the optimised scaffolds (225). The reported porosities ranged from 89 to 92 %; additionally the pore sizes were much larger, ranging from 510 to 720 µm. This may account for the low flexural strengths which ranged from 0.4 to 0.5 MPa, the use of 45S5 Bioglass® may also account for these low values.

The vast majority of mechanical characterisation presented within the literature uses uniaxial compression; these values are summarised in Table 5.13 for clarity. As stated in section 5.3.3.6. the uniaxial compressive strengths of the scaffolds tested ranged from 2.32 (± 0.47) to 3.61 (± 0.42) MPa. These values are within the recommended ranges for trabecular bone (2-12 MPa); additionally the compressive strengths of the scaffolds tested are comparable to values reported within the literature. In general, compressive strengths reported for scaffolds produced using the sol-gel method are lower (0.36 – 2.26 MPa), however this again can be explained through their higher porosities. When compared to freeze casting the compressive strengths reported are often much higher, however this can be explained through the use of materials known to exhibit high mechanical strengths, î.e. alumina.

The key comparison to make is with scaffolds produced through the foam replica technique, specifically the work conducted by Vitale-Brovarone *et al* (231-233, 235). The porosities reported in these studies are higher than those of the optimised scaffolds (443B and 543B), the lowest porosities reported were 53.5 (± 3.7) and 54.8 (± 4.5), which are roughly 10 % higher than both 443B and 543B scaffolds. However the compressive strengths of the optimised scaffolds (443B and 543B) are well within the ranges reported, 0.4 (± 0.2) to 5.4 (± 1.5). This implies that increasing the porosity, with an expected decrease in compressive strength, would still be feasible for future studies.

Table 5.13: Uniaxial compressive values for various scaffolds reported

Method	Glass powder	Pore Sizes (µm)	Porosity (%)	Strength (MPa)	Year	Author	Ref
Organic filler	SNCM	20 -100	40	6	2005	Vitale-Brovarone *et al*	(197)
Sol-gel	70S30C	87 - 122	82-88	0.36 – 2.26	2006	Jones *et al*	(203)
	45S5	200 - 1000	>90	~ 0.5 – 2	2011	Chen and Thouas	(206)
Freeze casting	Alumina (AKP 30)	102 - 210	59 - 82	11 - 95	2008	Yoon *et al*	(211)
	CaP	121 (± 33) – 163 (± 47)	62 - 65	Normally – 4.6 (± 1); Parallel – 9.3 (± 1.6)	2009	Soon *et al*	(208)
	HA	277 (± 47) - 141 (±11)	71-73	1.1 (± 0.2) - 2.3 (± 0.5);	2009	Yook *et al*	(212)
	Baghdadite powder	/	58.2 – 64.3	1.3 - 2.1	2014	Sadeghpour *et al*	(214)
Foam replica	45S5	510 - 720	89 - 92	0.27-0.42	2006	Chen *et al*	(225)
	CEL2	100 - 600	~ 70	1 (± 0.4)	2007	Vitale - Brovarone *et al*	(231)
	HA and A/W	300 - 800	~ 93	~1 MPa	2007	Jun *et al*	(228)
	Fa-GC	0-50: 53 %, 50 – 600: 47 %	74.6 (+/- 3.4)	2 (± 0.6)	2008	Vitale - Brovarone *et al*	(232)
	13-93	~ 100 - 500	85 (± 2)	11 (±1)	2008	Fu *et al*	(234)
	CEL2	0 - 100: 84 %, 100 - 1000: 16 %	53.5 (± 3.7) – 72.3 (± 3.3)	1.3 (± 0.4) - 5.4 (± 1.5)	2009	Vitale - Brovarone *et al*	(235)
	CEL and ICEL2	100 - 500	54.8 (± 4.5) and 82.0 (± 6.7)	5.2 (± 2.0) and 0.4 (± 0.2)	2009	Vitale - Brovarone *et al*	(233)
	0160	105 – 510	68 (optimised scaffold)	0.40 (±0.05) - 0.60 (±0.08)	2009	Mantsos *et al*	(236)
	13-93, 1393B1, 13-93B3	100 - 500	78 (± 2) to 82 (± 3.0)	5 (± 0.5) to 11 (± 1)	2010	Fu *et al*	(238)
	13-93B1	400 - 650	78 (±8)	5.1 (±1.7)	2014	Gu *et al*	(240)

5.6.2. Burn out artefacts

It was repeatedly observed (regardless of the heat treatment applied or slurry constituents used) that artefacts would remain from the burn out process, as illustrated in Figure 5.68 and Figure 5.69. Considering the fracture mechanisms associated with brittle materials, it is fair to assume that crack propagation would begin at these sites. Whether the accumulation of these artefacts was higher for lower glass content scaffolds (i.e. scaffolds produced using a 2:1 or 20:13 slurry) is not known at this time, these artefacts may explain the “multiple failure” profiles associated with these scaffold types. It was found overall that a reduction in the amount of glass present (through slurry constituents or compression during the coating process) resulted in necking reduction and lower mechanical strengths. A sufficient amount of glass must surround each foam template strut, to not only sinter, but also allow the glass to seal up the voids left after the burn out process.

Previous work has shown that an additional coating of PDLLA can fill in the micropores associated with sintering glass-ceramics and improve the mechanical properties (280); the aim of such a coating is to produce a composite material, similar to that of the organic and inorganic phases present in the natural tissue (236). Such work has shown limited success however, the polymer is shown to begin degradation after only 1 day of submersion in SBF. However, in the short term such a coating could be used to improve the initial mechanical stability of the scaffold.

Zhang *et al* (2012) have produced hydroxyapatite scaffolds through a double slip casting method combined with a foam template and claim that these materials have a flexural strength of 75 MPa and a porosity of 52 %, similar to the materials in the current thesis. Like in this study, the authors found that a high ceramic concentration in the slurry was required for better density and mechanical properties in the sintered products. They noted that too high a slurry viscosity could result in poor foam infiltration and refined their slurries accordingly with the addition of a suitable deflocculant and foaming agent. The second dip coating was analogous in one way to the approach taken with the FA coating in the current study in that it was designed to strengthen the connection between the pore walls and repair any defects.

Martinez-Vazquez *et al* (2014) used polymer infiltration in a similar manner for β –TCP ceramic scaffold and claimed that an improved flexural strength was obtained when using a PCL infiltrate. They argued that unhealed defects (as seen in this study due to the burn out process and as a consequence of sintering) of the rods/struts facilitated crack propagation and effectively reduced the overall strength of the scaffold. Healing these defects through infiltration resulted in a significant increase in bending strength. The authors also commented that bending tests provided a much better means than compression to analyse toughening mechanisms on impregnated scaffolds.

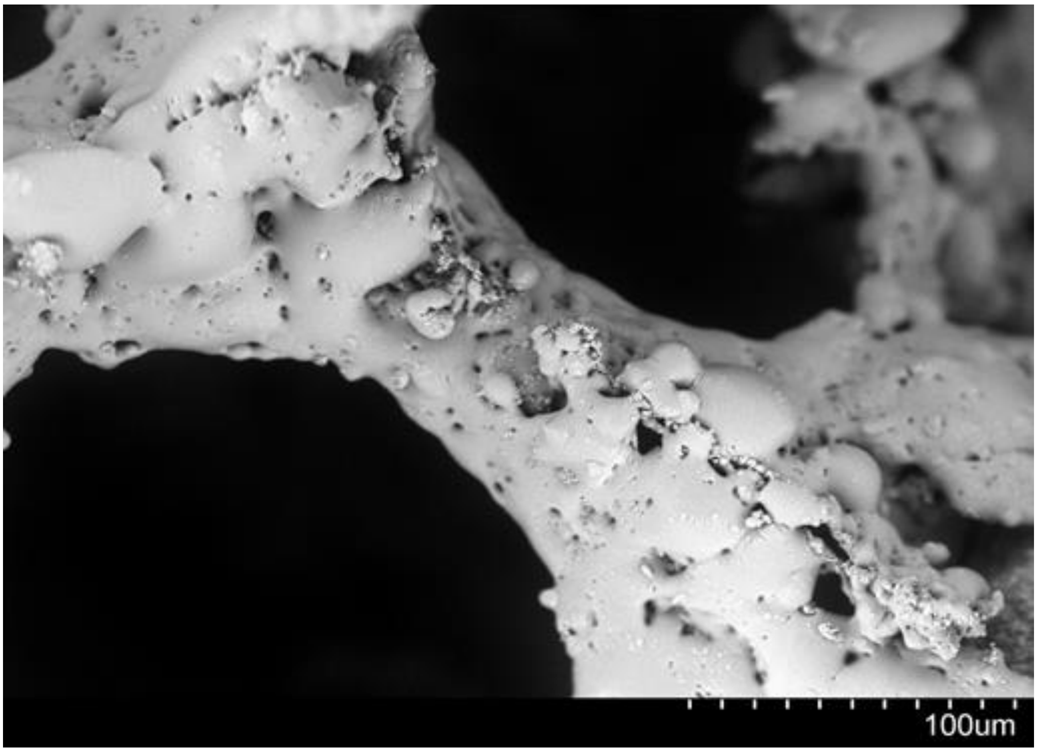

Figure 5.68 – Burn out artefact along the length of a strut, scaffold produced through heat treatment A.

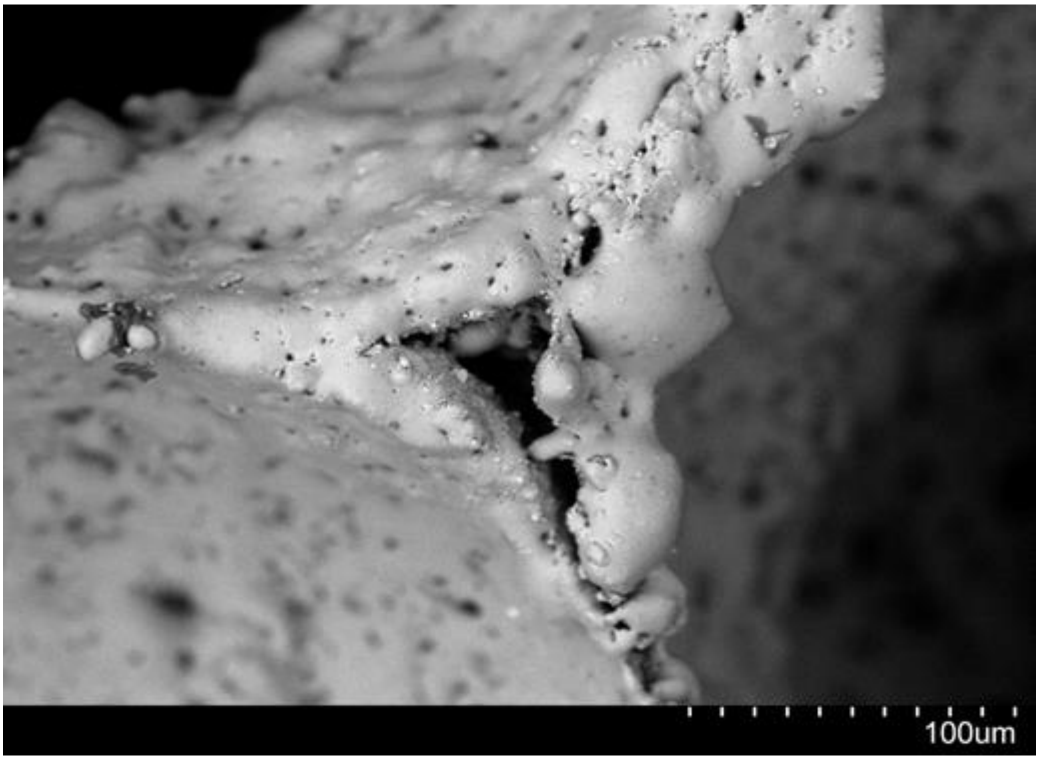

Figure 5.69 – Burn out artefact through the centre of a strut, scaffold produced through heat treatment A.

It was observed during *in vitro* testing however that within these artefacts cells migrated, attached and proliferated within a short time frame as shown in Figure 5.70. Previous work has shown the benefits of coating polyurethane grafts with a mixed solution containing cytokines, primarily VEGF (281). If these artefacts cannot be removed from the scaffold production process, they could be utilised as growth factor carrier sites.

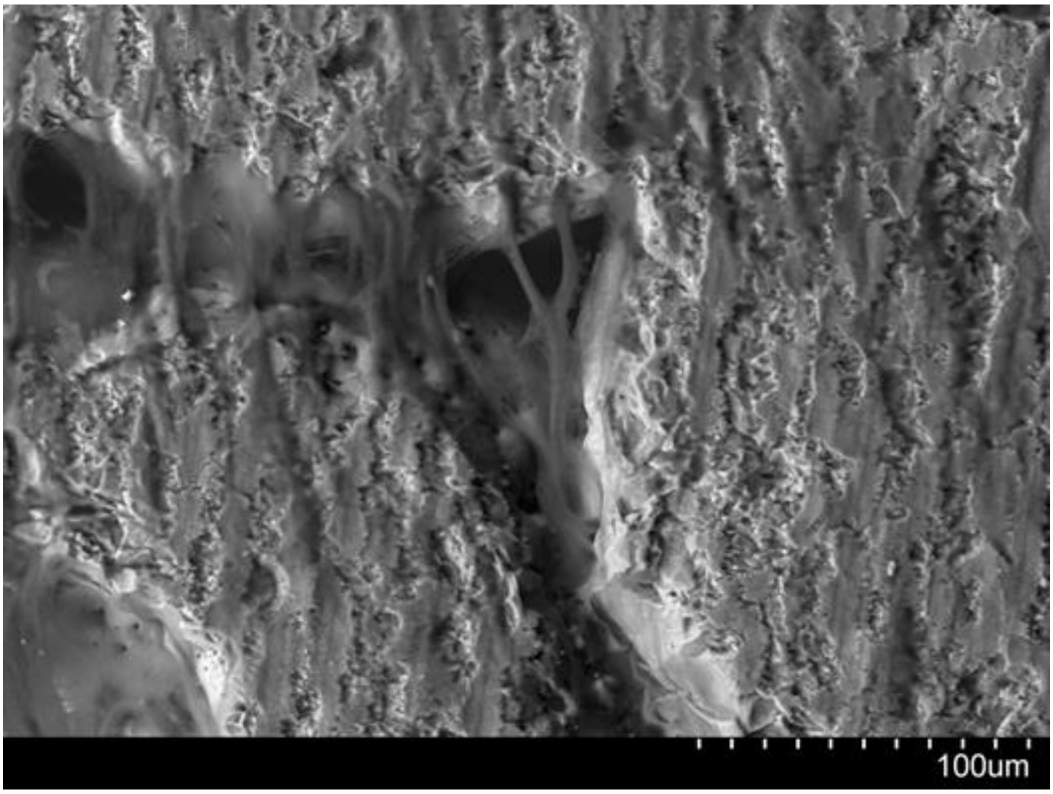

Figure 5.70 – hADSC's bridging a burn out artefact gap, 8 day culture time point.

5.6.3. FA sonication

Removal of the disordered precipitate after the hydrothermal process has been applied to a substrate is desirable; previous work has reported the ordered FA layer results in an 80 % increase in substrate integration *in vivo*, compared to 40 % due to disordered precipitate. Sectioned discs were sonicated under 15 min cycles for a maximum of 4 cycles; even then the removal of the disordered precipitate was almost random. Some cases showed complete removal; others showed damage to the underlying ordered layer, implying that 1 h of sonication can begin to remove the ordered FA coating. It is worth noting that the sonication process can actually be applied when the substrate is A/W; sonicating stainless steel etched discs for example, almost entirely removes the FA coated layer, implying that the interface with the A/W substrate is stronger.

However; when considering the full sized scaffold (see section 5.4.2) there was almost no disordered precipitate visible within, simply sectioning of the outer surfaces removed the bulk of the precipitate. Therefore, it is suggested that applying the hydrothermal process to a 3-D, interconnected structure would not only optimise the substrate for osteointegration, but additionally it would alleviate the need to develop a method to remove the disordered precipitate whilst retaining the ordered.

5.7. Future Work

As stated previously several variables were discounted for characterisation; considering the slurry, the viscosity was not characterised during this study, only the wt % of glass and PVA. Comparisons could be drawn between the architecture and specifically the apparent density of the scaffold produced from slurries of specific viscosities. This would allow for further optimisation of the coating regime in conjunction with optimising the sacrificial template. Foams ranged from 45 PPI – 90 PPI; it was found that below 75 PPI an insufficient amount of glass coated the struts, at 90 PPI good strut morphology was achieved but large areas of the scaffold remained blocked. Considering the low cost of the starting materials it would be reasonable to introduce 3-D printing to construct a sacrificial template of a specific pore size distribution. It is suggested that if the slurry viscosity and sacrificial template were specifically characterised the overall porosity of the resultant scaffolds could approach that of physiological values, whilst retaining sufficient coating of individual struts.

Mechanical testing during this project focused on loading until failure, where this allows for characterisation of the upper limits of the scaffold it does not predict stability of the scaffold with respect to time. Cyclic loading of the scaffold could give insight into the potential success of the scaffold when subjected to repeat loading, which is more comparable to the *in vivo* scenario (282, 283). It is predicted that scaffolds composed of a broader pore size distribution, an SMI value approaching that of a rod-like model or lower crystallinity would fail at lower cycles. Such testing could also be applied to scaffolds seeded with cells; comparison could be drawn between static and mechanically stimulated *in vitro* culturing to estimate the potential increase in remodelling rates.

From the micro-CT scans an FE model could be developed by converting to DICOM or .STL format; from this through the use of software such as ScanIP, an FE model could be generated to study the stress distributions throughout the scaffold (284, 285). Mechanotransduction is a relatively new field; where it is generally agreed upon that mechanical forces govern numerous cell signalling processes, it is difficult to estimate whether the mechanical environment invokes changes to the chemical environment or if the chemical environment governs the remodelling processes (286). It is possible they are both one in the same; creating a positive feedback loop in healthy bone healing processes or a negative cascade leading to osteoporosis. If a computational model could simulate physiological loading to scaffolds of varying characteristics (i.e. varying porosity) the internal stress concentrations could be characterised and compared to remodelling rates of such scaffolds from ex-vivo samples.

Analysis of glass-ceramic scaffolds coated with FA has only been qualitative up to this point; where it was shown through SEM analysis that the substrate crystallinity and 3-D architecture affected the resultant crystal morphologies, quantitative assessment is still required. In combination with Reitveld refinement both the substrate crystallinity and resultant FA coating could be assessed, allowing for further scaffold optimisation; not only with respect to mechanical properties, but additionally the scaffolds potential to support an ordered FA layer. Quantifying the differentiation potential of differing FA coatings could be achieved through the use of a recently developed reporter gene assay (287); comparisons could be drawn to scaffolds cultured with or without osteoinduction, and with or without FA coating, similar to previous studies undertaken with etched stainless steel discs (187).

6. Conclusions

This work investigated the production and characterisation of porous apatite-wollastonite glass ceramic scaffolds. The primary focus was upon developing a methodology that resulted in reproducible scaffolds that would allow for characterisation and ultimately conclusions to be drawn for future optimisation. Further assessment was carried out to estimate the biocompatibility of the scaffold and its potential to be optimised for bone healing. The following section summarises the findings of this work:

- A/W can be used in conjunction with the foam replica technique to consistently produce porous glass-ceramic scaffolds.

- Slurries consisting of a 4:3 ratio of binder solution to glass produce the most consistent scaffold type, mechanically and architecturally.

- Excessive use of a binder within the slurry (i.e. > 5 wt % PVA) has a detrimental effect upon the resultant scaffold properties

- A controlled burn out phase was defined as heating at 4K/min to 400 °C followed by a 1h dwell at this temperature.

- Sintering of the sub 45 µm A/W particles requires a 5h dwell at 800 °C.

- Application of a tertiary dwell step at 950 °C for 1 h results in a crystallised scaffold composed of both apatite and wollastonite phases.

- Application of a tertiary dwell step at temperature higher than 950 °C is detrimental to the resultant scaffold properties.

- Porosities of scaffolds ranged from 40 % - 56 %, with increasing porosity the mechanical stability diminished.

- Scaffolds produced from slurries with less than 20:13 glass to binder ratio exhibited multiple failure regions, implying they were less mechanically stable.

- The Weibull modulus decreases with respect to glass content within the slurry

- A fluorapatite layer could be formed on a heat treated A/W substrate in all 3-D spatial directions

- The crystallinity of the substrate dictates the FA crystal morphology.

- Application of the hydrothermal process to an interconnected structure vastly decreases the resultant FA crystals, both in size and number.

- Porous A/W scaffolds supported human adipose derived stem cells up to 28 days at seeding densities of $5x10^5$ and $1x10^6$.

In conclusion, porous A/W glass-ceramic scaffolds were produced using the foam replica technique. The scaffolds were shown to exhibit properties within physiological limits; an ordered fluorapatite layer can be applied to further optimise the scaffold for bone healing, and the scaffold was shown to support human adipose derived stem cells. Several production aspects remain to be investigated; however, this study has shown the potential of this technique to provide a treatment for bone defect repair.

7. References

1. Affatato, S. 1 - The history of total hip arthroplasty (THA). In: Affatato, S. ed. *Perspectives in Total Hip Arthroplasty*. Woodhead Publishing, 2014, pp.3-18.
2. Affatato, S. 6 - Recent developments and future trends in total hip arthroplasty (THA). In: Affatato, S. ed. *Perspectives in Total Hip Arthroplasty*. Woodhead Publishing, 2014, pp.76-95.
3. Mann, K.A., Miller, M.A., Costa, P.A., Race, A. and Izant, T.H. Interface Micromotion of Uncemented Femoral Components from Postmortem Retrieved Total Hip Replacements. *The Journal of Arthroplasty.* 2012, **27**(2), pp.238-245.e231.
4. Holzapfel, B.M., Reichert, J.C., Schantz, J.T., Gbureck, U., Rackwitz, L., Noth, U., Jakob, F., Rudert, M., Groll, J. and Hutmacher, D.W. How smart do biomaterials need to be? A translational science and clinical point of view. *Advanced Drug Delivery Reviews.* 2013, **65**(4), pp.581-603.
5. Zaulyanov, L. and Kirsner, R.S. A review of a bi-layered living cell treatment (Apligraf (®)) in the treatment of venous leg ulcers and diabetic foot ulcers. *Clinical Interventions in Aging.* 2007, **2**(1), pp.93-98.
6. Dimitriou, R., Mataliotakis, G.I., Angoules, A.G., Kanakaris, N.K. and Giannoudis, P.V. Complications following autologous bone graft harvesting from the iliac crest and using the RIA: a systematic review. *Injury.* 2011, **42 (Supplement 2)**, pp.S3-15.
7. Jones, J.R. Reprint of: Review of bioactive glass: From Hench to hybrids. *Acta Biomaterialia.* 2015, **23 (Supplement)**, pp.S53-82.
8. Charalambous, C.P. Calcium Phosphate Ceramics as Hard Tissue Prosthetics. In: Banaszkiewicz, A.P. and Kader, F.D. eds. *Classic Papers in Orthopaedics*. London: Springer London, 2014, pp.419-421.
9. Dias, A.G., Gibson, I.R., Santos, J.D. and Lopes, M.A. Physicochemical degradation studies of calcium phosphate glass ceramic in the CaO-P2O5-MgO-TiO2 system. *Acta Biomaterialia.* 2007, **3**(2), pp.263-269.

10. Navarro, M., Michiardi, A., Castaño, O. and Planell, J.A. Biomaterials in orthopaedics. *Journal of the Royal Society Interface.* 2008, **5**(27), pp.1137-1158.

11. Vaverka, M. and Hrabalek, L. Anterior cervical dissectomy with intervertebral bioactive glass-ceramic prostheses replacement. *International Congress Series.* 2002, **1247**, pp.587-589.

12. Dubok, V.A. Bioceramics — Yesterday, Today, Tomorrow. *Powder Metallurgy and Metal Ceramics.* 2000, **39**(7), pp.381-394.

13. Hench, L.L. and Jones, J.R. Bioactive Glasses: Frontiers and Challenges. *Frontiers in Bioengineering and Biotechnology.* 2015, **3**, p.194.

14. Cao, W. and Hench, L.L. Bioactive materials. *Ceramics International.* 1996, **22**(6), pp.493-507.

15. Ohtsuki, C., Kushitani, H., Kokubo, T., Kotani, S. and Yamamuro, T. Apatite formation on the surface of Ceravital-type glass-ceramic in the body. *Journal of Biomedical Materials Research. Part A.* 1991, **25**(11), pp.1363-1370.

16. Kokubo, T., Shigematsu, M., Nagashima, Y., Tashiro, M., Nakamura, T., Yamamuro, T. and Higashi, S. Apatite- and Wollastonite-Containg Glass-Ceramics for Prosthetic Application. *Bulletin of the Institute for Chemical Research, Kyoto University.* 1982, **60**(3-4), pp.260-268.

17. Kokubo, T., Ito, S. and Sakka, S. Formation of a high-strength bioactive glass-ceramic in the system MgO-CaO-SiO2-P205. *Journal of Materials Science.* 1986, **21**, pp.536-540.

18. Kokubo, T. Bioactive glass ceramics: properties and application. *Biomaterials.* 1991, **12**, pp.155-163.

19. Kokubo, T. Surface chemisty of bioactive glass-ceramics. *Journal of Non-Crystalline Solids.* 1990, **120**(1), pp.138-151.

20. Ono, K., Yamamuro, T., Nakamura, T., Kakutani, Y., Kitsugi, T., Hyakuna, K., Kokubo, T., Oka, M. and Kotoura, Y. Apatite-wollastonite containing glass ceramic-fibrin mixture as a bone defect filler. *Journal of Biomedical Materials Research. Part A.* 1988, **22**(10), pp.869-885.

21. Wolff, J.D. *Das gesetz der transformation der knochen*. Berlin: Verlag von August Hirschwald. 1892.

22. Cowin, S.C. Wolff's Law of Trabecular Architecture at Remodeling Equilibrium. *Journal of Biomechanical Engineering.* 1986, **108**(1), pp.83-88.
23. Rice, J.C., Cowin, S.C. and Bowman, J.A. On the dependence of the elasticity and strength of cancellous bone on apparent density. *Journal of Biomechanics.* 1988, **21**(2), pp.155-168.
24. Hernandez, C.J., Hazelwood, S.J. and Martin, R.B. The relationship between basic multicellular unit activation and origination in cancellous bone. *Bone.* 1999, **25**(5), pp.585-587.
25. Fazzalari, N.L., Martin, B.L., Reynolds, K.J., Cleek, T.M., Badiei, A. and Bottema, M.J. A model for the change of cancellous bone volume and structure over time. *Mathematical Biosciences.* 2012, **240**(2), pp.132-140.
26. Kristensen, H.B., Andersen, T.L., Marcussen, N., Rolighed, L. and Delaisse, J.-M. Osteoblast Recruitment Routes in Human Cancellous Bone Remodeling. *The American Journal of Pathology.* 2014, **184**(3), pp.778-789.
27. Grundnes, O. and Reikerås, O. Blood flow and mechanical properties of healing bone. *Acta Orthopaedica.* 1992, **63**(5), pp.487-491.
28. Huiskes, V.C.M.R. *Basic Orthopaedic Biomechanics & Mechano-Biology.* Philadelphia, USA: LIPPINCOTT WILLIAMS & WILKINS, 2005.
29. Marcus, R., Feldman, D., Nelson, D. and Rosen, C.J. *Osteoporosis.* Elsevier Science, 2007.
30. Eyre, D.R., Weis, M.A. and Wu, J.-J. Advances in collagen cross-link analysis. *Methods.* 2008, **45**(1), pp.65-74.
31. Eyre, D.R., Dickson, I.R. and Van Ness, K. Collagen cross-linking in human bone and articular cartilage. Age-related changes in the content of mature hydroxypyridinium residues. *Biochemical Journal.* 1988, **252**(2), pp.495-500.
32. Murugan, R. and Ramakrishna, S. Development of nanocomposites for bone grafting. *Composites Science and Technology.* 2005, **65**(15–16), pp.2385-2406.
33. Orbay, H., Tobita, M. and Mizuno, H. Mesenchymal stem cells isolated from adipose and other tissues: basic biological properties and clinical applications. *Stem Cells International.* 2012, **2012**, p.461718.

34. Porter, J.R., Ruckh, T.T. and Popat, K.C. Bone tissue engineering: a review in bone biomimetics and drug delivery strategies. *Biotechnology Progress.* 2009, **25**(6), pp.1539-1560.
35. Choi, K.M., Seo, Y.K., Yoon, H.H., Song, K.Y., Kwon, S.Y., Lee, H.S. and Park, J.K. Effect of ascorbic acid on bone marrow-derived mesenchymal stem cell proliferation and differentiation. *Journal of Bioscience and Bioengineering.* 2008, **105**(6), pp.586-594.
36. Coelho, M.J. and Fernandes, M.H. Human bone cell cultures in biocompatibility testing. Part II: effect of ascorbic acid, beta-glycerophosphate and dexamethasone on osteoblastic differentiation. *Biomaterials.* 2000, **21**(11), pp.1095-1102.
37. Holzer, G., Einhorn, T.A. and Majeska, R.J. Estrogen regulation of growth and alkaline phosphatase expression by cultured human bone marrow stromal cells. *Journal of Orthopaedic Research.* 2002, **20**(2), pp.281-288.
38. Spinella-Jaegle, S., Rawadi, G., Kawai, S., Gallea, S., Faucheu, C., Mollat, P., Courtois, B., Bergaud, B., Ramez, V., Blanchet, A.M., Adelmant, G., Baron, R. and Roman-Roman, S. Sonic hedgehog increases the commitment of pluripotent mesenchymal cells into the osteoblastic lineage and abolishes adipocytic differentiation. *Journal of Cell Science.* 2001, **114**(Pt 11), pp.2085-2094.
39. Jaiswal, R.K., Jaiswal, N., Bruder, S.P., Mbalaviele, G., Marshak, D.R. and Pittenger, M.F. Adult human mesenchymal stem cell differentiation to the osteogenic or adipogenic lineage is regulated by mitogen-activated protein kinase. *The Journal of Biological Chemistry.* 2000, **275**(13), pp.9645-9652.
40. Hagmann, S., Moradi, B., Frank, S., Dreher, T., Kammerer, P.W., Richter, W. and Gotterbarm, T. FGF-2 addition during expansion of human bone marrow-derived stromal cells alters MSC surface marker distribution and chondrogenic differentiation potential. *Cell Proliferation.* 2013, **46**(4), pp.396-407.
41. Berendsen, A.D. and Olsen, B.R. How vascular endothelial growth factor-A (VEGF) regulates differentiation of mesenchymal stem cells. *The Journal of Histochemistry and Cytochemistry: Official Journal of the Histochemistry Society.* 2014, **62**(2), pp.103-108.

42. Gori, F., Thomas, T., Hicok, K.C., Spelsberg, T.C. and Riggs, B.L. Differentiation of human marrow stromal precursor cells: bone morphogenetic protein-2 increases OSF2/CBFA1, enhances osteoblast commitment, and inhibits late adipocyte maturation. *Journal of Bone and Mineral Research: The Official Journal of the American society for Bone and Mineral Research.* 1999, **14**(9), pp.1522-1535.

43. Beederman, M., Lamplot, J.D., Nan, G., Wang, J., Liu, X., Yin, L., Li, R., Shui, W., Zhang, H., Kim, S.H., Zhang, W., Zhang, J., Kong, Y., Denduluri, S., Rogers, M.R., Pratt, A., Haydon, R.C., Luu, H.H., Angeles, J., Shi, L.L. and He, T.-C. BMP signaling in mesenchymal stem cell differentiation and bone formation. *Journal of Biomedical Science and Engineering.* 2013, **6**(8A), pp.32-52.

44. Kang, Q., Sun, M.H., Cheng, H., Peng, Y., Montag, A.G., Deyrup, A.T., Jiang, W., Luu, H.H., Luo, J., Szatkowski, J.P., Vanichakarn, P., Park, J.Y., Li, Y., Haydon, R.C. and He, T.C. Characterization of the distinct orthotopic bone-forming activity of 14 BMPs using recombinant adenovirus-mediated gene delivery. *Gene Therapy.* 2004, **11**(17), pp.1312-1320.

45. Shields, L.B., Raque, G.H., Glassman, S.D., Campbell, M., Vitaz, T., Harpring, J. and Shields, C.B. Adverse effects associated with high-dose recombinant human bone morphogenetic protein-2 use in anterior cervical spine fusion. *Spine (Phila Pa 1976).* 2006, **31**(5), pp.542-547.

46. Harrison, R.G. On the Stereotropism of Embryonic Cells. *Science.* 1911, **34**(870), pp.279-281.

47. Weiss, P. Experiments on cell and axon orientation in vitro: The role of colloidal exudates in tissue organization. *Journal of Experimental Zoology.* 1945, **100**(3), pp.353-386.

48. Curtis, A. and Wilkinson, C. Nantotechniques and approaches in biotechnology. *Trends in Biotechnology.* 2001, **19**(3), pp.97-101.

49. Yang, W., Han, W., He, W., Li, J., Wang, J., Feng, H. and Qian, Y. Surface topography of hydroxyapatite promotes osteogenic differentiation of human bone marrow mesenchymal stem cells. *Materials Science and Engineering. C, Materials for Biological Applications.* 2016, **60**, pp.45-53.

50. Faia-Torres, A.B., Charnley, M., Goren, T., Guimond-Lischer, S., Rottmar, M., Maniura-Weber, K., Spencer, N.D., Reis, R.L., Textor, M. and Neves, N.M. Osteogenic differentiation of human mesenchymal stem cells in the absence of osteogenic supplements: A surface-roughness gradient study. *Acta Biomaterialia.* 2015, **28**, pp.64-75.

51. Biggs, M.J.P., Richards, R.G., Gadegaard, N., Wilkinson, C.D.W., Oreffo, R.O.C. and Dalby, M.J. The use of nanoscale topography to modulate the dynamics of adhesion formation in primary osteoblasts and ERK/MAPK signalling in STRO-1+ enriched skeletal stem cells. *Biomaterials.* 2009, **30**(28), pp.5094-5103.

52. Fiedler, J., Ozdemir, B., Bartholoma, J., Plettl, A., Brenner, R.E. and Ziemann, P. The effect of substrate surface nanotopography on the behavior of multipotnent mesenchymal stromal cells and osteoblasts. *Biomaterials.* 2013, **34**(35), pp.8851-8859.

53. Lentz, T.L. *Cell fine structure: an atlas of drawings of whole-cell structure.* 1st ed. Philadelphia: Saunders (W.B.) Co Ltd, 1971.

54. Clarke, B. Normal Bone Anatomy and Physiology. *Clinical Journal of the American Society of Nephrology : CJASN.* 2008, **3**(Suppl 3), pp.S131-S139.

55. Roodman, G.D. Cell biology of the osteoclast. *Experimental Hematology.* 1999, **27**(8), pp.1229-1241.

56. Boyde, A. and Hobdell, M.H. Scanning electron microscopy of lamellar bone. *Zeitschrift für Zellforschung und Mikroskopische Anatomie.* 1968, **93**(2), pp.213-231.

57. Reznikov, N., Shahar, R. and Weiner, S. Three-dimensional structure of human lamellar bone: The presence of two different materials and new insights into the hierarchical organization. *Bone.* 2014, **59**(0), pp.93-104.

58. Parfitt, A.M. Osteonal and hemi-osteonal remodeling: the spatial and temporal framework for signal traffic in adult human bone. *Journal of Cellular Biochemistry.* 1994, **55**(3), pp.273-286.

59. Marotti, G. and Zallone, A.Z. Changes in the vascular network during the formation of Haversian systems. *Acta Anatomica (Basel).* 1980, **106**(1), pp.84-100.

60. Currey, J.D. *Bones: Structure and Mechanics.* Princeton, NJ: Princeton University Press, 2002.

61. Bayraktar, H.H., Morgan, E.F., Niebur, G.L., Morris, G.E., Wong, E.K. and Keaveny, T.M. Comparison of the elastic and yield properties of human femoral trabecular and cortical bone tissue. *Journal of Biomechanics.* 2004, **37**(1), pp.27-35.

62. Reilly, D.T. and Burstein, A.H. The elastic and ultimate properties of compact bone tissue. *Journal of Biomechanics.* 1975, **8**(6), pp.393-405.

63. Ashman, R.B., Cowin, S.C., Van Buskirk, W.C. and Rice, J.C. A continuous wave technique for the measurement of the elastic properties of cortical bone. *Journal of Biomechanics.* 1984, **17**(5), pp.349-361.

64. Carter, D.R. and Hayes, W.C. Bone compressive strength: the influence of density and strain rate. *Science.* 1976, **194**(4270), pp.1174-1176.

65. Carter, D.R. and Hayes, W.C. The compressive behavior of bone as a two-phase porous structure. *The Journal of Bone and Joint Surgery. American volume.* 1977, **59**(7), pp.954-962.

66. Katz, J.L. Hard tissue as a composite material—I. Bounds on the elastic behavior. *Journal of Biomechanics.* 1971, **4**(5), pp.455-473.

67. Piekarski, K. Analysis of bone as a composite material. *International Journal of Engineering Science.* 1973, **11**(6), pp.557-565.

68. Katz, J.L. Anisotropy of Young's modulus of bone. *Nature.* 1980, **283**(5742), pp.106-107.

69. Frasca, P., Harper, R. and Katz, J.L. Strain and frequency dependence of shear storage modulus for human single osteons and cortical bone microsamples—Size and hydration effects. *Journal of Biomechanics.* 1981, **14**(10), pp.679-690.

70. Sasaki, N., Ikawa, T. and Fukuda, A. Orientation of mineral in bovine bone and the anisotropic mechanical properties of plexiform bone. *Journal of Biomechanics.* 1991, **24**(1), pp.57-61.

71. Wagner, H.D. and Weiner, S. On the relationship between the microstructure of bone and its mechanical stiffness. *Journal of Biomechanics.* 1992, **25**(11), pp.1311-1320.

72. Rho, J.-Y., Kuhn-Spearing, L. and Zioupos, P. Mechanical properties and the hierarchical structure of bone. *Medical Engineering and Physics.* 1998, **20**(2), pp.92-102.

73. Jäger, I. and Fratzl, P. Mineralized Collagen Fibrils: A Mechanical Model with a Staggered Arrangement of Mineral Particles. *Biophysical Journal.* 2000, **79**(4), pp.1737-1746.
74. Schaffler, M.B., Radin, E.L. and Burr, D.B. Mechanical and morphological effects of strain rate on fatigue of compact bone. *Bone.* 1989, **10**(3), pp.207-214.
75. Choi, K., Kuhn, J.L., Ciarelli, M.J. and Goldstein, S.A. The elastic moduli of human subchondral, trabecular, and cortical bone tissue and the size-dependency of cortical bone modulus. *Journal of Biomechanics.* 1990, **23**(11), pp.1103-1113.
76. Runkle, J.C. and Pugh, J. The micro-mechanics of cancellous bone. II. Determination of the elastic modulus of individual trabeculae by a buckling analysis. *Bulletin of the Hospital for Joint Diseases.* 1975, **36**(1), pp.2-10.
77. Townsend, P.R., Rose, R.M. and Radin, E.L. Buckling studies of single human trabeculae. *Journal of Biomechanics.* 1975, **8**(3–4), pp.199-201.
78. Kuhn, J.L., Goldstein, S.A., Choi, K., London, M., Feldkamp, L.A. and Matthews, L.S. Comparison of the trabecular and cortical tissue moduli from human iliac crests. *Journal of Orthopaedic Research: Official Publication of the Orthopaedic Research Society.* 1989, **7**(6), pp.876-884.
79. Rho, J.Y., Ashman, R.B. and Turner, C.H. Young's modulus of trabecular and cortical bone material: Ultrasonic and microtensile measurements. *Journal of Biomechanics.* 1993, **26**(2), pp.111-119.
80. Hodgskinson, R. and Currey, J.D. Young's modulus, density and material properties in cancellous bone over a large density range. *Journal of Materials Science: Materials in Medicine.* 1992, **3**(5), pp.377-381.
81. Hodgskinson, R., Currey, J.D. and Evans, G.P. Hardness, an indicator of the mechanical competence of cancellous bone. *Journal of Orthopaedic Research: Official Publication of the Orthopaedic Research Society.* 1989, **7**(5), pp.754-758.
82. Turner, C.H. and Burr, D.B. Basic biomechanical measurements of bone: A tutorial. *Bone.* 1993, **14**(4), pp.595-608.
83. Keaveny, T.M., Borchers, R.E., Gibson, L.J. and Hayes, W.C. Theoretical analysis of the experimental artifact in trabecular bone compressive modulus. *Journal of Biomechanics.* 1993, **26**(4-5), pp.599-607.

84. Jacobs, C.R., Davis, B.R., Rieger, C.J., Francis, J.J., Saad, M. and Fyhrie, D.P. The impact of boundary conditions and mesh size on the accuracy of cancellous bone tissue modulus determination using large-scale finite-element modeling. *Journal of Biomechanics.* 1999, **32**(11), pp.1159-1164.

85. Ladd, A.J., Kinney, J.H., Haupt, D.L. and Goldstein, S.A. Finite-element modeling of trabecular bone: comparison with mechanical testing and determination of tissue modulus. *Journal of Orthopaedic Research: Official Publication of the Orthopaedic Research Society.* 1998, **16**(5), pp.622-628.

86. Homminga, J., McCreadie, B.R., Weinans, H. and Huiskes, R. The dependence of the elastic properties of osteoporotic cancellous bone on volume fraction and fabric. *Journal of Biomechanics.* 2003, **36**(10), pp.1461-1467.

87. Turner, C.H., Cowin, S.C., Rho, J.Y., Ashman, R.B. and Rice, J.C. The fabric dependence of the orthotropic elastic constants of cancellous bone. *Journal of Biomechanics.* 1990, **23**(6), pp.549-561.

88. Linde, F., Pongsoipetch, B., Frich, L.H. and Hvid, I. Three-axial strain controlled testing applied to bone specimens from the proximal tibial epiphysis. *Journal of Biomechanics.* 1990, **23**(11), pp.1167-1172.

89. Fyhrie, D.P. and Schaffler, M.B. Failure mechanisms in human vertebral cancellous bone. *Bone.* 1994, **15**(1), pp.105-109.

90. Kempson, G.E. Age-related changes in the tensile properties of human articular cartilage: a comparative study between the femoral head of the hip joint and the talus of the ankle joint. *Biochimica et Biophysica Acta.* 1991, **1075**(3), pp.223-230.

91. Kerin, A.J., Wisnom, M.R. and Adams, M.A. The compressive strength of articular cartilage. *Proceedings of the Institution of Mechanical Engineers. Part H, Journal of Engineering in Medicine.* 1998, **212**(4), pp.273-280.

92. Marsell, R. and Einhorn, T.A. THE BIOLOGY OF FRACTURE HEALING. *Injury.* 2011, **42**(6), pp.551-555.

93. Bigham-Sadegh, A. and Oryan, A. Basic concepts regarding fracture healing and the current options and future directions in managing bone fractures. *International Wound Journal.* 2015, **12**(3), pp.238-247.

94. Bauer, T.W. and Schils, J. The pathology of total joint arthroplasty.II. Mechanisms of implant failure. *Skeletal Radiology*. 1999, **28**(9), pp.483-97.

95. Fu, Q., Saiz, E., Rahaman, M.N. and Tomsia, A.P. Bioactive glass scaffolds for bone tissue engineering: state of the art and future perspectives. *Materials Science and Engineering: C.* 2011, **31**(7), pp.1245-1256.

96. Samavedi, S., Whittington, A.R. and Goldstein, A.S. Calcium phosphate ceramics in bone tissue engineering: A review of properties and their influence on cell behavior. *Acta Biomaterialia.* 2013, **9**(9), pp.8037-8045.

97. Damien, C.J. and Parsons, J.R. Bone graft and bone graft substitutes: a review of current technology and applications. *Journal of Applied Biomaterials: An Official Journal of the Society for Biomaterials.* 1991, **2**(3), pp.187-208.

98. Wilson, C.E., Kruyt, M.C., de Bruijn, J.D., van Blitterswijk, C.A., Oner, F.C., Verbout, A.J. and Dhert, W.J. A new in vivo screening model for posterior spinal bone formation: comparison of ten calcium phosphate ceramic material treatments. *Biomaterials.* 2006, **27**(3), pp.302-314.

99. Klawitter, J.J. and Hulbert, S.F. Application of porous ceramics for the attachment of load bearing internal orthopedic applications. *Journal of Biomedical Materials Research. Part A.* 1971, **5**(6), pp.161-229.

100. Burg, K.J.L., Porter, S. and Kellam, J.F. Biomaterial developments for bone tissue engineering. *Biomaterials.* 2000, **21**(23), pp.2347-2359.

101. Daculsi, G., Laboux, O., Malard, O. and Weiss, P. Current state of the art of biphasic calcium phosphate bioceramics. *Journal of Materials Science: Materials in Medicine.* 2003, **14**(3), pp.195-200.

102. Huang, J. and Best, S. 1 - Ceramic biomaterials for tissue engineering. In: Boccaccini, A.R. and Ma, P.X. eds. *Tissue Engineering Using Ceramics and Polymers (Second Edition).* Woodhead Publishing, 2014, pp.3-34.

103. Cameron, H.U. Tibial component wear in total knee replacement. *Clinical Orthopaedics and Related Research.* 1994, (309), pp.29-32.

104. Tjellstrom, A., Lindstrom, J., Nylen, O., Albrektsson, T. and Branemark, P.I. Directly bone-anchored implants for fixation of aural epistheses. *Biomaterials.* 1983, **4**(1), pp.55-57.

105. Hernández-Vaquero, D., Suárez-Vazquez, A. and Fernandez-Lombardia, J. Charnley low-friction arthroplasty of the hip. Five to 25 years survivorship in a general hospital. *BMC Musculoskeletal Disorders.* 2008, **9**(1), pp.1-5.

106. Neumann, L., Freund, K.G. and Sorenson, K.H. Long-term results of Charnley total hip replacement. Review of 92 patients at 15 to 20 years. *The Journal of Bone and Joint Surgery. British volume.* 1994, **76**(2), pp.245-251.

107. Okamoto, T., Inao, S., Gotoh, E. and Ando, M. Primary Charnley total hip arthroplasty for congenital dysplasia: effect of improved techniques of cementing. *The Journal of Bone and Joint Surgery. British volume.* 1997, **79**(1), pp.83-86.

108. Ramakrishna, S., Mayer, J., Wintermantel, E. and Leong, K.W. Biomedical applications of polymer-composite materials: a review. *Composites Science and Technology.* 2001, **61**(9), pp.1189-1224.

109. Revell, P.A., Braden, M. and Freeman, M.A.R. Review of the biological response to a novel bone cement containing poly(ethyl methacrylate) and n-butyl methacrylate. *Biomaterials.* 1998, **19**(17), pp.1579-1586.

110. Santin, M., Motta, A., Borzachiello, A., Nicolais, L. and Ambrosio, L. Effect of PMMA cement radical polymerisation on the inflammatory response. *Journal of Materials Science: Materials in medicine.* 2004, **15**(11), pp.1175-1180.

111. Strnad, Z. Role of the glass phase in bioactive glass-ceramics. *Biomaterials.* 1992, **13**(5), pp.317-321.

112. Cooper, D.K. A brief history of cross-species organ transplantation. *Baylor University Medical Center Proceedings.* 2012, **25**(1), pp.49-57.

113. Klymiuk, N., Aigner, B., Brem, G. and Wolf, E. Genetic modification of pigs as organ donors for xenotransplantation. *Molecular Reproduction and Devlopment.* 2010, **77**(3), pp.209-221.

114. French, A.J., Greenstein, J.L., Loveland, B.E. and Mountford, P.S. Current and future prospects for xenotransplantation. *Reproduction Fertility and Development.* 1998, **10**(7-8), pp.683-696.

115. Gun, G. and Kues, W.A. Current progress of genetically engineered pig models for biomedical research. *Bioresearch Open Access.* 2014, **3**(6), pp.255-264.

116. Leopold, S.S., Jacobs, J.J. and Rosenberg, A.G. Cancellous allograft in revision total hip arthroplasty. A clinical review. *Clinical Orthopaedics and Related Research.* 2000, (371), pp.86-97.

117. Ehrler, D.M. and Vaccaro, A.R. The use of allograft bone in lumbar spine surgery. *Clinical Orthopaedics and Related Research.* 2000, (371), pp.38-45.

118. Dashe, J., Parisien, R.L., Cusano, A., Curry, E.J., Bedi, A. and Li, X. Allograft tissue irradiation and failure rate after anterior cruciate ligament reconstruction: A systematic review. *World Journal of Orthopedics.* 2016, **7**(6), pp.392-400.

119. Müller, S.A., Barg, A., Vavken, P., Valderrabano, V. and Müller, A.M. Autograft versus sterilized allograft for lateral calcaneal lengthening osteotomies: Comparison of 50 patients. *Medicine.* 2016, **95**(30), p.e4343.

120. Summers, B. and Eisenstein, S. Donor site pain from the ilium. A complication of lumbar spine fusion. *Journal of Bone and Joint Surgery. British Volume.* 1989, **71-B**(4), pp.677-680.

121. Barkhuysen, R., Meijer, G.J., Soehardi, A., Merkx, M.A.W., Borstlap, W.A., Bergé, S.J., Bronkhorst, E.M. and Hoppenreijs, T.J.M. The effect of a single dose of bupivacaine on donor site pain after anterior iliac crest bone harvesting. *International Journal of Oral and Maxillofacial Surgery.* 2010, **39**(3), pp.260-265.

122. Kim, D.H., Rhim, R., Li, L., Martha, J., Swaim, B.H., Banco, R.J., Jenis, L.G. and Tromanhauser, S.G. Prospective study of iliac crest bone graft harvest site pain and morbidity. *The Spine Journal.* 2009, **9**(11), pp.886-892.

123. Noshchenko, A., Hoffecker, L., Lindley, E.M., Burger, E.L., Cain, C.M.J. and Patel, V.V. Perioperative and long-term clinical outcomes for bone morphogenetic protein versus iliac crest bone graft for lumbar fusion in degenerative disk disease: Systematic review with meta-analysis. *Journal of Spinal Disorders and Techniques.* 2014, **27**(3), pp.117-135.

124. Kurtz, S.M., Muratoglu, O.K., Evans, M. and Edidin, A.A. Advances in the processing, sterilization, and crosslinking of ultra-high molecular weight polyethylene for total joint arthroplasty. *Biomaterials.* 1999, **20**(18), pp.1659-1688.

125. Geesink, R.G., de Groot, K. and Klein, C.P. Bonding of bone to apatite-coated implants. *Journal of Bone and Joint Surgery. British Volume.* 1988, **70**(1), pp.17-22.

126. Hardy, D.C., Frayssinet, P., Guilhem, A., Lafontaine, M.A. and Delince, P.E. Bonding of hydroxyapatite-coated femoral prostheses. Histopathology of specimens from four cases. *Journal of Bone and Joint Surgery. British Volume.* 1991, **73**(5), pp.732-740.

127. Buma, P. and Gardeniers, J.W. Tissue reactions around a hydroxyapatite-coated hip prosthesis. Case report of a retrieved specimen. *The Journal of Arthroplasty.* 1995, **10**(3), pp.389-395.

128. Adell, R., Lekholm, U., Rockler, B., Branemark, P.I., Lindhe, J., Eriksson, B. and Sbordone, L. Marginal tissue reactions at osseointegrated titanium fixtures (I). A 3-year longitudinal prospective study. *International Journal of Oral and Maxillofacial Surgery.* 1986, **15**(1), pp.39-52.

129. Friedman, R.J., Black, J., Galante, J.O., Jacobs, J.J. and Skinner, H.B. Current Concepts in Orthopaedic Biomaterials and Implant Fixation. *The Journal of Bone and Joint Surgery. American volume.* 1993, **75**(7), p.1086.

130. Jarcho, M. Calcium phosphate ceramics as hard tissue prosthetics. *Clinical Orthopaedics and Related Research.* 1981, (157), pp.259-278.

131. Rawlings, R.D. Bioactive glasses and glass-ceramics. *Clinical Materials.* 1993, **14**(2), pp.155-179.

132. Balta, B.P.a.E. *Introduction to the Physical Chemistry of the Vitrous State.* Tubridge Wells: Abacus Press, 1976.

133. J, B. *Glass.* London: Morgan-Grampian Ltd., 1969.

134. Zachariasen, W.H. THE ATOMIC ARRANGEMENT IN GLASS. *Journal of the American Chemical Society.* 1932, **54**(10), pp.3841-3851.

135. Beall, H.W.a.G. *Glass-ceramic technology*. 2002. At: Westerville: The American Ceramic Society.

136. Hu, A.-M., Liang, K.-M., Li, M. and Mao, D.-L. Effect of nucleation temperatures and time on crystallization behavior and properties of Li_2O–Al_2O_3–SiO_2 glasses. *Materials Chemistry and Physics.* 2006, **98**(2–3), pp.430-433.

137. Xiao, K., Dalgarno, K.W., Wood, D.J., Goodridge, R.D. and Ohtsuki, C. Indirect selective laser sintering of apatite-wollostonite glass-ceramic.

Proceedings of the Institution of Mechanical Engineers. Part H, Journal of Engineering in Medicine. 2008, **222**(7), pp.1107-1114.

138. German, R., Suri, P. and Park, S. Review: liquid phase sintering. *Journal of Materials Science.* 2009, **44**(1), pp.1-39.

139. German, R.M. *Sintering Theory and Practice.* New York: John Wiley & Sons, 1996.

140. Menczel, J.D., Judovits, L., Prime, R.B., Bair, H.E., Reading, M. and Swier, S. Differential Scanning Calorimetry (DSC). In: *Thermal Analysis of Polymers*. John Wiley & Sons, Inc., 2008, pp.7-239.

141. Likitvanichkul, S. and Lacourse, W.C. Apatite–wollastonite glass-ceramics part I Crystallization kinetics by differential thermal analysis. *Journal of Materials Science.* 1998, **33**(24), pp.5901-5904.

142. Hench, L.L., Splinter, R.J., Allen, W.C. and Greenlee, T.K. Bonding mechanisms at the interface of ceramic prosthetic materials. *Journal of Biomedical Materials Research.* 1971, **5**(6), pp.117-141.

143. Hench, L.L. Bioceramics: From Concept to Clinic. *Journal of the American Ceramic Society.* 1991, **74**(7), pp.1487-1510.

144. Jones, J.R. and Hench, L.L. Biomedical materials for new millennium: perspective on the future. *Materials Science and Technology.* 2001, **17**(8), pp.891-900.

145. Carlisle, E.M. Silicon: An essential element for the chick. *Science.* 1972, **178**(4061), pp.619-621.

146. Schwarz, K. A Bound Form of Silicon in Glycosaminoglycans and Polyuronides. *Proceedings of the National Academy of Sciences.* 1973, **70**(5), pp.1608-1612.

147. Reffitt, D.M., Ogston, N., Jugdaohsingh, R., Cheung, H.F., Evans, B.A., Thompson, R.P., Powell, J.J. and Hampson, G.N. Orthosilicic acid stimulates collagen type 1 synthesis and osteoblastic differentiation in human osteoblast-like cells in vitro. *Bone.* 2003, **32**(2), pp.127-135.

148. Reffitt, D.M., Ogston, N., Jugdaohsingh, R., Cheung, H.F.J., Evans, B.A.J., Thompson, R.P.H., Powell, J.J. and Hampson, G.N. Orthosilicic acid stimulates collagen type 1 synthesis and osteoblastic differentiation in human osteoblast-like cells in vitro. *Bone.* 2003, **32**(2), pp.127-135.

149. Jones, J.R. Review of bioactive glass: From Hench to hybrids. *Acta Biomaterialia.* 2013, **9**(1), pp.4457-4486.

150. Hench, L. The story of Bioglass®. *Journal of Materials Science: Materials in Medicine.* 2006, **17**(11), pp.967-978.

151. Thomas, M.V., Puleo, D.A. and Al-Sabbagh, M. Bioactive glass three decades on. *Journal of Long-Term Effects of Medical Implants.* 2005, **15**(6), pp.585-597.

152. Hench, L.L. and Paschall, H.A. Direct chemical bond of bioactive glass-ceramic materials to bone and muscle. *Journal of Biomedical Materials Research.* 1973, **7**(3), pp.25-42.

153. Höland, W. Glass CrystallizationBiocompatible and bioactive glass-ceramics — state of the art and new directions. *Journal of Non-Crystalline Solids.* 1997, **219**, pp.192-197.

154. Neo, M., Kotani, S., Nakamura, T., Yamamuro, T., Ohtsuki, C., Kokubo, T. and Bando, Y. A comparative study of ultrastructures of the interfaces between four kinds of surface-active ceramic and bone. *Journal of Biomedical Materials Research.* 1992, **26**(11), pp.1419-1432.

155. Kokubo, T., Ito, S., Sakka, S. and Yamamuro, T. Formation of a high-strength bioactive glass-ceramic in the system MgO-CaO-SiO2-P2O5. *Journal of Materials Science.* 1986, **21**(2), pp.536-540.

156. Kokubo, T., Ito, S., Shigematsu, M., Sakka, S. and Yamamuro, T. Mechanical properties of a new type of apatite-containing glass-ceramic for prosthetic application. *Journal of Materials Science.* 1985, **20**(6), pp.2001-2004.

157. Yamamuro, T. and Shimizu, K. [Clinical application of AW glass ceramic prosthesis in spinal surgery]. *Nihon Seikeigeka Gakkai Zasshi.* 1994, **68**(7), pp.505-515.

158. Nakamura, T., Yamamuro, T., Higashi, S., Kokubo, T. and Itoo, S. A new glass-ceramic for bone replacement: evaluation of its bonding to bone tissue. *Journal of Biomedical Materials Research.* 1985, **19**(6), pp.685-698.

159. Kokubo, T. A/W Glass-Ceramic: Processing and Properties. In: Hench, L.L. and Wilson, J. eds. *An Introduction to Bioceramics*. World Scientific, 1993, pp.75-88.

160. Oonishi, H., Hench, L.L., Wilson, J., Sugihara, F., Tsuji, E., Matsuura, M., Kin, S., Yamamoto, T. and Mizokawa, S. Quantitative comparison of bone growth behavior in granules of Bioglass, A-W glass-ceramic, and hydroxyapatite. *Journal of Biomedical Materials Research.* 2000, **51**(1), pp.37-46.

161. Ohgushi, H., Okumura, M., Yoshikawa, T., Inoue, K., Senpuku, N., Tamai, S. and Shors, E.C. Bone formation process in porous calcium carbonate and hydroxyapatite. *Journal of Biomedical Materials Research.* 1992, **26**(7), pp.885-895.

162. Shyu, J.-J. and Wu, J.-M. Journal. Effects of Composition Changes on the Crystallization Behavior of MgO-CaO-SiO2-P2O5 Glass-Ceramics. *Journal of the American Ceramic Society.* 1991, **74**(9), pp.2123-2130.

163. Ohura, K., Nakamura, T., Yamamuro, T., Ebisawa, Y., Kokubo, T., Kotoura, Y. and Oka, M. Bioactivity of CaO·SiO2 glasses added with various ions. *Journal of Materials Science: Materials in Medicine.* 1992, **3**(2), pp.95-100.

164. Ebisawa, Y., Kokubo, T., Ohura, K. and Yamamuro, T. Bioactivity of CaO·SiO2-based glasses:in vitro evaluation. *Journal of Materials Science: Materials in Medicine.* 1990, **1**(4), pp.239-244.

165. Kitsugi, T., Yamamuro, T., Nakamura, T. and Kokubo, T. The bonding of glass ceramics to bone. *International Orthopaedics.* 1989, **13**(3), pp.199-206.

166. Epinette, J.A. and Manley, M.T. Hydroxyapatite-coated total knee replacement: clinical experience at 10 to 15 years. *The Journal of Bone and Joint Surgery. Bristish volume.* 2007, **89**(1), pp.34-38.

167. Nilsson, K.G., Kärrholm, J., Carlsson, L. and Dalén, T. Hydroxyapatite coating versus cemented fixation of the tibial component in total knee arthroplasty: Prospective randomized comparison of hydroxyapatite-coated and cemented tibial components with 5-year follow-up using radiostereometry. *The Journal of Arthroplasty.* 1999, **14**(1), pp.9-20.

168. Dumbleton, J. and Manley, M.T. Hydroxyapatite-Coated Prostheses in Total Hip and Knee Arthroplasty. *The Journal of Bone and Joint Surgery. American volume.* 2004, **86**(11), pp.2526-2540.

169. Heimann, R.B. Structure, properties, and biomedical performance of osteoconductive bioceramic coatings. *Surface and Coatings Technology.* 2013, **233**(0), pp.27-38.

170. Gomez-Vega, J.M., Saiz, E., Tomsia, A.P., Marshall, G.W. and Marshall, S.J. Bioactive glass coatings with hydroxyapatite and Bioglass® particles on Ti-based implants. 1. Processing. *Biomaterials.* 2000, **21**(2), pp.105-111.

171. Martorana, S., Fedele, A., Mazzocchi, M. and Bellosi, A. Surface coatings of bioactive glasses on high strength ceramic composites. *Applied Surface Science.* 2009, **255**(13–14), pp.6679-6685.

172. Bharati, S., Soundrapandian, C., Basu, D. and Datta, S. Studies on a novel bioactive glass and composite coating with hydroxyapatite on titanium based alloys: Effect of γ-sterilization on coating. *Journal of the European Ceramic Society.* 2009, **29**(12), pp.2527-2535.

173. Balamurugan, A., Balossier, G., Michel, J. and Ferreira, J.M.F. Electrochemical and structural evaluation of functionally graded bioglass-apatite composites electrophoretically deposited onto Ti6Al4V alloy. *Electrochimica Acta.* 2009, **54**(4), pp.1192-1198.

174. Boccaccini, A.R., Peters, C., Roether, J.A., Eifler, D., Misra, S.K. and Minay, E.J. Electrophoretic deposition of polyetheretherketone (PEEK) and PEEK/Bioglass® coatings on NiTi shape memory alloy wires. *Journal of Materials Science.* 2006, **41**(24), pp.8152-8159.

175. Lee, T.M., Chang, E., Wang, B.C. and Yang, C.Y. Characteristics of plasma-sprayed bioactive glass coatings on Ti-6A1-4V alloy: an in vitro study. *Surface and Coatings Technology.* 1996, **79**(1–3), pp.170-177.

176. Verné, E., Ferraris, M., Ventrella, A., Paracchini, L., Krajewski, A. and Ravaglioli, A. Sintering and plasma spray deposition of bioactive glass-Matrix composites for medical applications. *Journal of the European Ceramic Society.* 1998, **18**(4), pp.363-372.

177. Bolelli, G., Cannillo, V., Gadow, R., Killinger, A., Lusvarghi, L. and Rauch, J. Microstructural and in vitro characterisation of high-velocity suspension flame sprayed (HVSFS) bioactive glass coatings. *Journal of the European Ceramic Society.* 2009, **29**(11), pp.2249-2257.

178. D'Alessio, L., Teghil, R., Zaccagnino, M., Zaccardo, I., Ferro, D. and Marotta, V. Pulsed laser ablation and deposition of bioactive glass as coating material for biomedical applications. *Applied Surface Science.* 1999, **138–139**(0), pp.527-532.

179. Zhao, Y., Song, M., Chen, C. and Liu, J. The role of the pressure in pulsed laser deposition of bioactive glass films. *Journal of Non-Crystalline Solids.* 2008, **354**(33), pp.4000-4004.

180. Stan, G.E., Pina, S., Tulyaganov, D.U., Ferreira, J.M.F., Pasuk, I. and Morosanu, C.O. Biomineralization capability of adherent bio-glass films prepared by magnetron sputtering. *Journal of Materials Science: Materials in Medicine.* 2010, **21**(4), pp.1047-1055.

181. Dhert, W.J.A., Klein, C.P.A.T., Wolke, J.G.C., van der Velde, E.A., de Groot, K. and Rozing, P.M. Student research award in the graduate degree candidate category, 17th annual meeting of the society for biomaterials, scottsdale, AZ may 1–5,1991. A mechanical investigation of fluorapatite, magnesiumwhitlockite, and hydroxylapatite plasma-sprayed coatings in goats. *Journal of Biomedical Materials Research.* 1991, **25**(10), pp.1183-1200.

182. Fazan, F. and Marquis, P.M. Dissolution behavior of plasma-sprayed hydroxyapatite coatings. *Journal of Materials Science: Materials in Medicine.* 2000, **11**(12), pp.787-792.

183. Bhadang, K.A. and Gross, K.A. Influence of fluorapatite on the properties of thermally sprayed hydroxyapatite coatings. *Biomaterials.* 2004, **25**(20), pp.4935-4945.

184. Dhert, W.J., Klein, C.P., Wolke, J.G., van der Velde, E.A., de Groot, K. and Rozing, P.M. A mechanical investigation of fluorapatite, magnesiumwhitlockite, and hydroxylapatite plasma-sprayed coatings in goats. *Journal of Biomedical Materials Research.* 1991, **25**(10), pp.1183-1200.

185. Seifalian, A., Mel, d.A. and Kalaskar, D.M. *Nanomedicine.* [Online]. One Central Press (OCP), 2014.

186. Valen, M. *Fluorapatite nano-crystalline coated non-ceramic hydrophilic hydroxylapatite bone grafting compositions and methods for promoting*

bone regeneration. Google Patents. 2016. Available from: https://www.google.com/patents/US9238047

187. Liu, J., Wang, X., Jin, Q., Jin, T., Chang, S., Zhang, Z., Czajka-Jakubowska, A., Giannobile, W.V., Nor, J.E. and Clarkson, B.H. The stimulation of adipose-derived stem cell differentiation and mineralization by ordered rod-like fluorapatite coatings. *Biomaterials.* 2012, **33**(20), pp.5036-5046.

188. Liu, J., Jin, T.C., Chang, S., Czajka-Jakubowska, A. and Clarkson, B.H. Adhesion and growth of dental pulp stem cells on enamel-like fluorapatite surfaces. *Journal of Biomedical Materials Research. Part A.* 2011, **96**(3), pp.528-534.

189. Chen, H., Tang, Z., Liu, J., Sun, K., Chang, S.R., Peters, M.C., Mansfield, J.F., Czajka-Jakubowska, A. and Clarkson, B.H. Acellular Synthesis of a Human Enamel-like Microstructure. *Advanced Materials.* 2006, **18**(14), pp.1846-1851.

190. Alhilou, A., Do, T., Mizban, L., Clarkson, B.H., Wood, D.J. and Katsikogianni, M.G. Physicochemical and Antibacterial Characterization of a Novel Fluorapatite Coating. *ACS Omega.* 2016, **1**(2), pp.264-276.

191. Hutmacher, D.W. Scaffolds in tissue engineering bone and cartilage. *Biomaterials.* 2000, **21**(24), pp.2529-2543.

192. Mallick, K.K. and Winnett, J. 6 - 3D bioceramic foams for bone tissue engineering. In: Mallick, K. ed. *Bone Substitute Biomaterials*. Woodhead Publishing, 2014, pp.118-141.

193. Dorozhkin, S. Calcium orthophosphate-based biocomposites and hybrid biomaterials. *Journal of Materials Science.* 2009, **44**(9), pp.2343-2387.

194. Boccaccini, A.R. and Blaker, J.J. Bioactive composite materials for tissue engineering scaffolds. *Expert Review of Medical Devices* 2005, **2**(3), pp.303-317.

195. Chen, Q., Roether, J., Boccaccini, A., Ashammakhi, N., Reis, R. and Chiellini, F. Tissue engineering scaffolds from bioactive glass and composite materials. *Topics in Tissue Engineering.* 2008, **4**, pp.1-27.

196. Tancret, F., Bouler, J.M., Chamousset, J. and Minois, L.M. Modelling the mechanical properties of microporous and macroporous biphasic calcium

phosphate bioceramics. *Journal of the European Ceramic Society*. 2006, **26**(16), pp.3647-3656.

197. Vitale-Brovarone, C., Vernè, E., Bosetti, M., Appendino, P. and Cannas, M. Microstructural and in vitro characterization of SiO2-Na2O-CaO-MgO glass-ceramic bioactive scaffolds for bone substitutes. *Journal of Materials Science: Materials in Medicine*. 2005, **16**(10), pp.909-917.

198. Jones, J.R., Ahir, S. and Hench, L.L. Large-Scale Production of 3D Bioactive Glass Macroporous Scaffolds for Tissue Engineering. *Journal of Sol-Gel Science and Technology*. 2004, **29**(3), pp.179-188.

199. Sepulveda, P., Jones, J.R. and Hench, L.L. Bioactive sol-gel foams for tissue repair. *Journal of Biomedical Materials Research*. 2002, **59**(2), pp.340-348.

200. Tomita, T., Kawasaki, S. and Okada, K. A Novel Preparation Method for Foamed Silica Ceramics by Sol-Gel Reaction and Mechanical Foaming. *Journal of Porous Materials*. 2004, **11**(2), pp.107-115.

201. Jones, J.R. and Hench, L.L. Effect of surfactant concentration and composition on the structure and properties of sol-gel-derived bioactive glass foam scaffolds for tissue engineering. *Journal of Materials Science*. 2003, **38**(18), pp.3783-3790.

202. Jones, J.R. and Hench, L.L. Factors affecting the structure and properties of bioactive foam scaffolds for tissue engineering. *Journal of Biomedical Materials Research. Part B, Applied Biomaterials*. 2004, **68**(1), pp.36-44.

203. Jones, J.R., Ehrenfried, L.M. and Hench, L.L. Optimising bioactive glass scaffolds for bone tissue engineering. *Biomaterials*. 2006, **27**(7), pp.964-973.

204. Jones, J.R., Poologasundarampillai, G., Atwood, R.C., Bernard, D. and Lee, P.D. Non-destructive quantitative 3D analysis for the optimisation of tissue scaffolds. *Biomaterials*. 2007, **28**(7), pp.1404-1413.

205. Marques, A.C., Almeida, R.M., Thiema, A., Wang, S., Falk, M. and Jain, H. Sol-gel-derived glass scaffold with high pore interconnectivity and enhanced bioactivity. *Journal of Materials Research*. 2009, **24**(12), pp.3495-3502.

206. Chen, Q.Z. and Thouas, G.A. Fabrication and characterization of sol-gel derived 45S5 Bioglass(R)-ceramic scaffolds. *Acta Biomaterialia*. 2011, **7**(10), pp.3616-3626.

207. Almeida, R.M., Gama, A. and Vueva, Y. Bioactive sol–gel scaffolds with dual porosity for tissue engineering. *Journal of Sol-Gel Science and Technology*. 2011, **57**(3), pp.336-342.

208. Soon, Y.-M., Shin, K.-H., Koh, Y.-H., Lee, J.-H. and Kim, H.-E. Compressive strength and processing of camphene-based freeze cast calcium phosphate scaffolds with aligned pores. *Materials Letters*. 2009, **63**(17), pp.1548-1550.

209. Araki, K. and Halloran, J.W. Porous Ceramic Bodies with Interconnected Pore Channels by a Novel Freeze Casting Technique. *Journal of the American Ceramic Society*. 2005, **88**(5), pp.1108-1114.

210. Song, J.-H., Koh, Y.-H., Kim, H.-E., Li, L.-H. and Bahn, H.-J. Fabrication of a Porous Bioactive Glass–Ceramic Using Room-Temperature Freeze Casting. *Journal of the American Ceramic Society*. 2006, **89**(8), pp.2649-2653.

211. Yoon, B.-H., Choi, W.-Y., Kim, H.-E., Kim, J.-H. and Koh, Y.-H. Aligned porous alumina ceramics with high compressive strengths for bone tissue engineering. *Scripta Materialia*. 2008, **58**(7), pp.537-540.

212. Yook, S.-W., Kim, H.-E., Yoon, B.-H., Soon, Y.-M. and Koh, Y.-H. Improvement of compressive strength of porous hydroxyapatite scaffolds by adding polystyrene to camphene-based slurries. *Materials Letters*. 2009, **63**(11), pp.955-958.

213. Liu, X., Rahaman, M.N. and Fu, Q. Oriented bioactive glass (13-93) scaffolds with controllable pore size by unidirectional freezing of camphene-based suspensions: Microstructure and mechanical response. *Acta Biomaterialia*. 2011, **7**(1), pp.406-416.

214. Sadeghpour, S., Amirjani, A., Hafezi, M. and Zamanian, A. Fabrication of a novel nanostructured calcium zirconium silicate scaffolds prepared by a freeze-casting method for bone tissue engineering. *Ceramics International*. 2014, **40**(10), pp.16107-16114.

215. Liu, X., Rahaman, M.N., Hilmas, G.E. and Bal, B.S. Mechanical properties of bioactive glass (13-93) scaffolds fabricated by robotic deposition for structural bone repair. *Acta Biomaterialia.* 2013, **9**(6), pp.7025-7034.

216. Huang, T.S., Rahaman, M.N., Doiphode, N.D., Leu, M.C., Bal, B.S., Day, D.E. and Liu, X. Porous and strong bioactive glass (13–93) scaffolds fabricated by freeze extrusion technique. *Materials Science and Engineering: C.* 2011, **31**(7), pp.1482-1489.

217. Lorrison, J., Dalgarno, K. and Wood, D. Processing of an apatite-mullite glass-ceramic and an hydroxyapatite/phosphate glass composite by selective laser sintering. *Journal of Materials Science: Materials in Medicine.* 2005, **16**(8), pp.775-781.

218. Goodridge, R.D., Wood, D.J., Ohtsuki, C. and Dalgarno, K.W. Biological evaluation of an apatite-mullite glass-ceramic produced via selective laser sintering. *Acta Biomaterialia.* 2007, **3**(2), pp.221-231.

219. Kolan, K.C., Leu, M.C., Hilmas, G.E., Brown, R.F. and Velez, M. Fabrication of 13-93 bioactive glass scaffolds for bone tissue engineering using indirect selective laser sintering. *Biofabrication.* 2011, **3**(2), p.025004.

220. Fu, Q., Saiz, E. and Tomsia, A.P. Bioinspired Strong and Highly Porous Glass Scaffolds. *Advanced Functional Materials.* 2011, **21**(6), pp.1058-1063.

221. Fu, Q., Saiz, E. and Tomsia, A.P. Direct ink writing of highly porous and strong glass scaffolds for load-bearing bone defects repair and regeneration. *Acta Biomaterialia.* 2011, **7**(10), pp.3547-3554.

222. Ijiri, S., Nakamura, T., Fujisawa, Y., Hazama, M. and Komatsudani, S. Ectopic bone induction in porous apatite-wollastonite-containing glass ceramic combined with bone morphogenetic protein. *Journal of Biomedical Materials Research.* 1997, **35**(4), pp.421-432.

223. Fujita, H., Iida, H., Ido, K., Matsuda, Y., Oka, M. and Nakamura, T. Porous apatite-wollastonite glass-ceramic as an intramedullary plug. *The Journal of Bone and Joint Surgery. British volume.* 2000, **82-B**(4), p.614.

224. Teramoto, H., Kawai, A., Sugihara, S., Yoshida, A. and Inoue, H. Resorption of apatite-wollastonite containing glass-ceramic and beta-

tricalcium phosphate in vivo. *Acta Medica Okayama.* 2005, **59**(5), pp.201-207.

225. Chen, Q.Z., Thompson, I.D. and Boccaccini, A.R. 45S5 Bioglass®-derived glass–ceramic scaffolds for bone tissue engineering. *Biomaterials.* 2006, **27**(11), pp.2414-2425.

226. Kokubo, T., Hata, K., Nakamura, T. and Yamamuro, T. Apatite Formation on Ceramics, Metals and Polymers Induced by a CaO SiO2 Based Glass in a Simulated Body Fluid. In: *Bioceramics*. Butterworth-Heinemann, 1991, pp.113-120.

227. Ramay, H.R. and Zhang, M. Preparation of porous hydroxyapatite scaffolds by combination of the gel-casting and polymer sponge methods. *Biomaterials.* 2003, **24**(19), pp.3293-3302.

228. Jun, I.-K., Song, J.-H., Choi, W.-Y., Koh, Y.-H., Kim, H.-E. and Kim, H.-W. Porous Hydroxyapatite Scaffolds Coated With Bioactive Apatite–Wollastonite Glass–Ceramics. *Journal of the American Ceramic Society.* 2007, **90**(9), pp.2703-2708.

229. Hsu, Y.H., Turner, I.G. and Miles, A.W. Fabrication of porous bioceramics with porosity gradients similar to the bimodal structure of cortical and cancellous bone. *Journal of Materials Science. Materials in Medicine.* 2007, **18**(12), pp.2251-2256.

230. Bretcanu, O., Samaille, C. and Boccaccini, A.R. Simple methods to fabricate Bioglass®-derived glass–ceramic scaffolds exhibiting porosity gradient. *Journal of Materials Science.* 2008, **43**(12), pp.4127-4134.

231. Vitale-Brovarone, C., Verne, E., Robiglio, L., Appendino, P., Bassi, F., Martinasso, G., Muzio, G. and Canuto, R. Development of glass-ceramic scaffolds for bone tissue engineering: characterisation, proliferation of human osteoblasts and nodule formation. *Acta Biomaterialia.* 2007, **3**(2), pp.199-208.

232. Vitale-Brovarone, C., Miola, M., Balagna, C. and Verné, E. 3D-glass–ceramic scaffolds with antibacterial properties for bone grafting. *Chemical Engineering Journal.* 2008, **137**(1), pp.129-136.

233. Vitale-Brovarone, C., Baino, F., Bretcanu, O. and Verne, E. Foam-like scaffolds for bone tissue engineering based on a novel couple of silicate-

phosphate specular glasses: synthesis and properties. *Journal of Materials Science. Materials in Medicine.* 2009, **20**(11), pp.2197-2205.

234. Fu, Q., Rahaman, M.N., Bal, B.S., Brown, R.F. and Day, D.E. Mechanical and in vitro performance of 13-93 bioactive glass scaffolds prepared by a polymer foam replication technique. *Acta Biomaterialia.* 2008, **4**(6), pp.1854-1864.

235. Vitale-Brovarone, C., Baino, F. and Verne, E. High strength bioactive glass-ceramic scaffolds for bone regeneration. *Journal of Materials Science. Materials in Medicine.* 2009, **20**(2), pp.643-653.

236. Mantsos, T., Chatzistavrou, X., Roether, J.A., Hupa, L., Arstila, H. and Boccaccini, A.R. Non-crystalline composite tissue engineering scaffolds using boron-containing bioactive glass and poly(D,L-lactic acid) coatings. *Biomedical Materials (Bristol, England).* 2009, **4**(5), p.055002.

237. Chen, Q.Z. and Boccaccini, A.R. Poly(D,L-lactic acid) coated 45S5 Bioglass®-based scaffolds: Processing and characterization. *Journal of Biomedical Materials Research. Part A.* 2006, **77A**(3), pp.445-457.

238. Fu, Q., Rahaman, M.N., Fu, H. and Liu, X. Silicate, borosilicate, and borate bioactive glass scaffolds with controllable degradation rate for bone tissue engineering applications. I. Preparation and in vitro degradation. *Journal of Biomedical Materials Research. Part A.* 2010, **95**(1), pp.164-171.

239. Fu, Q., Rahaman, M.N., Bal, B.S., Bonewald, L.F., Kuroki, K. and Brown, R.F. Silicate, borosilicate, and borate bioactive glass scaffolds with controllable degradation rate for bone tissue engineering applications. II. In vitro and in vivo biological evaluation. *Journal of Biomedical Materials Research. Part A.* 2010, **95**(1), pp.172-179.

240. Gu, Y., Wang, G., Zhang, X., Zhang, Y., Zhang, C., Liu, X., Rahaman, M.N., Huang, W. and Pan, H. Biodegradable borosilicate bioactive glass scaffolds with a trabecular microstructure for bone repair. *Materials Science & Engineering. C, Materials for Biological Applications.* 2014, **36**, pp.294-300.

241. Ochoa, I., Sanz-Herrera, J.A., Garcia-Aznar, J.M., Doblare, M., Yunos, D.M. and Boccaccini, A.R. Permeability evaluation of 45S5 Bioglass-based scaffolds for bone tissue engineering. *Journal of Biomechanics.* 2009, **42**(3), pp.257-260.

242. Renghini, C., Komlev, V., Fiori, F., Verne, E., Baino, F. and Vitale-Brovarone, C. Micro-CT studies on 3-D bioactive glass-ceramic scaffolds for bone regeneration. *Acta Biomaterialia.* 2009, **5**(4), pp.1328-1337.

243. Huang, C.W. and Hsueh, C.H. Piston-on-three-ball versus piston-on-ring in evaluating the biaxial strength of dental ceramics. *Dental materials: Official Publication of the Academy of Dental Materials*. 2011, **27**(6), pp.e117-123.

244. Ban, S. and Anusavice, K.J. Influence of test method on failure stress of brittle dental materials. *Journal of Dental Research.* 1990, **69**(12), pp.1791-1799.

245. Fan, X., Case, E.D., Gheorghita, I. and Baumann, M.J. Weibull modulus and fracture strength of highly porous hydroxyapatite. *Journal of the Mechanical Behavior of Biomedical Materials.* 2013, **20**, pp.283-295.

246. Vickers, W.O.M. *The Effect of Strontium Substitution on Apatite-Wollastonite Glass-Ceramics*. Doctor of Philosophy thesis, University of Leeds, 2013.

247. Dyson, J.A., Genever, P.G., Dalgarno, K.W. and Wood, D.J. Development of custom-built bone scaffolds using mesenchymal stem cells and apatite-wollastonite glass-ceramics. *Tissue Engineering.* 2007, **13**(12), pp.2891-2901.

248. Lee, J.A., Knight, C.A., Kun, X., Yang, X.B., Wood, D.J., Dalgarno, K.W. and Genever, P.G. In vivo biocompatibility of custom-fabricated apatite-wollastonite-mesenchymal stromal cell constructs. *Journal of Biomedical Materials Research. Part A.* 2015, **103**(10), pp.3188-3200.

249. Chen, Q., Baino, F., Spriano, S., Pugno, N.M. and Vitale-Brovarone, C. Modelling of the strength–porosity relationship in glass-ceramic foam scaffolds for bone repair. *Journal of the European Ceramic Society.* 2014, **34**(11), pp.2663-2673.

250. Vitale-Brovarone, C., Baino, F. and Verné, E. High strength bioactive glass-ceramic scaffolds for bone regeneration. *Journal of Materials Science. Materials in Medicine.* 2009, **20**(2), pp.643-653.

251. Jun, I.K., Song, J.H., Choi, W.Y., Koh, Y.H., Kim, H.E. and Kim, H.W. Porous hydroxyapatite scaffolds coated with bioactive apatite–wollastonite

glass–ceramics. *Journal of the American Ceramic Society.* 2007, **90**(9), pp.2703-2708.

252. Devin, J.E., Attawia, M.A. and Laurencin, C.T. Three-dimensional degradable porous polymer-ceramic matrices for use in bone repair. *Journal of Biomaterials Science Polymer Edition.* 1996, **7**(8), pp.661-669.

253. Ambrosio, A.M., Sahota, J.S., Khan, Y. and Laurencin, C.T. A novel amorphous calcium phosphate polymer ceramic for bone repair: I. Synthesis and characterization. *Journal of Biomedical Materials Research.* 2001, **58**(3), pp.295-301.

254. Vitale-Brovarone, C., Baino, F. and Verne, E. Feasibility and tailoring of bioactive glass-ceramic scaffolds with gradient of porosity for bone grafting. *Journal of Biomaterials Application.* 2010, **24**(8), pp.693-712.

255. Zhang, K., Wang, Y., Hillmyer, M.A. and Francis, L.F. Processing and properties of porous poly(l-lactide)/bioactive glass composites. *Biomaterials.* 2004, **25**(13), pp.2489-2500.

256. Blaker, J.J., Maquet, V., Jérôme, R., Boccaccini, A.R. and Nazhat, S.N. Mechanical properties of highly porous PDLLA/Bioglass® composite foams as scaffolds for bone tissue engineering. *Acta Biomaterialia.* 2005, **1**(6), pp.643-652.

257. Chen, Q., Mohn, D. and Stark, W.J. Optimization of Bioglass® Scaffold Fabrication Process. *Journal of the American Ceramic Society.* 2011, **94**(12), pp.4184-4190.

258. Karageorgiou, V. and Kaplan, D. Porosity of 3D biomaterial scaffolds and osteogenesis. *Biomaterials.* 2005, **26**(27), pp.5474-5491.

259. Marcos-Campos, I., Marolt, D., Petridis, P., Bhumiratana, S., Schmidt, D. and Vunjak-Novakovic, G. Bone scaffold architecture modulates the development of mineralized bone matrix by human embryonic stem cells. *Biomaterials.* 2012, **33**(33), pp.8329-8342.

260. Zhang, C., Wang, J., Feng, H., Lu, B., Song, Z. and Zhang, X. Replacement of segmental bone defects using porous bioceramic cylinders: A biomechanical and X-ray diffraction study. *Journal of Biomedical Materials Research.* 2001, **54**(3), pp.407-411.

261. Chu, T.-M.G., Orton, D.G., Hollister, S.J., Feinberg, S.E. and Halloran, J.W. Mechanical and in vivo performance of hydroxyapatite implants with controlled architectures. *Biomaterials.* 2002, **23**(5), pp.1283-1293.

262. Kuboki, Y., Takita, H., Kobayashi, D., Tsuruga, E., Inoue, M., Murata, M., Nagai, N., Dohi, Y. and Ohgushi, H. BMP-induced osteogenesis on the surface of hydroxyapatite with geometrically feasible and nonfeasible structures: topology of osteogenesis. *Journal of Biomedical Materials Research.* 1998, **39**(2), pp.190-199.

263. Habibovic, P., Sees, T.M., van den Doel, M.A., van Blitterswijk, C.A. and de Groot, K. Osteoinduction by biomaterials—Physicochemical and structural influences. *Journal of Biomedical Materials Research. Part A.* 2006, **77A**(4), pp.747-762.

264. Hildebrand, T., Laib, A., Muller, R., Dequeker, J. and Ruegsegger, P. Direct three-dimensional morphometric analysis of human cancellous bone: microstructural data from spine, femur, iliac crest, and calcaneus. *Journal of Bone and Mineral Research: The Official Journal of the American Society for Bone and Mineral Research.* 1999, **14**(7), pp.1167-1174.

265. Magdeski, J. The porosity dependence of mechanical properties of sintered alumina. *Journal of the University of Chemical Technology and Metallurgy.* 2010, **45**(2), pp.143-148.

266. Sabree, I., Gough, J. and Derby, B. Mechanical properties of porous ceramic scaffolds: Influence of internal dimensions. *Ceramics International.* 2015, **41**(7), pp.8425-8432.

267. Gibson, L.J. The mechanical behaviour of cancellous bone. *Journal of Biomechanics.* 1985, **18**(5), pp.317-328.

268. Fan, X. *Mechanical Characterization of Hydroxyapatite, Thermoelectric Materials and Doped Ceria.* PhD Thesis Michigan State University, 2013.

269. Liu, J., Jin, T., Chang, S., Czajka-Jakubowska, A., Zhang, Z., Nor, J.E. and Clarkson, B.H. The effect of novel fluorapatite surfaces on osteoblast-like cell adhesion, growth, and mineralization. *Tissue Engineering. Part A.* 2010, **16**(9), pp.2977-2986.

270. Macchetta, A., Turner, I.G. and Bowen, C.R. Fabrication of HA/TCP scaffolds with a graded and porous structure using a camphene-based freeze-casting method. *Acta Biomaterialia.* 2009, **5**(4), pp.1319-1327.

271. Ryshkewitch, E. Compression strength of porous sintered alumina and zirconia. *Journal of the American Ceramic Society*. 1953, **36**(2), pp.65-68.

272. Liu, D.-M. Influence of porosity and pore size on the compressive strength of porous hydroxyapatite ceramic. *Ceramics International*. 1997, **23**(2), pp.135-139.

273. Rice, R. Comparison of stress concentration versus minimum solid area based mechanical property-porosity relations. *Journal of Materials Science*. 1993, **28**(8), pp.2187-2190.

274. Le Huec, J., Schaeverbeke, T., Clement, D., Faber, J. and Le Rebeller, A. Influence of porosity on the mechanical resistance of hydroxyapatite ceramics under compressive stress. *Biomaterials*. 1995, **16**(2), pp.113-118.

275. Latella, B., Henkel, L. and Mehrtens, E. Permeability and high temperature strength of porous mullite-alumina ceramics for hot gas filtration. *Journal of Materials Science*. 2006, **41**(2), pp.423-430.

276. Kwan, Y., Stephenson, D. and Alcock, J. The porosity dependence of flexural modulus and strength for capsule-free hot isostatically pressed porous alumina. *Journal of Materials Science*. 2000, **35**(5), pp.1205-1211.

277. Peng, J.Y., Luo, X.P. and Zhang, L. Flexural strength and open porosity of two different veneering ceramics for zirconia framework. *International Journal of Applied Ceramic Technology*. 2015, **12**(2), pp.383-389.

278. Lopes, M.A., Monteiro, F.J. and Santos, J.D. Glass-reinforced hydroxyapatite composites: secondary phase proportions and densification effects on biaxial bending strength. *Journal of Biomedical Materials Research*. 1999, **48**(5), pp.734-740.

279. Huang, C. and Hsueh, C. Piston-on-three-ball versus piston-on-ring in evaluating the biaxial strength of dental ceramics. *Dental Materials*. 2011, **27**(6), pp.e117-e123.

280. Chatzistavrou, X., Newby, P. and Boccaccini, A.R. 5 - Bioactive glass and glass-ceramic scaffolds for bone tissue engineering. In: Ylänen, H.O. ed. *Bioactive Glasses*. Woodhead Publishing, 2011, pp.107-128.

281. Masuda, S., Doi, K., Satoh, S., Oka, T. and Matsuda, T. Vascular endothelial growth factor enhances vascularization in microporous small caliber polyurethane grafts. *ASAIO journal (American Society of Artificial Internal Organs)*. 1997, **43**(5), pp.M530-534.

282. Lambers, F.M., Schulte, F.A., Kuhn, G., Webster, D.J. and Müller, R. Mouse tail vertebrae adapt to cyclic mechanical loading by increasing bone formation rate and decreasing bone resorption rate as shown by time-lapsed in vivo imaging of dynamic bone morphometry. *Bone.* 2011, **49**(6), pp.1340-1350.

283. Roshan-Ghias, A., Lambers, F.M., Gholam-Rezaee, M., Müller, R. and Pioletti, D.P. In vivo loading increases mechanical properties of scaffold by affecting bone formation and bone resorption rates. *Bone.* 2011, **49**(6), pp.1357-1364.

284. Schulte, F.A., Lambers, F.M., Kuhn, G. and Müller, R. In vivo micro-computed tomography allows direct three-dimensional quantification of both bone formation and bone resorption parameters using time-lapsed imaging. *Bone.* 2011, **48**(3), pp.433-442.

285. Boccaccio, A., Messina, A., Pappalettere, C. and Scaraggi, M. 16 - Finite element modelling of bone tissue scaffolds. In: Jin, Z. ed. *Computational Modelling of Biomechanics and Biotribology in the Musculoskeletal System*. Woodhead Publishing, 2014, pp.485-511.

286. Silver, F.H. *Mechanosensing and Mechanochemical Transduction in Extracellular Matrix.* Springer, 2006.

287. Feichtinger, G.A., Morton, T.J., Zimmermann, A., Dopler, D., Banerjee, A., Redl, H. and van Griensven, M. Enhanced reporter gene assay for the detection of osteogenic differentiation. *Tissue Engineering. Part C, Methods.* 2011, **17**(4), pp.401-410.

8. Appendix

8.1. Appendix A – Work flow of double batch production

🟨	1st Batch
🟦	2nd Batch

Time	Weigh	Mix	Pack	Elite BCF 13/12-2416 furnace	Pyrotherm 1600°C furnace	Pour
08:00	🟨					
08:15	🟨	▨				
08:30		🟨				
08:45		🟨				
09:00		🟨				
09:15		🟨	▨			
09:30			🟨			
09:45			🟨			
10:00			🟨			
10:15			🟨			
10:30	🟦			🟨		
10:45	🟦	▨		🟨		
11:00		🟦		🟨		
11:15		🟦			🟨	
11:30		🟦			🟨	
11:45		🟦	▨		🟨	
12:00			🟦		🟨	
12:15			🟦		🟨	
12:30			🟦		🟨	

12:45			🟦		🟨	
Time	Weigh	Mix	Pack	Elite BCF 13/12-2416 furnace	Pyrotherm 1600°C furnace	Pour
13:00				🟦	🟨	
13:15				🟦		🟨
13:30				🟦		
13:45					🟦	
14:00					🟦	
14:15					🟦	
14:30					🟦	
14:45					🟦	
15:00					🟦	
15:15					🟦	
15:30					🟦	
15:45						🟦

8.2. Appendix B – SEM analysis of FA coated scaffolds seeded with hADSC's (36 hours)

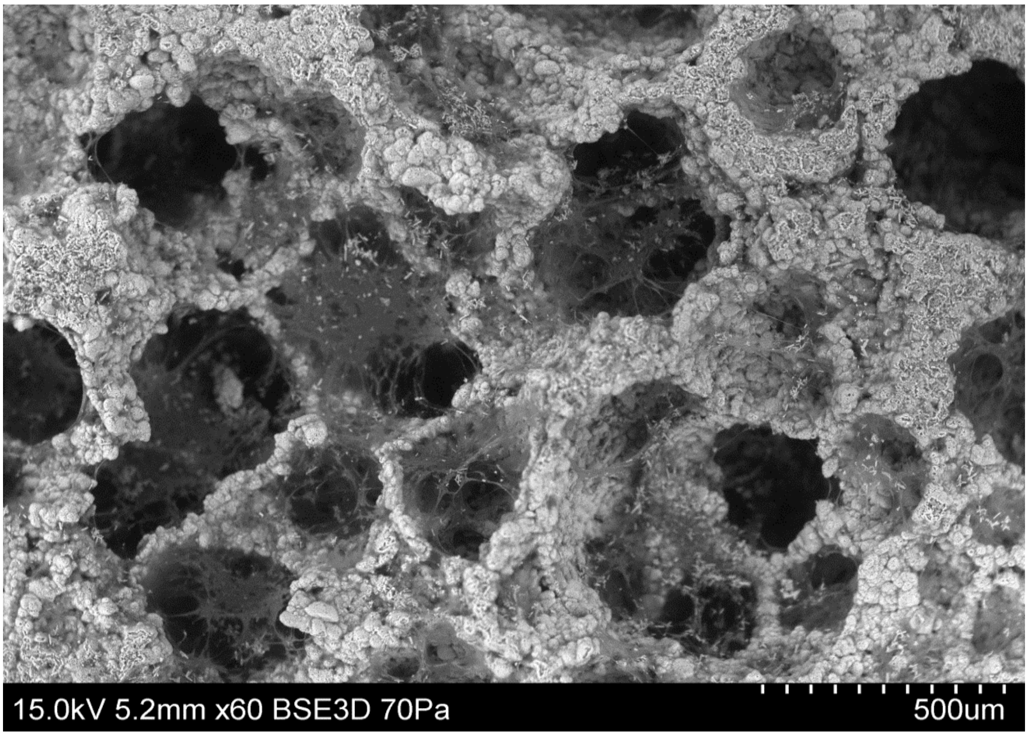

Figure 8.1 - FA coated scaffold cultured for 36 h, seeding density 1x10^6.

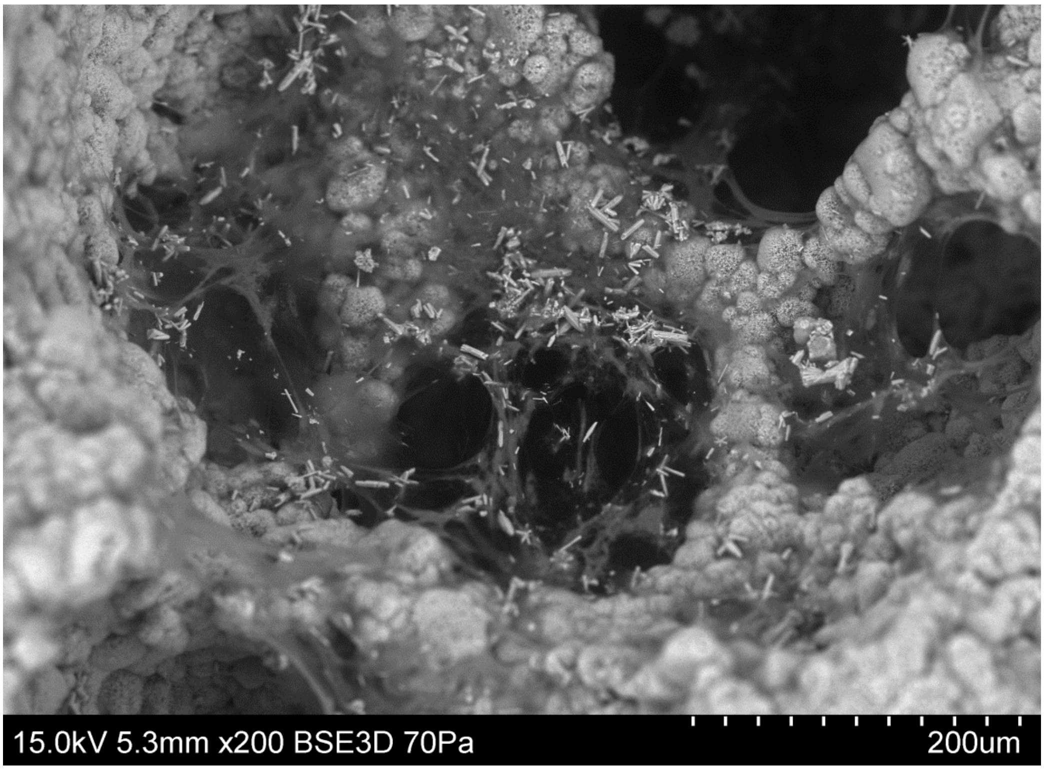

Figure 8.2 - FA coated scaffold cultured for 36 h, seeding density 1x10^6.

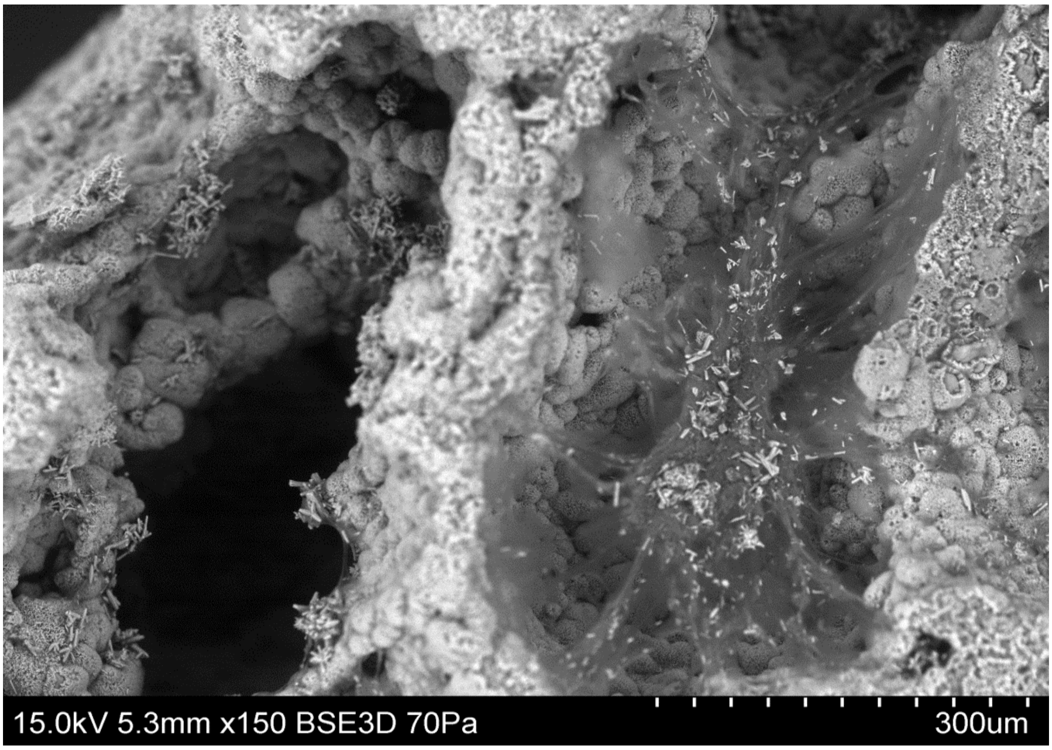

Figure 8.3 - FA coated scaffold cultured for 36 h, seeding density 1x10^6.

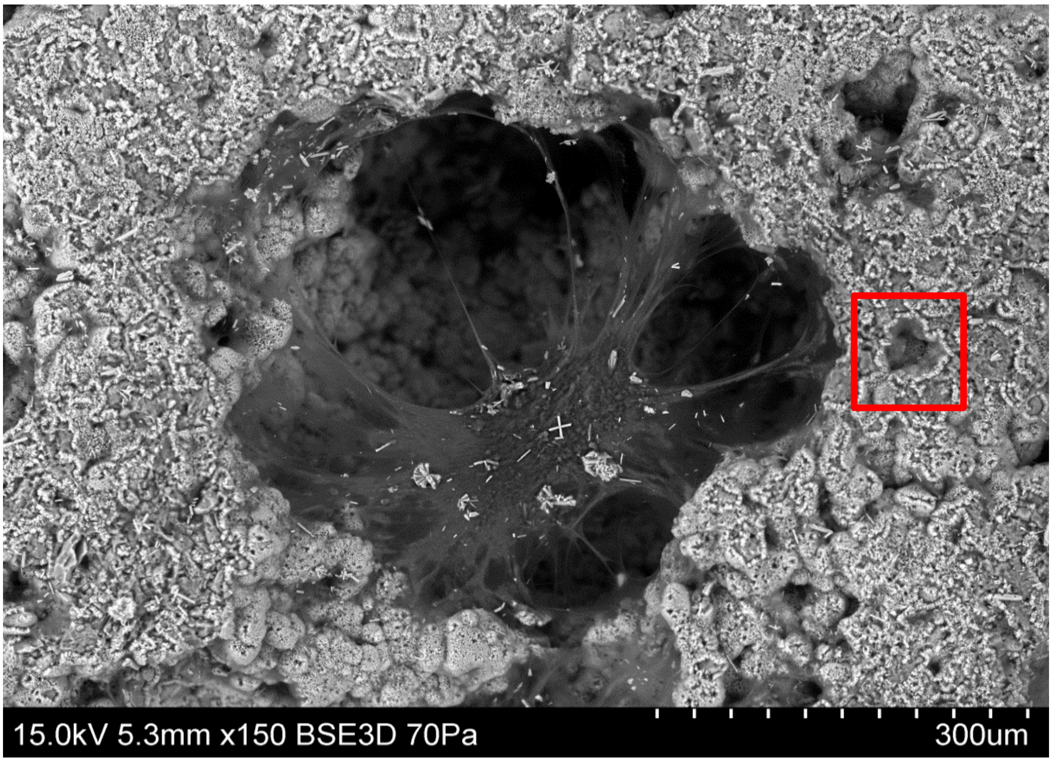

Figure 8.4 - FA coated scaffold cultured for 36 h, seeding density 1x10^6. Thin white bands show evidence of FA loss.

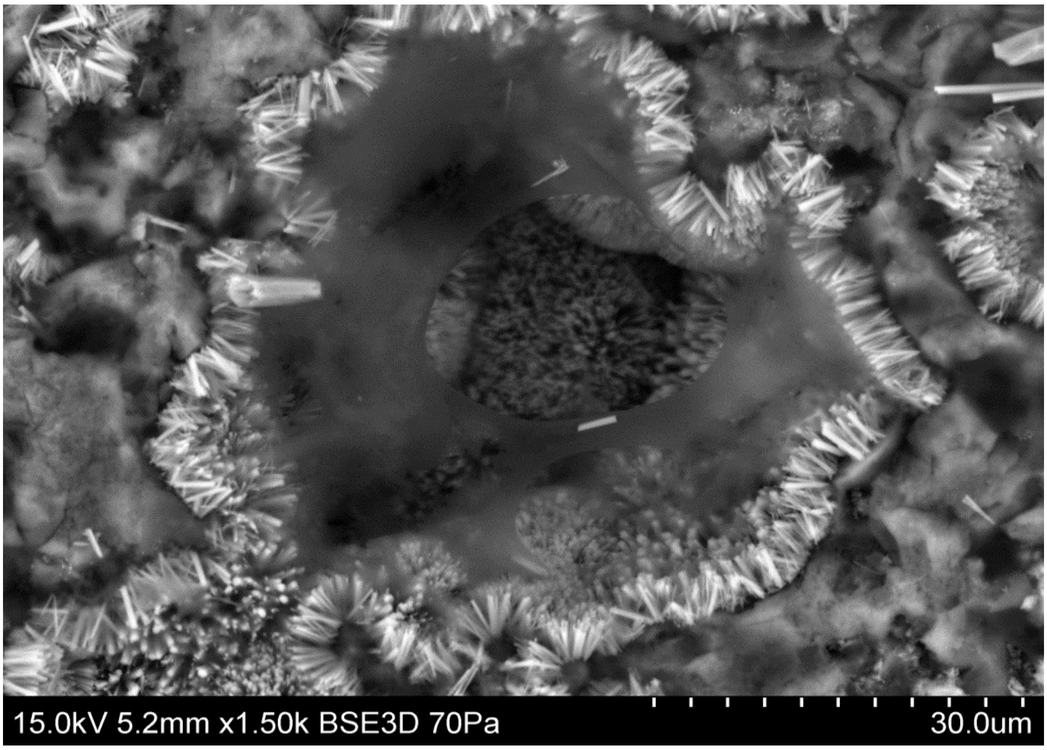

Figure 8.5 – Magnified image of region highlighted in Figure 8.4, cross section of FA layer clearly visible.

8.3. Appendix C – SPSS output of Biaxial Flexural Testing

SPSS statistical outputs for the biaxial flexural tests,

Tests of Normality

	Group	Kolmogorov-Smirnov[a]			Shapiro-Wilk		
		Statistic	df	Sig.	Statistic	df	Sig.
Biaxial Flexural Strength (MPa)	70%,4%,800(5h)	.156	19	.200*	.878	19	.020
	70%,4%,800(5h)->950(1h)	.119	20	.200*	.948	20	.342
	MICRO_75%, 5%, 800(5h)-950(1h)	.106	48	.200*	.971	48	.283
	MICRO_75%,4%, 800(5h)-950(1h)	.115	48	.135	.972	48	.304
	MICRO_50%,5%, 800(5h)-950(1h)	.059	44	.200*	.979	44	.607
	75%,5%,800(5h)-1025(1h)	.232	20	.006	.888	20	.025
	75%,4%,800(5h)	.184	20	.074	.922	20	.110
	50%,5%,800(5h)	.154	14	.200*	.937	14	.376
	50%,5%,800(5h) - 1025(1h)	.124	17	.200*	.946	17	.393
	75%,6%, 800(5h), 950(1h)	.092	24	.200*	.978	24	.860
	65%, 4%, 800(5h) 950(1h)	.287	12	.007	.697	12	.001
	75%, 5% B, Cortical Shell	.125	22	.200*	.950	22	.309

*. This is a lower bound of the true significance, a. Lilliefors Significance Correction

ANOVA

Biaxial Flexural Strength (MPa)

	Sum of Squares	df	Mean Square	F	Sig.
Between Groups	2213.559	11	201.233	142.897	.000
Within Groups	416.838	296	1.408		
Total	2630.396	307			

Multiple Comparisons

Dependent Variable: Biaxial Flexural Strength (MPa)

Bonferroni

(I) Group	(J) Group	Mean Diff (I-J)	Std. Error	Sig.	95% Confidence Interval	
					Lower Bound	Upper Bound
70%,4%, 800(5h)	70%,4%,800(5h) ->950(1h)	-1.57128*	.38017	.003	-2.8651	-.2775
	MICRO_75%, 5%, 800(5h) -950(1h)	-5.73483*	.32165	.000	-6.8295	-4.6402
	MICRO_75%,4%, 800(5h)-950(1h)	-4.76095*	.32165	.000	-5.8556	-3.6663
	MICRO_50%,5%, 800(5h)-950(1h)	.48555	.32577	1.000	-.6231	1.5942
	75%,5%,800(5h) -1025(1h)	-.62068	.38017	1.000	-1.9145	.6732
	75%,4%,800(5h)	-2.97780*	.38017	.000	-4.2716	-1.6840
	50%,5%,800(5h)	2.02158*	.41798	.000	.5991	3.4441
	50%,5%,800(5h) - 1025(1h)	2.12470*	.39618	.000	.7764	3.4730
	75%,6%, 800(5h), 950(1h)	-1.37169*	.36441	.013	-2.6119	-.1315
	65%, 4%, 800(5h) 950(1h)	-1.95949*	.43757	.001	-3.4487	-.4703

	75%, 5% B, Cortical Shell	-5.47934*	.37166	.000	-6.7442	-4.2145
70%,4%, 800(5h)->950(1h)	70%,4%,800(5h)	1.57128*	.38017	.003	.2775	2.8651
	MICRO_75%, 5%, 800(5h)-950(1h)	-4.16355*	.31583	.000	-5.2384	-3.0887
	MICRO_75%,4%, 800(5h)-950(1h)	-3.18967*	.31583	.000	-4.2645	-2.1148
	MICRO_50%,5%, 800(5h)-950(1h)	2.05684*	.32003	.000	.9677	3.1460
	75%,5%,800(5h)-1025(1h)	.95061	.37526	.780	-.3265	2.2277
	75%,4%,800(5h)	-1.40652*	.37526	.014	-2.6837	-.1294
	50%,5%,800(5h)	3.59286*	.41352	.000	2.1855	5.0002
	50%,5%,800(5h) -1025(1h)	3.69598*	.39147	.000	2.3637	5.0283
	75%,6%, 800(5h), 950(1h)	.19959	.35929	1.000	-1.0232	1.4224
	65%, 4%, 800(5h) 950(1h)	-.38820	.43332	1.000	-1.8629	1.0865
	75%, 5% B, Cortical Shell	-3.90806*	.36664	.000	-5.1558	-2.6603
MICRO_75%, 5%, 800(5h)-950(1h)	70%,4%,800(5h)	5.73483*	.32165	.000	4.6402	6.8295
	70%,4%,800(5h)->950(1h)	4.16355*	.31583	.000	3.0887	5.2384
	MICRO_75%,4%, 800(5h)-950(1h)	.97388*	.24223	.005	.1495	1.7983

	MICRO_50%,5%, 800(5h)-950(1h)	6.22038*	.24768	.000	5.3775	7.0633
	75%,5%,800(5h)-1025(1h)	5.11415*	.31583	.000	4.0393	6.1890
	75%,4%,800(5h)	2.75703*	.31583	.000	1.6822	3.8319
	50%,5%,800(5h)	7.75641*	.36045	.000	6.5297	8.9831
	50%,5%,800(5h) -1025(1h)	7.85953*	.33493	.000	6.7197	8.9994
	75%,6%, 800(5h), 950(1h)	4.36314*	.29667	.000	3.3535	5.3728
	65%, 4%, 800(5h) 950(1h)	3.77535*	.38300	.000	2.4719	5.0788
	75%, 5% B, Cortical Shell	.25549	.30553	1.000	-.7843	1.2953
MICRO_75%,4%, 800(5h)-950(1h)	70%,4%,800(5h)	4.76095*	.32165	.000	3.6663	5.8556
	70%,4%,800(5h)->950(1h)	3.18967*	.31583	.000	2.1148	4.2645
	MICRO_75%, 5%, 800(5h)-950(1h)	-.97388*	.24223	.005	-1.7983	-.1495
	MICRO_50%,5%, 800(5h)-950(1h)	5.24651*	.24768	.000	4.4036	6.0894
	75%,5%,800(5h)-1025(1h)	4.14028*	.31583	.000	3.0654	5.2151
	75%,4%,800(5h)	1.78315*	.31583	.000	.7083	2.8580
	50%,5%,800(5h)	6.78253*	.36045	.000	5.5558	8.0093
	50%,5%,800(5h) -1025(1h)	6.88565*	.33493	.000	5.7458	8.0255
	75%,6%, 800(5h), 950(1h)	3.38926*	.29667	.000	2.3796	4.3989

	65%, 4%, 800(5h) 950(1h)	2.80147*	.38300	.000	1.4980	4.1049
	75%, 5% B, Cortical Shell	-.71839	.30553	1.000	-1.7582	.3214
MICRO 50%,5%, 800(5h)-950(1h)	70%,4%,800(5h)	-.48555	.32577	1.000	-1.5942	.6231
	70%,4%,800(5h)->950(1h)	-2.05684*	.32003	.000	-3.1460	-.9677
	MICRO_75%, 5%, 800(5h)-950(1h)	-6.22038*	.24768	.000	-7.0633	-5.3775
	MICRO_75%,4%, 800(5h)-950(1h)	-5.24651*	.24768	.000	-6.0894	-4.4036
	75%,5%,800(5h)-1025(1h)	-1.10623*	.32003	.041	-2.1954	-.0171
	75%,4%,800(5h)	-3.46336*	.32003	.000	-4.5525	-2.3742
	50%,5%,800(5h)	1.53603*	.36413	.002	.2968	2.7753
	50%,5%,800(5h) - 1025(1h)	1.63915*	.33888	.000	.4858	2.7925
	75%,6%, 800(5h), 950(1h)	-1.85725*	.30113	.000	-2.8821	-.8324
	65%, 4%, 800(5h) 950(1h)	-2.44504*	.38647	.000	-3.7603	-1.1298
	75%, 5% B, Cortical Shell	-5.96489*	.30986	.000	-7.0195	-4.9103
75%,5%, 800(5h)-1025(1h)	70%,4%,800(5h)	.62068	.38017	1.000	-.6732	1.9145
	70%,4%,800(5h)->950(1h)	-.95061	.37526	.780	-2.2277	.3265

	MICRO_75%, 5%, 800(5h)-950(1h)	-5.11415*	.31583	.000	-6.1890	-4.0393
	MICRO_75%,4%, 800(5h)-950(1h)	-4.14028*	.31583	.000	-5.2151	-3.0654
	MICRO_50%,5%, 800(5h)-950(1h)	1.10623*	.32003	.041	.0171	2.1954
	75%,4%,800(5h)	-2.35713*	.37526	.000	-3.6343	-1.0800
	50%,5%,800(5h)	2.64226*	.41352	.000	1.2349	4.0496
	50%,5%,800(5h) - 1025(1h)	2.74538*	.39147	.000	1.4131	4.0777
	75%,6%, 800(5h), 950(1h)	-.75101	.35929	1.000	-1.9738	.4717
	65%, 4%, 800(5h) 950(1h)	-1.33881	.43332	.145	-2.8135	.1359
	75%, 5% B, Cortical Shell	-4.85866*	.36664	.000	-6.1064	-3.6109
75%,4%, 800(5h)	70%,4%,800(5h)	2.97780*	.38017	.000	1.6840	4.2716
	70%,4%,800(5h)->950(1h)	1.40652*	.37526	.014	.1294	2.6837
	MICRO_75%, 5%, 800(5h)-950(1h)	-2.75703*	.31583	.000	-3.8319	-1.6822
	MICRO_75%,4%, 800(5h)-950(1h)	-1.78315*	.31583	.000	-2.8580	-.7083
	MICRO_50%,5%, 800(5h)-950(1h)	3.46336*	.32003	.000	2.3742	4.5525
	75%,5%,800(5h)-1025(1h)	2.35713*	.37526	.000	1.0800	3.6343

	50%,5%,800(5h)	4.99938*	.41352	.000	3.5920	6.4067
	50%,5%,800(5h) - 1025(1h)	5.10250*	.39147	.000	3.7702	6.4348
	75%,6%, 800(5h), 950(1h)	1.60611*	.35929	.001	.3833	2.8289
	65%, 4%, 800(5h) 950(1h)	1.01832	.43332	1.000	-.4564	2.4930
	75%, 5% B, Cortical Shell	-2.50154*	.36664	.000	-3.7493	-1.2538
50%,5%, 800(5h)	70%,4%,800(5h)	-2.02158*	.41798	.000	-3.4441	-.5991
	70%,4%,800(5h)->950(1h)	-3.59286*	.41352	.000	-5.0002	-2.1855
	MICRO_75%, 5%, 800(5h)-950(1h)	-7.75641*	.36045	.000	-8.9831	-6.5297
	MICRO_75%,4%, 800(5h)-950(1h)	-6.78253*	.36045	.000	-8.0093	-5.5558
	MICRO_50%,5%, 800(5h)-950(1h)	-1.53603*	.36413	.002	-2.7753	-.2968
	75%,5%,800(5h)-1025(1h)	-2.64226*	.41352	.000	-4.0496	-1.2349
	75%,4%,800(5h)	-4.99938*	.41352	.000	-6.4067	-3.5920
	50%,5%,800(5h) - 1025(1h)	.10312	.42828	1.000	-1.3544	1.5607
	75%,6%, 800(5h), 950(1h)	-3.39327*	.39908	.000	-4.7515	-2.0351
	65%, 4%, 800(5h) 950(1h)	-3.98106*	.46684	.000	-5.5699	-2.3923

	75%, 5% B, Cortical Shell	-7.50092*	.40571	.000	-8.8817	-6.1202
50%,5%, 800(5h) - 1025(1h)	70%,4%,800(5h)	-2.12470*	.39618	.000	-3.4730	-.7764
	70%,4%,800(5h)->950(1h)	-3.69598*	.39147	.000	-5.0283	-2.3637
	MICRO_75%, 5%, 800(5h)-950(1h)	-7.85953*	.33493	.000	-8.9994	-6.7197
	MICRO_75%,4%, 800(5h)-950(1h)	-6.88565*	.33493	.000	-8.0255	-5.7458
	MICRO_50%,5%, 800(5h)-950(1h)	-1.63915*	.33888	.000	-2.7925	-.4858
	75%,5%,800(5h)-1025(1h)	-2.74538*	.39147	.000	-4.0777	-1.4131
	75%,4%,800(5h)	-5.10250*	.39147	.000	-6.4348	-3.7702
	50%,5%,800(5h)	-.10312	.42828	1.000	-1.5607	1.3544
	75%,6%, 800(5h), 950(1h)	-3.49639*	.37618	.000	-4.7767	-2.2161
	65%, 4%, 800(5h) 950(1h)	-4.08419*	.44743	.000	-5.6069	-2.5615
	75%, 5% B, Cortical Shell	-7.60404*	.38321	.000	-8.9082	-6.2999
75%,6%, 800(5h), 950(1h)	70%,4%,800(5h)	1.37169*	.36441	.013	.1315	2.6119
	70%,4%,800(5h)->950(1h)	-.19959	.35929	1.000	-1.4224	1.0232
	MICRO_75%, 5%, 800(5h)-950(1h)	-4.36314*	.29667	.000	-5.3728	-3.3535

	MICRO_75%,4%, 800(5h)-950(1h)	-3.38926*	.29667	.000	-4.3989	-2.3796
	MICRO_50%,5%, 800(5h)-950(1h)	1.85725*	.30113	.000	.8324	2.8821
	75%,5%,800(5h)-1025(1h)	.75101	.35929	1.000	-.4717	1.9738
	75%,4%,800(5h)	-1.60611*	.35929	.001	-2.8289	-.3833
	50%,5%,800(5h)	3.39327*	.39908	.000	2.0351	4.7515
	50%,5%,800(5h) - 1025(1h)	3.49639*	.37618	.000	2.2161	4.7767
	65%, 4%, 800(5h) 950(1h)	-.58779	.41956	1.000	-2.0157	.8401
	75%, 5% B, Cortical Shell	-4.10765*	.35027	.000	-5.2997	-2.9156
65%, 4%, 800(5h) 950(1h)	70%,4%,800(5h)	1.95949*	.43757	.001	.4703	3.4487
	70%,4%,800(5h)->950(1h)	.38820	.43332	1.000	-1.0865	1.8629
	MICRO_75%, 5%, 800(5h)-950(1h)	-3.77535*	.38300	.000	-5.0788	-2.4719
	MICRO_75%,4%, 800(5h)-950(1h)	-2.80147*	.38300	.000	-4.1049	-1.4980
	MICRO_50%,5%, 800(5h)-950(1h)	2.44504*	.38647	.000	1.1298	3.7603
	75%,5%,800(5h)-1025(1h)	1.33881	.43332	.145	-.1359	2.8135
	75%,4%,800(5h)	-1.01832	.43332	1.000	-2.4930	.4564
	50%,5%,800(5h)	3.98106*	.46684	.000	2.3923	5.5699

	50%,5%,800(5h) - 1025(1h)	4.08419*	.44743	.000	2.5615	5.6069
	75%,6%, 800(5h), 950(1h)	.58779	.41956	1.000	-.8401	2.0157
	75%, 5% B, Cortical Shell	-3.51986*	.42587	.000	-4.9692	-2.0705
75%, 5% B, Cortical Shell	70%,4%,800(5h)	5.47934*	.37166	.000	4.2145	6.7442
	70%,4%,800(5h)->950(1h)	3.90806*	.36664	.000	2.6603	5.1558
	MICRO_75%, 5%, 800(5h)-950(1h)	-.25549	.30553	1.000	-1.2953	.7843
	MICRO_75%,4%, 800(5h)-950(1h)	.71839	.30553	1.000	-.3214	1.7582
	MICRO_50%,5%, 800(5h)-950(1h)	5.96489*	.30986	.000	4.9103	7.0195
	75%,5%,800(5h)-1025(1h)	4.85866*	.36664	.000	3.6109	6.1064
	75%,4%,800(5h)	2.50154*	.36664	.000	1.2538	3.7493
	50%,5%,800(5h)	7.50092*	.40571	.000	6.1202	8.8817
	50%,5%,800(5h) - 1025(1h)	7.60404*	.38321	.000	6.2999	8.9082
	75%,6%, 800(5h), 950(1h)	4.10765*	.35027	.000	2.9156	5.2997
	65%, 4%, 800(5h) 950(1h)	3.51986*	.42587	.000	2.0705	4.9692

*. The mean difference is significant at the 0.05 level.